

From Albatrosses to Long Range UAV Flight by Dynamic Soaring

Vincent Bonnin

A Thesis submitted in partial fulfilment of requirements of the University
of The West of England, Bristol, and ISAE, Toulouse,
for the degree of Doctor of Philosophy

Abstract

In the domain of UAVs, endurance and range are key utility factors. However, small-sized UAVs are faced with serious limitations regarding energy storage options. A way to address this challenge is to seek for energy from the surrounding environment. One flight technique, called dynamic soaring, has been perfected by large seabirds like the albatross, which enables them to wander effortlessly in southern oceans. This thesis investigates the feasibility to find inspiration from the biological world in order to address the issue of limited endurance.

First of all, an extensive literature background sums-up a range of technical aspects that can be learnt out of the flight of albatrosses. It reviews their morphology, flight performance and sensitivity to wind strength, their flight characteristics and energy expenditure management.

Then, a methodology to simulate dynamic soaring flight is built-up by focusing first on adequate models for the vehicle and for the environment. It details the way those models are described quantitatively and qualitatively. As for the vehicle, a point mass model is chosen and applied to fixed-wing gliders of several scales, as well as to an albatross of generic dimensions. The environment is first modelled by classical boundary layer theory on a rather flat surface and then refined by taking into account specificity about the ocean boundary layer, such as varying roughness length and surface waves.

Equations of motion are detailed for both points of views, earth-relative and air relative. This yields two different sets of equations of motion, eventually representing equivalent physics. An optimization problem is then set in order to determine, for the vehicle, how to extract energy from its environment. Variations in objective function and in constraints are described before presenting the numerical integration scheme which converts the optimization problem into that of finite-dimension. The solving tools and their specificity are presented, followed by a validation of the overall methodology with a particular study case from the literature.

Basic principles of dynamic soaring flight are explicated by using a specific closed-loop study case. Energy-harvesting mechanisms are disclosed locally and next integrated over the whole flight path. A further illustration of dynamic soaring is

provided by relaxing some periodicity constraints and opening the trajectory. The specificity of the ocean boundary layer environment is finally implemented and a refined energy-harvesting strategy is presented.

Air relative equations of motion are dimensionless so as to highlight specific dynamic soaring behaviours, in the case of a simplified linear wind profile and eventually by finding an appropriate non-dimensionalization for a logarithmic wind profile. Conditions of similarities between dimensionless solutions are described and some basic DS characteristics are outlined.

Finally, various dynamic soaring performance study case are computed. Optimized trajectories are implemented for the selected vehicles and compared on a required wind strength basis. The sensitivity of the required wind strength to the net flight heading as well as to the ground clearance and to the surface roughness length is determined by drawing performance charts. In order to enlarge the scope of favourable dynamic soaring conditions, thrust-augmented trajectories are considered. The range improvements offered by dynamic soaring are compared to the straight line case, for different wind strength and different net flight headings.

Résumé de la thèse en français

Dans le domaine des drones, l'endurance et l'autonomie sont reconnues comme étant des facteurs d'utilité clés. Ces véhicules sans pilotes permettent d'élargir le spectre des missions accessibles aux aéronefs, notamment, pour certaines applications, en réduisant leur taille. Cependant, les drones de faibles dimensions sont confrontés à des limitations importantes concernant les options de stockage d'énergie. Des solutions alternatives de propulsion ont été approchées dans la littérature, comme le recours aux piles à combustible qui permet de tirer parti de l'importante densité énergétique du dihydrogène. Ou encore la modification de la chaîne énergétique à bord, en déportant la source au sol et en transmettant au véhicule l'énergie via un laser. Chacune de ces options a ses limites à l'heure actuelle. Une autre façon de répondre à cet enjeu est d'extraire de l'énergie à l'environnement ambiant au véhicule. Cela peut se décliner sous plusieurs formes et des solutions ont été abordées par le passé, comme le vol de pente, le vol de thermique ou encore l'exploitation photovoltaïque de l'énergie solaire. Ce sujet se rallie à la même démarche générale d'exploitation de l'énergie ambiante, mais se base sur des principes d'extraction différents. Par ailleurs, ces problématiques s'inscrivent dans un contexte de bio-mimétisme, où la nature est considérée comme une source d'inspiration, d'autant plus alors que les drones peuvent atteindre des dimensions comparables à celles des oiseaux.

Une technique de vol a été perfectionnée par de grands oiseaux de mer comme l'albatros, ce qui leur permet de parcourir les océans de l'hémisphère sud, sur des milliers de kilomètres, sans effort. En effet, les travaux de biologistes ont permis d'identifier certaines caractéristiques du vol de l'albatros. Parmi les plus significatives figurent leur vol non battu et les distances considérables qu'ils parcourent, ce qui sous-entend une gestion énergétique intéressante. Afin de bénéficier d'une source d'informations aussi large que possible concernant le vol de l'albatros, une vaste revue bibliographique est faite des contributions biologistes offrant un éclairage sur les aspects physiques de l'albatros et de son vol. A ce titre, cette bibliographie s'attache à se distancer des aspects comportementaux, ou du moins à les distinguer, pour se concentrer sur les informations physiques du vol.

Ainsi, on peut apprendre que des spécimens équipés de balises GPS ont parcouru des distances de voyages considérables, allant même jusqu'à des circonvolutions dans les latitudes sud. Ces performances sont associées à des vitesses de

voyage pouvant dépasser 900 kilomètres par jour. Cette vaste couverture des mers s'explique, pour l'aspect comportemental, par un besoin de l'oiseau de maximiser la probabilité de rencontrer des proies qui ont une distribution très sporadique en surface. Ces performances soulèvent d'autant plus d'interrogations que la morphologie des albatros démontre une incapacité à battre durablement des ailes. En outre, toutes les observations font de fait état d'un vol strictement plané, pour lequel l'albatros est en revanche particulièrement adapté. En effet, ses ailes ont un grand allongement et peuvent être maintenues déployées sans que l'oiseau force, par l'intermédiaire d'un tendon. Dès la fin du XX^{ème} siècle, il a été conjecturé que ces oiseaux tiraient parti du vent. De fait, la répartition de leurs colonies sur les îles isolées des mers du sud correspond effectivement aux zones qui voient les vents les plus fréquents et les plus puissants. Cette dépendance au vent est même marquée par des oiseaux bloqués sur l'eau lorsque le vent vient à tomber, alors qu'ils passent la majorité de leur temps en l'air. D'autres informations sont utiles pour enrichir la compréhension de ce rapport au vent. Leur direction de vol par rapport au vent est orientée dans le même sens que le vent, mais avec une composante de travers fortement prononcée, de telle sorte que l'oiseau vole aux alentours de 45° par rapport au sens du vent. Enfin, à plus faible échelle, leur vol fait apparaître des trajectoires sinueuses et cycliques, avec des virages successifs en montée et en descente, entre la surface et des altitudes aux alentours de 15-20 mètres maximum. Il apparaît que les albatros tirent profit des gradients de vents qui se forment à la surface, dues aux interactions de couches limites atmosphériques.

L'ensemble de ces considérations, associées au fait qu'un drone de faibles dimensions peut, à priori, reproduire les dimensions et performances planés de l'albatros, font de cette technique un sujet de recherche prometteur dans le domaine des drones. En effet, la source d'énergie requiert uniquement la présence de vent et est uniformément présente sur de vastes zones géographiques, au contraire des thermiques par exemples, qui sont limitées à des zones réduites et clairsemées. La technique de vol démontrée par les albatros est quelquefois appelée vol de gradient en français, mais on lui préférera l'expression anglo-saxonne *dynamic soaring* (DS), plus couramment usitée. Elle traduit en effet la dynamique nécessaire à l'extraction d'énergie, là où d'autres techniques, comme le vol de thermique ou de pente, voit l'extraction se faire sous forme constante, via un régime de vol statique. Lors du vol par DS, au contraire, les échanges d'énergie sont périodiques, avec des gains et des pertes, au travers de manœuvres dynamiques de vol. La question principale de ce travail de recherche consiste à savoir s'il est faisable, et dans quelle mesure, d'exploiter le DS afin de répondre aux enjeux de vol longue distance pour des drones. Ce travail de recherche a une dimension

clairement multidisciplinaire et on conceptualisera trois domaines de recherche afin de structurer notre raisonnement. Il s'agit du véhicule, de l'environnement et des trajectoires. Différents objectifs de recherche sont déterminés, relatifs à chacun de ces concepts et à la façon dont ils s'influencent.

Afin de circonscrire le sujet et ses développements, une bibliographie de la littérature est faite, parcourant les différentes approches d'extraction d'énergie au vent qui ont pu être étudiées. Cela comprend le *gust soaring*, ou vol de rafale, qui exploite les variations stochastiques des composantes verticales de la masse d'air, au sein de la couche limite atmosphérique turbulente. Les échelles de temps considérées sont faibles, comparés au DS, qui exploite la répétabilité des conditions rencontrées au cours de cycles identiques de trajectoires. Le *dynamic soaring* nécessite la présence de gradient de vent ainsi que leur connaissance à priori et peut donc être envisagée sous différentes formes. La revue bibliographique parcourt ainsi les études du DS qui ont été faites non seulement sur une surface pseudo-plane, mais aussi en aval d'une colline, dans le courant d'altitude *jet stream* ou encore au sein d'une tempête avec un champ rotationnel. Cette revue permet de fixer les bases de notre étude et de confirmer ses objectifs, en révélant la nécessité de réunir les différents points de vue existants, notamment concernant les principes d'extraction d'énergie.

Notre étude s'est tout d'abord attachée à modéliser l'environnement et le véhicule, avant de faire interagir les deux. Le chapitre III expose cette approche, en détaillant tout d'abord le choix des modèles physiques représentatifs de l'environnement et du véhicule avant de s'attarder sur leurs quantifications. Concernant le véhicule, un modèle de masse ponctuelle est choisi, qui concentre tous les efforts au centre de gravité. La simplicité de ce modèle est attractive pour l'application qui est recherchée et se justifie par le fait que l'échelle des gradients de vent permet d'utiliser une masse ponctuelle pour représenter la dynamique du vol. En revanche, certaines contraintes opérationnelles, liées à l'évolution du véhicule, comme la limitation du taux de roulis, doivent alors être déterminées intuitivement car leur évolution n'est régie par aucune équation. Une fois ce choix fait, le premier véhicule considéré reprend la morphologie de l'albatros, établie par les biologistes. Puis, afin de s'affranchir des disparités liées aux dimorphismes entre spécimens et aux incertitudes des mesures anatomiques, trois plateformes à voilure fixe, basées sur des architectures de moto-planeurs, sont considérées. Elles correspondent à trois échelles de véhicule différentes, choisies pour représenter le compromis entre taille et performances de vol plané et permettre ainsi d'explorer la faisabilité du vol par *dynamic soaring* pour différentes dimensions de drone.

En ce qui concerne l'environnement, dans un premier temps, une surface pseudo-plane est considérée et un profil logarithmique, représentatif d'un profil de vitesse moyen de couche limite atmosphérique, est choisi. En raison des irrégularités de surface, la loi logarithmique fait intervenir la longueur de rugosité, qui est en directe correspondance avec l'état de surface considéré. Elle fait aussi intervenir, plus classiquement, la vitesse de friction qui est une représentation directe de la contrainte pariétale. Ainsi, ces deux variables permettent de définir un profil de vitesse moyen, qui prend statistiquement en compte les irrégularités de surface. Or il apparaît que les longueurs de rugosité utilisées dans la littérature sur le DS sont d'un ordre de grandeur trop important pour correspondre à celles rencontrées en mer. Une correction est proposée avec la prise en compte d'un modèle de rugosité qui lie directement la longueur de rugosité au vent rencontré, suggérant ainsi une corrélation implicite entre contrainte pariétale et état de surface. Le profil de vitesse n'est alors plus figé mais dépendant des conditions environnementales. En outre, il apparaît dans la littérature que les vagues jouent probablement un rôle dans la technique de vol des albatros. Si l'interaction vent-vague est un très vaste sujet, il a été décidé de se concentrer sur l'influence d'un vague sinusoidale, corrélée aux conditions de vent via une méthodologie simple, reprenant des mesures faites en mer. Cette vague, peu creusée, est représentative d'une houle et engendre des déplacements d'air à son voisinage, due au mouvement ondulatoire de la vague. Ainsi, la face montante de la vague voit l'apparition d'une composante verticale montante de la vitesse air à son voisinage, alors qu'elle est pourtant sous le vent.

Une fois que les modèles environnement et véhicule sont déterminés, les trajectoires permettant d'exploiter le DS doivent être établies. L'unique façon de prouver la faisabilité de cette technique de vol est en effet de montrer l'existence d'une trajectoire de vol y correspondant. A cet effet, il est dans un premier lieu nécessaire de mettre en place les équations qui régissent l'évolution de véhicule au sein de son environnement. Le point de vue choisi pour l'observation de cette évolution est primordial pour l'écriture des équations. Deux options sont possibles, se baser dans un repère galiléen lié à la terre ou alors se déplacer avec la masse d'air que le véhicule traverse. Les échanges d'énergie entre véhicule et masse d'air ont aussi des interprétations différentes suivant le référentiel, dans la mesure où la définition même de l'énergie dépend du point de vue. Le point de vue terrestre est choisi et les six équations de la dynamique, gouvernant l'évolution de six variables d'état liées au véhicule, sont écrites. Celles-ci dépendent de l'état même de ces variables ainsi que des variables de contrôle, en l'occurrence le coefficient de portance et l'angle de roulis. Si

ces paramètres ne sont en réalité pas contrôlables directement lors du pilotage réaliste du véhicule, ce sont les variables de plus bas niveau disponibles avec le modèle de masse ponctuelle. Pour garantir toutefois que l'évolution de ces variables n'est pas fantaisiste, il est nécessaire de borner leurs taux d'évolution ainsi que leurs dérivées première et seconde, ceci afin d'obtenir des fonctions doublement continue, physiquement cohérentes.

La singularité du problème vient du fait de la dépendance aux variables de contrôle, qui pilotent la trajectoire et doivent être, d'une certaine manière, guidées dans leur évolution afin de trouver la trajectoire permettant d'exploiter le *dynamic soaring*. La méthodologie employée consiste à trouver la meilleure trajectoire, en mettant en place et en résolvant un problème d'optimisation. La formulation générale du problème est assez générique, avec une fonction exprimant l'objectif et des contraintes associées. L'objectif est de minimiser la vitesse du vent nécessaire à l'établissement d'une trajectoire énergétiquement neutre, c'est-à-dire qui voit les pertes du véhicules compensées exactement par ses gains. Un critère important est la périodicité de la trajectoire. En effet, il est aisé pour un véhicule d'extraire durant une certaine période de l'énergie au vent. En revanche, rendre ce processus reproductible est le défi du vol par DS. Les contraintes du problème d'optimisation incluent ainsi une périodicité des variables, à l'exception, pour certains cas, où un déplacement horizontal est permis entre situation initiale et finale. Il est à noter que la reproductibilité des cycles de trajectoires se base ainsi sur l'hypothèse d'une homogénéité de la loi de vitesse de vent.

Une étape plus complexe est la conversion de ce problème purement mathématique en un problème de dimension finie, qui peut être ensuite abordé par des techniques numériques d'optimisation. La première tâche consiste à diviser l'intervalle de temps en sous-intervalles et en exprimant les équations de la dynamique sous forme de contraintes, grâce à un schéma d'intégration numérique sur chaque intervalle. Sans rentrer dans les détails, la fonction dérivée, pour chaque équation, est interpolée, sur chaque intervalle, par un polynôme quadratique en trois points de collocation, tandis que les variables d'états sont interpolés par un polynôme de Hermite. De cette manière l'intégration des équations est implicitement effectuée au cours de l'optimisation. D'autres contraintes opérationnelles sont ajoutées, en plus de celles de périodicité, comme par exemple le non-décrochage ou la garde au sol. Le problème engendré est un problème d'optimisation contrainte non linéaire, que l'on résout avec le solveur SNOPT. Un cas de validation est effectué en reproduisant des conditions déjà étudiées dans la littérature et la correspondance entre les deux valide la méthodologie.

Une fois la méthodologie établie, le chapitre V s'attache à l'interprétation des résultats, avec un accent particulier porté sur la compréhension des mécanismes d'extraction d'énergie. Les phases caractéristiques des trajectoires par DS sont décrites en se basant sur un cas de trajectoires fermées, pour laquelle le véhicule revient exactement à sa position de départ, avec la même énergie. Cela démontre au passage la faisabilité de se maintenir en position, virtuellement indéfiniment, indépendamment de la direction du vent. La trajectoire n'est alors pas une boucle simple mais constituée de deux boucles internes, enchainées pour former l'aspect d'un 8. Quatre phases de vol forment invariablement les trajectoires par *dynamic soaring* : une montée face au vent, un virage dans le vent en haut de boucle, une descente vent arrière et un virage contre le vent proche de la surface. Si ces quatre phases se retrouvent invariablement, leurs amplitudes dépendent de la nature de la trajectoire (ouverte ou fermée) et du cap net de voyage souhaité. On montre que l'extraction d'énergie se fait lors de la montée face au vent, du virage haut et de la descente et que le virage contre le vent concentre les principales pertes. Il est montré que ces échanges d'énergie sont les résultats du travail des forces non conservatives qui s'appliquent sur le système, en l'occurrence les forces aérodynamiques. Des graphiques présentant les triangles des vitesses et projections des forces permettent de montrer comment la portance, orientée par la vitesse aérodynamique, est déviée dans le sens du mouvement lors des trois phases citées et de manière opposée lors virage bas. En outre, l'expression de la puissance des forces se développe et fait apparaître que la traînée peut, elle aussi, avoir une composante qui joue un rôle moteur, tandis que la seule composante invariablement négative provient de la composante de la traînée opposée à la vitesse air. La propension du véhicule à exposer sa face inférieure orthogonalement à la direction du vent lorsque l'altitude maximale est atteinte est similaire à ce qui est observé chez les albatros et correspond à la configuration qui maximise la puissance extraite au vent. Il est montré comment le gradient de vent permet au véhicule de ne pas perdre trop d'énergie lors du virage bas, mais qu'en aucun cas l'énergie est extraite du gradient de vent. A ce titre, le virage contre le vent est une phase particulièrement critique pour le vol par DS, dans la mesure où un changement mineur d'altitude a un impact direct sur la vitesse du vent rencontrée lors du virage, en raison du fort gradient présent à faible hauteur. La contrainte de garde au sol minimum représente des conditions favorables au vol par DS lorsqu'elle autorise des faibles séparations entre surface et véhicule.

Après s'être intéressés au fondamentaux du vol par *dynamic soaring*, un cas d'étude simulant le vol de l'albatros de la manière la plus réaliste possible est mis en place. Dans un premier temps, l'impact d'une longueur de rugosité est évalué. Il est

montré que la prise en compte d'une longueur de rugosité représentative des conditions océaniques engendre une augmentation de la vitesse du vent nécessaire pour voler par DS (Il est montré plus tard que la vitesse de friction n'est en revanche pas impactée). Cela suggère que les albatros, dont le vol est observé à des vitesses de vent plus faibles, utilisent des mécanismes de vol non pris en compte par la simulation sur une surface pseudo-plane. Celle-ci est donc enrichie par la présence de vagues, et il est montré que le véhicule se déporte du côté de la face montante de la vague pour y effectuer son virage bas, là où la vague produit une composante verticale montante. Il est ainsi établi que le véhicule peut bénéficier de la présence de vagues, afin d'abaisser la vitesse de vent requise au vol par DS. Toutefois, des écarts significatifs persistent entre la vitesse de vent théorique obtenue et celles relevées lors des vols des albatros. Cela souligne des raffinements utilisés par les albatros que la simulation proposée ne couvre pas. On peut conjecturer sur l'exploitation des rafales au sein d'un environnement en vent non pas stationnaire mais turbulent, l'exploitation de vagues plus formées du spectre qui font apparaître des phénomènes de nature différente, comme le décollement de la couche limite, ainsi qu'une rugosité de surface plus prononcée que dans notre modèle, correspondant à une mer plus jeune.

La thèse, s'intéresse, au cours du chapitre VI, à une approche plus mathématique du DS, afin de comprendre comment les variables du problème peuvent être liées entre elles. En effet, un inconvénient des simulations faites dans le chapitre précédent est qu'elles sont propres à un véhicule, à des contraintes opérationnelles précises et à des conditions de vent particulières. Afin de rechercher comment les variables liées à ces paramètres interagissent entre elles, indépendamment des métriques associées, une analyse adimensionnelle des équations est effectuée. Les équations de la dynamique, écrites dans le référentiel lié à la masse d'air, se prêtent bien à cette approche en limitant les angles de projection. Elles sont donc normalisées, via un choix de variables de références pour chaque unité. Dans un premier temps, un profil de vent linéaire est choisi (avec un gradient constant) et l'adimension se fait aisément, en faisant apparaître un paramètre de similitude qui implique notamment la charge alaire et le gradient de vent. Ainsi l'étude fait apparaître, en théorie, des familles de problèmes dont les solutions adimensionnées sont identiques entre elles. Il est donc possible, à partir d'une solution, d'extrapoler celles qui ont le même paramètre de similitude. Cela est vérifié via des simulations, validant au passage la méthodologie. En revanche, une limitation du profil de vent linéaire est qu'il ne fait pas apparaître l'augmentation du gradient de vitesse en proche surface, qui semble pourtant primordial dans le vol par DS, au vu des observations faites des albatros et des simulations établies plus tôt. Ainsi,

cette même approche est reprise pour un profil de vitesse qui suit la loi logarithmique définie précédemment. Une normalisation est trouvée et validée par des simulations, mais les solutions identiques entre elles impliquent des contraintes particulières entre l'altitude minimale et la vitesse de friction, ce qui, en pratique, semble peu utile. En revanche, cette approche illustre quelques résultats intéressants, notamment en faisant apparaître la charge alaire comme paramètre de similitude et en montrant que la vitesse de friction nécessaire ne varie pas quand la longueur de rugosité change.

Enfin, une fois quelques propriétés remarquables fournies par l'analyse adimensionnelle, la thèse s'attache, lors du dernier chapitre, à simuler les variations de performances qui peuvent être obtenues lors du vol par DS, en changeant le véhicule, les conditions opérationnelles ou encore les conditions environnementales. Ainsi, les trois véhicules sont testés, et il apparaît que le compromis entre faible envergure et performances de plané tourne à l'avantage de ces dernières. En effet, le véhicule de plus grande envergure parvient à voler par DS avec le minimum de vent requis. Il apparaît ainsi que le DS s'adapte moins bien, dans les conditions simulées, aux véhicules de faibles dimensions, mais que les perspectives pour des drones de plus grandes tailles sont intéressantes. Ensuite, pour un véhicule donné, les conditions opérationnelles et de surface sont changées. Il apparaît qu'une forte rugosité permet de réduire la vitesse du vent nécessaire (même si la vitesse de friction est constante) et qu'elle permet aussi de maximiser l'étendue des angles de voyage accessible par DS. D'autre part, une faible garde au sol a aussi les deux avantages cités précédemment. Enfin, dans la mesure où du vol purement plané exige des conditions particulières en vent, le vol motorisé est approché pour compléter le DS lorsque le vent est trop faible pour permettre du vol purement plané. L'autonomie permise alors par le DS est alors étudiée en fonction du cap net de voyage choisi par rapport au vent. Puis, le vent est progressivement diminué. Il apparaît que le DS permet d'améliorer significativement l'autonomie du véhicule en conditions de vent, mais qu'au fur et à mesure que le vent diminue, l'avantage procuré par le DS faiblit et se rétrécit à une zone de direction de vol de plus en plus faible.

Ainsi il apparaît que le DS, tel que simulé sur une plaque rugueuse pseudo-plane, permet au véhicule de se maintenir en l'air et de se déplacer gratuitement. La diminution du vent proche de la surface dispense la perte de trop d'énergie lors du virage contre le vent et permet ainsi de limiter la puissance du vent nécessaire au vol par DS. En revanche, il semble peu probable que les albatros parviennent à leurs performances en se contentant de ces seuls phénomènes. En effet, même en ajoutant un modèle de vague aux simulations, les vents théoriques obtenus sont encore trop élevés pour correspondre aux conditions mesurées en mer. Si les albatros tirent aussi parti

d'interactions de surface plus complexes que celles modélisées, il apparaît difficile pour un drone de piloter son vol en proche surface, au sein d'un environnement hautement turbulent. En revanche, une option peut être d'exploiter justement ces turbulences, à la manière du *gust soaring*, le long des trajectoires de *dynamic soaring*. Les simulations destinées à reproduire ces conditions devront probablement approcher un modèle de véhicule plus complexe que celui de masse ponctuelle, au vu de la faible échelle des gradients de vent turbulents. D'autre part, une voie de développement nécessaire concerne le pilotage du *dynamic soaring*. Deux approches peuvent être suivies, en mémorisant des dizaines de cycles de trajectoires, pour différentes conditions, puis en sélectionnant celles qui correspondent aux conditions souhaitées. Ou alors en mettant en place des lois de contrôle qui se basent sur la compréhension physique du *dynamic soaring*. Quel que soit le choix du mode de pilotage, la faisabilité du vol par DS reposera sur la capacité du véhicule à voler en proche surface, en présence de vent.

Acknowledgements

This PhD was the first to be financed by the DGA as part of the Fr-UK co-agreement with the DSTL, which aims at funding research in areas of joint interest. I would like to express my gratitude to both institutions for their support and interest in this topic. I thank especially Peter Wilkins at DSTL for his kind follow-up of my progress.

I would like to thank and praise the association *Le Tomato*, for believing in my rather utopic project, at that time, to make a PhD about the flight of the albatross. I am very grateful to Sébastien Lefebvre and Bruno Révelli-Falcoz for their role as godfathers. But one must give honour where honour is due and the beautiful impulse I have been granted owes everything to the dedication of an exceptional woman, Brigitte Révelli-Falcoz.

I would like to thank my supervisors, Jean-Marc Moschetta, Emmanuel Bénard and Chris Toomer, for embarking on this journey and accepting to supervise this jointly-conducted project. Seeing how the topic gained interest to their eyes is a real reward to me and I would like to thank them for their time, support and somehow tolerance towards my stubbornness.

I feel honoured by the presence of Eric Poquillon, Sanja Dogramadzi, Allan Bonnet, Kevin Knowles and Pascal Morin in the jury and would like to thank especially Kevin Knowles, Sanja Dogramadzi and Pascal Morin for accepting to review my thesis.

I would like to kindly salute and express my gratitude to my Mum and Dad, for their love, support and for the great education they provided me with. They raised me with inspiration and discernment, and turned me into a curious analytical young adult.

I am fortunate to know a few remarkable human beings that I feel privileged to count as friends. Their ability to make me put things in perspective and to raise a childish and raw enthusiasm is something very precious. Their care and their support towards this PhD have been real landmarks regarding the personal relevance of such a project. I would like to name Sylvain Aubry, Sylvain Carrozza and Florian Gaudin-Delrieu from those inspiring high school years, as well as Zaki Leghtas and Hicham Sabir, for providing me with an acute and down to earth point of view.

Finally, in the course of this PhD, I have been soaring alongside a very beautiful bird, unique to me in many ways. Crossing paths at the beginning of this period has been one my greatest luck and started a prolific period, both emotionally and intellectually. I would like to thank Audrey for the best she sees in me, for her support and it is fair to say, for her patience. To clear skies ahead and far beyond.

*Souvent, pour s'amuser, les hommes d'équipage
Prennent des albatros, vastes oiseaux des mers,
Qui suivent, indolents compagnons de voyage,
Le navire glissant sur les gouffres amers.*

*A peine les ont-ils déposés sur les planches,
Que ces rois de l'azur, maladroits et honteux,
Laissent piteusement leurs grandes ailes blanches
Comme des avirons traîner à côté d'eux.*

*Ce voyageur ailé, comme il est gauche et veule !
Lui, naguère si beau, qu'il est comique et laid !
L'un agace son bec avec un brûle-gueule,
L'autre mime, en boitant, l'infirme qui volait !*

*Le Poète est semblable au prince des nuées
Qui hante la tempête et se rit de l'archer ;
Exilé sur le sol au milieu des huées,
Ses ailes de géant l'empêchent de marcher.*

Charles Baudelaire, *L'Albatros*, in *Les Fleurs du Mal*, 1861

Contents

Abstract	i
Résumé de la thèse en français.....	iii
Acknowledgements	xiii
Nomenclature	xxi
Chapter I Finding Guidance from Albatross Flight	1
I.1 The UAV Context.....	2
I.2 The Albatross Legacy	7
I.2.1 Morphology Characteristics	7
I.2.2 Travelling Performances & Sensitivity to Wind.....	9
I.2.3 Flight Behaviour and Energetics	16
I.2.4 Summary of Inputs from the Biological World.....	20
I.2.5 Promising Perspectives.....	21
I.3 Main features of Dynamic Soaring Flight.....	22
I.4 Research Question & Objectives.....	24
I.4.1 Research Question	24
I.4.2 Research Areas Breakdown.....	24
I.4.3 Underlying Research Questions	25
I.4.4 Research Objectives.....	25
I.4.5 Thesis Outline.....	26
I.5 Summary of Chapter I.....	27
Chapter II Background of Wind Energy Extraction	29
II.1 Contributions to Knowledge	29
II.2 Literature Background	30
II.2.1 Point of view	30
II.2.2 Simulation of Dynamic Soaring	30
II.2.3 Jet Stream	32
II.2.4 DS in hurricanes	33
II.2.5 DS at Ridges	34

II.2.6	Gust Soaring	34
II.2.7	Practical Aspects.....	35
II.3	Overview and Critical Summary	38
Chapter III	Modelling a Vehicle and its Environment.....	39
III.1	The Vehicle Model.....	39
III.1.1	Baseline Designs.....	39
III.1.2	Quantification of Vehicles	42
III.1.3	Point Mass Model.....	52
III.2	Environment Model.....	53
III.2.1	Wind Profiles over rather Flat Surfaces.....	53
III.2.2	Ocean Waves.....	58
III.2.3	Wind field over Waves	61
III.3	Summary of Chapter III.....	68
Chapter IV	Motion & Optimization.....	69
IV.1	Equations of Motion.....	69
IV.1.1	Point of View	69
IV.1.2	Earth Point of View	74
IV.1.3	Air relative point of view.....	77
IV.2	Optimization.....	80
IV.2.1	Optimal Control Problem.....	80
IV.2.2	Conversion into a Parameter Optimization Problem	84
IV.2.3	Solving Methodology and Tools	88
IV.2.4	Local Optimizer and Sensitivity to Initiation Variables ..	90
IV.3	Validation.....	90
IV.3.1	Simulating Albatross Flight.....	90
IV.4	Summary of Chapter IV.....	93
Chapter V	Fundamentals of DS Flight.....	95
V.1	The 3D Closed-Trajectory.....	95
V.2	Energy-Harvesting Mechanisms	101
V.2.1	Contributions from Aerodynamic Forces.....	101
V.2.2	Acceleration in the direction of the wind	104
V.2.3	Overall cycle of total Energy	105

V.2.4	Exploiting Wind Power within the Wind Gradient	109
V.3	Opening the Loop.....	112
V.4	Albatross Flight in the Ocean Boundary Layer	117
V.4.1	Realistic Roughness	118
V.4.2	Influence of Waves.....	118
V.5	Summary of Chapter V	123
Chapter VI	Non-Dimensionalization of DS Flight.....	125
VI.1	Linear Wind Profile	125
VI.1.1	Theory	125
VI.1.2	Dimensionless Optimization Problem.....	128
VI.1.3	Simulation with Identical Wing Loading	129
VI.1.4	Simulation with Various Wing Loadings	131
VI.2	Logarithmic Wind Profile.....	135
VI.2.1	Non-dimensionalization of EoM.....	135
VI.2.2	Application with Identical Wing Loading.....	139
VI.2.3	Application with Various Wing Loadings.....	141
VI.2.4	Non-dimensionalization of Thrust-Powered DS	144
VI.2.5	Condition to equivalence	148
VI.3	Summary of Chapter VI.....	150
Chapter VII	DS Flight Performances	151
VII.1	Comparisons between UAVs.....	151
VII.1.1	Delair-Tech DT-18.....	152
VII.1.2	Mariner.....	155
VII.1.3	Cloud Swift.....	157
VII.1.4	Discussion on Vehicle Performances	163
VII.2	Variation in DS performance.....	166
VII.2.1	Sensitivity to Surface Roughness Length.....	166
VII.2.2	Sensitivity to Wing Tip Clearance.....	170
VII.3	Thrust-Augmented Dynamic Soaring	171
VII.3.1	Basic features.....	172
VII.3.2	Range Sensitivity to the Wind.....	175
VII.3.3	Range enhancement by DS.....	182
VII.4	Summary on DS Performances	189

Conclusion.....	191
Summary of findings.....	191
Perspectives.....	194

Nomenclature

Acronyms

AMPL	A Mathematical Programming Language
BVLOS	Beyond Visual Line-Of Sight
DS	Dynamic Soaring
EoM	Equations of Motion
GTE	Global Truncation Error
LTE	Local Truncation Error
MAC	Mean Aerodynamic Chord
SNOPT	Sparse Nonlinear OPTimizer
UAV	Unmanned Aerial Vehicle
RC	Radio-Controlled

Greek Symbols

α	Charnock's parameter
β	Local wind gradient, s^{-1}
γ	Flight path angle, <i>rad</i>
Δt	Time step, <i>s</i>
η_{prop}	Propulsion efficiency
λ	Wavelength, <i>m</i>
ν	Viscosity, m^2/s
ρ	Air density, kg/m^3
τ_p	Shear stress, N/m^2
ϕ	Bank angle, <i>rad</i>
χ	Von Karman constant
ψ	Azimuth angle, <i>rad</i>

ψ_{net}	Net travelling direction, <i>rad</i>
ω	Wave angular frequency, s^{-1}

Roman Symbols

a	Wave amplitude, <i>m</i>
AoA	Angle of attack, <i>rad</i>
AR	Wing aspect ratio
b	Wing span, <i>m</i>
Bat	Charge state of the battery, <i>J</i>
c	Wave phase velocity, <i>m/s</i>
C_{D0}	Zero-lift drag coefficient
C_{Di}	Induced drag coefficient
$C_{Dk}, k \in \{1,2,3,4\}$	Drag coefficients of C_L terms of degree <i>k</i>
C_f	Boundary layer friction coefficient
C_L	Lift coefficient
$C_{L,max}$	Maximum lift coefficient
$Conso_{min}$	Minimum specific consumption in straight line, <i>J/km</i>
Co_s	Energy consumption per net distance travelled, <i>J/km</i>
C_{Roll}	Rolling moment coefficient
D	Drag, <i>N</i>
e	Oswald's coefficient
E_{tot}	Vehicle total energy, <i>J</i>
g	Gravitational acceleration, m/s^2
G_{clear}	Ground clearance, <i>m</i>
I_{xx}	Vehicle longitudinal inertia, $kg.m^2$
k	Wave spatial frequency, m^{-1}
L	Lift, <i>N</i>
m	Vehicle mass, <i>kg</i>

MAC	Mean aerodynamic chord, m
n	Load factor
N_t	Number of time nodes
$Power_{min}$	Minimum required power, W
R_k^i	Residual at node k of state variable i
S	Wing area, m^2
t_f	Final DS cycle time, s
t_k	Time at node k , s
t_{SNOPT}	SNOPT calculation time, s
T	Vehicle thrust, N
u_*	Friction velocity, m/s
\bar{u}	Mean wind velocity profile on rather flat surface, m/s
V	Vehicle speed, m/s
$V_{z,min}$	Minimum sink rate, m/s
W_N	Norm of mean wind velocity, m/s
$W_{19.5}$	Wind velocity measured on top of a 19.5 meter-high-mast, m/s
W_x	Horizontal mean wind velocity, m/s
W_z	Vertical mean wind velocity, m/s
WL	Wing loading, N/m^2
z_*	Friction length, m
z_0	Surface roughness length, m
Z_{wave}	Wave vertical surface displacement, m

Subscripts

a	Air relative
c	Characteristic
f	Final value
i	Inertial

max Maximum

min Minimum

CHAPTER I

FINDING GUIDANCE FROM ALBATROSS FLIGHT

For many years, in the early infancy of aeronautics, human beings have been inspired by birds and have tried to mimic some of their features in order to take their first steps into the air. However, their theoretical background was sometimes lacking and the empirical field of knowledge was built through many hurdles. Since then, aircraft have explored a vast domain of flight, pushing boundaries of size, altitude and speed to levels respectively bigger, higher and faster than any living bird. Yet, scientific advances in the aeronautical field have not turned engineers away from other potential guidance that could be found by looking at nature [1]. In the recent-developing field of small Unmanned Aerial Vehicles (UAV), vehicles have been reduced in size to dimensions where birds and even insects compare on a 1:1 scale ratio, opening new perspectives for the potential of bio-mimicry. Festo's *SmartBird* was among the first vehicles of that size to master flapping flight with kinematics inspired from birds and a design based on the herring gull [2]. Aerovironment's *Nano Hummingbird* mimics the high-frequency flapping of the bird it is inspired from so as to enable hovering flight [3]. Georgia Institute of Technology's *Dragonfly* is based on the eponymous insect with similar dimensions [4]. A general introduction to the area of small UAVs will first be presented, which will lead to developments on the issue of long endurance flight, and then some of the explored solutions will be presented. An alternative that addresses this issue will be emphasized by shedding light on a peculiar biological system represented by the albatross genus. Finally the main features of their flight technique, called *dynamic soaring*, will be provided. *Dynamic soaring* will be referred to as DS in the remaining of this thesis

I.1 The UAV Context

UAVs date from the early hours of aviation and have been developed alongside their manned siblings in order to address three specific aspects of flight: “dirty”, “dull” and “dangerous”. By replacing the human being on board, UAVs can be used in “dirty” environments, such as contaminated areas or high altitude, where preserving human health is a challenge with significant associated engineering constraints. Or it can be used in “dangerous” environments, such as military conflicts, where the integrity of the vehicle and the life of a potential pilot are deliberately put at risk to perform a mission. On top of that, “dull” missions, such as surveillance and monitoring, where the presence of a human being is not required, can be performed by UAVs. Often, a UAV is developed to combine several of those aspects. For instance, the Northrop X-47B, which recently achieved the first autonomous landing on an aircraft carrier [5], is a large UAV of several tons, with a fighter-type profile. It prefigures a generation of UAVs that will be exposed to obvious dangerous environments while taking advantage of the absence of a human being on board to achieve higher levels of stealth, aerodynamics and situation awareness. Another example is the development of high-altitude solar-powered Titan UAVs [6], which will stay aloft for up to five years to provide communication coverage and hence perform a satellite-like mission anywhere around the globe, whilst having the flexibility and cost of an aircraft. Not only is a human presence not needed for the job, but it would jeopardize any chance of mission feasibility by significantly increasing the mass of the ultra-lightweight airframe and by requiring regular stops to avoid pilot exhaustion. To that respect, it is somehow ironic that for the challenge set by *Solar Impulse* [7] of flying around the world on solar power, many technical hurdles and performance limitations are entailed by the presence of a human on board, which is more symbolic than necessary.

The domain of small-sized UAVs, which are designed for much lower loads than manned-airframes, has seen a significant boost in recent years thanks to the miniaturization of technology, the development of lightweight materials and the progressive development of artificial intelligence. Once the pilot is removed, all size constraints related to the presence of a human being on board can be withdrawn and UAVs can be downsized to a scale which best suits their requirements. They address a potentially vast scope of mission scenarios. Advantages are numerous, such as providing a constrained volume of flight for indoor applications, reducing overall costs, or lowering the environmental impact. However, in the domain of small-sized UAVs, the limited mass and volume significantly challenge energy storage options.

Besides, those vehicles usually fly at rather low *Reynolds* numbers which are characteristic of a degraded aerodynamic efficiency. This leads to significant endurance limitations while, in fact, long-endurance is acknowledged to be a key factor of UAV utility [8]. In other words, without any pilot on board, endurance is only limited by the amount of available energy, which is part of the appeal for UAVs, but small vehicles are still faced with low endurance constraints. Innovative approaches are therefore sought in order to address that conundrum.



Figure I.1: *Ion Tiger*, a fuel-cell-powered, 5.15 metres-wingspan, which sustained flight for 48 hours in April 2013 [9] using liquid hydrogen.



Figure I.2: Photovoltaic panels installed as a laser receiver unit under the right wing of the 3 metres-wingspan *Lockheed Stalker*.

One plan of attack concerns the on board electric energy supply chain and looks at new technical solutions as for energy storage that departs from the traditional battery power source. Research on fuel-cell propulsion for long endurance UAVs is particularly active since their high energy density has the potential to dramatically extend endurance [9]. Fuel-cells take advantage of the high specific energy of hydrogen fuel, which can be stored under high pressure in a specific vessel or in its liquid form to benefit from an even higher energy per unit volume [10]. Recently, the *Ion Tiger*, pictured in Fig. I.1, performed a flight of 48 hours using only 500 grams of liquefied hydrogen to feed its fuel-cell [11]. However, although fuel-cells provide high specific energy together with high power, their size and volume can only be constrained to a limited level. On *Ion Tiger*, the fuel-cell system only (fuel cell, fuel tank, regulator, cooling) weights 5.5 kg without either fuel or propulsion system [9]. Moreover, the need for heat transfer area increases the size of the fuselage, leading to increasing parasitic drag. In order to achieve a maximum lift to drag ratio of 17, *Ion Tiger* has a wingspan of up to 5.15 metres, for a practical payload of 2.3 kg and an overall mass of 16 kg. Further advances are required to benefit from the high efficiency of fuel-cell propulsion on smaller scale vehicles.

Another approach to cope with energy storage constraints is to leave the power supply on the ground and to establish a transmitting power link between the ground and the

station. That has been achieved recently with the *Lockheed Stalker*, seen in Fig. I.2, by using a laser as an illuminating power source beamed to photovoltaic cells on the UAV [12]. As long as the vehicle remains in line of sight of the ground platform, it can benefit from a charge in mid-air to cope with power requirement in-flight [13]. On top of enabling a virtually unlimited endurance, the high energy density of the laser can enlarge the performance envelope of the vehicle, such as increased payload or higher airspeed, by allowing higher power requirements. It has been underlined that this technology could multiply the power received by an otherwise similar solar-powered UAV by a factor ranging from 2 to 10, depending on the technology used for laser and photovoltaic cells, with more consistent charge availability [14]. However, the efficiency of the power transmission is rather low and suffers from dependence on cloud coverage. The theoretical beamed-power is also limited by the heating of the illuminated surface of the receiver on the UAV, due to the high energy density of the laser. Besides, the ground station must be equipped with accurate fully-automated tracking to target only the laser receiver area of the UAV. Moreover, the laser-powered UAV is limited to areas where it is at range of a ground station, which itself must have abundant power resources, even though the transmission can be intermittent. Hence, the virtually unlimited endurance does not translate much into improved vehicle range but rather enables to keep the UAV aloft without the need for landing and take-off.

One different option for improving endurance is to seek energy from the surrounding environment. Studies about long endurance vehicles have mainly focused on using solar power to maintain a vehicle aloft. Prototypes began in the seventies with flights durations under 30 minutes [15]. With developments in lightweight materials and of photovoltaic cells, vehicles have started to benefit from solar power in excess of their minimum requirements, therefore unlocking the potential to overcome periods of sun shortage of increasing lengths. This trend finally opened the way for solar-powered flights all around the clock. The shortage of solar exposition during the night is balanced by the excess of power received throughout daylight that is stored into potential energy and battery charge [16]. The *Qinetiq Zephyr*, a 30 kg, 18-metres-wingspan-solar-powered UAV, displayed in Fig. I.3, paved the way by performing a two-week-long flight in 2010, setting the absolute record for flight duration by a winged vehicle heavier than air [17]. Up-scaled ongoing projects, such as *Titan Solara* or *Boeing Solar Eagle* aim at demonstrating and exploiting solar-powered perpetual flights, with the latest claiming a five-year-duration objective. However, those projects are among the largest UAVs and cannot be quite representative of the small UAV class. Indeed, those vehicles have low wing loadings and are designed for altitudes above 50,000 ft. Smaller UAVs, destined to fly in the lower

atmosphere, do not abide by the same constraints. Still, *Aerovironment* derived a solar-powered version of its *Puma* UAV, see Fig. I.4, which sustained flight for 9 hours in August 2013 [18]. This range of performance, for such small-typed UAV, is however highly dependent on the daily sun coverage.



Figure I.3: *Qinetiq Zephyr*, a solar-powered, 18 metres-wingspan-UAV, which sustained flight for two weeks in July 2010.



Figure I.4: *Aerovironment Puma AE*, a solar-powered, 2.8-metres-wingspan, which sustained flight for up to 9 hours in August 2013.

Solar array is not the only exploitable energy source in the direct environment of UAVs. Indeed, aerology mechanisms in the lower atmosphere, induced by local or global difference in temperature, entail movements of air of different scale and represent a vast source of energy. This alternative largely remains to be explored in the domain of UAVs, all the more as their eventual smaller mass may allow them to benefit from atmospheric phenomena of smaller scale compared with manned-gliders. For instance, some of these convective mechanisms are called thermals and occur when pockets of air near the ground become less dense, due to either heating or humidity change [19]. The challenge consists in finding a way to exploit it without compromising the mission scenario, since convective mechanisms directly affect the kinematics of any vehicle, all the more if those are of little mass. Some birds of prey take advantage of thermals by flying into those pockets of rising air and increasing their altitude, hence increasing their total energy, without flapping their wings [20]. Their subsequent elevated position, combined with a sharp sight, enables them to spot their prey and to gain the necessary speed to catch them off-guard. This technique of flight is called thermal soaring and has been investigated [21] and demonstrated to be practically feasible for a UAV by Allen in 2007 [19]. In this study, a 4.30 metres-wingspan, 6.8 kilograms-weight, *Cloud Swift* UAV is modified in order to detect and exploit thermals. Flight tests have attested that autonomous soaring was possible and multiple thermals were used to achieve a flight time of one hour. The wind can also be deflected upwards on the windward side of a ridge or a slope, where it would be possible to perform slope soaring by flying inside the area of rising air.

Those above techniques can be qualified by a broader term, as static soaring, which expresses the fact that a static regime of flight enables a steady increase in energy. The bird or the vehicle can therefore, in theory, continuously extract energy by flying steadily in the appropriate zone of rising air.

However, another type of flight, more subtle, has yet again emerged by looking at nature. It is the main focus of the present research work and is inspired by the flight of albatrosses.

I.2 The Albatross Legacy

Albatrosses have been at the origin of the discovery and understanding of DS flight technique. To this day, they remain the only ones to sustainably exploit DS flight over open ocean surfaces. Besides, the lack of experimental data on DS makes their study all the more critical. Albatross genres form a family of fascinating birds, with peculiar behaviours, which have led to wide biological research over past decades. In the framework of this research, an extensive review of these contributions is achieved in order to retrieve potential inputs to DS knowledge within the biological scope of albatross flight.



Figure I.5: Wandering Albatross (*Diomedea Exulans*) in flight close to the surface. Copyrights Kimball Chen, www.keaphotography.org

I.2.1 Morphology Characteristics

Albatrosses are among the biggest birds on the planet. One gender in particular, the Wandering Albatross (*Diomedea Exulans*), see Fig. I.5 and Fig. I.6, has been recorded with a weight of 12.7 kg and the maximum wingspan at 3.7 metres [22]. Most individuals would weigh from 7 kg to 10 kg [23, 24], with mean weights estimated, at Crozet Islands, around 7.84 kg for the female and at 9.44 kg for the male [24]. As for the wingspan, the sexual dimorphism is less

pronounced with mean values of 2.99 metres for the female and 3.11 metres for the male [24].

Table I-1 sums up other mean values, adapted from Schaffer *et al.* [24].

Table I-1: Mean characteristics of *Wandering Albatross*, measured on Crozet Islands in 1999, adapted from Schaffer *et al.* [24].

Parameter	Female (mean)	Male (mean)
mass (<i>kg</i>)	7.84	9.44
span (<i>m</i>)	2.99	3.11
Wing area (m^2)	0.586	0.626
Wing loading (N/m^2)	132	148
Mean wing chord (<i>m</i>)	0.196	0.201
Aspect Ratio	15.3	15.5

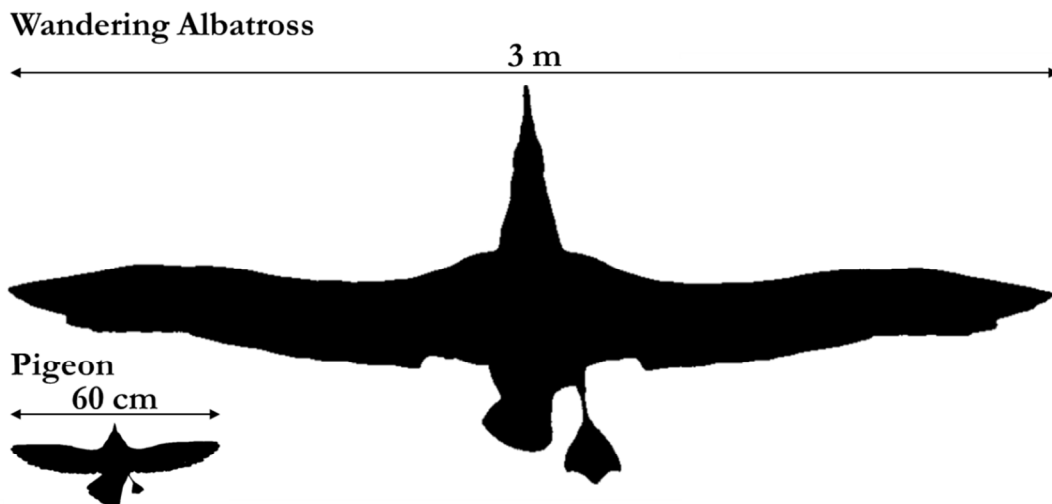


Figure I.6: Planform of Wandering Albatross, compared on the same scale with that of a common pigeon. Adapted from Pennycuick [23].

One of the first striking features of albatross morphology is their long and slender wings, with the highest aspect ratio of any other living bird [23, 25]. For the sake of comparison, vultures are other remarkable soaring birds, but have an estimated aspect ratio around 6.9 [26], less than half of those of albatrosses. Another peculiar aspect of the anatomy of albatrosses is their subsequent high wing loading, see Table I-1, which is also significantly

higher than those of vultures, with a mean wing loading estimated at 76.5 N/m^2 [26]. Such a heavy-loaded, high-aspect-ratio-wing trivially entails a high bending moment at the base of the wing, which requires significant force in order to maintain wings level or even to flap. This concurs with all observations that albatrosses do not sustain flapping flight, apart from rare take-off and landings [23, 27, 28, 29]. Besides, Pennycuick [23] observed that when fully extended, wings of albatrosses have a lock that prevents it to raise above the horizontal and level position. This materialized following dissections by the presence of a tendon which can maintain tension indefinitely at no metabolic cost [25, 23]. Hence, it allows albatrosses to sustain wings level at no energy expenditure, for any load factor within their structural limits. It can be concluded that the morphology of albatrosses is particularly adapted to gliding flight with a tolerance to high load factors, enabling them to cope with soaring flight within a windy and turbulent environment. Besides, their wing loadings and wing aspect ratio suggest high flying airspeeds and superior lift-to-drag ratio. Pennycuick calculates for the *Wandering Albatross*, using its software *Flight* [25], a best glide ratio of 21.2 at an airspeed of 16 m.s^{-1} .

I.2.2 Travelling Performances & Sensitivity to Wind

Nothing much was known about their behaviour at sea until a breakthrough study was published in 1990 [30], following the first satellite-tracking campaign of wandering albatrosses. It shows that foraging specimens performed trips of several thousand kilometres out of the breeding site in Crozet Islands, the maximum standing out at 15 000 kilometres. It also highlights travelling speeds up to 80 km.h^{-1} and daily speeds up to 936 km/day for the *Wandering Albatross*. This study revealed travelling performances that were far greater than the highest estimates at the time. Those flight performances were later confirmed by Prince *et al.* [31] from South Georgia and by Weimerskirch *et al.* [32, 33]. More recent tracking studies conducted by Croxall *et al.* [34] were focused on year-round behaviour, outside of the breeding phase of albatrosses. It shows that some specimens achieved a complete circumnavigation of the southern ocean, the fastest in just 46 days. By analysing travelling performances over three sub-segments of those circumnavigations, where averages up to 950 kilometres per day were achieved for periods up to 13 days, authors suggest that the round-the-world journey could be completed in 30 days. Subsequent data are summed up in Table I-2. Those indicate that albatrosses are able to sustain net travelling speeds, that is to say ground speeds averaged over large-scale movements, around 55 km.h^{-1} over distances up to 800 kilometres. Those travelling speeds could reach up to 85 km.h^{-1} over shorter distances while maximum ground speeds have been recorded at 135 km.h^{-1} , during a specific high-frequency GPS-tracking study [33].

Table I-2: Summary of findings from satellite tracking studies of foraging wandering albatrosses, adapted from [30, 31, 32, 33, 34].

Reference	Mean trip duration (days)	Mean trip length (km)	Average distance per day (km)	Mean net ground speed (km/h)	Max ground speed (km/h)	Average GPS rate
Jouventin <i>et al.</i> , 1990, [30]	24.4	8045	313	54.6	81.2	11.8 GPS locations per day
Prince <i>et al.</i> , 1992, [31]	6.9	4646	675	27.5*	88.1	15 GPS locations per day
Weimerskirch <i>et al.</i> , 1993, [32]	11.6	6091	525	21.8*	N.A.	Every 90 s
Weimerskirch <i>et al.</i> , 2002, [33]	N.A.	N.A.	N.A.	54.5	135	Every 1 s
Croxall <i>et al.</i> , 2005, [34]**	9.9	8718	872	36.3†	N.A.	Twice a day

*Mean net ground speeds were simply averaged over the whole foraging trip, hence taking into account periods when birds are sitting on the water. Besides, foraging trips were closed loops, so those speeds are representative of travelling performances over a closed circuit. Other net speeds are calculated between two specific landings, along an open segment of travel, regardless of the direction of travel.

**Tagged specimens were gray-headed albatrosses and trips were open-loops.

†Speed averaged over the whole mean duration.

Another common conclusion between those studies is the correlation between albatross travelling performances and wind speed. It was estimated that such travelling performances were energetically impossible for albatrosses to reach in the absence of wind [29, 35]. Besides, it was measured that albatrosses usually spent most of their time aloft, with only short stops on the water [30], but that high-pressure weather systems, with their associated absence of winds, were grounding albatross on the water for much longer periods until stronger winds reappeared [30]. On a global scale, both Fig. I.7 and Fig. I.8 highlight the explicit correlation between albatross and wind distributions. Albatross species are endemic to remote islands such as Crozet, Kerguelen, South Georgia... Their wide distribution, exposed in Fig I.7, is therefore only the result of singular travel abilities, as underlined before, which carries them over all longitudes. However their presence is strictly out of tropical latitudes, with the only exception being the *Chatam Albatross* seen in orange on Fig. I.7. Albatross species are reported

in every zone of average wind velocity above 9 m.s^{-1} , but north Atlantic, and reciprocally very little albatross presence is seen outside of those areas.

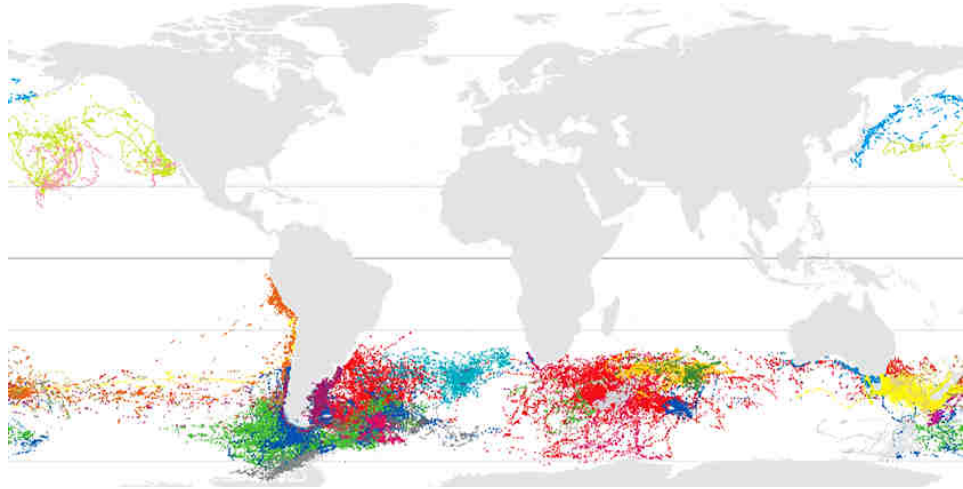


Figure I.7: Satellite tracking locations of albatrosses and petrels, reproduced with permission from *Birdlife International* [36]. All coloured-locations represent albatross species, the *Wandering Albatross* is pictured in bright red.

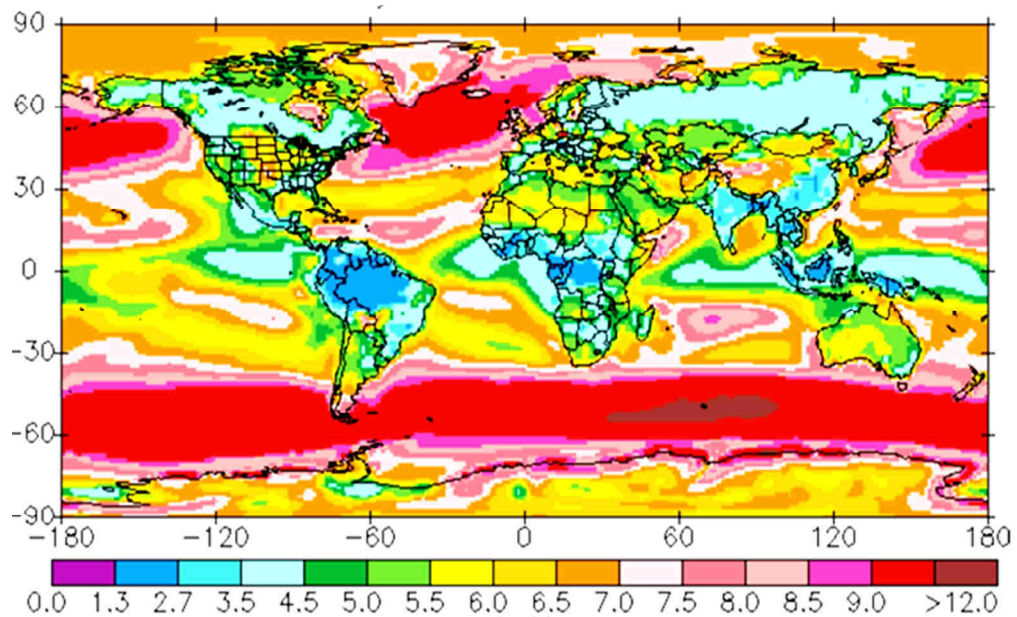


Figure I.8: Estimate of wind velocity (m.s^{-1}) at 50m, average over a 10-year period [37]. These data were obtained from the NASA Langley Research Center Atmospheric Science Data Center Surface meteorological and Solar Energy (SSE) web portal supported by the NASA LaRC POWER Project.

Zones of strong winds are very much delimited by certain latitudes, pictured in Fig. I.8, where prevailing winds are west-to-east currents, called the westerlies. Those are the strongest in the southern hemisphere, within the $-40^\circ, -50^\circ, -60^\circ$ latitudes [38], referred to as the *Roaring Forties, Furious Fifties, Screaming Sixties*.

Although the wind strength cannot explain in itself the distribution of albatrosses, it reinforces the assertion that albatrosses use a wind-related phenomenon to propel themselves effortlessly around the globe. More precisely, it was measured that albatrosses rarely sustain flight for winds under 8 m.s^{-1} [39], that small albatrosses species are never observed gliding below 5 m.s^{-1} [28] and that the distribution of wandering albatrosses is limited to areas where the average annual wind speed exceeds 7.5 m.s^{-1} [38], which is very much consistent with what can be observed from Fig. I.7 and Fig. I.8. Weimerskirch *et al.* [38] even describe how a shift in wind patterns over the last 20 years affected the distribution and the average mass of wandering albatrosses. Moreover, traveling performances of albatrosses have been measured to be intrinsically correlated with wind strength [29, 38]. Weimerskirch *et al.* [38] show indeed a correlation between the evolution of average travelling speeds of albatrosses and mean wind strength at Crozet Islands over the past 20 years, seen in Fig. I.9. Although data do not permit to establish a one-to-one correspondence, the year 2010 appears to confirm a dependence of travelling performances of albatrosses on wind strength.

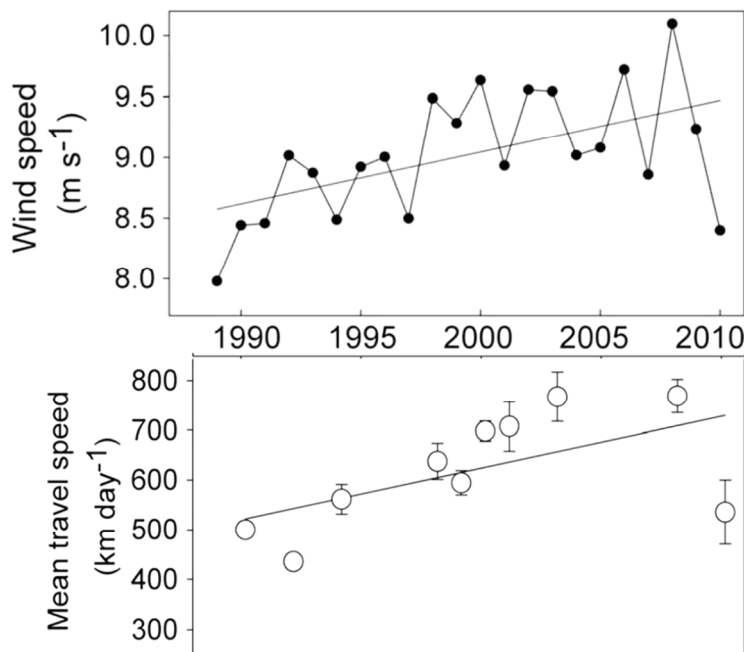


Figure I.9: Evolution of mean wind strength at Crozet Islands over years 1990-2010 (top) and the associate evolution of travelling performances of female wandering albatrosses (bottom). Adapted from Weimerskirch *et al.* [38], reprinted with permission from AAAS.

Further refinements about the flight technique of albatrosses can be learnt by getting a closer look at the way birds and wind currents interact. To start with, albatrosses have almost never been recorded to fly routes directly against the wind [30, 38, 35, 29, 32]. In particular, out of the 15 round-the-world journeys tracked by Croxall *et al.* [34], all were performed eastward,

in the direction of prevailing winds. This result seems somehow intuitive as the mass of air would have an overall tendency to carry the albatross throughout its displacement. Yet, travel directions of albatrosses show a predominant tendency to have a sidewind component [30, 29, 35, 38]. That is to say that albatrosses rarely fly leeward either, directly with the wind, but rather show a travel direction tilted with respect to the wind direction, as seen in Fig. I.11.

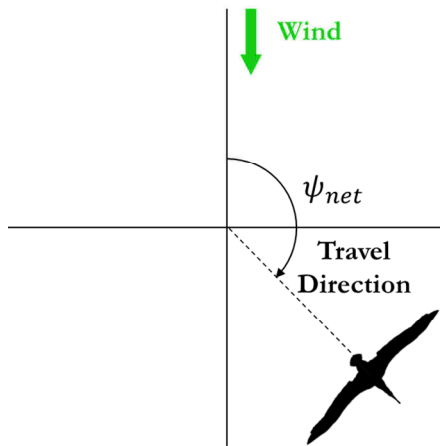


Figure I.10 (above): Definition of an azimuth angle ψ between the albatross travel direction and the direction from which the wind is coming.

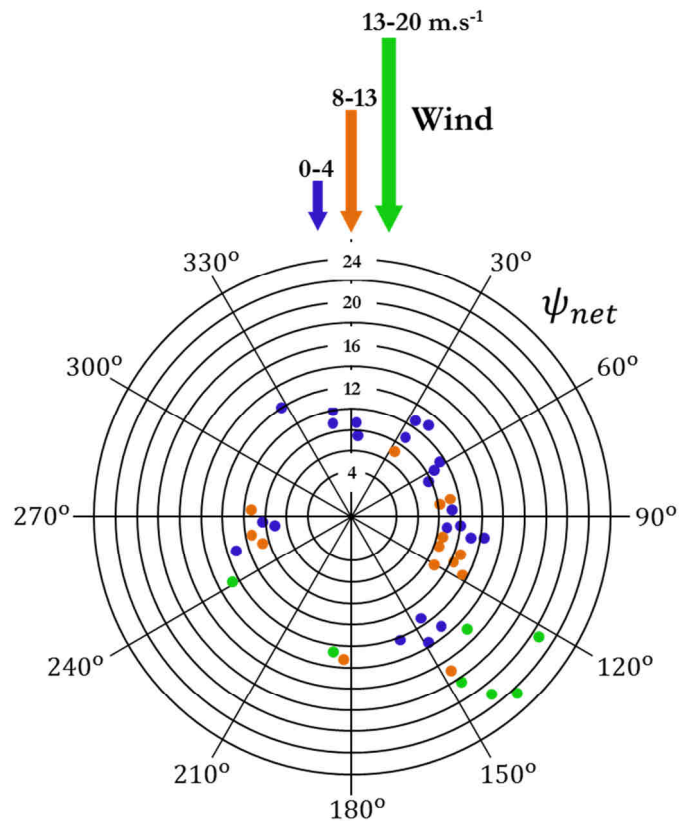


Figure I.11 (right): Speed and direction of travel of albatrosses, with the wind direction, obtained by radar tracking. Adapted from Alerstam *et al.* [29].

The azimuth angle between the albatross travel direction and wind origin is defined in Fig. I.10. Jouventin *et al.* [30] estimates that 40 % of the time, albatrosses fly at an angle ψ between 112.5° and 157.5° during the outward journey and that 90 % of the time, ψ is between 67.5° and 180° . Quite identically, Weimerskirch *et al.* [35] estimates that 35 % of the time, ψ is between 120° and 150° and that the ratio goes up to 80 % between 90° and 180° . Results from Alerstam *et al.* [29] are mapped on Fig. I.11 and plot the ψ -distribution and the travelling speed related to the mean wind strength. It shows that the stronger the wind is, the higher both the average ψ and the travelling speed are. It hence highlights the tendency of the mean travel direction to shift leeward when the wind increases and the way travelling performances improve with the wind strength. Furthermore, although the sample size is rather reduced and precise values of wind strength are unknown, the speed of travel appears to be maximum for values of ψ close to 140° . It can be observed that for winds above $13 m.s^{-1}$, no albatross was seen to progress against the

wind, which partly explains why circumnavigations recorded by Croxall *et al.* [34] were all achieved in the direction of prevailing winds. The travel direction should have a symmetrical distribution with respect to the wind direction. Indeed, albatrosses should behave indifferently whether the wind is coming from their left or their right. In most of studies, values of ψ are spread between 0° and 180° , without even mentioning if the wind comes from port or starboard with respect to the bird. The unsymmetrical distribution found by Alertsam *et al.* in Fig. I.11 could be explained by a behavioural preference for certain routes in the area where the study was conducted.

Those observations however question how those birds then manage to perform closed loops from their colonies. They manage to come back to their breeding site after thousand-kilometres-long-foraging trips, within an area where west-to-east winds significantly prevail [38], while it has been evidenced that their ability to go against the wind is very much limited. The Figure I.12 has more about their overall flight strategies: two albatrosses were tracked leaving Crozet Islands at the same time, on the same day. The simultaneity of tracks is particularly interesting as it reveals the flight strategies of two specimens exposed to identical wind conditions.

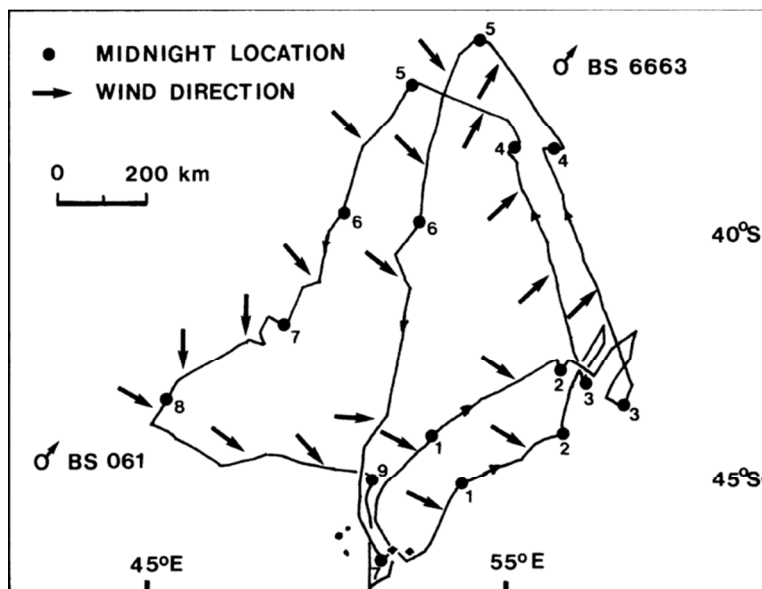


Figure I.12: Simultaneous trips of two males from Crozet Islands. Numbers indicates the successive counts of midnight locations. Reproduced with permission from Weimerskirch *et al.* [32].

It can be observed that although the two birds are most of the time over 50 kilometres apart, their overall trajectories follow very similar patterns over time. Moreover, changes in travel headings are correlated with changes in wind direction. First, this confirms that albatross

movements are intrinsically correlated with wind conditions. Then, it also concurs that albatross fly with the wind coming from their back and on their side the majority of the time. The azimuth angle defined in Fig. I.10 can be estimated to vary between 90° and 150° with the wind coming from either side of the birds. Still, for periods up to several days, birds were flying with the wind coming from only one side, which could explain asymmetries in measurements made by Alerstam *et al.* [29] on Fig. I.11. Furthermore, most of the time, the angle between wind and travel heading is close to 120° . This is especially explicit on the second leg and the fourth leg of the trip and quite consistent too, as large scale movements are very much straight lines with a constant heading with respect to the wind. Moreover, it shows that birds are able to perform a closed loop while the zonal wind, *ie* the component of the wind along the west-east direction, is always directed from east to west, as it is typically the case within those latitudes [38]. The flight strategy takes advantage of changes in the north-south component of the wind, also called the meridional wind. Indeed, those shifts enable birds to change their travel headings and to progress westwards, even though the zonal wind is constantly directed eastwards.

Up to 90 % of the time, the northern loop from Crozet Islands has been recorded to be anti-clockwise [35], just like the two examples pictured in Fig. I.12. Similarly, the southern loop is performed clockwise 90 % of the time. This reveals that the significant travel performances of albatrosses are possible thanks to predictable overall wind patterns over latitudes around the colony, which is confirmed by Fig. I.13.

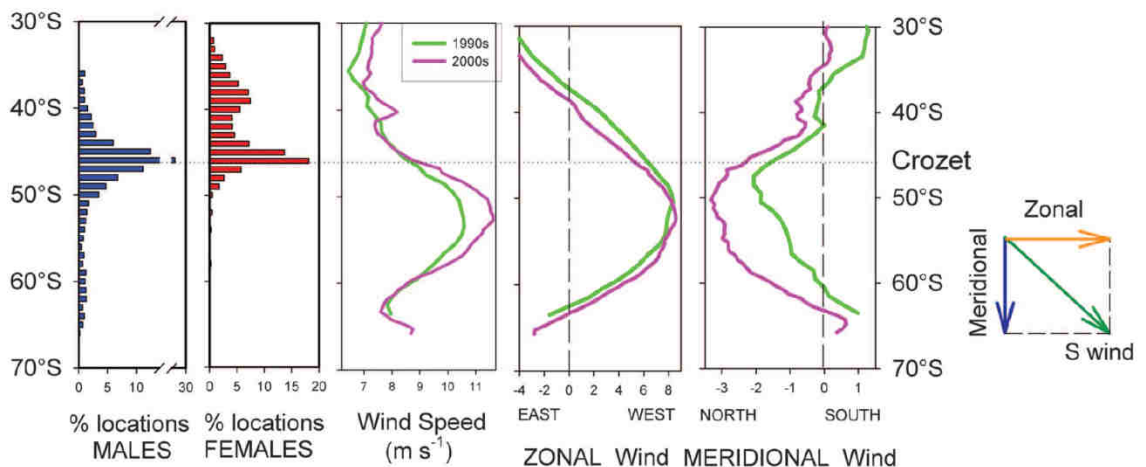


Figure I.13: Distribution of the *Wandering Albatross* with respect to mean wind strength and direction. From Weimerskirch *et al.* [38], reprinted with permission from AAAS.

The distribution of albatrosses, depicted in Fig. I.13, depicts that the maximum is trivially located on the colony, but local peaks can be observed at the very same latitudes which see

changes in mean wind directions, for both zonal and meridional components. One is particularly marked, for females, north of the colony, around 38° south. This latitude corresponds to change in mean zonal wind from eastward to westward and in meridional wind from southward to northward. Such changes have been demonstrated to be necessary for albatrosses to alter their travel headings. The local peak in albatross presence at this latitude can therefore be interpreted as the average upper edge of the northern loop they perform, where they would change heading. This is consistent with loops displayed in Fig. I.12. This area is by definition more prone to uncertainties regarding the wind direction, as mean values are close to zero, which would locally affect travel performances and explain the increase in albatross presence. Again, Fig. I.12 is very much consistent with this interpretation as birds spent two successive nights, number 4 and 5, in this area before starting their journey back to the colony. It can be assumed that the duration of foraging trips, which is directly correlated to the speed of travel, varies depending whether mean wind predictions are met or not.

I.2.3 Flight Behaviour and Energetics

Figure I.13 contains another valuable piece of information. It depicts that the distribution is quite uneven regarding males and females and a closer look show that females tend to prefer areas of lower wind strength, while males seem to favour higher winds. This is very much relative, as females travel areas where the mean wind speed is over 7 m.s^{-1} . One explanation to it could be the sexual dimorphism observed for the *Wandering Albatross* [24]. Indeed, as summed up in Table I-1, males have a wing loading that is on average 12 % higher than that of females. It results in an aerodynamic polar shifted towards higher airspeeds, which translates into a best-glide efficiency at a higher airspeed and a faster minimal sink rate [40]. It means that males could favour higher winds, where they could extract the higher energy they require to sustain aloft while also optimizing gliding flight at higher airspeeds which are characteristics to windier conditions [24, 35]. Inversely, females could take advantage of lighter wind conditions.

This trend can be generalized for different albatross species, where wing loadings can vary up to 60 % [39]. Suryan *et al.* [39] specifically focus on specific albatross subspecies, including two with peculiar wing loadings with respect to their body size. The *Waved Albatross* is the only albatross located in the tropics, on Galapagos Islands and has a rather low wing loading of around 90 N/m^2 . The *Short-tailed Albatross* is the largest albatross species in the north hemisphere and has a wing loading of around 130 N/m^2 . It was measured that the *Short-tailed Albatross*, was the only species to travel long distances under windier conditions

compared to their short-range movements. The lighter *Waved Albatross* did not appear affected by such a disparity and was the species which sustained flight for the lowest wind strength, around 6 m.s^{-1} . Besides, it was also the only albatross to apparently fly in any heading disregarding of the wind direction. On the contrary, the heavier *Waved Albatross* were most of the time flying in the general direction of the wind. Hence the flight technique used by albatrosses seems to associate a higher wing loading to a greater dependence on the required wind strength as well as to a stronger bound between wind and flight direction.

In order to fully understand the energetics involved in the flight strategy of albatrosses, it is important to somehow measure their energy expenditure in flight. It is assumed to be rather low since albatrosses mainly glide without flapping of their wings and do not exert power to maintain their wings level thanks to a specific tendon. Besides, the eating frequency of albatrosses is rather low, as they feed from rare floating preys only, with on average one prey every 100 kilometres [32]. Pennycuick [23] assumed that albatrosses in flight consumed twice their basal metabolic power, and estimated that they could fly 936 kilometres while consuming fat equivalent to 1 % of their body mass. As a matter of comparison, a small petrel would stand at 38.8 kilometres. Weimerskirch *et al.* [35] explores further the problematic of in-flight energy expenditure, in particular in relation to wind conditions, by measuring the heart rate of tracked albatrosses. Average results are presented in Fig. I.14.

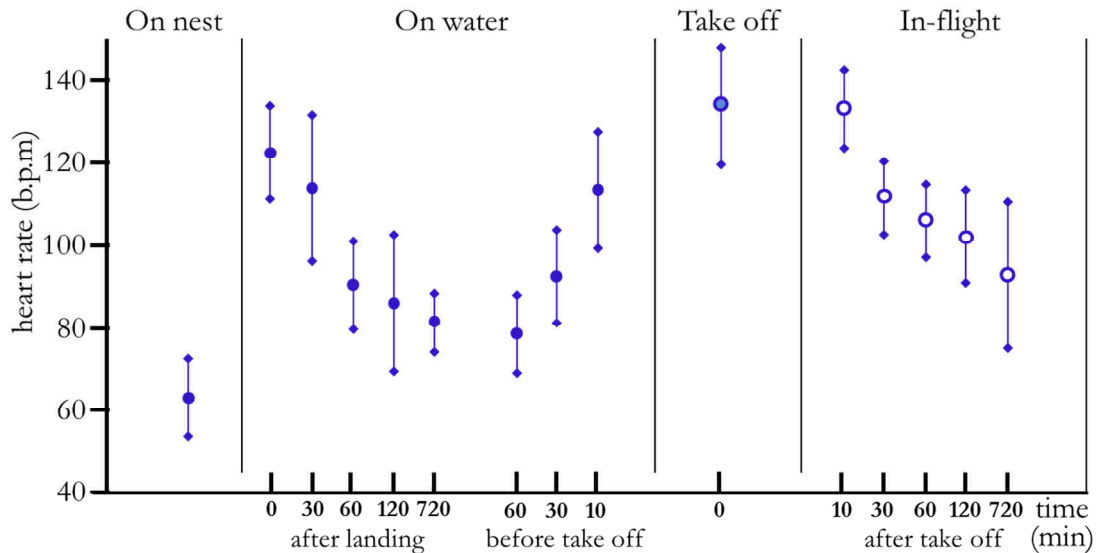


Figure I.14: Average heart rates of albatrosses for each activity. Adapted from Weimerskirch *et al.* [35].

The metabolic basal rate is obtained when birds are on their nest; the average is slightly above 60 *b.p.m* (beats per minute). The biggest power requirement comes during take-off with an

averaged heart rate that peaks close to 130 *b.p.m.*. During this phase, which typically occurs 15 times per day [35], albatrosses not only have to flap their wings but also to gain speed, quite similarly to an aircraft, in order to generate sufficient lift. It reinforces the assertion that albatrosses are not adapted to frequent landings and take-offs. The heart rate decreases progressively for long periods up to several hours after take-off to reach an average value slightly above 95 *b.p.m.*, which is only 50 % higher than the basal metabolic rate, showing that the assumption from Pennycuik of twice the basal rate was rather conservative. In-flight power requirements are actually significantly lower than when walking on the ground. This emphasizes the peculiarity of their flight technique energy-wise. The longer albatrosses are airborne, the wider is the range of measured heart rates, as seen in Fig. I.14. We understand it as an increasing dependence on flight conditions, such as the travel heading with respect to the wind direction, which have a higher probability to change for extended flights. This is somehow corroborated by the analysis of the evolution of average heart rate with relative travel heading, as displayed in Fig. I.15.

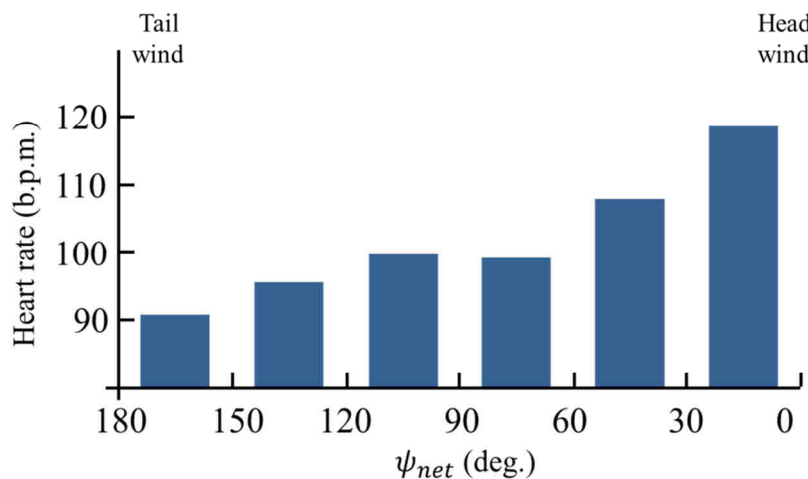


Figure I.15: Heart rates varied according to the angle between the wind direction and the flight direction. Adapted from Weimerskirch *et al.* [35].

Hearts rates and therefore power requirements are the highest when birds are facing the wind, which happens less than 5 % of the time. Then, heart rates decrease regularly when the flight heading shift windward. The overall average of 90 *b.p.m.* indicates that most of the time, birds are within 90° to 180° with respect to the wind incoming direction. However, given the assumption that albatrosses do not sustain flapping flight, whatever the relative flight heading is, it is a priori rather difficult to interpret the slight but clear evolution of power consumption in the 90° to 180° range. This concludes on the fact that their flight technique is

optimized for a delimited range of travelling angles with respect of the wind. Outside of that range, not only flight speeds decrease, but power requirements surge.

Further contributions to the knowledge of albatross flight technique is based on observations or on high-frequency, small scale tracking, which in their vast majority are only two dimensional in the horizontal plane. Still, it could be both recorded and observed that on a small scale, albatross movements are rather intricate, with turns, descents and pull-ups [32, 23, 29]. One metric which is representative to this sinuous path is the straightness ratio, which is obtained by dividing the straight-line distance over large scale movements by the actual distance covered. Data however usually only take horizontal distance covered. For albatrosses, straightness ratio is probably dependent on wind conditions, and estimates are between 0.7 [23] and 0.9 [29]. A 0.7 value for the straightness ratio means that albatrosses fly an actual distance 50 % higher than the straight-line distance they travel. In terms of variation in height, albatrosses have never been observed higher than 30 metres [23, 41, 42, 43, 44], where the average maximum height should be between 10 metres and 15 metres. A rather recent high-frequency acquisition campaigned by Sachs *et al.* [44] could obtain accurate measurements of the *Wandering Albatross* in flight. A typical trajectory is pictured on Fig. I.16, using sampling rates of 10 Hertz.

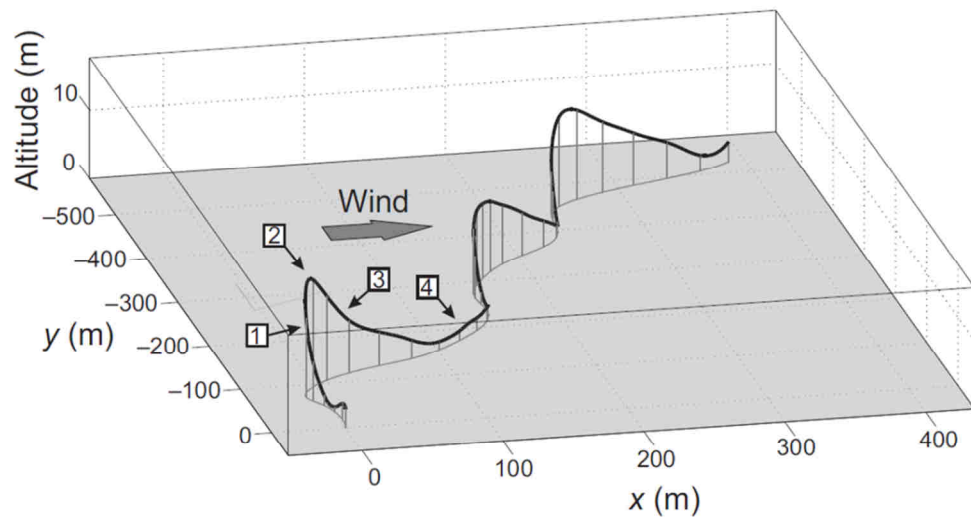


Figure I.16: Small-scale movements recorded by Sachs *et al.* on a *Wandering Albatross* gliding under windy conditions. Wind is 11.2 m.s^{-1} at 10 metres, the direction is shown by the arrow. From Sachs *et al.* [44], reproduced with permission from Journal of Experimental Biology.

The albatross trajectory appears to combine repetitive cycles of similar aspects, which themselves are composed of pull-ups, turns and descents. The low straightness ratio of the

albatross flight path mentioned in earlier observations is confirmed and well pictured in Fig I.16. Those small-scale movements are summed into medium-scale movements which indicate a clear flight heading. It appears, from measurements by Sachs *et al.* [44], that the more birds are progressing against the wind, the more intricate the flight path becomes and the lower the straightness ratio is.

Albatrosses indeed seem to take advantage of various flight techniques. Some observations and measurements witness cases where albatrosses were seen gliding in zero wind, taking advantage of propagating swell waves [23]. Authors suggest various theories to explain the flight of albatrosses. A majority refer to dynamic soaring, which exploits the vertical variation in horizontal winds, due to the boundary layer effect entailed by the air-sea interface. This technique was unknown before the flight of albatrosses was investigated. Others suggest wave soaring or slope soaring on waves, where waves play a significant role in disturbing the wind field close to the surface. Pennycuik has long held the view that albatrosses used gust soaring, where birds would exploit the separation of boundary layer leeward of waves to benefit from sharp local increases in wind strength, referred as gusts. Finally, Richardson actually supports that those theories are not mutually exclusive and that albatrosses probably take advantages of a combination of all those techniques.

I.2.4 Summary of Inputs from the Biological World

The general anatomy of albatrosses outlines an aspect ratio around 15, which is exceptionally high for a bird and makes them resemble small fixed-wing gliders. Their morphology suggests they are unsuitable to flapping flight, which is confirmed by all observations, but rather optimized for fast gliding flight.

It is indeed established that they regularly travel thousands of kilometres with travelling speeds that can top 900 kilometres per day. Those performances are intrinsically correlated to wind strength, as albatrosses would not even be able to sustain flight in the absence of it. It explains their geographical distribution within south latitudes, where the strongest winds on earth blow predominantly from west to east at average speeds that can top 10 m.s^{-1} .

Their travel heading can be observed to be very much dependent on wind direction, with an angle between the two such that they usually perform best with the wind coming from their back with a side component. Their ability to go against the wind is very limited and rarely used. It has been evidenced that it comes at a greater energy expense and that it results in

drastically reduced speeds of travel. They still manage to come back to their departure point while sustaining rather high speeds. To achieve that, it has been demonstrated that they have developed a large-scale strategy which takes advantage of predictable wind patterns. Changes in zonal wind direction (north-south component) are sufficient to enable them to alter their travel heading and to close the loop back to the colony.

There are strong indications that there is an interrelation between their wing loadings and the wind strength they exploit. To that respect, albatross species of lower wing loadings are seen in lighter wind areas and it is supported that the sexual dimorphism in wandering albatrosses explains the different distribution between males and female.

Their own in-flight energy expenditure was measured to be very low, not much higher than their basal rate. On the other hand, their performances of travel are theoretically high-demanding energy-wise, since albatrosses, as any flying vehicle, are subject to energy losses due to drag. This contrast emphasizes an inherent energy-extraction process and raises questions regarding the underlying technique they have developed.

On a small scale, intricate trajectories, far from being straight, have been observed. The altitude rarely exceeds 20 metres and albatrosses are most of the time in the nearest vicinity of the surface. Although there still lacks a general agreement regarding their energy-harvesting strategy, there is a concord on the fact that albatross exploit surface-induced wind phenomena. The predominant theory focuses on the most generic of those phenomena, which is the boundary layer effect that forms due to air-sea interactions. This technique is called dynamic soaring.

I.2.5 Promising Perspectives

Years of evolution have created a very adapted biological system which relies on two different energy resources: surface food distribution and wind. The practical response is a foraging flying technique which renders those two resources compatible. It consists in exploiting wind energy in order to fly long distances and therefore statistically increase the probability to harvest from scarcely distributed preys.

No fundamental deadlocks appear to prevent the approach of transposing the flight technique of albatrosses to the UAV world. Although albatrosses are a class of their own among birds, nothing stands out in terms of their general architecture compared to a fixed wing glider platform. Their estimated gliding performances are well within the reach of

vehicles of similar size and nothing indicates that it should be otherwise in terms of manoeuvrability. The wind resource is evenly distributed over large areas, which suppresses the constraint of exploring for a sparse phenomenon of unknown location, as it is the case for thermals. As for the large-scale flight strategy, a vehicle would actually hold a strong advantage over albatrosses, as it could adapt its route by taking into account weather forecast data. In terms of energetics, apart from potential mission requirements, most of the expenditure comes from propulsion on a small UAV. Endurance would then only be limited by on board energetics. The feasibility for a small UAV to extract energy from the wind, in the same fashion as albatrosses, is therefore a promising topic, which requires further investigations.

I.3 Main features of Dynamic Soaring Flight

The technique of DS consists in taking advantage of vertical variations in horizontal wind, also called vertical wind shear gradient. One way to define DS is trivially by opposing it to static soaring, such as thermal soaring or slope soaring.

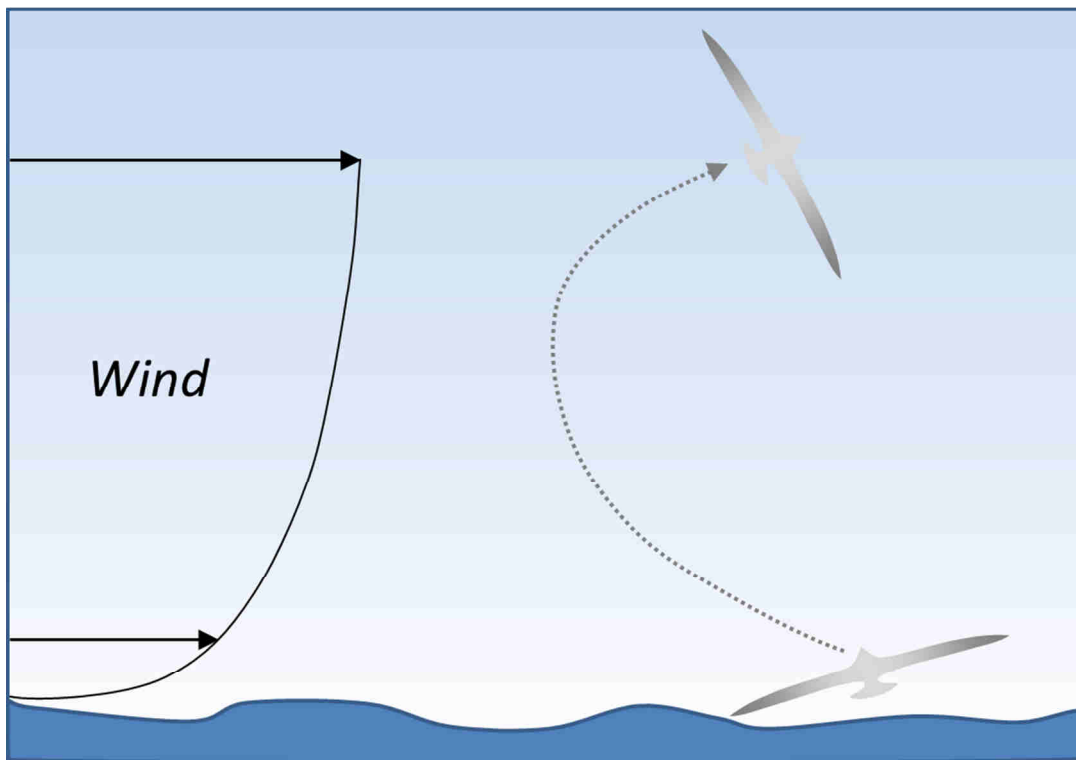


Figure I.17: Schematic 2D display of a dynamic soaring path within the wind shear gradient.

The latter techniques manage to extract energy at a positive and continuous rate through steady flight kinematics. In such cases, the variation in total energy of the vehicle

would depend whether it can maintain its air relative sinking speed lower than the rising speed of the surrounding mass of air. However, the mechanisms of energy-extraction would remain effective, whatever the kinematics of the vehicle is. Practically, it means that a vehicle, no matter how it is flown, would benefit from the uplift of the surrounding air as long as the vertical motion of it remains upwards. In static soaring, energy-extraction mechanisms are hence not correlated to the vehicle kinematics. On the opposite, DS is characterized by an energy-extraction which is not steady and that varies to form repetitive cycles composed of energy losses and gains. Losses are necessary in order to sustain respective gains and the periodicity of the process is ensured if gains and losses balance out along the cycle.

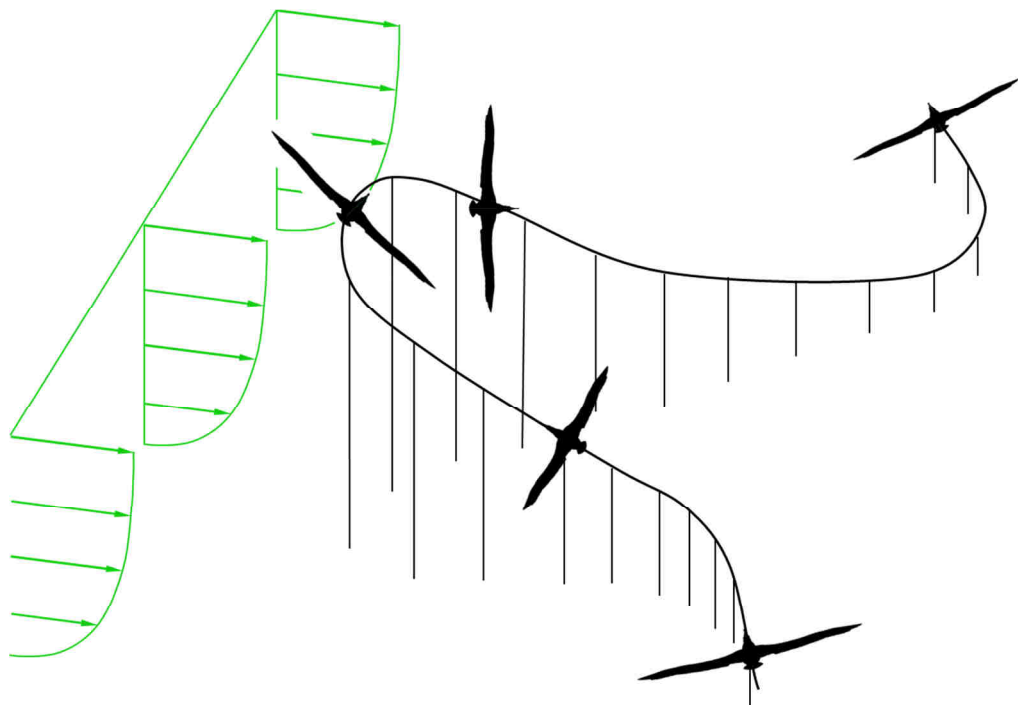


Figure I.18: Overall aspect of a dynamic soaring trajectory.

Practically, this translates into periodic dynamic manoeuvres within a zone where wind gradients form, as displayed in Figs. I.17 and I.18. More specifically, in dynamic soaring, the bird or vehicle would extract energy from the layer of strong wind and would be able to repeat the process by flying back in the zone of weaker wind. This concept can be apprehended by considering a ball bouncing on a wall which is moving at a fixed horizontal speed. Each time the ball bounces, it gains momentum from the wall, and the same principle applies to the bird flying in the zone of strong winds. It means that gains in total energy come through variations in inertial speed, as opposed to static soaring, where those gains relate to an increase in height.

Besides, variations in inertial speed themselves alter the dynamics of the vehicle during the manoeuvre. That is different again different from static soaring.

To put in a nutshell, some particular trajectories are required through dynamic manoeuvres with respect to the wind. Those entail a transfer of energy from the wind to the vehicle, which in turn alters the dynamics of the vehicle and influences its trajectory. So the mechanisms of energy-harvesting are inherently bound up with the dynamics of the vehicle, which is specific to DS. For this reason, the mechanisms that lead to the energy extraction are challenging to understand and to model as they are related with other variations of kinetic and potential energy along the flight path. It means that flight dynamics and energy-harvesting strategy have to be investigated together.

I.4 Research Question & Objectives

I.4.1 Research Question

The context outlined that the research is focused on the use of sustainable energy extracted from the wind applied to the flight of small autonomous vehicle. Therefore, one wants to know:

Is it feasible for UAVs to exploit dynamic soaring in the purpose of long duration, or long distance autonomous flight?

I.4.2 Research Areas Breakdown

In order to fully understand the way the main question would breakdown into underlying research questions and then the way research objectives would be structured, some specified self-contained research areas can be derived quite straightforwardly out of the context.

- What would fly? The potential vehicle would have to be compliant with the requirements of DS flight. That is the Vehicle Model.
- Where would that vehicle fly? That is the first 30 metres over land or waves, the lower atmospheric boundary layer over earth oceans. A model of the wind field at the interaction air/sea or air/land would have to be developed. That is the Environment Model.

- How would the vehicle interact with that environment? In other words, the way it is going to fly within that boundary layer. The flight path and dynamic parameters would have to be investigated. It is the core of that research work and corresponds to the Flight Model.

I.4.3 Underlying Research Questions

Answering the main research question consists in trying to build up a solution to the problem, which would ultimately be the only way to prove the feasibility. However, during the demonstration, or the construction of the solution, some deadlocks might arise and an alternative answer would be to bring out which variables govern the feasibility to exploit DS.

The main research question breakdowns into three underlying research questions, which concerns each of the three models introduced above:

- *What trajectories would enable energy-harvesting in the framework of DS flight?*
- *What is the environment, and the corresponding wind field, required for DS energy-extraction and what is the likelihood of favourable conditions?*
- *Which vehicle design would be suitable for DS flight and how do general design variables govern performances?*

I.4.4 Research Objectives

The research question is there to support different aims. Their numbering is arbitrary.

Objective 1_ “Understand”: Get a complete understanding about the energy-harvesting mechanisms involved in the DS, applicable to the flight of albatrosses. This objective might see underlying challenges arise as it emerges that albatrosses seem to combine different processes to extract energy from the wind.

Objective 2_ “Simulate”: Set up a methodology to simulate the physics of DS flight, which would give a practical answer, in terms of trajectories, to a particular mathematical problem, given some vehicle and environment models adequately formulated to fit the problem. Use those derived optimized trajectories to support the physical understanding assumed for DS. Get an understanding of mathematical tools used when writing down the algebraic formulation of the problem and of how they influence the output.

Objective 3_ “Model”: Understand and model the environment where the vehicle would perform; in particular aerodynamics of sea/wind or earth/wind interfaces. Also provide models of potential flying vehicles and understand how general design variables influence DS performances.

Objective 4_ “Assess”: Assess potential DS performances for different key variables, which may influence the feasibility to exploit DS under realistic conditions.

I.4.5 Thesis Outline

In order to address the research question and support the aforementioned objectives, the following outline has been selected.

First of all, the literature background on the topic will be reviewed to draw a sum-up of the current state of the art. This will be the objective of Chapter II. Then the understanding of DS energy-harvesting strategy would only be approached after modelling the environment and the vehicle in order to get to a simulation of DS. Hence Chapter III focuses on building up a vehicle model that applies to different UAV designs, and also on building up models of their environment, by focusing on a refined earth/wind interaction such as waves. The physics of the evolution of the vehicle within its environment is the point of Chapter IV, which then also presents a methodology to pilot and optimize this evolution. With simulations of DS flight available, Chapter V forms the core of the present work as it focuses on the characteristics of DS flight and on understanding the principles of energy-harvesting. Chapter VI goes further by conducting a mathematical analysis of EoM and the associated optimization problem in order to highlight some key variables about DS flight. Finally, various case scenarios are investigated in Chapter VII, by varying key parameters in order to assess how those govern the energy-harvesting strategy. It includes the refined case of a powered vehicle, where DS makes sense by enabling range improvements.

I.5 Summary of Chapter I

The advance of small scale UAVs opens up for a wide range plenty of potential applications, however those may be hampered by range and endurance limitations. Several options are being investigated to cope with this conundrum and the state of the art is presented. A particular scope is given to techniques which take advantage of the surrounding energy available to the vehicle. It bears the advantage of keeping the logistics of flying simple and the overall technical solutions rather unchanged. The breakthrough comes from the flight management approach, which is adapted to benefit from atmospheric convective inputs. Among those techniques, one is inspired by the flight of albatrosses.

It appears that those big birds are actually quite close, in their morphology, to a small gliding UAV. Indeed, their wings have the highest aspect ratio of the living world and are locked in deployed position most of the flight. Yet, their flight performances are impressive, both in terms of speed of travel and range covered. They take advantage of the wind in a way that is not completely understood yet but that enables them to achieve round trips of several thousand kilometres out and back at their remote colonies. This peculiar flight, called dynamic soaring, associated with promising perspectives, makes it a consistent research subject.

The main question associated to it concerns the feasibility for a UAV to exploit dynamic soaring for the purpose of long endurance, long range flight. Hence this research work focuses on understanding the energetics of DS, simulating this type of flight and assessing the constraints it implies for the vehicle and its flight.

CHAPTER II

BACKGROUND OF WIND ENERGY EXTRACTION

This Chapter aims at providing a review of the literature of wind energy extraction for UAV, with a specific scope on DS contributions. It will enable this present work to benefit from previous studies and will help to structure the research in order to focus on required contributions to knowledge.

II.1 Contributions to Knowledge

Research about flying techniques which extract energy from the wind started in late 19th century with observations of albatrosses from Lord Rayleigh [27]. In 1925, a first analytical analysis was undertaken by Idrac [45], in order to underline the fundamental differences between static and dynamic soaring. Idrac imagined different trajectories, which are reproduced on Fig. II.1, that could take advantage of a vertical gradient in horizontal winds.

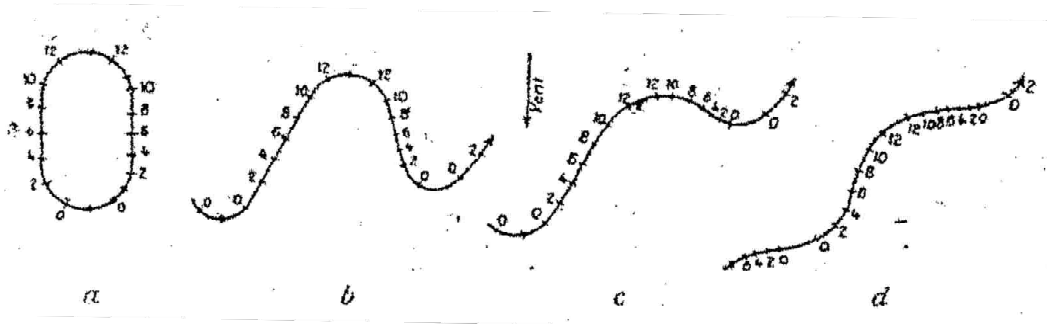


Figure II.1: Various eventual shapes of DS flight path, reprint from Idrac [45].

A few numerical approaches were attempted later in 1975 by Wood [46], taking advantage for the first time of computer power. Then in 1990, the first satellite tracking campaign of albatrosses enlightened the biological community with unexpected flying performances from albatrosses [30]. As reported before, further tracking campaigns were conducted during the following decade. From late 1990s, the improved knowledge of albatrosses performances combined with the emergence of UAVs highlighted the potential of DS research. Major publications on the matter appeared from 2000, while certain biologists

started to criticize the limited scope of numerical models developed by researchers [41]. Several further studies, from different institutions, followed during the decade, while research on miniaturized UAVs with autonomous flying capacities started to flourish from 2005. From 2010, researchers started to implement in-flight measurement cells on albatrosses with recent publications in 2011 and 2013 [43, 44]. Also in 2011, for the first time a publication from an oceanographer mentioned and detailed the importance of waves as part of the energy extraction mechanism [42].

II.2 Literature Background

II.2.1 Point of view

The literature available on the subject comes from different authors with different backgrounds. Although we are looking at a type of flight which exploits DS, other types of potential contributions are reviewed. Indeed, multi-disciplinary aspects of the research involve different sciences and give a pretty broad literature background.

II.2.2 Simulation of Dynamic Soaring

The first numerical approaches to DS flight appeared in the late 1990s. Sachs *et al.* provided one of the main publications on that matter [47]. His aim is to compute typical optimized DS trajectories and to understand the influence of external parameters such as the wind strength. Very early in the paper, the author acknowledges some limitations in the understanding of the energy extraction phenomenon and proposes to describe his vision of the energy extraction mechanism. Sachs therefore suggests a different understanding of the energy extraction phenomenon than the classical DS theory, which claims that the wind gradient is responsible for providing energy to the bird. He writes down equations of motion in a three dimensional reference frame linked to earth, thus inertial. He isolates a point mass vehicle within an environment described using a logarithm model for the wind gradient over a flat ocean. The aim of his model is to determine energy neutral trajectories using optimization in order to minimize the required wind shear strength, although the optimization process is not clarified. He therefore provides 3D trajectories corresponding to DS flight, such as the one displayed in Fig. II. 2. The UAV is apparently able to maintain a crosswind net heading while taking advantage of the wind through a curvy flight path. Sachs provides an energy-point-of-view-interpretation: the energy is transferred from the wind to the vehicle during the upper

turn, when the vehicle finishes its upwind leg and starts to turn into the wind to start its downwind descent, without detailing the underlying mechanisms.

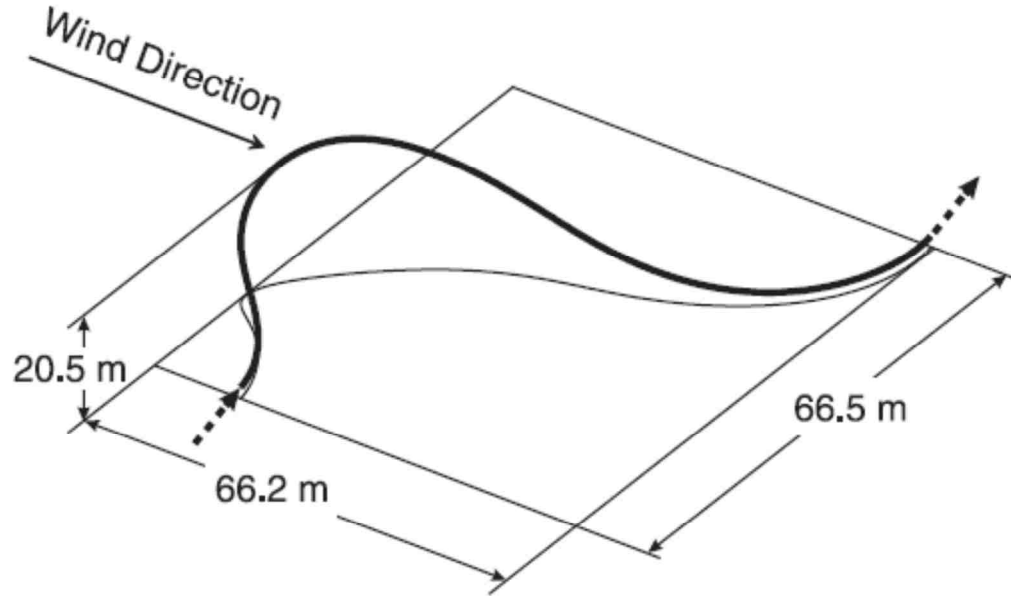


Figure II.2: Overall open loop obtained by Sachs *et al.* [47], reproduced with permission from Ibis.

Zhao *et al.* provides a slightly different approach of the same overall problem [48, 49]. His aim is to derive trajectories which minimize the average thrust required by the vehicle, taking benefits of the wind gradient over the ocean. He also isolates a point mass vehicle but this time in the reference frame of the wind, which is not inertial, since the wind increases with height. The wind gradient profile chosen is linear, which is again a strong difference compared to Sachs. The equations of motions see the apparition of a fictitious force (or inertial force) due to the non-inertial reference frame. He derives an optimization problem clearly stated out of equations of motion, where constraints are derived from vehicle operational limits, surface avoidance consideration and periodicity consideration while the objective is to compute critical trajectories with minimal wind condition, the same as Sachs *et al.* He then converts the infinite dimensional optimization problem into a parameterized optimization problem using collocation techniques and finally solves it using NPSOL software. It is to be noted that he suggests tracking variations of energy by computing air frame based energy, *i.e.* energy calculated towards the mass of moving air, which is fundamentally different from Sachs' earth-based energy. With this choice, as the lift is directed perpendicular to the relative airspeed vector, the lift does not work and hence does not contribute to the energy variation. He then provides results through optimized 3D trajectories for different case study. He concludes that the average thrust required for periodic trajectories is lower when the UAV aerodynamic efficiency

increases and when the wind strength increases. It is to be noted that the average thrust mentioned is positive, which means that an energy contribution from the vehicle is required to perform periodic trajectories, which was not the conclusion of Sachs *et al.*

Another numerical approach was proposed by Deittert *et al.* [50], which aims at providing clarification about the flight performance and the likelihood of favourable winds. Like Zhao *et al.*, he also opts for a point mass model observed from a wind reference point of view. The wind model is the same as Sachs' and he also assumes a flat ocean surface. However, he decides to optimize his trajectories with a differential flatness technique which is different from Zhao's collocation. He then validates his results by comparing his critical trajectory parameters with the one obtained by Sachs. His results consist in a detailed analysis of how the vehicle design variables influence the required minimal wind strength and he provides travel performances polar depending on wind strength. Deittert *et al.* identifies the ability to fly close to the surface as a key factor governing DS performance, as the strongest wind gradient is located in the first metres above the surface. The author concludes that DS would benefit from further research investigating the airflow over water surfaces; including the flow between waves and that a higher degree of fidelity would be reached by taking into account a six degree of freedom vehicle model.

Lissaman [51], focuses on the principles of energy-extraction, applies DS to a linear wind profile to finally derive some general approximation rules. Lawrance *et al.* [52] derives low-complexity guidance and control algorithms and apply it to the case of a UAV travelling with the wind. Sukumar *et al.* [53] derive DS trajectories over open field and study the effect of aircraft properties. Other contributions to the topic include Akhtar *et al.* [54], Barate *et al.* [55] and Gao *et al.* [56].

II.2.3 Jet Stream

Dynamic soaring flight could potentially be extended to any environment where wind gradient form. Grenestedt *et al.* investigates the feasibility to fly perpetually in the jet stream, where gradients are generated in the upper atmosphere between bands of strong winds [57, 58]. The author undertakes the same approach as Zhao *et al.* by deriving air relative equations of motion from a point mass vehicle within a linear wind gradient and using collocation techniques. His main contribution is to extend the optimization process to the aircraft design, where he provides a clear definition of the aircraft model. He then goes another step forward by optimizing solar-assisted DS trajectories. Therefore the optimization process takes into account control and state variables as well as design parameters assuming solar augmented

trajectories. However, the author does not go into much detail regarding the results. The resulting trajectory is displayed in Fig. II.3, authors force the vehicle back to its initial position such that the flight path is closed. It seems quite similar to a circular flight path in an inclined plane performed at high altitude (over 10,000 metres). The overall amplitude of the flight path is wider than the trajectory obtained by Sachs, with a vertical amplitude of the order of 80 metres.

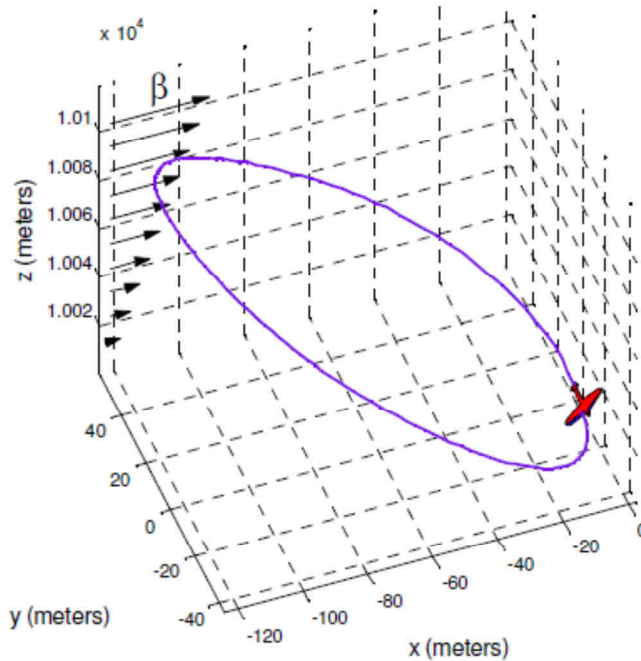


Figure II.3: Dynamic Soaring closed-loop within a linear gradient, reproduced with permission from Grenestedt *et al.* [57], © 2011 IEEE.

II.2.4 DS in hurricanes

Another environment where strong wind shear from is within hurricanes, and the same authors Grenestedt *et al.* give a go at DS simulation within this peculiar wind field [59]. A standard hurricane wind model is chosen, where the wind speed, for a constant height, varies with the radius of the hurricane considered. The methodology is otherwise rather equivalent to their paper in the Jet Stream [58]. They conclude that the theoretical feasibility to perform DS within a hurricane depends on the wind section profile encountered. We see the main contribution of this paper as a demonstration that DS can be exploited where any wind gradient form. Indeed, whether the wind sees a vertical variation in its horizontal component or a horizontal variation of that same component, DS trajectories can potentially be found.

II.2.5 DS at Ridges

Another potential source of wind gradient comes from wind blowing over mountain ridges. Richardson provides an analysis of the DS flight performed by RC gliders which enable vehicles to reach speeds up to 450 mph without any engine [60, 61]. His contribution consists in modelling ridge soaring through a simple Rayleigh cycle, which consists in assuming a circular loop trajectory along a plane tilted upward into the wind and crossing a two layer wind shear structure. This highly simplistic model still enables the author to compute the overall wind strength to vehicle maximal velocity behaviour. He also outlines optimal values for loop periodicity thanks to simple analytic calculation from the model. The main advantage of his approach is to be able to compare his model with achieved RC gliders flights thanks to measurements conducted from the ground (mainly radar speed measurement) He concludes that further research would consist in implementing instruments on vehicles in order to get more accurate elements of comparison between theory and experiment. Besides, he suggests that some numerical modelling would help to refine the flight model.

II.2.6 Gust Soaring

Gust soaring cannot quite be considered as classical DS technique. Indeed, the vehicle does not perform regular cycles, but rather aims at taking the maximum out of a sudden and unpredictable gust. However, it is nonetheless a way to extract energy from a horizontal variation in wind, for which the dynamics of the vehicle and the energy extraction are also bound up together. The main difference with DS is the time scale and the stochastic nature of the problem, which makes it impossible to plan trajectories.

Patel *et al.* [62] detail the basic principles of gust-energy extraction in Fig. II.4, in the case of vertical gusts. It consists in orientating the lift in the direction of the vertical motion of air met by the vehicle, respectively upwards and downwards for an updraft and a downdraft. Although authors do not provide a scale length on the figure, those variations, both in time and space, are at high frequency, such that conventional pitch control is inappropriate to control the lift in such a way.

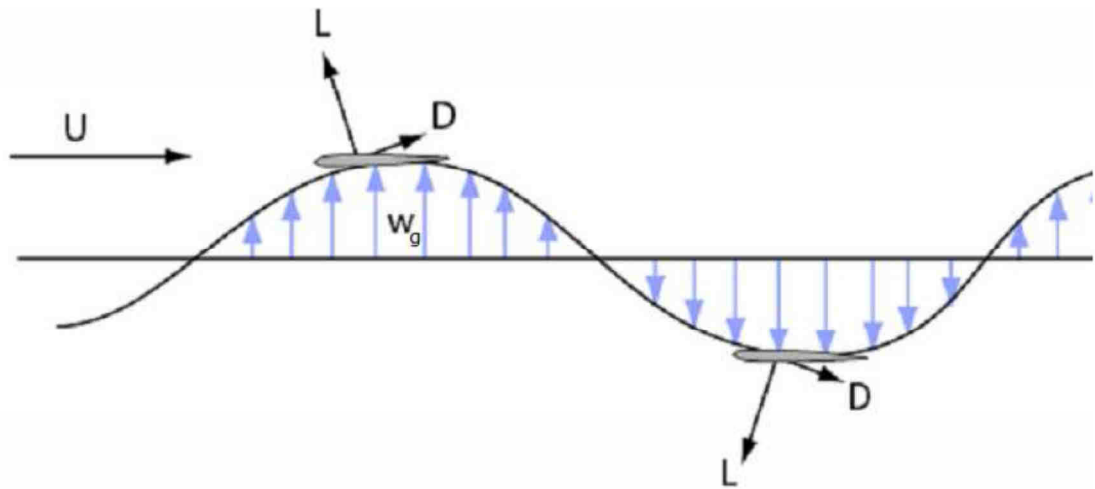


Figure II.4: Fundamental concepts of gust soaring, with the vehicle performing pull-ups within an updraft and pulling negative acceleration during downdrafts. Adapted from Patel *et al.* [62].

It is yet probable that albatrosses take advantage of gust soaring along their overall DS cycles [41, 42]. Several authors have focused on gust soaring [63, 62, 64, 65]. Lissaman *et al.* concentrated on the general understanding and simulations of the energy-extraction principles [63] with a methodology which is rather close to what can be done for DS, while Langelaan *et al.* [64, 65] as well as Patel *et al.* [62] investigate control laws. Gains were demonstrated to be theoretically and practically feasible.

II.2.7 Practical Aspects

One of the challenges of DS flight is that inherent dynamic manoeuvres make it difficult to comprehend and to analyse from an experimental point of view. Dynamic conditions obviously cannot be recreated in a static wind tunnel environment. Some publications have focused on the way DS flight could be practically implemented with an autonomous vehicle as well as on experimental processes to improve the knowledge of DS flight.

Even before reaching the capabilities to perform DS flight, vehicles would need to gain autonomous capacity, including path planning and environment recognition. In the case of DS, the knowledge of the wind field is essential and usually assumed to be known in research approaches so far. Langelaan suggests a way to estimate the wind field for a small flying vehicle [66]. The approach utilizes sensors which are already part of a standard autopilot sensor suite available on the vehicle and its primary motivation is energy-harvesting perspectives. Therefore, hardware only consists of on board GPS, Inertial Measurement Unit (IMU), magnetometers, static pressure and dynamic pressure. A flight model associated with sensor

fusion capacity is used to derivate a wind field estimation algorithm. The author concludes that errors in the estimation can be maintained low by increasing the accuracy of airspeeds measurements. Simulations are performed with this wind estimation algorithm and a gust energy-harvesting controller. It shows that energy-harvesting is still possible using a wind estimate and not an implicitly assumed wind field at the cost of greater control actuation, since the vehicle is discovering its environment in real time.

Bower undertakes another approach to bring DS flight closer to practical feasibility [67, 68]. He sums up the different enabling technologies required for the practical use of DS for a small UAV and he underlines that technology in the field of sensing and communications already reached a sufficient level of maturity and miniaturization to be utilized in the purpose of his research. He identifies the need for measuring height over the ground in order to control the proximity to the waves, without being able to select an appropriate ready-to-use technical solution. The author then undertakes the same approach as Zhao *et al.* by deriving optimized solar augmented trajectories for a point mass model of a vehicle within an environment simplified to a logarithmic vertical evolution of the wind. The optimization process uses collocation techniques and is solved with SNOPT. He finally undertakes a vehicle design trade study to analyse trajectory optimization parameter sensitivity about a baseline design. He mentions the need for a more realistic environmental model as well as for a refined vehicle model with inertias He then concludes that trajectory generation and guidance capabilities are major challenges to overcome before DS flight can be performed and underlines that accurate estimation of aircraft state and wind field must be developed on the experimental side.

Rather than recreating DS flight conditions so as to eventually validate the flight model, one alternative option is to compare the theory with the biological system which initially inspired DS. Sachs intends to prove albatross can make progress against the wind using DS, which is one key parameter to the feasibility to perform long endurance flight in any direction. Papers [43, 44] sum up the results of the first in-flight measurement campaign applied to DS research. The experiment is based on a GPS logger attached on the back of an albatross, as seen on Fig. II.5, from which raw data are post-processed with a trajectory reconstruction algorithm. This requires liaising with biologists on the field to set up and recover the device as-well-as significant logistics to perform such a test at those distant and remote locations.



Figure II.5: GPS logger attached on the back of an albatross. From Sachs *et al.* [43].

In the meantime, wind parameters were obtained using SeaWinds. Different scenarios of strong and weak winds are recorded and resulting trajectories are computed. The author then analyses and compares the patterns which show that progress against the wind was achieved by the tagged albatross. The bird's trajectories are clearly different depending whether it goes with or against the wind. The wind strength also seems to have an influence on the way the bird makes progress. One of the main observations was the use of more pronounced tacking manoeuvres, when progressing against a stronger wind. Reconstructed altitude time history cycles presented in annex shows that the height reached by the bird is on average much lower than predicted on Sachs and Deittert numerical models. It also shows that an important part of the time, albatrosses are flying below 2 metres altitude, i.e. in the vicinity of waves.

II.3 Overview and Critical Summary

The subject of DS has provided several points of views which seem to lack consistency so far. Even with the same and simple environment model, authors still remain vague in describing the energy-extraction process in their model. On this matter, Sachs underlines that the energy-extraction occurs during the higher turn, without providing further details. Zhao highlights that with an air-based point of view, energy is extracted through the work of a fictitious force, also called dynamic soaring force by Deittert, when the vehicle crosses the region of strongest wind shear, that is to say at low altitude. Lissaman details how energy can be locally gained from convective mechanisms via the work provided by the lift, without focusing on overall DS flight path, while Patel *et. al* applies it in the case of vertical drafts.

Models developed by numerical studies hardly seem to represent the reality of the field observed by biologists. While biologists provides useful qualitative data but lack parameters to go into quantitative details, one of the main limitations about numerical studies is to rely on a clean model of wind gradient over a wave-less surface, which all biologists acknowledge as a limitation. All authors from numerical studies agree on the need to improve the environmental model in order to get closer to reality, by taking into account wind-waves interactions.

Furthermore, all theoretical studies lack some experimental validation. Sachs in-flight measurement campaign was a first but lacks the measurement of further flight parameters to permit a thorough comparison with the flight model developed by the theory. Among those, the relative airspeed, the air relative flight path angles as well as the accelerations would give more elements of comparison.

Another limitation acknowledged by different authors is the lack of practical point of view among the numerical studies. Those papers investigate DS, without assessing changes in vehicle properties, in flight path constraints or in environmental conditions, which is necessary before concluding on the eventual feasibility to exploit DS.

To put in a nutshell, an overview of existing literature shows a lack of consistence between the different points of views as well as a lack of maturity in the concept of exploiting DS. Those limitations comfort us in our choice of research question and of research objectives

CHAPTER III

MODELLING A VEHICLE AND ITS ENVIRONMENT

The scope of DS research involves interdependent concepts, which have been introduced to be the vehicle, the environment and the flight model. Each has its own variables, as well as its own representation with respect to other models. Variables translate into properties for each respective representative model. Design variables for the vehicle translate into aerodynamic and inertial properties; direction and strength of high altitude winds combined with surface properties form a representation of a three dimensional wind field above the surface and finally, state and control variables are varied over time to form a consistent flight path. The core of our subject is the way for a vehicle to harvest energy from its windy environment in a specific fashion. Hence a vehicle and an environment model must be a priori determined in order to establish a flight path that relates them. This part aims at presenting the variables involved in both model, as well as quantifying the way those influence the respective representation of each.

III.1 The Vehicle Model

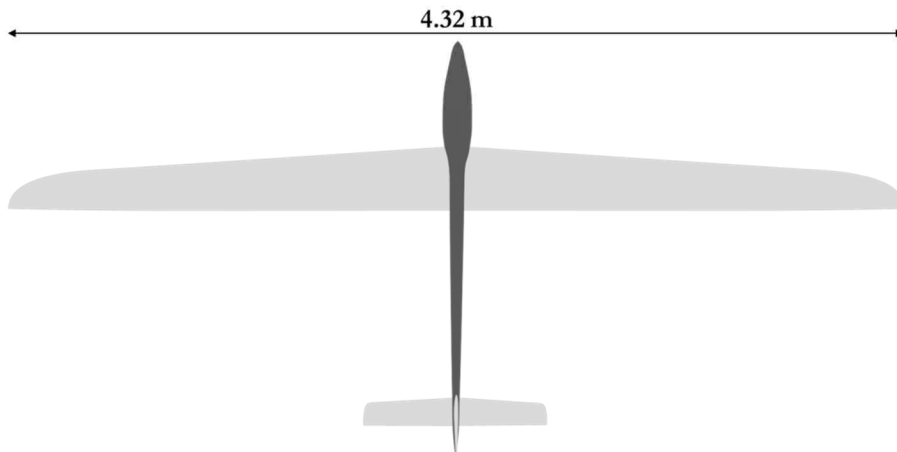
The vehicle flies a whole range of functioning point during a DS cycle, which makes it unappropriated to optimize a specific design. Besides, as wind field conditions change, and as the type of mission scenario relative to this wind field are most likely to alter, it makes it difficult to optimize a vehicle over such various conditions. Hence it was chosen, so far, to break down the research problem by isolating the vehicle design to something conventional and well-known. Without getting into great details, any glider-shaped vehicle with good lift to drag ratio has the potential to fly DS trajectories and classic architectures have been demonstrated to perform best in this area.

III.1.1 Baseline Designs

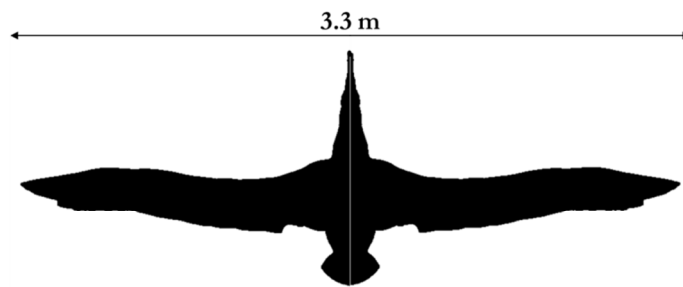
In order to understand the way general design variables can influence DS performances, it was still chosen to try out different vehicles, of various sizes. Indeed, one of

the objectives of this research is to assess whether the flight of albatrosses can be transposed to vehicles that could differ from albatrosses, in particular in terms of size.

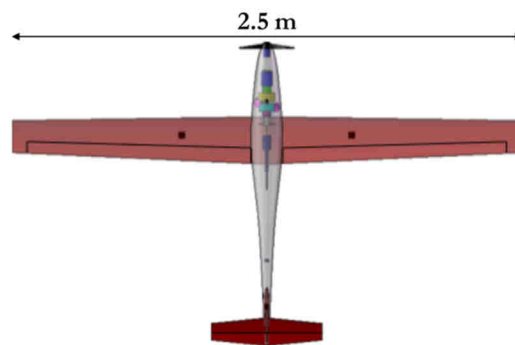
Cloud Swift



Wandering Albatross



Mariner



DT-18

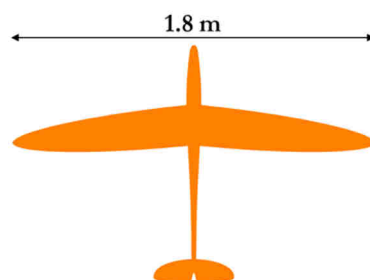


Figure III.1: Planforms of the UAVs considered, on the same scale. From top to bottom, *Cloud Swift* [19], *Wandering Albatross*, *Mariner*, reproduced from Bower [67], *DT-18*, reproduced from Delair-Tech [69].

Figure III.1 presents the different vehicles chosen. It naturally starts with what will be called *Wandering Albatross* in the remaining of the document. Based on data from different authors on the biological field, an average geometry is outlined by Sachs [47]. Although variables somehow differ slightly from data gathered in Table I-1, the advantage to stick by Sachs' chosen geometry is to have a support for validation. However, for the vast majority of simulations, UAV models were chosen, based on the architecture of a small-scale glider rather than that of a bird. That suppresses the need to estimate and to average a geometry between different albatross specimens and it makes sure that the performances of the model are achievable by an engineering-designed vehicle.

Among those vehicles, the biggest is named *Cloud Swift* from Allen's work [19]. It is based on the radio-controlled cross-country glider *SBXC* from *RnR Products*. It was chosen for its wide representation in other research works [19, 70] and in the way that it represents a performant glider in the upper range of small UAVs. It has the highest aspect ratio (AR) of the four designs and can be expected to have the best gliding performances.

Next on the list is Bower's *Mariner* [67], which has been developed to minimize the wind strength required to perform DS, under certain wind field conditions. Contrary to albatrosses which can have their wing tip touching the water, as presented in Fig. I.5, the ability of a UAV to fly very close to the surface is limited. However, in order to keep the centre of gravity as close to the surface as possible during manoeuvres at low height and high bank angles, the methodology developed by Bower limits the span, at the expense of sacrificing the aspect ratio.

Finally, the smallest model is based on the *DT-18*, engineered by *Delair-Tech* [69], a French start-up based in Toulouse. It takes the most of the 2 kg UAV class (including mission payload) and is the only small civilian UAV to be approved for Beyond Visual Line-of Sight operations (BVLOS) by an official rule-making body [69]. Main features include an elliptical shape of the wing planform, which is assumed to optimize the span-wise lift distribution. Furthermore, the aspect ratio is lower than the other two UAVs and we interpret that as a way to keep the mean aerodynamic chord (MAC) at a relative high value and thus avoid local low-*Reynolds* numbers on the majority of the wing.

Each of the three UAV designs has been selected in its powered version, where an electric motor and a folding propeller allow the vehicle to sustain flight under its own power.

III.1.2 Quantification of Vehicles

The baseline design characteristics of the four vehicles, in terms of size and weights, were given by respective authors and are summed up in Table III-1. It is to be mentioned that for the sake of comparison, the baseline mass was taken for vehicles in a ready-to-fly configuration, including battery, propulsion hardware, sensors, autonomous capabilities, but excluding any extra payload. The mass would then be eventually increased from their baseline values for later simulations, hence virtually adding a payload.

The aerodynamic behaviour of small-scaled slender bodied vehicle, like the ones we are interested in, is quite well modelled by tools such as *Xflr5* [71] or *AVL* [72]. Those software extrapolate a 2D pressure distribution around airfoils to a full 3D behaviour, by means of different theories, such as lifting line, 3D panels or vortex lattice methods. Initially designed for Radio-Controlled (RC) gliders applications, they are particularly adapted to the geometries of chosen vehicles. *Mariner* aerodynamic characteristics were obtained by Bower through *AVL* [67], while those of *Cloud Swift* were obtained by building a strip model from *XFOIL* [70].

Another approach is to apply a technique called *Prandtl's lifting line theory* in order to get first-order approximation for the drag coefficient [73]. It gives fairly good results for a finite wing with no sweep and a reasonably large aspect ratio. By modelling the wing as a fixed vortex with a series of trailing vortices extending behind it, contributions from each vortex are summed into a resulting force called the induced drag, represented by its coefficient C_{Di} . The zero-lift drag, represented by C_{D0} , is added so that the overall drag is represented by a quadratic drag polar as shown in Eq. III.1. The *Oswald* coefficient (e) is a correction factor that accounts for disparity between the elliptical lift distribution assumed in the theory and the realistic lift distribution.

$$C_D = C_{D0} + C_{Di} = C_{D0} + \frac{C_L^2}{e\pi AR} \quad (\text{III.1})$$

For wings of relatively high aspect ratio and no sweep, the theory is rather consistent and an Oswald coefficient of 1 can be assumed. It is what Sachs has done to estimate the drag coefficient of the *Wandering Albatross*.

The *DT-18* is the smallest and lightest vehicle of the three UAVs considered. Besides, as it was mentioned before, the aspect ratio is also the lowest and a slight sweep is integrated in the wing design, which is apparent from Fig. III.1. Since conventional modelling techniques and

tools might reach some limits for the design of the *DT-18*, a wind tunnel testing campaign was conducted in order to get accurate data. Among others, the objective of the experiment is to provide an aerodynamic polar over the whole range of angles of attack and assess its sensitivity to the *Reynolds* number. Different vehicle configurations are tried out by combining variations in some of the vehicle degrees of freedoms, in terms of engine rate, control surfaces and flaps.

Among the two wind tunnels ISAE has at its disposal, the wind tunnel *S4*, (located on the ENSICA Campus) was selected thanks to the wide $3\text{ m} \times 2\text{ m}$ elliptical test section which enables to set up a full-scale instrumented replica of the *DT-18*. Besides, the range of speeds available made it possible to get data for realistic airspeeds seen in flight by the UAV.

The *S4* wind tunnel is an Eiffel-type wind tunnel with an open elliptical test section and a closed, non-streamlined, recirculation zone. Installation can be seen on Fig. III.2. The airspeed ranges from 0 to $42\text{ m}\cdot\text{s}^{-1}$ and the associated turbulence rate is 0.52% .

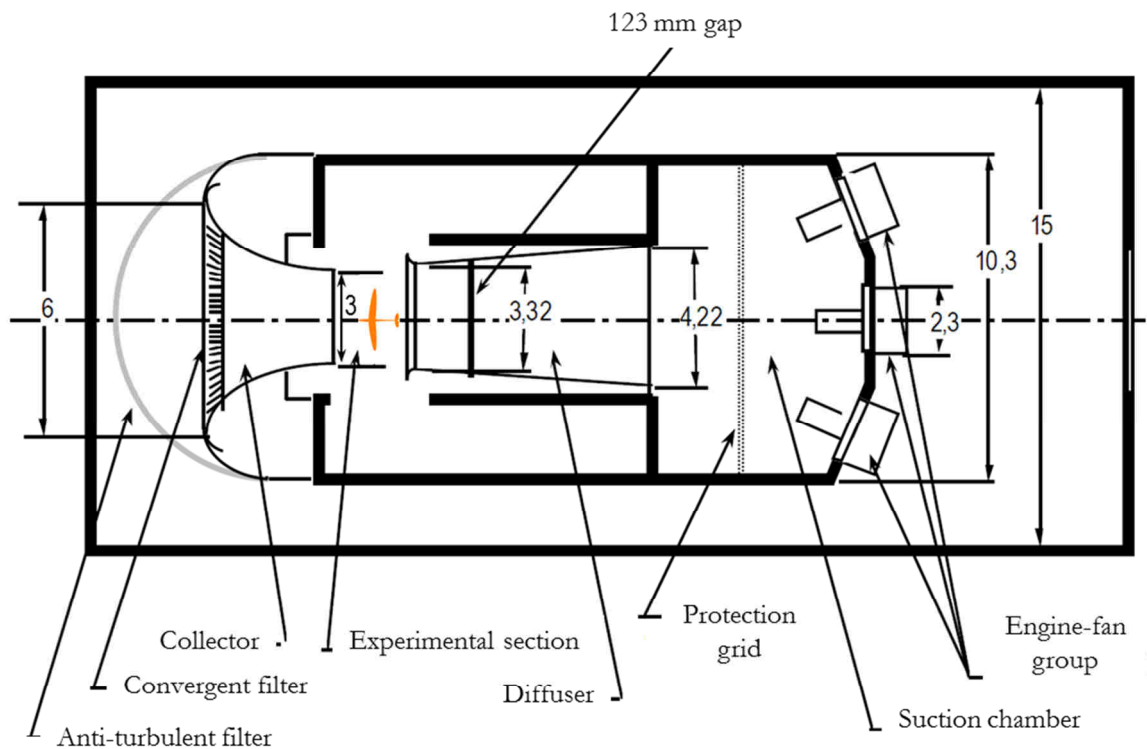


Figure III.2: Top view of the *S4* wind tunnel. All distances are in m , unless otherwise stated. The *DT-18*, colored in orange, is schematically included in the test section. Adapted from [74].

A factory-built *DT-18* was modified for the sake of the experiment. The external shape was not altered and main changes were conducted in order to link the replica to the rest of the experimental set-up. A ventral-docking configuration was selected, where the mock-up is hold

on top of a single mast, see Fig. III.3. Aerodynamic forces are determined via a measurement unit, sheltered inside the fuselage, which structurally links the mast with the aerodynamic mock-up. On the mock-up-side of the measurement unit, a specific holding plate was designed to link the standard cylinder-shaped-measurement-unit to the geometry of the *DT-18* while also maintaining the mock-up in the correct attitude. A cut was made on the ventral panel of the *DT-18*, just enough wide so that the wires and the mast could go through.

The mast is connected to a cradle on the ground of the test section. The cradle can move along two curved rails such that mock-up rotates along a fixed pitch axis (the top of the mast is the centre of the rotation). This change in longitudinal attitude with respect to the wind tunnel section is used to modify the simulated angle of attack (*AoA*). Another rotation is possible along the axis of the mast itself. This variation in yaw permits to simulate a side slip angle.

A majority of the on board electronics were kept inside the fuselage and powered from outside. It enabled to control the aerodynamic surfaces and the engine output through the same user interface, developed by *Delair-Tech*, as the off-the-shelf *DT-18*.

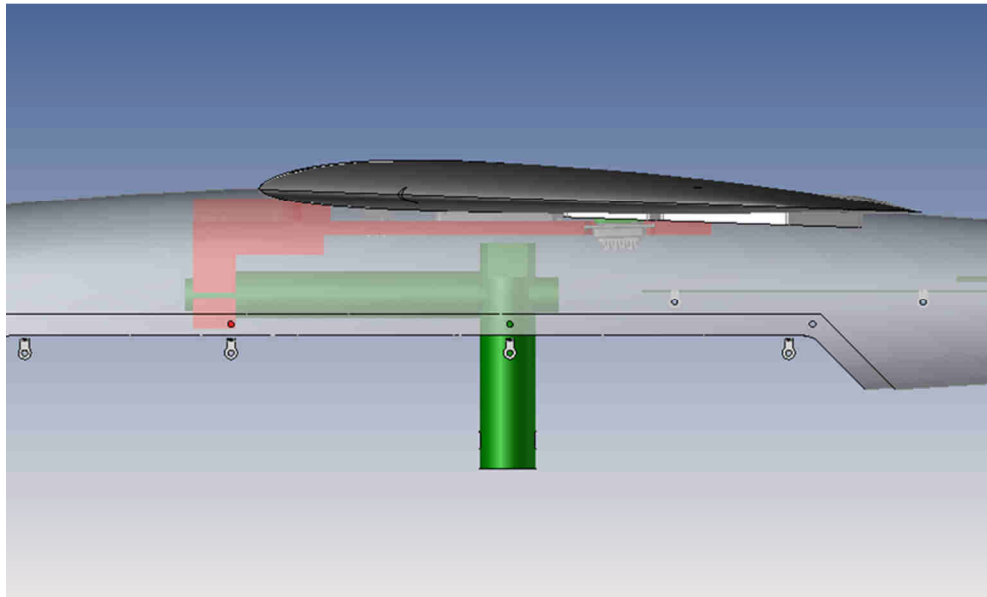


Figure III.3: Rendering of the mechanical set-up of the mock-up on the mast. The holding plate (red), supports the mock-up on its upper surface and clasp the measurement-unit (horizontal, green) in one of its forward extremity. The measurement-unit is encircled at its aft extremity by the ventral mast (vertical, green). Copyrights *Delair-Tech*.

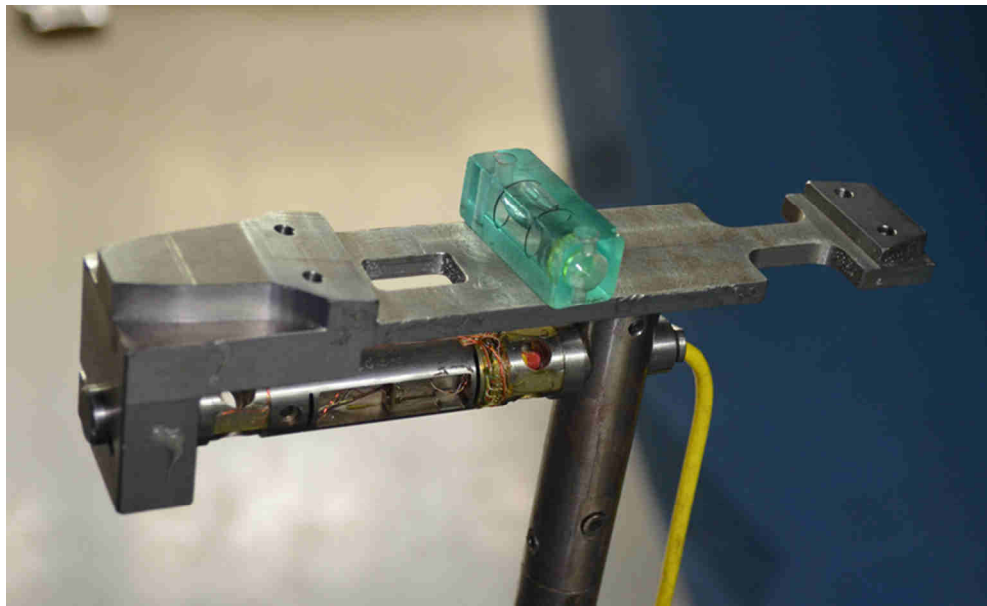


Figure III.4: Mechanical set-up, which evidences the holding plate (top, horizontal), the ventral mast (bottom, vertical) and the measurement unit (middle, horizontal) in between. Here, a spirit level is laid on the holding plate, in order to verify its horizontality and ensure that the mock-up will be in a wings-level-configuration, before locking the holding plate into position with respect to the measurement unit. The yellow cable transmits measurement data from the unit to the acquisition centre. It runs downwards along the mast out of the lower side of the fuselage.



Figure III.5: The *DT-18* experimental mock-up into place, through the single ventral mast, inside the elliptical test section of the *S4* wind tunnel. The open test section is clearly visible, as the workshop is visible (left) outside of the section. The suction fans are visible (top right) at the end of the suction chamber, leeward of the diffuser. The curved rails of the cradle can also be seen (bottom), as well as the external feed (bottom left) for powering on board electronics.

Forces and moments were measured locally on different places of the measurement unit and then could be calculated on different virtual points. Those were calculated at the virtual position of the centre of gravity of the *DT-18* (which is different than that of the mock-up). Practically, what is needed for DS simulations is the variation of the drag coefficient with the lift coefficient. For the sake of simplification, it can be reduced to a polynomial form of the following.

$$C_D = C_{D0} + C_{D1}C_L + C_{D2}C_L^2 + C_{D3}C_L^3 + C_{D4}C_L^4 \quad (\text{III.2})$$

The respective drag coefficients can show some sensitivity to the airspeed, all the more if that range of considered airspeed sees strong Reynolds-number effects. The $C_D = f(C_L)$ behavior defined by Eq. III.2 is hence dependent on the airspeed to some extent.

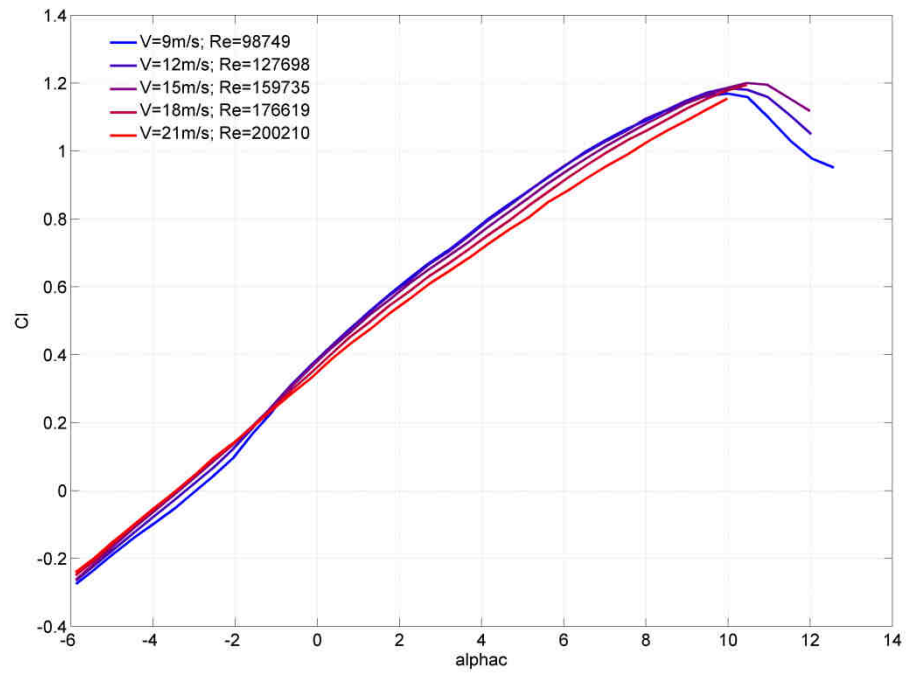


Figure III.6: Evolution of the coefficient of lift with the angle of attack (α) for the *DT-18*, for different wind tunnel speeds and their associated Reynolds number for the vehicle.

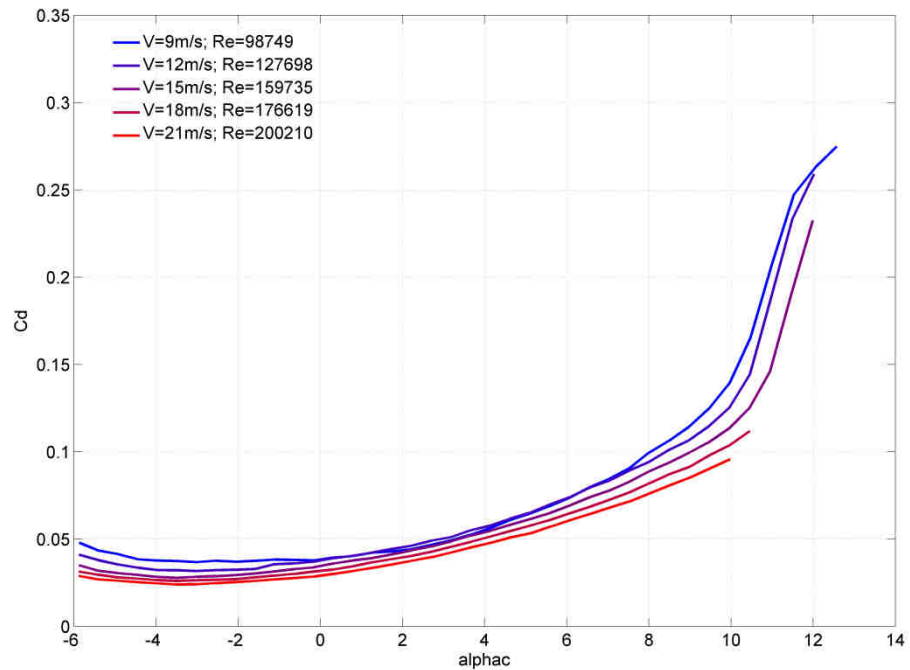


Figure III.7: Evolution of the coefficient of drag with the angle of attack (α) for the *DT-18*, for different wind tunnel speeds and their associated Reynolds number for the vehicle.

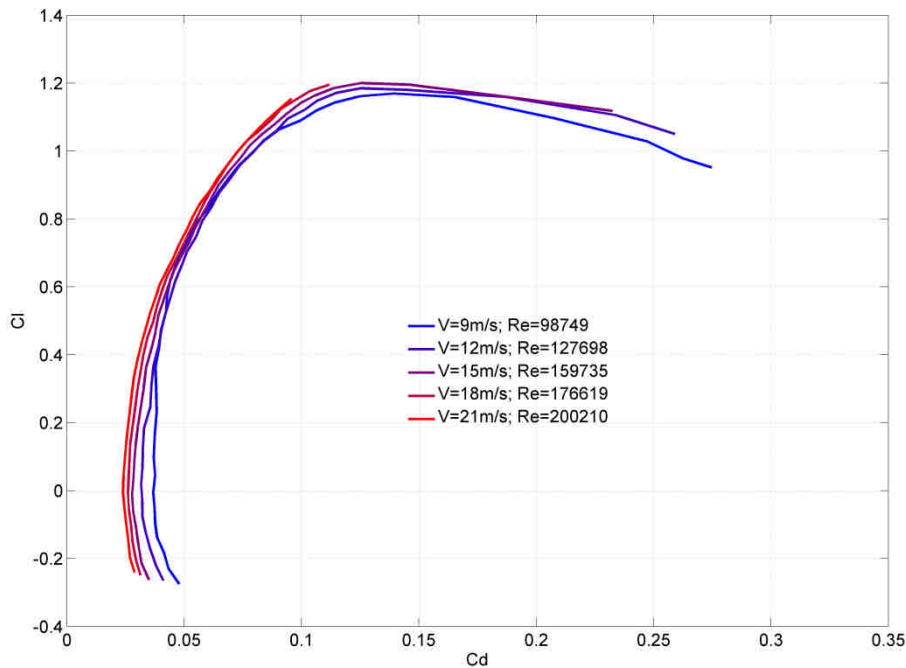


Figure III.8: Evolution of the coefficient of lift versus the coefficient of drag for the *DT-18*, for different wind tunnel speeds and their associated Reynolds number for the vehicle.

For wind tunnel speeds above 15 m.s^{-1} , the angle of attack was limited in order not to damage the mock-up or the balance. A way to generally represent glider performance is to represent the speed polar which shows the evolution, when the vehicle is in steady equilibrium gliding state, of the vertical sink speed versus the horizontal speed. This curve, representative of steady states of the vehicle at different airspeeds, can account for variations of the $C_D - C_L$ behavior with the airspeed. However, DS flights involve dynamic manoeuvres where the vehicle is rarely in an equilibrium position. Still, a relationship between lift and drag is needed for the vehicle and for the sake of simplification, Reynolds-number effects are neglected and the relationship is supposed to be independent of the airspeed. Figure III.8 displays how curves are mainly sensible to the airspeed for Reynolds numbers below $1.5 \cdot 10^5$. Gaps between the curves are narrowing for higher Reynolds numbers. Given those considerations and as the expected airspeed of DS flight are rather high, it was estimated that results obtained at 18 m.s^{-1} would be quite representative of aerodynamic performances of the *DT-18* for DS simulations.

Data of the four vehicles are gathered in Table III-1 and would serve to characterize their respective model in the remaining of this thesis.

Table III-1: Comparison data between the four vehicles considered.

Parameter	<i>Cloud Swift</i>	<i>Wandering Albatross</i>	<i>Mariner</i>	<i>DT-18</i>
m (kg)	6.8	8.5	2.0	1.7
b (m)	4.32	3.3	2.5	1.8
S (m ²)	0.957	0.65	0.485	0.248
AR	19.5	16.8	12.9	13.1
WL (N/m ²)	69.7	128.2	40.44	67.2
C_{D0}	0.017	0.033	0.0173	0.0259
C_{D1}	0	0	-0.0022	-0.0002
C_{D2}	0.0192	0.019	0.0629	0.0735
C_{D3}	0	0	-0.0578	-0.0858
C_{D4}	0	0	0.0314	0.0607
C_{Lmax}	1.0	1.5	1.17	1.195
$(L/D)_{max}$	27.7	20	20.5	15
Vz_{min} (m/s)	0.39	0.6	0.42	0.76
$Power_{min}$ (W)	25.7	49.7	8.2	12.7
$Conso_{min}$ (J/km)	2410	4174	956	1113

Mariner stands out in terms of wing loading, which is the lowest of all four. Besides, *Mariner* manages to reach a maximum lift to drag ratio $((L/D)_{max})$ comparable to the *Wandering Albatross*, which has a higher aspect ratio and a longer wingspan. This is partially achieved through a lower zero-lift drag coefficient C_{D0} , which could only be estimated for the *Wandering Albatross* and is therefore subject to greater uncertainties. However, Pennycuick's estimate of the $(L/D)_{max}$ for the *Wandering Albatross* does not come far at 21.2 [25]. Although the zero-lift drag coefficient seems rather low for *Mariner*, a comparable value is obtained for *Cloud Swift* which strengthens the assertion that it is an achievable value for this class of vehicles. Besides, another important piece of information regarding glider's performances is the minimum sink speed (Vz_{min}). Both *Cloud Swift* and *Mariner* achieve lower minimum sink speeds than the *Wandering Albatross*. *Cloud Swift* has the lowest minimum sink speed of all,

which underlines its background conception for thermal soaring [19]. Indeed, this low value of minimum sink speed allow it to maintain level flight by exploiting thermals rising at a correspondingly low minimum rate of climb, enabling it to take the most out of a wide range of potential thermals. The smaller *DT-18* does not reach such high value in $(L/D)_{max}$, nor low value in $V_{z_{min}}$, which can partly explained by the lower *Reynolds* number, which hamper the zero-lift drag coefficient. The *DT-18* is still rather interesting for our study case, precisely for its reduced dimensions, especially span-wise, which would allow it to get closer to the surface during DS manoeuvres. To put in a nutshell, the comparison between vehicles highlights that the *Wandering Albatross* has aerodynamic gliding performances that can be reached and even exceeded. *Mariner* is a sound illustration of this conclusion and combines a streamlined design with a lightweight architecture to outperform the *Wandering Albatross*. Therefore, the gliding performances of UAVs are not a deadlock regarding the feasibility to exploit DS flight.

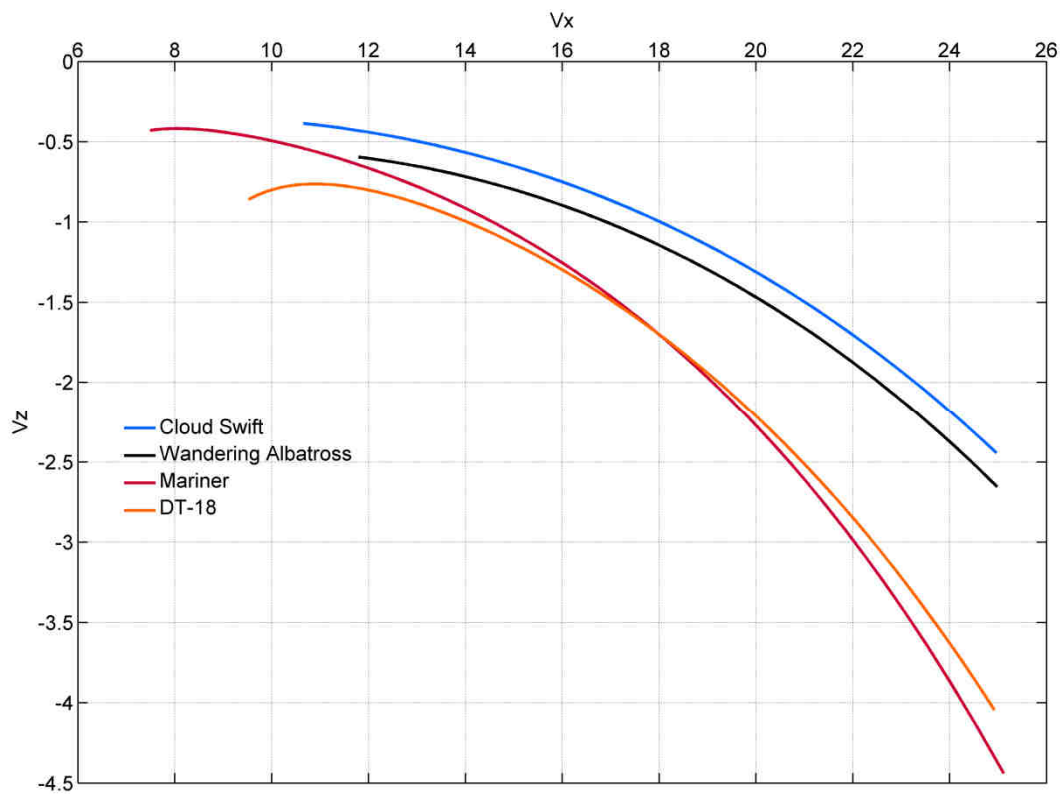


Figure III.9: Comparison of speed polar for each of the four vehicles.

Additional metrics can be compared when it comes to flight performance. The first is directly related to the sink rate and it is the minimum power required to sustain the vehicle airborne ($Power_{min}$). It relates to the minimum sink rate as follow.

$$Power_{min} = m g \dot{z} = m g [Vz_{min}] \quad (III.3)$$

It corresponds to the minimum power expenditure in flight, and intrinsically relates to the endurance of the vehicle. Indeed, if a vehicle needs to remain in the air for as long as possible, it should fly at the airspeed which allow for the minimum sink rate. If the vehicle is propelled, then by sustaining that airspeed and with a power output of its propeller equal to $Power_{min}$ it will maximize its endurance. For a given charge Bat_0 of its battery, and a propulsion efficiency given by η_{prop} , the vehicle can theoretically sustain level flight for a nominal period of time called $Endurance_{max}$ and given by the following equation.

$$Endurance_{max} = \frac{\eta_{prop} Bat_0}{Power_{min}} \quad (III.4)$$

Where η_{prop} is given by the following formula, T being the thrust and Bat the battery charge.

$$\eta_{prop} = \frac{T \cdot V_a}{Bat} \quad (III.5)$$

The energy expenditure of a gliding vehicle in steady flight over a horizontal-travelled distance $Dist$ can be related to the associated loss of height h and to the lift to drag ratio as follow.

$$E_{expenditure} = mg * h = mg * \frac{Dist}{L/D} \quad (III.6)$$

This expenditure corresponds to the energy needed by the vehicle to sustain level flight over the distance $Dist$. Therefore, the lowest nominal energy consumption per unit length travelled, called $Conso_{min}$, is given by the following formula.

$$Conso_{min} = \frac{mg}{(L/D)_{max}} \quad (III.7)$$

The lowest energy consumption per unit length travelled is obtained by flying at the functioning point corresponding to the maximum lift-over-drag ratio. It should be noted that $Conso_{min}$ is homogeneous to a force, expressed in *Newton*, and that it corresponds, to a slight

approximation, to the thrust required from the vehicle to sustain that functioning point. For a given charge Bat_0 of its battery, the maximal theoretical range of the vehicle called $Range_{max}$ is given by the following equation.

$$Range_{max} = \frac{\eta_{prop} Bat_0}{Conso_{min}} \quad (III.8)$$

It follows from those calculations that the maximal endurance and maximal range of a vehicle are respectively related to the minimum sink rate and the maximal lift-over-drag ratio of the UAV. Those performance parameters indeed permit to establish respectively the minimum in-flight power required, $Power_{min}$, and the minimum $Conso_{min}$.

Those latter metrics are summed up for each vehicle in Table III-1. It can be seen that *Mariner* reaches both the lowest power required and the lowest consumption. Therefore, if the four vehicles were equipped with the same battery and assuming they all share the same propulsion efficiency η_{prop} , *Mariner* would fly longer and farther than any of the other three vehicles.

III.1.3 Point Mass Model

For the sake of simplification, a point-mass model was chosen to represent vehicles. This type of representation allows simplifying the motion of the vehicle to three degrees of freedom, which are the three translations.

The main advantage is that the vehicle input to the flight model will be kept to the minimum, which is a strong plus for the methodology that lies behind the formulation of DS trajectories. Furthermore, the scale of the wind gradients is such that span-wise variations in wind can be neglected and that a point mass model is an adequate representation of vehicle dynamics. The main limitation is that the rotational behaviour of the vehicle around its centre of gravity is not modelled. However, it does not mean that rotations cannot be indirectly simulated or controlled to some extent. The lack of equations representative to the rotational behaviour of the aircraft would have to be partially covered by further assumptions. For instance, by assuming that the vehicle is in symmetric flight with respect to the surrounding air, there is hence no sideslip angle, and the aircraft can be simulated to be directly aligned by the airspeed. For a hypothetical six degree of freedom model, symmetric flight would indeed be sought, but this orientation would be physically modelled, rather than simply assumed.

Practically, all forces that apply to the vehicle are concentrated at the centre of gravity G . Those are respectively the lift (L) the drag (D) and the weight (W) and are expressed in Eqs. III.9 to III.11.

$$L = \frac{1}{2} \rho \cdot S \cdot C_L \cdot V_a^2 \quad (\text{III.9})$$

$$D = \frac{1}{2} \rho \cdot S \cdot C_D \cdot V_a^2 \quad (\text{III.10})$$

$$W = mg \quad (\text{III.11})$$

The orientation of the weight comes trivially, but the direction of aerodynamic forces is directed by the airspeed. The orientation of the lift requires the introduction of a parameter that is the bank angle. Once again, practically, this angle is a state of the aircraft which is piloted by deflections of control surfaces and which variations depend on the vehicle's inertia along its roll axis. With a point mass model, this angle will be directly piloted. Further precisions are detailed in the part dedicated to equations of motion.

III.2 Environment Model

Dynamic Soaring research is faced with a significant limitation on the environment model it uses. Although the ocean surface holds the significant advantage to be rather flat and uniform compared to earth variations, the wind profile encountered is not that of a flat plate. So far, the environment was only taken into account through steady boundary layer vertical wind profiles, either following power-law behaviour [50, 56] or logarithmic evolution [47, 67] or even selecting a linear wind profile [49]. However, those profiles are constant in space and time and are not correlated to any change in environment condition, apart from changing the reference wind itself. The purpose of this part is to refine the environment model used in simulations so as to correlate the wind field with environment conditions and to describe how DS could be affected by the presence of a moving wavy surface.

III.2.1 Wind Profiles over rather Flat Surfaces

In the present case of this study, we consider neutral conditions at sea, that is to say that convective exchanges or heat transmission are absent. Those conditions are met whenever

the surface is cooler than the air above. The subsequent boundary layer is therefore solely driven by wind shear turbulence and classical theory of the turbulent boundary layer can be used. A distinction between two cases is made, either the surface is considered smooth and therefore the mean velocity profile is that of a flat plate, or the roughness of the surface induces changes in the velocity profile. Some concepts related to that theory are introduced hereafter. The friction velocity u_* is defined by Eq. III.12. and is a representation of the stress τ_p exerted by the wind on the ocean surface. The air density is represented by ρ .

$$u_* = \sqrt{\frac{\tau_p}{\rho}} \quad (\text{III.12})$$

The friction length z_* of the boundary layer is the length scale of the internal sub-layer and is related to the viscosity ν by Eq. III.13.

$$z_* = \frac{\nu}{u_*} \quad (\text{III.13})$$

The general form of the dependence of the mean velocity profile over a flat rigid wall is called the *universal law of the wall* and is expressed in Eq. III.14.

$$\bar{u}(z) = u_* \cdot f\left(\frac{z}{z_*}\right) \quad (\text{III.14})$$

The former relation is only valid for surfaces considered as dynamically smooth, that is to say when eventual protrusions on the surface are small enough not to entail a change in the mean velocity profile. Monin and Yaglom [75] propose a quantitative explanation of the requirement of the smoothness: the wall will be considered as dynamically smooth if the mean height h_0 of the protrusions satisfies the condition given by Eq. III.15.

$$h_0 \leq z_* = \frac{\nu}{u_*} \quad (\text{III.15})$$

In the ocean atmosphere, for friction velocity of the order of 10 *cm/s*, the friction length does not exceed some tenth of a millimetre and quite trivially the ocean surface cannot be considered as dynamically smooth. Therefore, the main velocity profile departs from the case of a flat surface and will depend on irregularities of the surface. Those are considered in

the expression of the main wind profile, via the roughness length z_0 , defined in Eq. III.16, which is characteristic of the dynamic interaction between flow and surface [75]. There is a one to one correspondence between the state of the surface, with a set of protrusions h_0 irregularly spaced and the roughness length z_0 .

$$z_0 = z \exp\left(\frac{-\chi\sqrt{z}}{\sqrt{C_f(z)}}\right) \quad (\text{III.16})$$

C_f is the friction coefficient at the altitude z , and χ is the von Karman constant. The fact that the shear stress is almost the same within the boundary layer entails that z_0 is a constant [75]. The mean velocity profile over a rough surface is subsequently given in Eq. III.17 [75].

$$\bar{u}(z) = \frac{u_*}{\chi} \log\left(\frac{z}{z_0}\right) \quad (\text{III.17})$$

For the resulting log profile, the local increase in horizontal wind with altitude, or local wind gradient is expressed in Eq. III.18.

$$\frac{\partial W_x}{\partial z} = \frac{u_*}{\chi} \frac{1}{z} \quad (\text{III.18})$$

The vertical gradient in horizontal wind is highest when closest to the ground. Besides, the local wind gradient is directly proportional to the wind friction velocity and the resulting effect is graphically displayed in Fig. III.10 (left). An important remark to be deduced out of Eq. III.18 is that the local wind gradient is independent from the roughness length, which is displayed in Fig. III.10 (right). Indeed the curvature remains identical, for a constant altitude, from one profile to the other. Therefore, surface roughness conditions do not alter the shape of the mean wind profile but shift the local mean wind speed by an identical value for the whole profile.

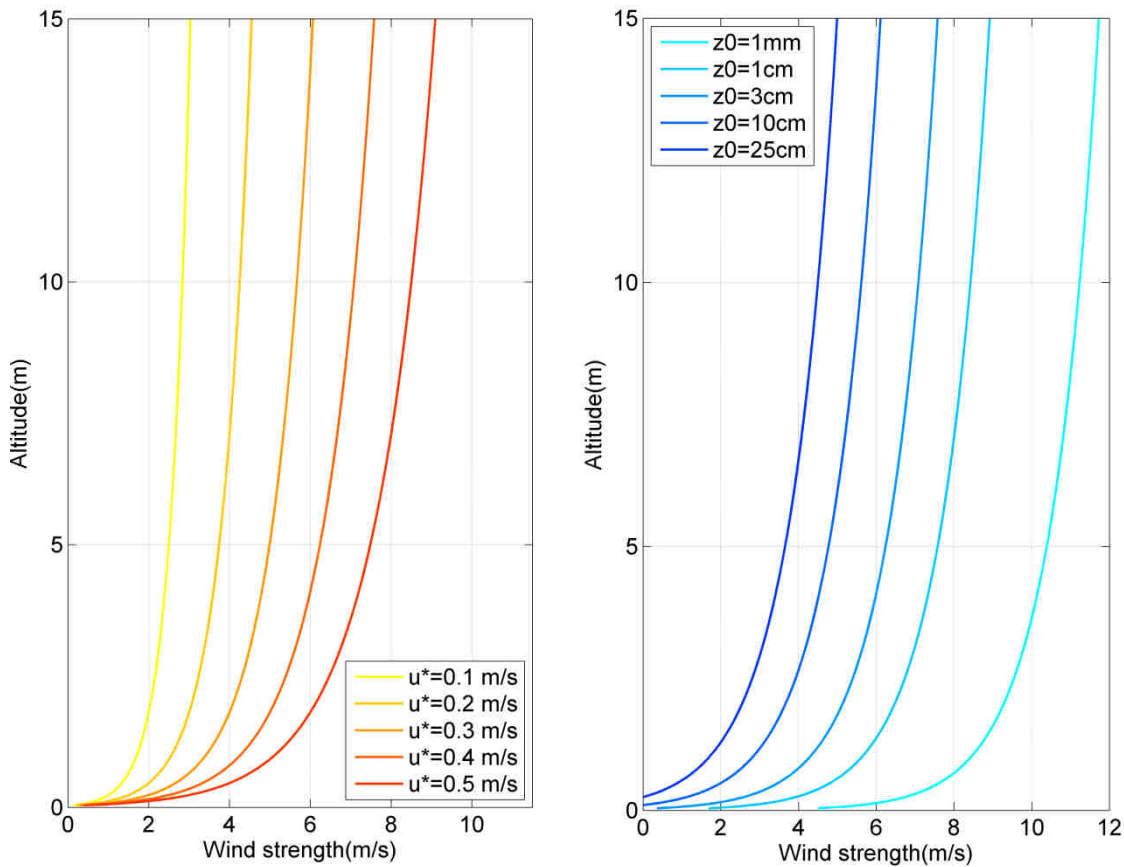


Figure III.10: Influence of variables from Eq. III.17 on the main wind profile. Left, variations in friction velocity for values representative of the atmospheric boundary layer. Right, variations in surface roughness length, representative, from the lowest to the highest, of open sea, open tarmac, open grass, low crops, and high crops respectively.

Earlier DS studies, such as Wood [46], Sachs [47], Barate [55] and Bower [68], use and mention values of z_0 around 3 cm, which is supposed to represent a typical value over *very rough seas*. They implicitly assume that ocean surface irregularities are of the order of the meter, which seems a priori fair for rugged conditions at sea. However, several limitations are going against the use of this estimation of z_0 for defining the mean wind velocity profile in the case of DS over oceans.

The first limitation is that specific literature on the topic refers to significant lower values. Stull [76] mentions values for z_0 of the order of the millimetre for *off-sea wind in coastal areas*, while all existing data indicate that the surface of the sea is considerably smoother than the majority of land surfaces, with $z_0 < 1$ mm even for a fairly strong wind. The same author mentions roughness lengths of the order of the cm for open flat terrain, typically covered with low grass and with few obstacles.

Moreover, the velocity profile defined in Eq. III.17 accounts for irregularities from the surface only in a statistical way. Although that velocity profile is mathematically defined down to z_0 , in fact the logarithmic equation loses its physical consistence at much larger values of altitude. Indeed, for altitudes comparable to the height h_0 of protrusions on the surface, the velocity profile would vary depending on the shape and spacing of the irregularities and on the relative position towards those. This is especially critical as it was established before that DS trajectories are composed in particular of a low turn close to the surface (Sachs [47] maintains a 1.5 metres ground clearance for the centre of gravity of the bird). So Eq. III.17, used with a z_0 of 3 cm, may reach some limitations in terms of accurate modelling of the wind field in the first metres above the surface.

A refined model must be approached in order to provide the roughness length z_0 of the ocean surface. Wind-waves interaction is a vast field of research, far from being completely explored. Nevertheless, Charnock's roughness length model, developed by the eponymous author, is a generally recognized way of relating roughness length to the wave spectrum [77]. The Charnock's relation follows in Eq. III.19.

$$z_0 = \alpha \frac{u_*^2}{g} \quad (\text{III.19})$$

Stronger shear stress induces higher irregularities, which results in a greater roughness length. The parameter α is called the Charnock's parameter and is estimated to be within the [0.01; 0.035] range. This parameter was shown to depend on the wave fetch, that is to say the length of water over which a given wind has blown. It is directly related to the wave age, but it can be assumed constant for some cases. Indeed, the Charnock's parameter $\alpha_c = 1/80$, which is then called the Charnock's constant, was demonstrated through wind field measurements [78] to be accurate for long fetch cases, corresponding to old waves. The use of Charnock's constant might reach some limits in coastal areas, where the surface roughness of young waves is higher than predicted. For a friction velocity of 50 cm/s, the corresponding surface roughness length obtained using Charnock's model is 0.28 mm, which is much more consistent with the order of magnitude given by Stull [76].

III.2.2 Ocean Waves

The way the mean wind velocity is subsequently defined with Eq. III.17, for a roughness length that follows Charnock's model with $\alpha = \alpha_c$, gives a model of shearing flow over a rigid ocean surface, where irregularities are taken into account statistically.

However, the ocean surface is obviously constantly moving, and so to the effect of turbulent shear flow over rigid surfaces must be added the effect of surface displacement. Besides, only small scale structures of the surface, of the order of the *cm* are taken into account using Charnock's model. It must be superposed an effect that accounts for larger structures, if the wind field in the vicinity of significant waves is to be modelled.

Ocean waves are stochastic; the surface appears to be composed of random waves of various lengths and periods with no simple repeating pattern. Yet, one way to model this surface is the concept of wave spectrum which distributes wave energy among different wave frequencies. This decomposition of the ocean surface into an infinite sum of independent propagating sinusoidal waves relies on the fair assumption that non-linear interactions between waves are weak. The wave spectrum is established by measurement of the height of the sea surface from a fixed location, independently of the direction of waves. Pierson and Moskowitz did such measurements at a deep-sea location in the North Atlantic and made the assumption of a fully-developed sea to propose a simple, yet commonly used Pierson-Moskowitz spectrum [79], where S_{PM} is the wave spectral density.

$$S_{PM}(\omega) = \frac{8.1}{10^3} \frac{g^2}{\omega^5} \exp\left(\frac{-5}{4} \left\{\frac{\omega_p}{\omega}\right\}^4\right) \quad (\text{III.20})$$

The notation ω_p refers to the peak angular frequency of the spectrum and is expressed in terms of wind speed measured at 19.5 metres, $W_{19.5}$, which was the height of the speed taps used in experiments.

$$\omega_p = 2\pi f_p = 0.8772 \frac{g}{W_{19.5}} \quad (\text{III.21})$$

The following condition is indeed verified.

$$\frac{dS_{PM}}{d\omega}(\omega_p) = 0 \quad (\text{III.22})$$

Assumption is going to be made that the wavy surface used in the reminder of this part consists in a single sinusoidal wave at the peak angular frequency, as presented in Fig. III.11, obtained after the wind blew steadily for a long time over long distances. Wind and waves have reached equilibrium: the sea is fully-developed. For notational convenience, it will be assumed that the wind comes from the North, the x -axis is pointing northbound against the wind and z is oriented downwards. The local wind considered is at the origin of the formation of the wave system so waves are propagating with a phase velocity c in the same direction as the wind. Dispersion relations follow in Eqs. III.23 to III.25.

$$c = \frac{g}{\omega_p} \quad (\text{III.23})$$

$$k = \frac{\omega_p^2}{g} \quad (\text{III.24})$$

$$\lambda = \frac{2\pi}{k} \quad (\text{III.25})$$

The equation of the surface Z_{wave} is given by Eq. III.26.

$$Z_{wave} = -a \cos(kx + \omega_p t) \quad (\text{III.26})$$

The amplitude a of the wave is also related to the wave spectrum by assuming the peak frequency concentrates all the energy from the wave spectrum. The standard deviation in surface displacement obtained from the spectrum is expressed in Eq. III.27.

$$\langle \zeta^2 \rangle = \int_0^\infty S_{PM}(\omega) d\omega = \frac{2.74}{10^3} \frac{W_{19.5}^4}{g^2} \quad (\text{III.27})$$

For the sinusoidal peak wave expressed in Eq. III.26, this translates into Eq. III.28.

$$\langle Surf_{wave}^2 \rangle = \frac{a^2}{2} \quad (\text{III.28})$$

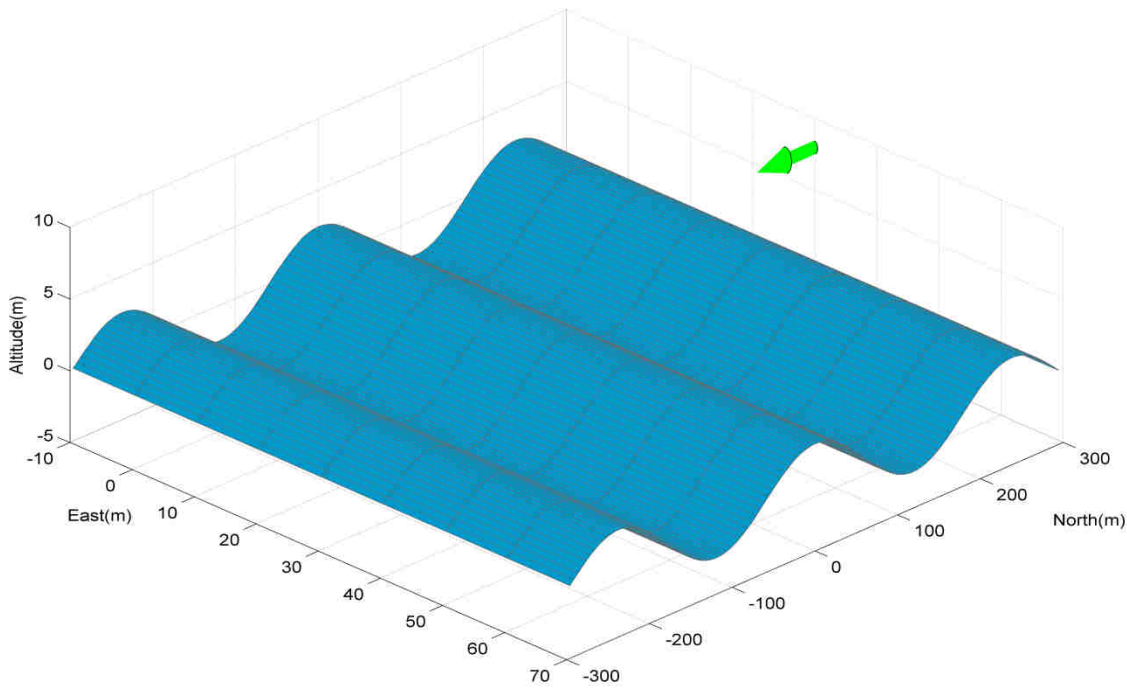


Figure III.11: Aspect of a sinusoidal wave induced by a wind blowing from the North. The wind direction is pictured by the green arrow

So the amplitude considered is given in Eq. III.29.

$$a = \left\{ 2 \int_0^{\infty} S_{PM}(\omega) d\omega \right\}^{1/2} \quad (\text{III.29})$$

The wave considered is therefore highly dependent on wind conditions. It should be noted by combining Eq. III.21 and Eq. III.23 into Eq. III.30 that the wave travels faster than the wind, as noted by Pierson and Moskowitz.

$$c = 1.14 W_{19.5} \quad (\text{III.30})$$

Therefore, the overall surface Z_{wave} of the wave is described by Eq. III.26 and it is associated with a surface roughness entailed by small irregularities from the main surface. Those are only taken into account statistically following Charnock's model, as described in Eq. III.19.

III.2.3 Wind field over Waves

The undisturbed flow over a rather flat surface has been investigated, together with properties of a peak-frequency wave which concentrates all the energy of the wave spectrum. The remaining of this part focuses on the way the latter wave alters the wind field around it. It is to be noted that several tens of metres above the surface, the mean velocity profile would be roughly unaffected so that $U_{19,5}$ is quasi constant, for a given friction velocity.

Several authors investigated turbulent flow over such a wavy surface, using numerical simulations [80] or a theoretical approach [81]. It was decided to use here expressions derived out of Benjamin's development [81], which provides approximations of analytical solutions applying stable laminar flow theory. Validity of the solution only requires that the wave amplitude is small relative to the wavelength in order to remain out of flow separation cases. This condition was chosen following results from [80, 81] and is given in Eq. III.31.

$$\frac{a}{\lambda} \leq 0.02 \text{ ie } ak \leq 0.126 \quad (\text{III.31})$$

In a region where there is no large adverse pressure gradient, the flow tends to follow the contour of the wave in such a way that main features of the undisturbed boundary layer are preserved. The flow is assumed to be two dimensional in the $\{x, z\}$ plane defined earlier, with the wind coming from x . An inertial reference frame $\{x_p, y_p, z_p\}$ in uniform rectilinear motion at phase velocity c is defined such that it translates with waves but keeps the same orientation as $\{x, y, z\}$. A surface-fitted curvilinear system of coordinates $\{\xi, \eta\}$ is defined, on the upper surface of the wave, as in Eq. III.32, from the set of Cartesian coordinates $\{x_p, z_p\}$.

$$\begin{cases} \xi = x_p - ia e^{-k(-z_p - ix_p)} \\ \eta = -z_p - a e^{-k(-z_p - ix_p)} \end{cases} \quad (\text{III.32})$$

Only the real part of Eq. III.32 is to be considered, which gives Eq. III.33.

$$\begin{cases} \xi = x_p - a \sin(kx_p) e^{kz_p} \\ \eta = -z_p - a \cos(kx_p) e^{kz_p} \end{cases} \quad (\text{III.33})$$

It should be observed that the equation of Z_{wave} in the inertial frame of reference $\{x_p, y_p, z_p\}$ is given by $\eta = 0$, to the first order in ak . Periodical variations of ξ and η with x_p

and z_p are damped by the exponential term in kz_p . Hence, far away from the surface, the curvilinear coordinates $\{\xi, \eta\}$ fits with the Cartesian system $\{x_p, y_p, z_p\}$. The undisturbed mean velocity profile is transformed into curvilinear coordinates to follow the contour of the wave so that it varies with η only.

$$\bar{u} = \bar{u}(\eta) = -\frac{u_*}{\chi} \log\left(\frac{\eta}{z_0}\right) \quad (\text{III.34})$$

In the present case, the wind is blowing against the x -axis such that the wave moves in the same direction. It means that the celerity c is expressed by Eq. III.35.

$$c = 1.14 W_{19.5} = -1.14 \frac{u_*}{\chi} \log\left(\frac{19.5}{z_0}\right) \quad (\text{III.35})$$

In the absence of waves, the stream function ψ_0 , characteristic of the flow observed from $\{x_p, y_p, z_p\}$, is expressed in Eq. III.36.

$$\psi_0 = \int_0^\eta \{\bar{u} - c\} d\eta \quad (\text{III.36})$$

For the disturbed flow, a periodic perturbation is introduced to ψ_0 , under the form specified by Eq. III.37.

$$\psi = \psi_0 + a \{F(\eta) + \{\bar{u} - c\} e^{-k\eta}\} e^{ik\xi} \quad (\text{III.37})$$

F is a perturbation velocity that must be determined. Components of the velocity parallel to ξ and η are expressed respectively in Eq. III.38.

$$\begin{cases} U(\eta, \xi) = J^{1/2} \frac{\partial \psi}{\partial \eta} \\ V(\eta, \xi) = -J^{1/2} \frac{\partial \psi}{\partial \xi} \end{cases} \quad (\text{III.38})$$

Where J is the Jacobian of the transformation given in Eq. III.39.

$$J = \left\{ \frac{\partial \xi}{\partial x_p} \right\}^2 + \left\{ \frac{\partial \xi}{\partial z_p} \right\}^2 \quad (\text{III.39})$$

The set of velocity components (U, V) abides by non-slipping boundary conditions at the surface of the wave.

$$\begin{cases} U(0, \xi) = -c \\ V(0, \xi) = 0 \end{cases} \quad (\text{III.40})$$

Benjamin [81] decomposes F in an inviscid solution ϕ completed with a rapid varying solution f which is a valid approximation of F close to the surface, where viscosity prevails. The region where f is significant is only several times the friction length, to the order of the millimetre. It was chosen to ignore that contribution that would have no incidence on flight dynamics since the vehicle flies well above. The following approximation for F was chosen.

$$F = \phi = -\{\bar{u} - c\} e^{-k\eta} \quad (\text{III.41})$$

Speeds in curvilinear coordinates can then be expressed in Eq. III.42.

$$\begin{cases} U(\eta, \xi) = J^{1/2} \{\bar{u} - c\} \\ V(\eta, \xi) = 0 \end{cases} \quad (\text{III.42})$$

The ξ -lines are thus streamlines according to this approximation, as visualized in Fig. III.12, and the wave influence on the streamlines decays with altitude.

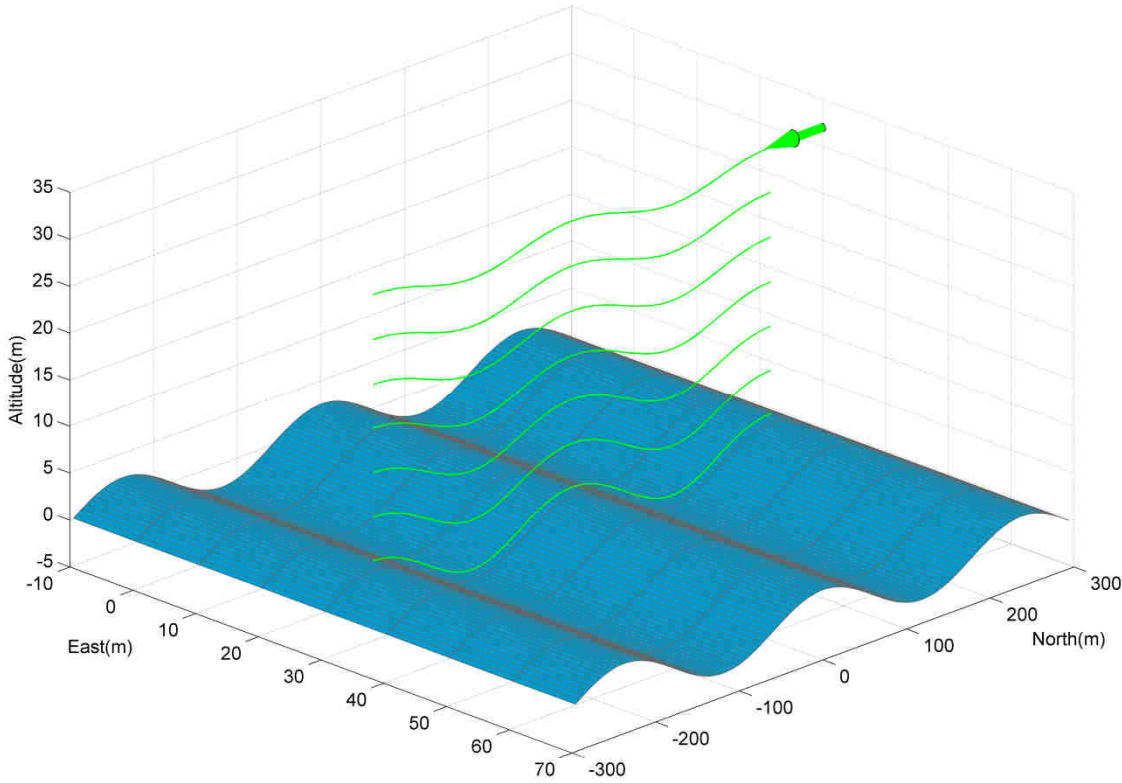


Figure III.12: Streamlines, pictured in a 2D plane, viewed from a reference frame translating at wave celerity. The wind direction is pictured by the green arrow.

Benjamin concludes that a fair approximation to the flow pattern is obtained simply by bending the primary profile. The transformation into Cartesian coordinates $\{x_p, y_p, z_p\}$ gives the respective components of the velocity parallel to y_p and z_p .

$$\begin{cases} W_{x_p} = \frac{U(\eta, \xi)}{J^{1/2}} \frac{\partial \xi}{\partial x_p} = \{\bar{u} - c\} \frac{\partial \xi}{\partial x_p} \\ W_{z_p} = \frac{U(\eta, \xi)}{J^{1/2}} \frac{\partial \xi}{\partial z_p} = \{\bar{u} - c\} \frac{\partial \xi}{\partial z_p} \end{cases} \quad (\text{III.43})$$

Finally, in the Earth's reference frame, the wind field is described by Eqs. III.44 to III.48.

$$\begin{cases} W_x = W_x^{bent} + W_x^{orbital} \\ W_z = W_z^{bent} + W_z^{orbital} \end{cases} \quad (\text{III.44})$$

$$W_x^{bent} = \bar{u} \{1 + ake^{kz} \cos(kx + \omega_p t)\} \quad (\text{III.45})$$

$$W_z^{bent} = \bar{u} \{ak e^{kz} \sin(kx + \omega_p t)\} \quad (\text{III.46})$$

$$W_x^{orbital} = -c \{ak e^{kz} \cos(kx + \omega_p t)\} \quad (\text{III.47})$$

$$W_z^{orbital} = -c \{ak e^{kz} \sin(kx + \omega_p t)\} \quad (\text{III.48})$$

The superposition of two contributions can be observed. The first comes from the main velocity profile being “bent” to follow the curve of the wave. Equation III.45 is applied successively at the wave crest and at the wave trough, in Eqs. III.49 and III.50, so as to highlight the speed up at wave crest and the slow down at wave trough, induced by the bent profile.

$$W_x^{bent}(\text{wave crest}) = \bar{u} \{1 + ake^{kz}\} \quad (\text{III.49})$$

$$W_x^{bent}(\text{wave trough}) = \bar{u} \{1 - ake^{kz}\} \quad (\text{III.50})$$

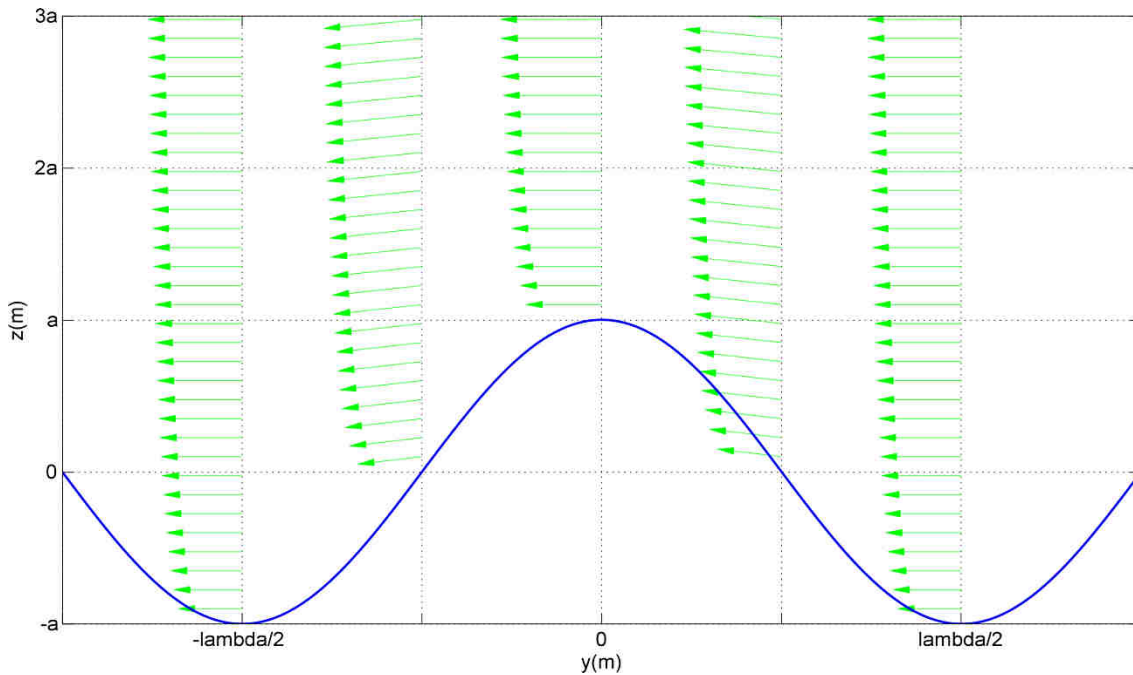


Figure III.13: Velocity profiles of the wind component due to the wave curvature. The vertical amplitude scale of the wave is voluntarily exaggerated.

Moreover, this bent wind field also induces an upward deflection of the wind on the windward side of the wave and a downward deflection on the leeward side, in a wind-over-hill fashion, as can be seen in Fig. III.13.

The second contribution is entailed by the orbital motion of the wave surface, with perturbations opposite to those due to the “bent” profile, see Fig. III.14. Indeed, the moving wave creates an upward motion of the surface on the forward moving side which is the leeward face of the wave, whereas the “bent” profile induces a downdraft component.

An opposite behaviour between “orbital” and “bent” contributions can also be observed on the other face of the wave, windward. It is to be noted, from Eq. III.46 and Eq. III.48, that wherever the celerity c of the wave exceeds the local mean wind speed \bar{u} , the orbital vertical contribution is predominant. This condition is verified up to large heights with the type of wave considered in the present case. Therefore, the overall wind field sees an updraft on the leeward face of the wave, as can be seen in Fig. III.15.

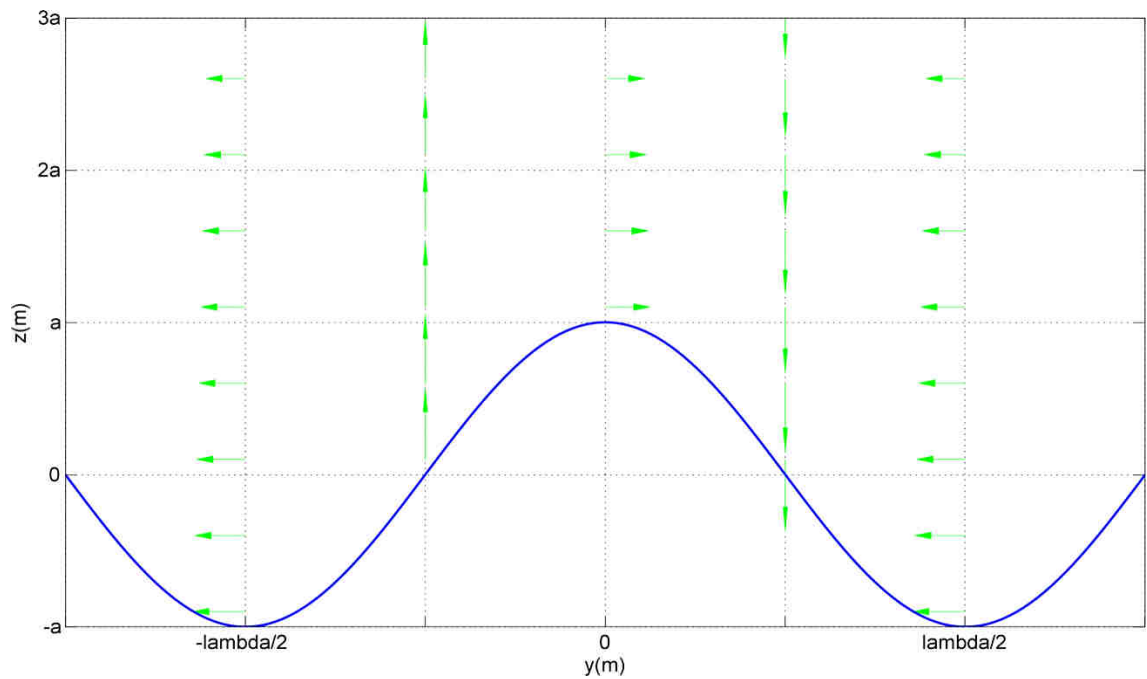


Figure III.14: Velocity profiles of the wind component entailed by the orbital motion of the wave. The velocity scale is five times that of Fig III.13.

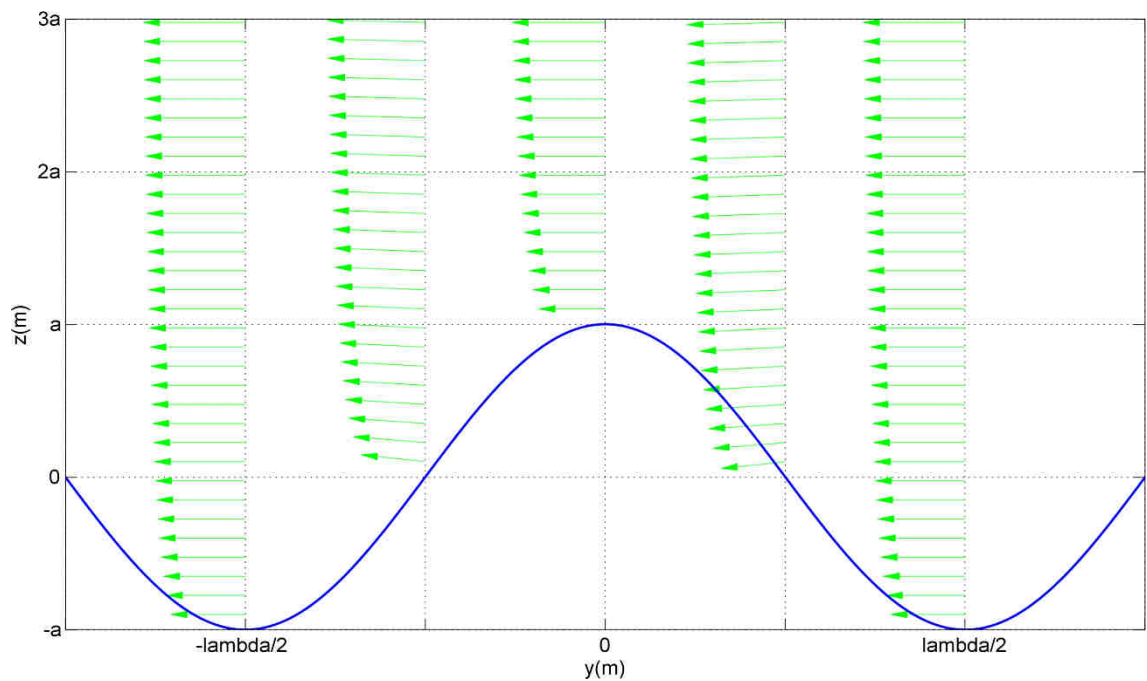


Figure III.15: Velocity profiles of the wind established over a moving wavy surface.

The methodology followed above enables to set up a model of the wind field within an environment that includes moving waves. There is hence an implicit dependence on time, even though all phenomena are steady. The vertical wind behaviour, in vicinity of the wave, is dictated by the orbital motion of the wave and not by its bending effect on the wind profile.

III.3 Summary of Chapter III

One top of the *Wandering Albatross* model, three vehicles architectures are considered, all based upon classic glider planforms, but equipped with propulsive systems. It enables to benefit from known designs, rather easy to quantify and to get rid of uncertainties linked to the dimorphism measured in albatrosses. Geometries chosen for those vehicles reflect variations in scale and would therefore question the feasibility of DS for various UAV sizes. Their aerodynamic quantification is done through simple models that are well-verified for this kind of high-aspect-ratio wings. Yet, the smaller UAV is tested during a wind tunnel campaign in order to address the issue of smaller *Reynolds* number. A point-mass model was chosen to represent the vehicle dynamics, for its simplicity. It is a sound choice given the scale of gradients that are involved in DS, however it bears limitations since any further degree of freedom would have to be synthetically constrained in its evolution rather than modelled.

The description of the environment is a two-fold process. First the theory of turbulent boundary layer is applied to a rough flat surface where irregularities are taken into account in a statistical way through the surface roughness length. The influence of the wind friction velocity and of the surface roughness length on the shape of the wind profile is assessed. This later value, which is representative of the nature of protrusions on the surface, must be adapted to match conditions encountered. In particular, the surface state, in the case of oceans, depends on the interaction between wind and waves and its evolution over time. A simple Charnock model is chosen to link the surface roughness length with the wind friction velocity, which is a good approximation for a long fetch. Secondly, the influence of surface variations of bigger scale is assessed. A regular sinusoidal wave is considered out of the Pierson-Moskowitz spectrum, at the peak frequency, and it is assumed to concentrate all the energy from the spectrum. The subsequent amplitude and wave length obtained make it correspond to a swell. The simplicity and regularity of the wave pattern is suitable for an analytical approach of the wind field. Stable laminar theory is applied to this shallow wave train, which highlights a predominant influence of the orbital motion of the wave on the vertical wind profile.

Models of the vehicle and of the environment are therefore set and ready to be considered as inputs to the flight model, which focuses on the motion of the vehicle within its environment.

CHAPTER IV

MOTION & OPTIMIZATION

Once respective models of the wind and the environment have been investigated, the trajectory that makes those two interact must be found. There lays a methodology which is specific to the general topic of atmospheric energy-extraction topics, and which consists in providing a trajectory that is considered an optimum. The success of the approach undertaken, which would lead into the formulation of a three dimensional trajectory, would not mean that DS flight is feasible for a UAV, but rather describe the trajectory it would fly, if it were to perform DS.

IV.1 Equations of Motion

IV.1.1 Point of View

Any motion is relative to the point of view of its observer. And so are the physical models built to explain it. If well expressed, they would eventually lead to a consistent picture, where the two versions of the analysis are simply two ways of approaching the problem. As it has been underlined already, two relative motions, and therefore point of views, are involved when it comes to analysing the flight of a vehicle in a windy environment. One is relative to earth, while the other is relative to the surrounding air. The following lines have more about how the choice of one of those two points of view affects the understanding of the physics involved.

Let's consider a vehicle and the mass of air altered by the vehicle path from instant t to instant $t + dt$, such that the system $\{vehicle + mass\ of\ air\}$ is isolated. Hence, it does not exchange any energy with the outside; all energy transfers are internal to the system. We aim here at getting a qualitative understanding of the internal transfers of total energy between the two systems $\{vehicle\}$ and $\{mass\ of\ air\}$, depending on the point of view chosen for observation.

From an Earth based point of view, it has been established that the vehicle gains energy during an upwind climb. As the system $\{vehicle + mass\ of\ air\}$ is isolated, when the

energy of the $\{vehicle\}$ increases, the energy of the $\{mass\ of\ air\}$ decreases by the same value. This case is represented in Fig. IV.1. The $\{vehicle\}$ extracts energy out of the $\{mass\ of\ air\}$ when the vehicle flies through the mass of air. The concept could be compared to wind turbines, where downstream air is less energized than the upwind air as the wind turbine gets energy out of it.

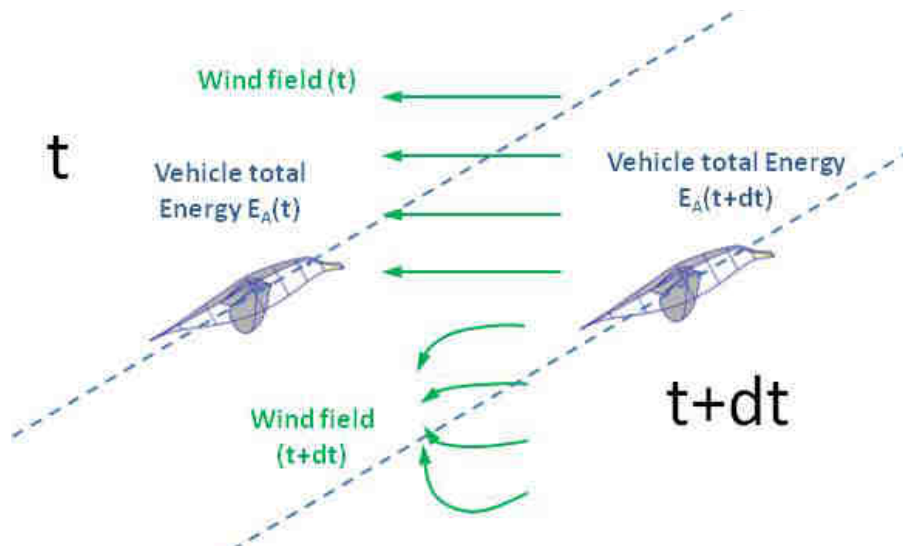


Figure IV.1: Energy transfer from an Earth based point of view.

When the same manoeuvre is observed from an air relative point of view, in Fig. IV.2, the $\{mass\ of\ air\}$ has initially no relative velocity, hence no kinetic energy. When the vehicle flies through it, the circulation around its wing entails some perturbations within the mass of air, creating vortexes and unsteadiness. The $\{mass\ of\ air\}$ receives some energy during the fly-through which is extracted from the $\{vehicle\}$ energy level.

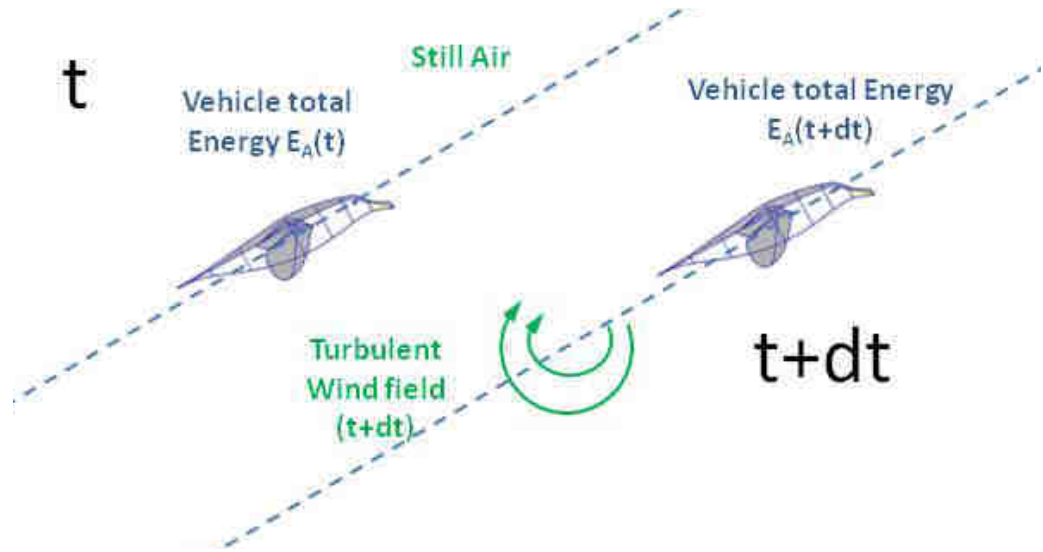


Figure IV.2: Energy transfer from a wind based point of view.

The very simple understanding of energy transfers differs depending on the point of view chosen. The notion of energy is therefore relative to the reference frame chosen to describe kinematics.

Three dimensional inertial state variables as well as their air relative counterparts are introduced in Fig. IV. 3 and Fig. IV. 4 respectively. The flight path angle (γ) and heading angle (ψ) are introduced, as well as the bank angle (ϕ). Lift (L) and drag (D) keep the same notations as before, as well as the speed (V). An inertial earth reference frame $\mathcal{R}_0(\vec{x}, \vec{y}, \vec{z})$ is arbitrarily defined by orientating axis \vec{x} , \vec{y} and \vec{z} northwards, eastwards and downwards respectively.

The inertial speed vector is oriented with respect to \mathcal{R}_0 through the inertial heading angle and flight path angle, as defined by Fig. IV. 3. The inertial speed vector orientates a frame $\mathcal{R}_i(\vec{x}_i, \vec{y}_i, \vec{z}_i)$ such that it stays directed along \vec{x}_i . The subsequent frame \mathcal{R}_i is then obtained from \mathcal{R}_0 by rotation of ψ_i along \vec{z} and of γ_i along \vec{y}_i . Despite the subscript “ i ”, the frame \mathcal{R}_i is not an inertial frame, since it rotates with the inertial speed. The same applies with the airspeed, with a subsequent frame \mathcal{R}_a , as can be seen in Fig. IV.4. Aerodynamic forces are oriented by the airspeed such that the drag is opposed to the airspeed while the lift can rotate by ϕ in a plane orthogonal to the airspeed vector. It should be mentioned that by assuming no sideslip angle, the attitude of the vehicle can be determined. Indeed, the longitudinal axis is therefore included within the (\vec{x}_a, \vec{z}_a) plane, while wings are orthogonal to the lift vector.

Following those early definitions, the inertial and air relative velocity vectors can hence be expressed as follow.

$$\vec{V}_i = V_i \cdot \vec{x}_i \quad (\text{IV.1})$$

$$\vec{V}_a = V_a \cdot \vec{x}_a \quad (\text{IV.2})$$

The relation between speeds is given by Eq. IV.3.

$$\vec{V}_i = \vec{V}_a + \vec{W} \quad (\text{IV.3})$$

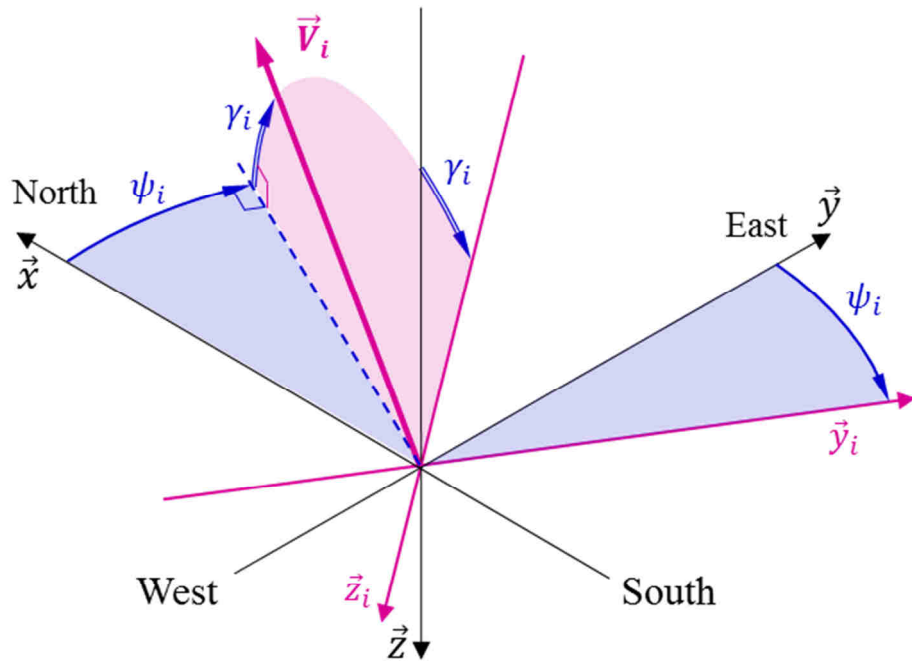


Figure IV.3: Orientation of the inertial speed with respect to the reference frame \mathcal{R}_0

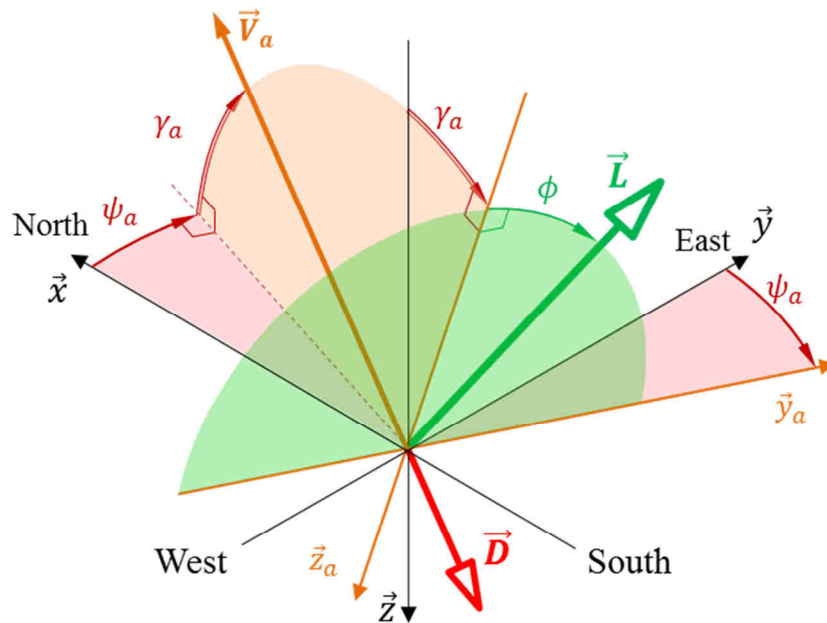


Figure IV.4: Orientation of the airspeed and of aerodynamic forces, with respect to the reference frame \mathcal{R}_0 .

Unless stated otherwise, it is assumed in the remaining of the document that the wind is unidirectional, coming from the North, such that it is opposed to \vec{x} . This decision is particularly convenient for both calculation and trajectory visualization since it emphasizes the behaviour of the vehicle with respect to the wind. Although this choice is arbitrary, the

decision to align \mathcal{R}_0 with the compass rose was all the same. Therefore no limitative assumption is involved in this choice and the whole spectrum of potential vehicle's kinematics, with respect to the wind, is unchanged. Therefore, the wind vector is expressed as follow.

$$\vec{W} = W_x(x, y, z, t) \cdot \vec{x} = W_x \cdot \vec{x} \quad (IV.4)$$

The airspeed can be expressed as a function of the local wind strength, the inertial speed and the inertial flight path and heading angles.

$$V_a = \sqrt{V_i^2 - 2 \cdot V_i \cdot W_x \cdot \cos \psi_i \cdot \cos \gamma_i + W_x^2} \quad (IV.5)$$

Besides, air relative angles can also be deduced as follow.

$$\sin \gamma_a = \frac{V_i}{V_a} \sin \gamma_i \quad (IV.6)$$

$$\sin \psi_a = \frac{V_i \cos \gamma_i \sin \psi_i}{V_a \cos \gamma_a} \quad (IV.7)$$

Practically, the flight path angle will be limited to the interval $]-\pi/2; \pi/2[$, such that Eq. IV.8 can be deduced from Eq. IV.6.

$$\cos \gamma_a = \sqrt{1 - \sin^2 \gamma_a} \quad (IV.8)$$

Eq. IV.9 completes the set of respective sinus and cosinus expressions.

$$\cos \psi_a = \frac{V_i \cos \gamma_i \cos \psi_i - W_x}{V_a \cos \gamma_a} \quad (IV.9)$$

IV.1.2 Earth Point of View

Equations of motion of a point-mass model flying through a windy environment are derived in this section. Equations of motion will be referred to as EoM in the remaining of this thesis. Kinematics is observed from the earth-based inertial reference frame \mathcal{R}_0 . Newton's second law is written down in Eq. IV.10.

$$m \frac{d\vec{V}_i}{dt})_{R_0} = \sum \overrightarrow{Forces}_{ext \rightarrow vehicle} \quad (IV.10)$$

The left-hand side of Eq. IV.10 is developed by applying the derivation formula to the inertial speed, as follow.

$$\frac{d\vec{V}_i}{dt})_{R_0} = \frac{d\vec{V}_i}{dt})_{R_i} + \vec{\Omega}_{R_i/R_0} \wedge \vec{V}_i \quad (IV.11)$$

The rotational speed of the reference frame \mathcal{R}_i with respect to \mathcal{R}_0 is given by Eq. IV.12

$$\vec{\Omega}_{R_i/R_0} = \dot{\gamma}_i \vec{y}_i + \dot{\psi}_i \vec{z}_i \quad (IV.12)$$

Eq. IV.13 is obtained by combining Eq. IV.11 and Eq. IV.12.

$$\frac{d\vec{V}_i}{dt})_{R_0} = \dot{V}_i \vec{x}_i + V_i \cos \gamma_i \dot{\psi}_i \vec{y}_i - V_i \dot{\gamma}_i \vec{z}_i \quad (IV.13)$$

External forces applied to the vehicles are the Lift, Drag and Weight. The lift is oriented by the bank angle with respect to the reference frame \mathcal{R}_a . The expression of the lift is reminded in Eq. IV.15. It should be mentioned that the air density ρ is considered constant over the small altitude ranges of interest.

$$\vec{L} = L \sin \phi \vec{y}_a - L \cos \phi \vec{z}_a \quad (IV.14)$$

$$L = \frac{1}{2} \rho \cdot S \cdot C_L \cdot V_a^2 \quad (IV.15)$$

The drag is opposed to the airspeed vector, along \vec{x}_a .

$$\vec{D} = -D \vec{x}_a \quad (IV.16)$$

$$D = \frac{1}{2} \rho \cdot S \cdot C_D \cdot V_a^2 \quad (IV.17)$$

And the weight is trivially expressed as follow.

$$\vec{W}_{weight} = +mg\vec{z} \quad (IV.18)$$

Equations are chosen to be projected on \mathcal{R}_i . All forces must therefore be successively projected on \mathcal{R}_a and then on \mathcal{R}_i . Contributions from the three forces listed above are summed up along the main axis $(\vec{x}, \vec{y}, \vec{z})$ of \mathcal{R}_0 .

$$\overrightarrow{Forces}_{ext \rightarrow vehicle} = F_x \vec{x} + F_y \vec{y} + F_z \vec{z} \quad (IV.19)$$

$$F_x = -L (\sin \phi \sin \psi_a + \cos \phi \cos \psi_a \sin \gamma_a) - D \cos \gamma_a \cos \psi_a \quad (IV.20)$$

$$F_y = L (\sin \phi \cos \psi_a - \cos \phi \sin \psi_a \sin \gamma_a) - D \cos \gamma_a \sin \psi_a \quad (IV.21)$$

$$F_z = -L \cos \phi \cos \gamma_a + D \cos \gamma_a + mg \quad (IV.22)$$

Then, a further projections along $(\vec{x}_i, \vec{y}_i, \vec{z}_i)$ of \mathcal{R}_i is conducted in order to get to the first three EoM.

$$m\dot{V}_i = F_x \cos \gamma_i \cos \psi_i + F_y \cos \gamma_i \sin \psi_i - F_z \sin \gamma_i \quad (IV.23)$$

$$mV_i \cos \gamma_i \dot{\psi}_i = -F_x \sin \psi_i + F_y \cos \psi_i \quad (IV.24)$$

$$-mV_i \dot{\gamma}_i = F_x \sin \gamma_i \cos \psi_i + F_y \sin \gamma_i \sin \psi_i + F_z \cos \gamma_i \quad (IV.25)$$

Those are completed by the three dimensional evolution of the position of the vehicle.

$$\dot{x} = V_i \cos \gamma_i \cos \psi_i \quad (IV.26)$$

$$\dot{y} = V_i \cos \gamma_i \sin \psi_i \quad (IV.27)$$

$$\dot{z} = -V_i \sin \gamma_i \quad (\text{IV.28})$$

Therefore, Eqs. IV.23 to IV.28 describe the evolution rate, with time, of inertial state variables $\{V_i, \psi_i, \gamma_i, x, y, z\}$. Those equations indirectly include variables that are not piloted by any others, that are $\{C_L, \phi\}$. Those are the variables which pilot the evolution of the system, they are *control variables*. Besides, it should be mentioned that the wind input consists only in the local wind strength W_x , which is taken into account as for $\{V_a, \psi_a, \gamma_a\}$. Therefore, the local evolution of inertial state variables depends only on the local wind strength encountered by the vehicle and is independent of the local wind gradient.

IV.1.3 Air relative point of view

An alternative choice is to base the point of view on the surrounding air, such that air relative kinematics is observed. The subtlety in the case of DS simulations is that the surrounding air moves at different speeds depending on where the vehicle is, due to the presence of wind gradients. Hence, a reference frame linked to the air around the vehicle would see accelerations when the vehicle crosses regions of wind shear, such that this reference frame is not inertial. Fictitious forces must be added in order to describe the motion from this point of view.

An air-based frame is defined such that it is moving at the speed $W_x(x, y, z, t) \cdot \vec{x}$, where $\{x, y, z\}$ is the position of the centre of gravity of the vehicle. All axes remain parallel to those of \mathcal{R}_0 . The inertial force is given by the local air acceleration at $\{x, y, z\}$.

$$\vec{F}_{inertial} = -m \cdot \left. \frac{DW_x}{Dt} \right)_{\mathcal{R}_0} \vec{x} = -m \cdot \left[\frac{\partial W_x}{\partial t} + \frac{\partial W_x}{\partial x} \cdot \dot{x} + \frac{\partial W_x}{\partial y} \cdot \dot{y} + \frac{\partial W_x}{\partial z} \cdot \dot{z} \right] \cdot \vec{x} \quad (\text{IV.29})$$

The wind is taken to be unidirectional and steady, coming from the North, defined by the following equation.

$$W_x = -\frac{u_*}{\chi} \log \frac{-z}{z_0} \quad (\text{IV.30})$$

Hence, the inertial force is expressed as follow.

$$\vec{F}_{inertial} = -m \cdot \frac{D W_x}{Dt} \Big|_{R_0} \vec{x} = -m \frac{\partial W_x}{\partial z} \cdot \dot{z} \vec{x} \quad (IV.31)$$

The local wind gradient is computed from Eq. IV.30 and gives the following expression.

$$\frac{\partial W_x}{\partial z} = -\frac{u_*}{\chi} \frac{1}{z} \quad (IV.32)$$

This yields the following expression as for the inertial force.

$$\vec{F}_{inertial} = m \frac{u_*}{\chi} \frac{\dot{z}}{z} \vec{x} \quad (IV.33)$$

The derivation formula is applied to the airspeed vector and generates the following components.

$$\frac{d\vec{V}_a}{dt} \Big|_{R_0} = \dot{V}_a \vec{x}_a + V_{air} \cos \gamma_a \dot{\psi}_a \vec{y}_a - V_a \dot{\gamma}_a \vec{z}_a \quad (IV.34)$$

Finally, vector equations are projected on \mathcal{R}_a to entail the following system of EoM.

$$m\dot{V}_a = -D - mg \sin \gamma_a + m \frac{u_*}{\chi} \frac{\dot{z}}{z} \cos \gamma_a \cos \psi_a \quad (IV.35)$$

$$mV_a \cos \gamma_a \dot{\psi}_a = L \sin \phi - m \frac{u_*}{\chi} \frac{\dot{z}}{z} \sin \psi_a \quad (IV.36)$$

$$-mV_a \dot{\gamma}_a = -L \cos \phi + mg \cos \gamma_a + m \frac{u_*}{\chi} \frac{\dot{z}}{z} \cos \psi_a \sin \gamma_a \quad (IV.37)$$

$$\dot{x} = V_a \cos \gamma_a \cos \psi_a + W_x \quad (IV.38)$$

$$\dot{y} = V_a \cos \gamma_a \sin \psi_a \quad (IV.39)$$

$$\dot{z} = -V_a \sin \gamma_a \quad (IV.40)$$

The set of Eqs. IV.35 to IV.37 shows that air relative state variables have their rate of evolution as a function of the local wind gradient, described in Eq. IV.32. This dependence comes through the presence of the inertial force that itself accounts for the acceleration of the air relative point of view. This term, which has indeed the dimension of a force, is sometimes referred to as the “*dynamic soaring force*” or the “*fictitious force*” [50]. Control variables $\{C_L, \phi\}$ are trivially the same as before.

To put in nutshell, two different sets of equations of motion can be considered. Those are representative of the same system evolution observed from two different points of views. One focuses on inertial variables, and highlights that their rate of evolution depends, among others, on the local wind strength encountered. From that perspective, the significance of wind gradients is not emphasized at that stage and the set of EoM is not much different than that of a point-mass glider in still air. The alternative is to use air relative variables and equations, which then makes the local wind gradient appear. The role of wind gradients in the energy extraction process can already be partially comprehended when observing the motion from an air relative point of view. Besides, different systems of EoM can be derived out of a single point of view, such that the proposed equations here are not exclusive [50, 67, 49, 47].

Yet, whatever the chosen point of view and the related set of equations, the local evolution rate of state variables, either inertial or air-based, is not sufficient to describe and simulate DS flight. Indeed, as it was underlined during Chapter I, DS can only be approached along a whole cycle of trajectory. For static soaring flight techniques, an instantaneous description of the system is repeated identically over time and can therefore be studied over any fixed time position, independently of the state and control histories. However, DS requires integrating the evolution rate, given by EoM, over an undetermined cycle, in order to simulate and understand energy-harvesting mechanisms. Hence, the fact that wind gradients terms do not appear in inertial EoM does not mean that wind gradients are not significant for the motion as a whole.

This raises the next challenge regarding DS flight simulations, which is to integrate EoM to form state and control histories over a cycle yet to be determined. The way control variables pilot the evolution of state variables over time is also unknown, such that state variables cannot be explicitly integrated. The problem consists in finding a cycle of coherent state and control evolution over time that permits to extract energy from the wind in the process.

It was chosen to conduct all calculations using the set of inertial equations of motion Eqs. IV.23 to IV.28. It was considered that it would be more intuitive to deal directly with inertial variables since ultimately earth-based travel performances are those of primary interest. Other studies opted for the same option [47, 43]. Still, the choice to go for air relative variables could also have been defended, as those are somehow more intuitive to deal with when it concerns a flying object. That was the choice of various authors [46, 49, 48, 67, 68, 50, 57].

IV.2 Optimization

One way to address the issue is to set and solve an optimization problem in order to yield the best achievable solution. It goes through a particular methodology that starts by identifying the objective and the constraints and then follows by converting the subsequent analytical problem into one of finite dimension, involving a limited number of parameters. Eventually, specific numerical techniques are applied to the underlying parameter optimization problem to converge to a solution.

IV.2.1 Optimal Control Problem

The classical approach to set-up an optimization problem is to identify the variables, the objective and the constraints. The general formulation of the optimization problem is then defined as follow.

Maximize/Minimize: *Objective(variables)*

with respect to: *variables*

subject to: *constraints*

In our case, variables would regroup all variables that must be iterated on as part of the optimization problem. Since both state and control variables are unknown, the set of variables includes at least those variables. Besides, the cycle duration is also unknown and should be set free for the optimization to run on it. Indeed the trajectory which optimizes the objective would have a specific duration, to be determined. Practically, an initial time t_1 is set to zero and the final time t_f is chosen as a variable. So the set of variables passed to the optimization problem is at least $\{V_i, \psi_i, \gamma_i, x, y, z, C_L, \phi, t_f\}$. However, further variables can be

considered, such as vehicle design variable or environment variable. Especially if the wind strength is also unknown, which would happen in many cases, the friction velocity u_* is also a variable to be determined.

Regarding the objective function, numerous choices can be considered. We would focus on two different ones. The first and most trivial consists in minimizing the wind strength required to perform DS under certain operational constraints. Then, another objective would be to minimize the consumption per unit distance travelled. This latter obviously only makes sense in the case of a powered vehicle. The battery state (Bat) must then be taken into account, its derivative is given by the power exerted by the thrust T . Just as a reminder, η_{prop} is the efficiency of the propulsive block, including electrical, mechanical and aerodynamic efficiencies.

$$\dot{Bat} = -\frac{T V_a}{\eta_{prop}} \quad (\text{IV.41})$$

Table IV-1 sums up the different objective functions that are approached in the framework of this research project. Once again, it constitutes a deliberate choice to focus on certain problematics and many further objectives can be considered.

Table IV-1: Variation in the objective function in the framework of this thesis

Explicit formulation	Objective	Function title	Function scalar	Associated Constraint
Obtain the lowest wind at which DS flight is sustainable.	<i>Minimize</i>	<i>Wind friction velocity</i>	u_*	$\left\{ \begin{array}{l} \text{Energy neutral cycle} \\ \text{No Thrust} \\ \text{Periodicity} \end{array} \right.$
Obtain the lowest electric consumption per unit distance travelled by taking advantage of DS.	<i>Minimize</i>	<i>Consumption per unit distance travelled</i>	$\frac{\Delta Bat}{\sqrt{\Delta x^2 + \Delta y^2}}$	$\left\{ \begin{array}{l} \text{Energy neutral cycle} \\ \text{Periodicity, all but Bat} \end{array} \right.$

Constraints encompass all the standards that must be complied with by the eventual solution of the optimization problem. To start with, equations of motion must obviously be verified such that the solution is physical in view of the models considered. Then, periodicity is an essential constraint regarding eventual DS trajectories. Indeed, the problem does not consist in extracting energy over a certain period, but in finding a way to make that energy-extraction process repeatable and therefore sustainable. The solution must hence consist in a path where

at least some of state and control variables come back to their initial values at the end. Depending on the mission scenario, those periodicity constraints can be eased out to allow for x, y displacement. Then operational constraints are considered. Some can be expressed quite straightforwardly, such as avoiding stall, or maintaining ground clearance. Others are implemented to make up for limitations inherent to the point-mass model of the vehicle. Limitations on control rates and angular accelerations would ideally be implicitly accounted for through the presence of further equations of motion, relative to further degrees of freedom. They can be rather estimated using alternative analysis, in order to augment the reality of the point mass model.

The control rate bounds, respectively \dot{C}_L and $\dot{\phi}$, are each associated to limitations in control surface deflections and size. Although the coefficient of lift is considered as a variable, it is in fact not piloted directly, since the attitude of the vehicle is piloted, not the angle of attack. However, limitations in pitch rate induce subsequent constraint on the feasible \dot{C}_L . Besides, using conservative values for this rate limit allows ensuring that the evolution in coefficient of lift corresponds to a feasible variation, despite the mentioned inaccuracy inherent to the point-mass model. A roll rate of $90^\circ/s$ was given for *Mariner* [68], while a much lower value of $30^\circ/s$ was given for *Cloud Swift* [70]. Such a strong disparity can be explained by the ailerons representing a large portion of the chord (35 %) over 90 % of the span for *Mariner*, while *Cloud Swift* was design as a classical glider, with ailerons on the outboard part of the wing only. The maximum rolling rate for the *DT-18* is considered to be $60^\circ/s$. Given the approximate similarity in horizontal tail control surface sizing for all three vehicles, the same bound value of $0.5/s$ for \dot{C}_L , given by Bower [67], is chosen.

Bounds on angular acceleration translate into limits in \ddot{C}_L and $\ddot{\phi}$. Those are significant to ensure that control variables follow a rather smooth evolution over time. One approach to get to a first-order approximation of the roll acceleration is to calculate the maximum rolling moment that ailerons can produce for a certain speed. The following equation expresses this dependence.

$$I_{xx} \ddot{\phi} = \frac{1}{2} \rho S l C_{Roll} V_a^2 \quad (IV.42)$$

I_{xx} is the longitudinal inertia, l the mean aerodynamic chord and C_{Roll} the rolling moment coefficient. The maximum rolling acceleration is hence given by:

$$|\ddot{\phi}|_{MAX} = \frac{1}{2 I_{xx}} \rho \cdot S \cdot l \cdot C_{Roll_{max}} \cdot V_a^2 \quad (IV.43)$$

The maximum rolling moment coefficient is given for the *DT-18* by the wind tunnel campaign and for *Mariner* from Bower [67]. No data is available for *Cloud Swift* and it is assumed that it achieves the same maximum rolling moment coefficient as the *DT-18*. The maximum value for \ddot{C}_L is much less intuitive and is considered to be 2 s^{-2} for all vehicles.

As for remaining constraints, the maximum load factor was considered to be $n_{max} = 3$ for all vehicles, although Lawrance [70] recommends only 2 for *Cloud Swift*. The reason for that is our wish to let structural considerations aside, when comparing vehicles in DS flight. On the contrary, a limitation that marks a difference between vehicles is the ground clearance constraint. One option is to limit the lowest altitude at the centre of gravity, which is the point where the wind is computed. A refined alternative is to impose a wing tip clearance, obviously on both wings, which permits to assess the influence of the span during turns close to the surface. The wing is oriented orthogonal to the airspeed vector and to the lift vector which yields the following expression for the semi span vector.

$$\overrightarrow{GT_{ip}} = \pm b/2 (\cos \phi \vec{y}_a + \sin \phi \vec{z}_a) \quad (IV.44)$$

Hence, by defining a positive ground clearance G_{clear} , the wing tip clearance is expressed by Eq. IV.45.

$$z \pm b/2 \sin \phi \cos \gamma_a \leq -G_{clear} \quad (IV.45)$$

A summary of the different bound and constraints values is summed up in Table IV-2.

Table IV-2: Summary of constraints expressions and bounds

Constraint	Formulation	Parameters		
		DT-18	Mariner	Cloud Swift
Equations of Motion	<i>Eqs. IV.23-IV.28</i>	<i>See Table III-1</i>		
Flight path bound	$ \gamma_i \leq \gamma_{max}$	$\gamma_{max} = 65^\circ$		
Final time bounds	$t_{min} \leq t_f \leq t_{sup}$	<i>to be determined and adapted</i>		
Periodicity	$\{V_i, \psi_i, \gamma_i, x, y, z, C_L, \phi\}_0$ $= \{V_i, \psi_i, \gamma_i, x, y, z, C_L, \phi\}_f$	<i>to be released for x,y in case of travel</i>		
Net travelling direction	$\Delta y = \tan \psi_{net} \Delta x$	ψ_{net} <i>to be adapted in function of heading wanted</i>		
Rolling bound	$ \phi \leq \phi_{max}$	$\phi_{max} = 85^\circ$		
No Stall	$C_L \leq C_{L_{max}}$	$C_{L_{max}} = 1.2$	$C_{L_{max}} = 1.17$	$C_{L_{max}} = 1.0$
Max. load factor	$\frac{\rho S C_L V_a^2}{2 m g} \leq n_{max}$	$n_{max} = 3$		
Ground Clearance	$z \pm \frac{b}{2} \sin \phi \cos \gamma_a \leq -G_{clear}$	$G_{clear} = 50 \text{ cm}$		
Rolling rate	$ \dot{\phi} \leq \dot{\phi}_{max}$	$\dot{\phi}_{max} = 60^\circ/s$	$\dot{\phi}_{max} = 90^\circ/s$	$\dot{\phi}_{max} = 30^\circ/s$
C_L rate	$ \dot{C}_L \leq \dot{C}_{L_{max}}$	$\dot{C}_{L_{max}} = 0.5 \text{ s}^{-1}$		
Rolling acceleration	$ \ddot{\phi} _{max} = \frac{\rho S l}{2 I_{xx}} C_{Roll_{max}} V_a^2$	$C_{Roll_{max}} = 0.32$ $I_{xx} = 0.184 \text{ kg.m}^2$	$C_{Roll_{max}} = 1.43$ $I_{xx} = 0.378 \text{ kg.m}^2$	$C_{Roll_{max}} = 0.32$ $I_{xx} = 1.344 \text{ kg.m}^2$
C_L double continuous	$ \ddot{C}_L \leq \ddot{C}_{L_{max}}$	$\ddot{C}_{L_{max}} = 2 \text{ s}^{-2}$		

The general formulation of the optimization problem has been stated and that its terms have been expressed. At this point, the problem is expressed throughout analytical expressions, whether those are objective function or constraints. Those must be converted into a limited number of parameters in order to take advantage of numerical optimization techniques.

IV.2.2 Conversion into a Parameter Optimization Problem

The optimization problem formulated above must be converted into a finite-dimension optimization problem. This process involves different calculations steps. First, the time interval is divided into a number of subintervals, which define the future calculation nodes. Although

the final time t_f is unknown and part of the variables passed to the optimization problem, a time step Δt can be implicitly defined by fixing the number N_t of time steps.

$$\Delta t = \frac{t_f - t_1}{N_t - 1} \quad (\text{IV.46})$$

Therefore a set of N_t time nodes $\{t_1, \dots, t_k, \dots, t_{N_t} = t_f\}$, equally spaced by Δt , forms a number $N_t - 1$ of time subintervals. Variables are also broke down into discrete sub-variables at each time node, where X_k represents the value of variable X at the time node t_k . Each state and control variable is then represented by N_t discrete variables over the time interval $[t_1; t_f]$. So far, the evolution of the system with time is modelled by equations of motion, which are of the following form, for a state variable X and a control variable U .

$$\dot{X} = f(X, U, t) \quad (\text{IV.47})$$

A way to involve the set $\{X_1, \dots, X_k, \dots, X_f\}$, of dimension N_t , in order to represent the behaviour expressed by Eq. IV.47 must be found. The analytical integration of Eq. IV.47 over one time subinterval $[t_k; t_{k+1}]$ gives Eq. IV.48.

$$X_{k+1} - X_k = \int_{t_k}^{t_{k+1}} f(X, U, t). dt \quad (\text{IV.48})$$

If the evolution of the control variable was the only unknown to be found and optimized, then Eq. IV.48 could be integrated explicitly through classical *Runge-Kutta* techniques. That can happen when a trajectory is to be followed (through some waypoints) but the optimal way to pilot that trajectory must be established. The Eq. IV.48 could be interpolated in one go from t_1 to t_f by using a time history of control variables formed by interpolation. This method is called direct shooting in the optimization literature [82].

However, in our case, state variables are also unknown and therefore the value of X_k is not available to evaluate $f(X_k, U_k, t_k)$ to get to X_{k+1} through classical Runge-Kutta integration techniques. Still, the integral in Eq. IV.48 can be approximated by involving discrete variables at nodes k and $k+1$ via a numerical integration scheme. The most basic of those

schemes would be the *rectangle rule*, where f is supposed to be constant over the subinterval $[t_k; t_{k+1}]$, which provides the following.

$$\text{Rectangle rule: } \int_{t_k}^{t_{k+1}} f(X, U, t). dt \approx f(X_k, U_k, t_k). \Delta t \quad (\text{IV.49})$$

Despite being of appealing simplicity, the calculation error inherent to this approximation is high. Indeed, the rectangle rule is a first-order rule, which means that for a given value of X_k , the obtained X_{k+1} only match the Taylor series expansion through the first term. The local truncation error (LTE), that is to say the error brought by the integration rule over one step, is proportional to Δt^2 , in the case of a first-order scheme. The global truncation error (GTE) is one order of the step size less than the LTE [82], that is to say is proportional to Δt in the case of a first-order integration technique. A more accurate approximation can be obtained by using a higher order integrator. Indeed, the function f can be approximated by a polynomial interpolant. One option for converting the optimization problem is named collocation technique and uses Simpson's one-third rule to approximate the integrand function f [83, 84]. This alternative is commonly used for trajectory optimization problems [83]. It was hence chosen to approximate f by a quadratic polynomial which interpolates the function at the endpoints of the subinterval $[t_k; t_{k+1}]$, as well as at the centre point t_c of the interval. Lagrange polynomial interpolation can be used to find the interpolant. After calculation, the integration over the time subinterval $[t_k; t_{k+1}]$ gives the following terms.

$$\int_{t_k}^{t_{k+1}} f(X, U, t). dt \approx \frac{\Delta t}{6} \cdot [f(X_k, U_k, t_k) + 4f(X_m, U_m, t_m) + f(X_{k+1}, U_{k+1}, t_{k+1})] \quad (\text{IV.50})$$

The three interpolation points are called collocation points. It should be noticed that nothing guarantees that the slope of the polynomial is continuous between two time subintervals. Indeed, each interpolant is only defined over one subinterval, independently of the previous and the following one. Simpson's one third rule is a fourth-order integration technique, which means that the GTE is proportional to Δt^4 . The integrand must be evaluated at the mid-point of the time subinterval, where state and controls are a priori not known, since they are only defined by their values at the endpoints of the subinterval. Hence, a state and control history must be approximated in order to get values at the centre of the interval. Because the interpolant f , which is the derivative of X over time, is approximated by a quadratic polynomial over $[t_k; t_{k+1}]$, X must be approximated by a cubic polynomial. Hence, four pieces

of information must be known about the state history in order to interpolate by a polynomial of order three. State values at the endpoints are used $\{X_k, X_{k+1}\}$, as well as the slope at the endpoints $\{f(X_k, U_k, t_k), f(X_{k+1}, U_{k+1}, t_{k+1})\}$. The interpolation is made with a Hermite-cubic polynomial P_H that is constructed out of those four pieces of information. By using notations $f(X_k, U_k, t_k) \Rightarrow f_k$ and $f(X_{k+1}, U_{k+1}, t_{k+1}) \Rightarrow f_{k+1}$, the polynomial P_H represents the time history of $X(t)$ as given by Eq. IV.51.

$$P_H(t) = \frac{(t - t_{k+1})^2}{(t_k - t_{k+1})^2} \left[\left(1 - \frac{2(t - t_k)}{t_k - t_{k+1}} \right) \cdot X_k + (t - t_k) \cdot f_k \right] + \frac{(t - t_k)^2}{(t_{k+1} - t_k)^2} \left[\left(1 - \frac{2(t - t_{k+1})}{t_{k+1} - t_k} \right) \cdot X_{k+1} + (t - t_{k+1}) \cdot f_{k+1} \right] \quad (\text{IV.51})$$

Further calculations give Eq. IV.52 by applying Eq. IV.51 at the centre of the interval.

$$P_H(t_m) = P_H\left(\frac{t_k + t_{k+1}}{2}\right) = \frac{X_k + X_{k+1}}{2} + \frac{\Delta t}{8}(f_k - f_{k+1}) \quad (\text{IV.52})$$

To put in a nutshell, EoM are implicitly integrated over each time subintervals by approximating the derivative function with a quadratic polynomial. Because state variables are not built through the numerical integration but rather involved in the calculation, the integration of EoM yield one subsequent constraint per time subinterval. For each one of those, this constraint is formed out of Eq. IV.50 and Eq. IV.52 and is called the *Hermite-Simpson* system constraint [83]. For each state variable $\{X^1, X^2, \dots, X^i\}$, over each time subinterval $[t_k; t_{k+1}]$, it comes in the form of a residual R_k^i , which is expressed in Eq. IV.53 and must be driven to zero in the iteration process. In the formulation below, X_k no longer represents the variable X at node k , but the vector of state variables $X_k = [X_k^1, \dots, X_k^i]^T$ at node k .

$$R_k^i = X_{k+1}^i - X_k^i - \frac{\Delta t}{6} \cdot [f(X_k, U_k, t_k) + 4f(X_m, U_m, t_m) + f(X_{k+1}, U_{k+1}, t_{k+1})]$$

$$\text{with } \begin{cases} X_m = \frac{X_k + X_{k+1}}{2} + \frac{\Delta t}{8} (f_k - f_{k+1}) \\ U_m = \frac{U_k + U_{k+1}}{2} \\ t_m = \frac{t_k + t_{k+1}}{2} \end{cases} \quad (\text{IV.53})$$

IV.2.3 Solving Methodology and Tools

Let's begin by defining two important terms that come into play in terms of optimization. A generic function of n -variables is defined in Eq. IV.54.

$$f: \begin{cases} \mathbb{R}^n \mapsto \mathbb{R} \\ (x_1, \dots, x_n) \mapsto f(x_1, \dots, x_n) \end{cases} \quad (\text{IV.54})$$

The gradient vector is given by Eq. IV.55.

$$\nabla f = \begin{bmatrix} \frac{\partial f}{\partial x_1} \\ \vdots \\ \frac{\partial f}{\partial x_n} \end{bmatrix} \quad (\text{IV.55})$$

The Hessian matrix is symmetric and given by Eq. IV.56 and is the matrix of second-order derivatives.

$$H_f = \begin{bmatrix} \frac{\partial^2 f}{\partial x_1^2} & \dots & \frac{\partial^2 f}{\partial x_1 \partial x_n} \\ \vdots & \ddots & \vdots \\ \frac{\partial^2 f}{\partial x_n \partial x_1} & \dots & \frac{\partial^2 f}{\partial x_n^2} \end{bmatrix} \quad (\text{IV.56})$$

Both the gradient vector and the Hessian matrix come into play when assessing the second-order condition, in order to conclude on the eventual optimality of a functioning point. This condition is stated in Eq. IV.57 [85, 86].

For $X^* \in \mathbb{R}^n$, if H_f is continuous over an open neighborhood of X^* , then

$$X^* \text{ is a local min. (max.)} \Leftrightarrow \begin{cases} H_f(X^*) \text{ is definite positive(negative)} \\ \nabla f(X^*) = 0 \end{cases} \quad (\text{IV.57})$$

The above standard comes from the Taylor series expansion of function f at the second order. It highlights that both the function gradient and Hessian are required in order to solve a basic unconstrained optimization problem where f is the objective function. Practically, in the field of numerical optimization, inequalities-constrained-problems are reduced to the form of a simpler unconstrained-problem, at the expense of adding further variables [85, 86]. For instance, constraints are taken into account through the set-up of a *Lagrangian merit function* which is the addition of the objective function with terms proportional to the constraints of the problem. The proportionality is set by *Lagrange multipliers*, one per constraint, that are new variables to the problem. An unconstrained problem, where the objective function is formed by the *Lagrangian merit function* is subsequently solved. It means that gradients of all constraints must be known, on top of that of the objective function. Those very brief lines are to introduce the basic features of the solver we chose to use. It was selected out of the different solver offered by the online NEOS server [87], as for nonlinearly constrained optimization. Further references are available about NEOS [88, 89, 90].

The Sparse Nonlinear OPTimizer (SNOPT) solver was selected after runs on the various solvers offered by the NEOS server, for its reliability as well as its rapid convergence. SNOPT uses sequential quadratic programming methods to solve nonlinear constrained optimization problems with smooth nonlinear functions and constraints [91]. Basic features are that the sequence of quadratic problems is guided by *line-search* techniques which requires first-order derivative to be available. Yet, the Hessian of the Lagrangian merit function is approximated by using a *quasi-Newton* method based on the *BFGS updating formula* [85, 91]. Besides, SNOPT assumes that constraint gradients are sparse. This fits quite well within the scope of our optimization problem, since a majority of our constraints come from EoM that are each discretized into a number $N_t - 1$ of residuals, expressed in Eq. IV.53. Those residuals, at time step k , only depend on state and control variables at time step k and $k+1$, therefore resulting in sparse gradient vectors.

SNOPT requires first-order derivatives to be available as well as the general structure of the optimization problem to be properly set. An intermediate modelling tool is used to that aim, it is A Mathematical Programming Language (AMPL). It provides an interface through three

input files that sum-up the optimization problem formulation (*.mod*), the value of parameters (*.dat*) and the solving and output options (*.run*) [92]. This interface permits to build up large scale problems through a step by step declaration of variable and constraints, while AMPL detects eventual substitutions as well as the general structure of the problem. It then communicates the problem representation to the solver SNOPT. This includes first-order derivatives, that are computed by AMPL using *Automatic Differentiation* [93].

IV.2.4 Local Optimizer and Sensitivity to Initiation Variables

The solver SNOPT is guaranteed only to find a locally optimal point [91]. However, it can be generalized into a global optimum point only if the objective function to be minimized (alternatively maximized) is convex (alternatively concave) and if the associated feasible constraint region is also convex [85]. Hence, results from the optimization process are a-priori local solutions.

Furthermore, the feasibility of the convergence, as well as the nature of the optimal point may depend on the way variables are initialized. Indeed, within the space of optimization variables, the solver starts to iterate from a specific set of variables and then guides its search until it eventually converges to an optimal point. Hence different sets of initiation variables may lead to a problem that is feasible or not and may influence the convergence towards a local optimal point rather than another. In our present case, there are a total of $9 * N_t$ variables passed to the solver. Assuming that each variable can take N_v values, the number of different combinations amounts to $N_v^{9 * N_t}$. Any reasonable assumption as for N_v and N_t yields a number of combination of such a magnitude that testing the whole range of starting points is out of the question. Not to mention that every combination would be tested by actually running the solver which takes several seconds for problems of our scale. Hence, selecting appropriate initiation variables would need a trial and error approach, associated with an eventual physical intuition of what the optimal solution may look like.

IV.3 Validation

IV.3.1 Simulating Albatross Flight

One computation is made with an optimization problem matching the case from Sachs [47], in order to validate the optimization methodology as well as provide a classical study case of DS over a flat surface. All vehicle properties, environment conditions and optimization constraints mentioned by Sachs are reproduced here. The wind field is that of a boundary layer

developed over a rather flat surface, the surface roughness length is 3 cm . The vehicle is the *Wandering Albatross*, the minimal altitude was set to 1.5 metres , the maximal load factor to 3 and the bank angle is limited to 80° .

Regarding discretization methods, the number of time steps N_t is varied to assess the influence on the resulting objective function, in this case the minimum wind friction velocity u_* , and on the calculation time from *SNOPT*, referred to as t_{SNOPT} . Results are summed up in Table IV-3. $N_t=51$.

Table IV-3: Variation in N_t and its influence on validation results

N_t	Objective u_* (cm.s^{-1})	t_{SNOPT} (s)	t_f (s)	dt (s)
41	60.533	3.07	7.018	0.175
51	60.555	3.85	7.010	0.14
61	60.566	8.13	7.008	0.117
81	60.574	8.44	7.007	0.088
101	60.577	25.47	7.000	0.070

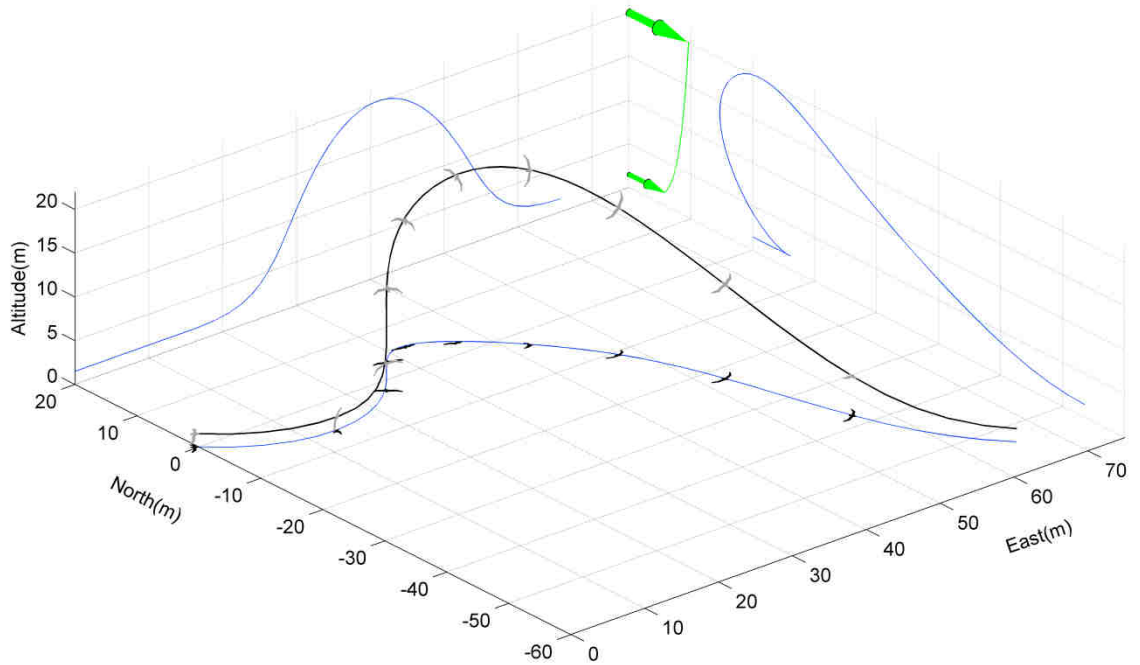


Figure IV.5: Energy-neutral trajectory for conditions representing Sachs [47]. The surface is rather flat with $z_0=3\text{ cm}$. The wind friction velocity required to sustain DS is 60.6 cm/s , the duration is 7 seconds.

In order to keep the calculation time rather acceptable without sacrificing on the accuracy of the solution, it was chosen to perform the validation case with $N_t=51$. This value could also enable to draw comparisons with results obtained by Bower [67].

The resulting energy-neutral cycle described in Fig. IV.5 is obtained by minimizing the friction velocity required to perform the neutral cycle without any power input from the vehicle. Figure. IV.5 pictures in black the overall flight path, while 2-D projections are in blue. The wind profile and direction are plotted in green and a schematic *Wandering Albatross* is plotted in grey, at the corresponding dimension scale, such that it gives an idea of the attitude adopted along the cycle. Overall results match very well the simulation made by Sachs, as can be compared in Table IV-4. Some minor disparities can be explained by differences in the methodology between Sachs' simulation and the present one. Indeed, some practical aspects, such as for instance the number of time discretization nodes N_t , or the selected integration scheme, are not specified in Sachs' publication and therefore probably differ between the two. Results obtained differ from Sachs' by less than 5 %, hence validating the methodology set in the case of DS over a rather flat surface with a 3 cm roughness length.

Table IV-4: Comparison with simulations obtained by Sachs [47] and Bower [67].

Variables	Sachs [47]	Bower [67]	Current	Disparity with Sachs [47]
t_f (s)	7.1	7.0025	7.0102	2.8 %
u_* (cm.s ⁻¹)	60.7	60.42	60.555	0.2 %
Max. height (m)	20.5	20.038	20.1	2.0 %
Eastern net speed(m.s⁻¹)	9.37	9.38	9.39	0.1 %
Eastern period(m)	66.5	65.71	65.8	1.1 %

Therefore, the validation case seems to validate our approach and the associated methodology. It entails a solution, in terms of trajectory, which appears both non-trivial as well as physically sound and corresponds to results obtained in the literature.

IV.4 Summary of Chapter IV

The observation of the physics of the vehicle and the equations that govern it are dependent on the point of observation. In the present case, it is either earth-based or air-relative. After the influence of this choice on the energetic consideration is discussed, the two corresponding sets of equations are expressed, which involve state and control variables. In the case of air relative equations, the inertial force, due to the acceleration of the point of view, leads to the expression of a term that is the driving force of the movement. This is more diffuse for the earth-relative point of view, but it is decided to go ahead with this set of equations, partly because range performances are earth-relative.

The evolution of state variable over time depends on that of control variables and those need a guiding line in order to pilot the trajectory. This is achieved by setting up an optimization problem in order to provide the set of values over time that yields an optimum. The objective constraint, at first, is to lower the wind strength required to perform an energy-neutral trajectory. This is complemented by constraints that include periodicity, in order to be able to repeat the flight path, and operational limitations, so as to ensure the flight path can be reasonably flown for the vehicle. The trajectory optimization problem is then converted into a parameter optimization problem by discretizing the time interval and allocating discrete values by mean of adequate interpolation and collocation technique. Equations of motion are included as constraints of the subsequent non-linear constrained optimization problem, which is solved by using a modelling language AMPL coupled with SNOPT.

CHAPTER V

FUNDAMENTALS OF DS FLIGHT

After the whole methodology is set up, it is time to step back and analyse the results obtained. This part aims at exposing those first simulation results and describing their features in order to build-up knowledge on DS out of those simulations. Those interpretations would start by simply describing the trajectory components and the evolution of variables along the path. The principles of DS energy extraction are somehow difficult to grasp, so a special care would be given to analysing those, as they are the real added value of DS flight and therefore questions its essence. Different trajectories would be used as case studies to support the analysis on energy-extraction mechanisms. The formulation of energy work and powers of forces would help to conceptualize the exchanges between the environment and the vehicle. The approach would be enriched by considering a simulation within a refined wavy environment.

V.1 The 3D Closed-Trajectory

Among different potential trajectories, the closed loop is of particular interest as the vehicle is forced to return back to its initial position, so that the initial and the final state are identical. The optimization process is run to derive a closed trajectory which minimizes the wind strength required to fly effortlessly, that is to say without any power supplied by the vehicle. In the formulation of the optimization problem, periodicity constraints are imposed for each state variable.

It may be possible that such a trajectory does not exist, whatever the wind friction velocity is, even very high. In such a case, there is no solution to the problem and DS cannot be considered as a viable way to loiter over a fixed location. It may require some adjustments over some design variables such as the mass of the vehicle for instance, or alterations of some environment variables, such as the surface roughness length.

Therefore, this approach questions the feasibility for the vehicle to perform a closed loop within an environment of positive vertical wind shear gradient of variable strength, as

well as provide a support to study variation in total energy during the cycle. It is to mention that the energy ratio between the initial state and the final state is 1, therefore the energy extracted along the path exactly compensates drag losses and the vehicle can stay aloft by repeating the exact same trajectory without the need to provide extra power.

In the case presented below, in Fig. V.1, the vehicle chosen is *Mariner*, as it was more representative of a mission scenario than the *Wandering Albatross*. Besides, a virtual payload has been arbitrarily added, such that the overall mass is 6.6 kg . Furthermore, contrary to the validation case displayed before, the lowest altitude is constrained by a wing-tip clearance limit of 50 cm and not net minimum altitude anymore. The load factor was chosen not to be limited in this case. The number of time steps is $N_t=171$.

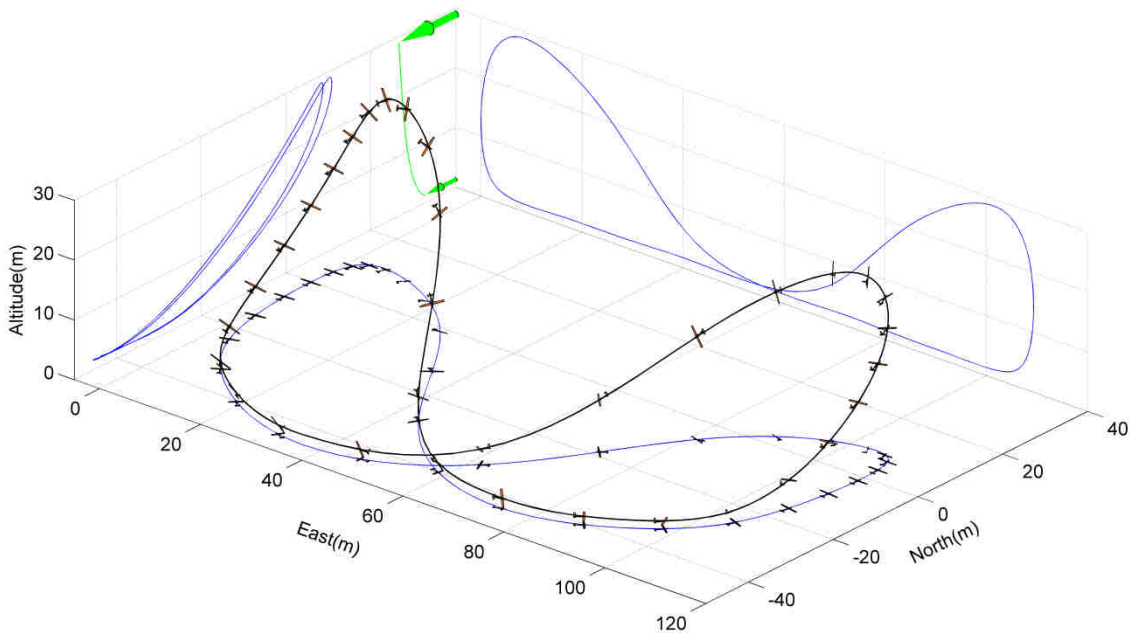


Figure V.1: Closed loop energy neutral trajectory obtained for a wing tip clearance of 50 cm , a surface roughness length of 3 cm and a wind friction velocity of 80 cm/s , which corresponds to a wind speed of 11.34 m/s at 10 metres . The trajectory is completed in 20.58 seconds . The wind profile and direction is represented by the green arrow. The scale of the vehicle (*Mariner*) is augmented by a factor 1.5 for better visibility.

The trajectory displayed in Fig. V.1 is the result of the optimization problem explained above. It is obtained for a wind friction velocity of 80 cm/s , which corresponds to a wind speed of 11.34 m/s at 10 metres . It represents a benchmark regarding the feasibility, for a vehicle, to remain effortlessly in the air over a fixed position by using DS. If the actual wind is less than the value obtained in this simulation, then some power must be provided by a 6.6 kg -*Mariner*, operating under conditions underlined before, so as to conserve the level of total energy over

one cycle. On the other hand, if the actual wind is more than the benchmark value, then the vehicle can enter the next cycle with some extra energy. It therefore allows a margin for additional manoeuvres, such as travelling in one direction, before repeating the same cycle. If the wind is at least equal to the benchmark value, then the endurance is virtually unlimited.

The optimal closed trajectory consists in an 8-shaped path rather than a simple loop. It combines different legs which are characteristic to DS flight. An upwind climb where the vehicle climbs straight into the wind, wings level, is followed by a turn from upwind heading to downwind heading where the maximal height is reached with a belly exposed to the wind attitude and a high bank angle, up to 80 degrees. Then starts a downwind dive, where the vehicle returns to wings-level and builds up inertial speed quickly. That is followed by the last maneuver, a turn into the wind at almost constant height close to the surface. The two inner loops which compose the 8-shaped path slightly differ in amplitude but are identical in their construction; therefore we can limit our scope to one loop of the overall trajectory, which consists of the four legs mentioned above. A colour scale is applied, in Fig. V.2, to the trajectory obtained, to highlight components of the DS trajectory.

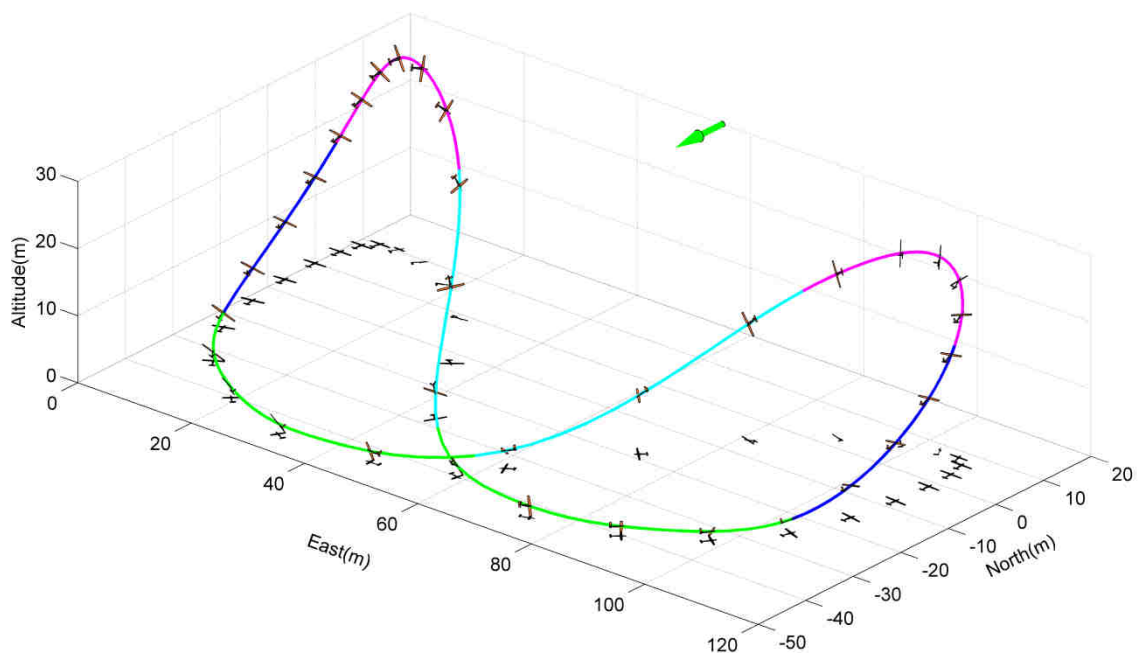


Figure V.2: Phases of flight are evidenced out using different colours. Blue for the upwind climb, magenta for the high turn, cyan for the downwind dive and green for the lower turn.

Figure V.3 details the variation of different speeds along the path, in order to improve the understanding of the way those are associated to the four phases of flight. The wind

strength at the vehicle's altitude is also pictured and gives a direct image of the height of the vehicle.

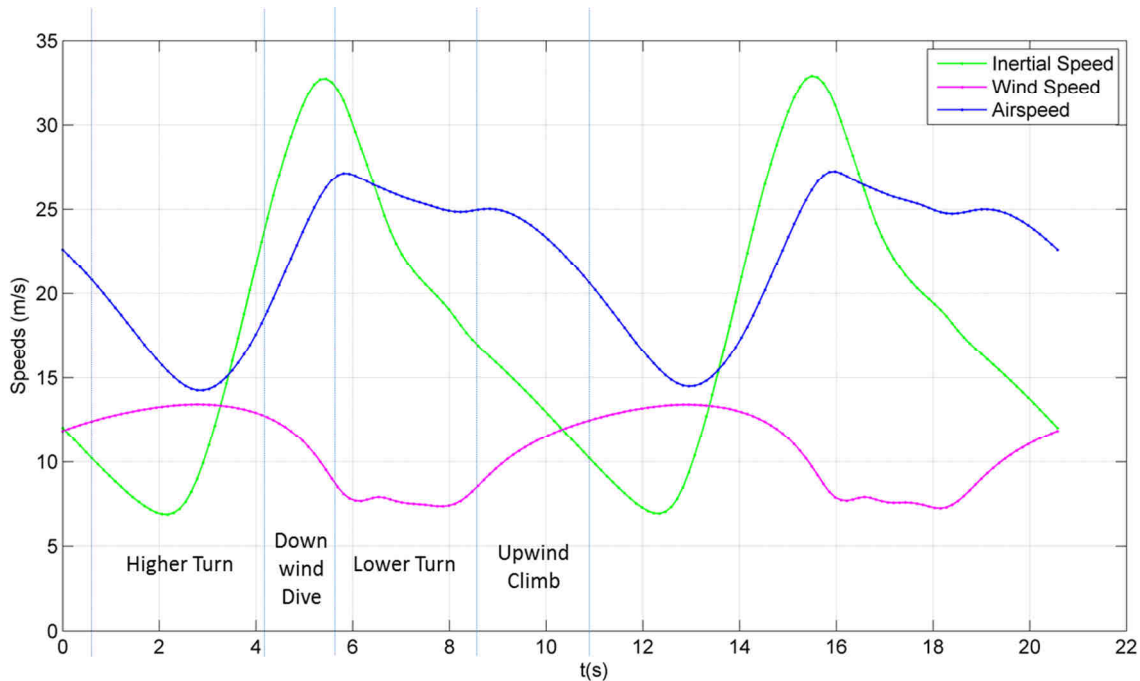


Figure V.3: Speeds along the path, correlated to the four phases of flight.

On the upwind climb, the vehicle starts to pull-up upwind and to climb through a zone where the vertical wind gradient is the strongest, since it is the lower part of the path, close to the surface. An associated local increase in airspeed can be observed, which is however not sustained for long as the wind gradient is not strong enough to allow for a steady airspeed. Besides, the rate of decrease in inertial speed gets lower as soon as the vehicle pulls up. This seems somehow counter-intuitive as the negative contribution of the weight adds up to drag losses as soon as the flight path deflects upwards, creating an even greater negative work contribution to the variation in kinetic energy. Hence, it can be deduced that another force provides a positive contribution to overcome this influence. Given that only three forces act on the vehicle, it can be deduced that the lift gives a positive work contribution during the headwind climb.

The vehicle then performs an upper turn from a windward heading to a leeward heading. The inertial speed sharply increases when the vehicle gets pulled by the wind before reaching its highest altitude of 29 metres. The rate of increase in inertial speed is significantly higher than the rate of increase in airspeed, suggesting that the lift provides a positive

contribution to the movement. The airspeed has a smoother variation and reaches a minimum at the top of the path, when the vehicle starts to head down.

The vehicle follows with the downwind dive. The inertial speed keeps increasing for some time before reaching a maximum when the vehicle starts the turn against the wind. The airspeed sees the combined effects of gain in kinetic energy during the descent and of decreasing tailwind as the vehicle goes down leeward through the vertical wind shear gradient. The latter effect is strong enough to keep the airspeed increasing after the inertial speed starts to reduce. The airspeed maximum is reached when the vehicle stabilizes at a low altitude at the end of the dive.

The last component of the trajectory is the lower turn, where the vehicle turns into the wind, from leeward to windward, close to the surface at a constant height, in a zone of weak wind. The inertial speed sharply decreases at a much higher rate than the airspeed, suggesting that the lift provides a negative contribution during the lower turn.

Overall, the vehicle manages to perform a non-powered closed trajectory and to maintain its energy level between the initial and the final state. It takes advantage of a wind gradient that is not strong enough to sustain steady airspeed during the climb, which takes aback a common misbelief about DS. Besides, that energy neutral trajectory was achieved for a nominal wind of 11.34 m/s at a 10 metres height, which is the minimal wind strength that enables an energy neutral closed trajectory.

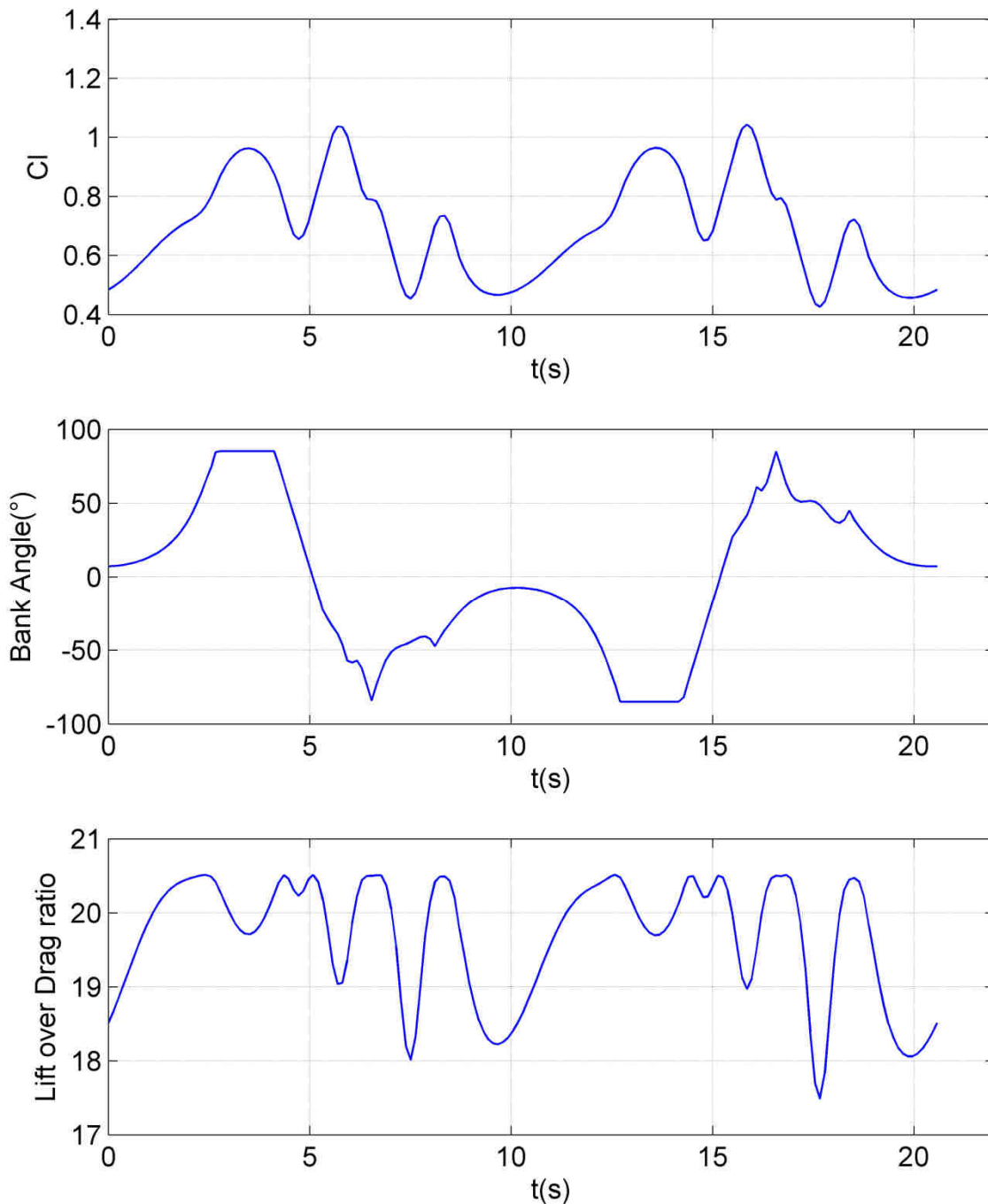


Figure V.4: Evolution of C_L , ϕ and C_L/C_D over time.

It can be observed from Fig. V.4 that the bank angle reaches its maximum during the two higher turns, first to the right and then to the left. The two lower turns see sharp variations in bank angle which occur when the wing tip hits the ground clearance constraint limit. Three local maxima can be observed as for C_L . In the case pictured, chronologically, the first occur at the top of the higher turn, when the vehicles banks leeward at maximum angle. The second is at the beginning of the lower turn, when the vehicle pulls-up to get out of the

dive at maximum airspeed and start to change heading. The maximum load factor ($n = 3.54$) is reached at that moment. The third local maximum, which is also the lowest by a significant margin, is the pull up at the end of the lower turn, when the vehicle starts to head upwards. The evolution of the lift to drag ratio is directly dependent on that of the lift coefficient.

V.2 Energy-Harvesting Mechanisms

V.2.1 Contributions from Aerodynamic Forces

Dynamic soaring manages to take advantage of local contributions of aerodynamic forces along the flight path by combining specific manoeuvres with respect to the wind field. In the case of static gliding flight in still air, airspeed and inertial speeds are the same and only the drag contributes to the variation of total energy, as the lift is orthogonal to the direction of motion. However, if the vehicle flies through a mass of moving air, variations in total energy, in the earth reference frame, will see a contribution from the lift as well. It is to be noted that the work done by forces varies with the point of view of the observer. From an earth-based point of view, Fig. V.5 shows how forces and speeds orientate during a windward climb.

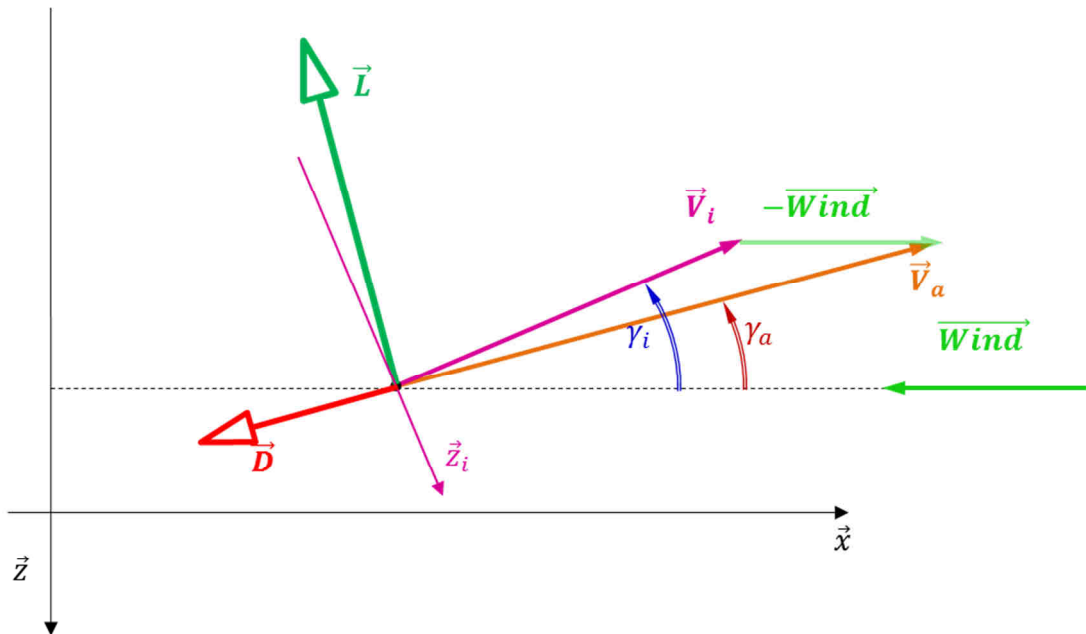


Figure V.5: Orientation of speeds and forces for a 2D-simplified windward climb. The lift is tilted by an angle $(\gamma_i - \gamma_a)$ towards the direction of motion \vec{x}_i . This entails a positive working component which governs the energy extraction.

It is assumed that wings are level and that airspeed, inertial speed and wind speed are in the same plane. The orientation of the inertial speed and of the wind speed induces that the

airspeed is not directed along the direction of motion, but forms an angle $(\gamma_i - \gamma_{air})$ with it. Aerodynamic forces are therefore also tilted with respect to the frame of reference \mathcal{R}_i since the lift and the airspeed are orthogonal while the drag and the airspeed are collinear.

The variation of total energy is only driven by contributions of non-conservative forces, that is to say only the lift and the drag. The calculation of the elementary variation in total energy takes into account the respective work done by those forces, as presented in Eqs. V.1 to V.3. The elementary displacement dl is along \vec{x}_i .

$$dE_{tot} = dW_{Non\ Conservative\ Forces} = \sum_{NCF} \vec{F} \cdot d\vec{l} = (\vec{L} + \vec{D}) \cdot (dl \cdot \vec{x}_i) \quad (V.1)$$

$$dE_{tot} = [L \sin(\gamma_i - \gamma_a) - D \cos(\gamma_i - \gamma_a)] dl \quad (V.2)$$

$$\Delta E_{tot_A}^B = \int_A^B [L \sin(\gamma_i - \gamma_a) - D \cos(\gamma_i - \gamma_a)] \cdot dl \quad (V.3)$$

Therefore, the condition to an increase in total energy is expressed in Eqs. V.4 and V.5. Equation V.5 is obtained through some calculations involving Eqs. IV.6 and IV.7.

$$dE_{tot} \geq 0 \text{ if } \frac{L}{D} \geq \frac{1}{\tan(\gamma_i - \gamma_a)} \quad (V.4)$$

$$dE_{tot} \geq 0 \text{ if } \frac{L}{D} \geq \frac{(V_i / -W_x) + \cos \gamma_i}{\sin \gamma_i} \quad (V.5)$$

Equation V.5 underlines how the local energy-extraction is sensible to the instantaneous lift to drag ratio, which should be as high as possible, and for a large range of C_L since the vehicle explores a full range of functioning points during the climb. Moreover, it shows the sensitivity of the energy-extraction to both the inertial flight path angle γ_i and to the local wind strength W_x . A steep climb into a strong wind represents a favorable case. It should be mentioned that for an inertial speed twice the value of the local wind and at a 30° climb angle, the lift to drag ratio has to be over 5.7 in order to extract energy, which is easily achievable. It can be concluded that any average glider can extract energy during an upwind

climb. The very same principles apply to any of the four phases of flight, as aerodynamic forces are tilted by the wind speed. Yet, it does not translate into the same conclusion regarding the energy-extraction, depending on the attitude of the vehicle with respect to the wind.

The rate of variation in total energy is expressed in Eq. V.6. The contribution of the lift can be simplified to the scalar product between the lift and the wind, as the lift is orthogonal to the airspeed vector. The power due to lift is developed in Eq. V.8, where components of two distinct contributions can be outlined.

$$\frac{dE_{tot}}{dt} = \sum_{NCF} \vec{F} \cdot \vec{V}_i = (\vec{L} + \vec{D}) \cdot (V_i \cdot \vec{x}_i) \quad (V.6)$$

$$\vec{L} \cdot \vec{V}_i = \vec{L} \cdot (\vec{V}_a + \vec{W}) = \vec{L} \cdot \vec{W} \quad (V.7)$$

$$\vec{L} \cdot \vec{W} = -\frac{1}{2} \rho S C_L V_a^2 W_x (\sin \phi \sin \psi_a + \cos \phi \cos \psi_a \sin \gamma_a) \quad (V.8)$$

The first corresponds to the case seen before, with wings level ($\phi = 0$). The lift works positively when either the vehicle is facing the wind and climbing ($\psi_a = 0$ and $\gamma_a > 0$), or when the vehicle flies leeward and the vehicle is descending ($\psi_a = \pi$ and $\gamma_a < 0$). Consequently, not only the lift contributes positively to an increase in total energy when the vehicle is climbing into the wind, but it does also provide power to the vehicle when it is diving downwind.

The other contribution corresponds to the case where the vehicle flies crosswind in such a way that the longitudinal axis of the vehicle is orthogonal to the wind direction, if it is assumed that there is no sideslip. Considering the case where the wind comes from the left of the vehicle ($\psi_a = \pi/2$), it can be seen that the lift works positively when the vehicle turns right ($\phi > 0$), that is to say opposite to the wind. This corresponds to the “belly to the wind” attitude of albatrosses described by Pennycuik [41]. Conversely, if the vehicle turns left into the wind ($\phi < 0$), then the lift contributes negatively. The same applies symmetrically when the wind comes from the right of the vehicle.

Those simplified calculations underline that during a closed loop, such as the one obtained in Fig. V.1, the lift contributes to an increase in total energy during the upwind climb, as well as during the higher turn and also through the downwind dive. The last phase which

appears during the loop is the turn into the wind, which sees conversely a negative contribution from the lift. It should be noted that those statements remains valid, whatever the wind profile $W_x(z)$ is, even if the wind is uniform with no vertical gradients. However, the wind profile will determine how those respective gains and losses would weigh in the overall energy balance respectively to each other.

V.2.2 Acceleration in the direction of the wind

Another way to develop calculations leads to an interesting point of view, linking the power due to aerodynamic forces to the acceleration in the direction of the wind. From Eq. V.6, a further step of calculation gives Eqs. V.9 and V.10.

$$\frac{dE_{tot}}{dt} = (\vec{L} + \vec{D}) \cdot (V_i \cdot \vec{x}_i) = \vec{L} \cdot \vec{W} + \vec{D} \cdot (\vec{V}_a + \vec{W}) \quad (\text{V.9})$$

$$\frac{dE_{tot}}{dt} = W_x [(\vec{L} + \vec{D}) \cdot \vec{x}] - D \cdot V_a \quad (\text{V.10})$$

The projection of aerodynamic forces on \vec{x} , in Eq. V.10, corresponds to the acceleration of the vehicle along that same axis, such that it yields Eq. V.11.

$$\frac{dE_{tot}}{dt} = m W_x \ddot{x} - D \cdot V_a \quad (\text{V.11})$$

The above equation conveys that the instantaneous rate of total energy is a function of the acceleration of the vehicle in the direction of the wind, minus a term due to drag that is invariably a loss. Indeed, it should be noted that in Eq. V.10, a component of the drag may provide a positive power. Although quite unintuitive, it comes from the fact that the drag, which is always opposed to the airspeed vector, can actually have a component in the inertial direction of motion, which is in such a case providing positive work. It leaves $D \cdot V_a$ as the only term invariably negative, therefore corresponding to an unavoidable loss. It should be mentioned that, as any instantaneous calculation, Eq. V.11 is not specific to DS, but rather applicable to any wind energy extraction technique. Albeit rather interesting from the understanding point of view, Eq. V.11 is also convenient as the instantaneous power extracted from the wind can be maximized in real time by monitoring the acceleration along the wind direction.

Equation V.11 can be further developed and combined with air relative EoM in order to evidence exact differentials. After some calculation steps, the expression the total energy can be integrated out of the power expression, it gives Eq.V.12.

$$E_{tot} = \frac{1}{2}mW_x^2 + mW_xV_a \cos \gamma_a + \frac{1}{2}mV_a^2 - mgz \quad (\text{V.12})$$

It provides an air-based alternative to the calculation of the total energy.

V.2.3 Overall cycle of total Energy

If local manoeuvres can be performed in order to extract energy through the mechanisms that have been specified, a closed trajectory must however combine a serie of those manoeuvres such that the vehicle gets back to its initial position. The set of successive manoeuvres is a delicate solution of an optimization problem that compromises the objective function in order to satisfy periodicity constraints. For the closed trajectory presented in Fig. V.1, the evolution of total energy with time is depicted in Fig. V.6 , together with the source of this evolution as it superposes the variation of aerodynamic power input with time. The power input displayed on the lower part of the figure can be seen as the source of the variation in total energy depicted on the upper chart.

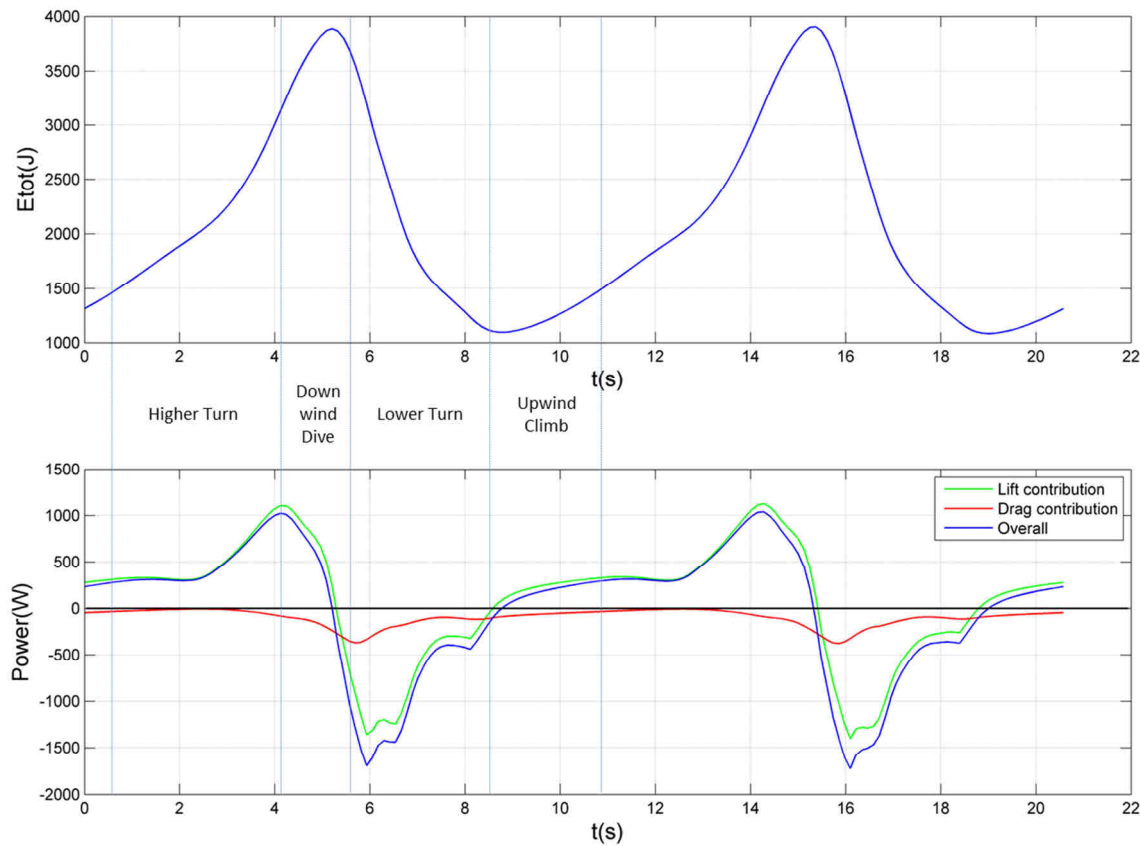


Figure V.6: Variation in total energy with time and in the associated rate of energy with time

As it was anticipated, the lift contributes positively on the upwind climb. The overall contribution is also positive and some energy is therefore extracted from the wind during the climb. The biggest increase in total energy comes from the higher turn. The drag contribution is negligible as the airspeed gets quite low and the lift contribution sharply increases from 2.3 seconds, when the vehicle gets “belly to the wind” and is being pulled by the wind. The vehicle still manages to gain some energy during the first part of the downwind dive but the drag quickly builds up as the airspeed increases and it can be seen from Fig. V.6 that the lift contribution turns negative as soon as the vehicle starts to bank into the wind. Finally, the lower turn is flown at a high airspeed while turning into the wind. The negative contribution brought by the lift is clearly noticeable from Fig. V.6 and it adds to significant drag losses to produce the highest loss in total energy along the path.

Overall, it can be seen from Figs. V.6 and V.7 that the energy gained on the three segments upwind climb, higher turn and downwind dive is lost along the lower turn. Even

though the wind faced at that height is at its lowest value, the lower turn is the major hurdle to overcome in order to complete the closed loop while maintaining an objective energy ratio of 1.

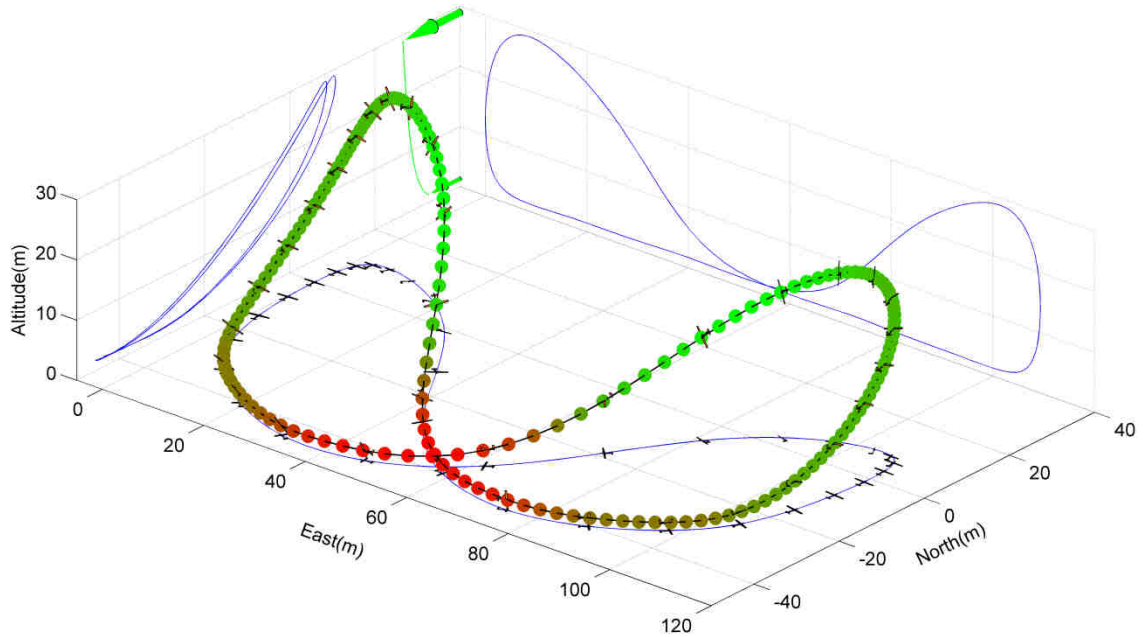


Figure V.7: Overall energy-harvesting strategy. The energy neutral closed loop trajectory from Fig. IV.1 is coloured following a red to green scale as a function of the local power input. Total energy is extracted at green-coloured positions and is lost at red-coloured positions.

It is apparent in Figs. V.6 and V.7 that the loss in total energy occurs during a rather limited amount of time and on a small spatial portion of the trajectory, but represents both the highest power output and the highest energy variation of any other segment of the trajectory. It can be concluded that parameters which may govern the energy loss during the lower turn should have a prevailing influence on the overall balance of total energy.

Another way to breakdown the energy extraction is to consider Eq. V.11, where the terms would be called *Leeward Acceleration* for $m W_x \ddot{x}$ and *Air relative Losses* for $-D \cdot V_a$.

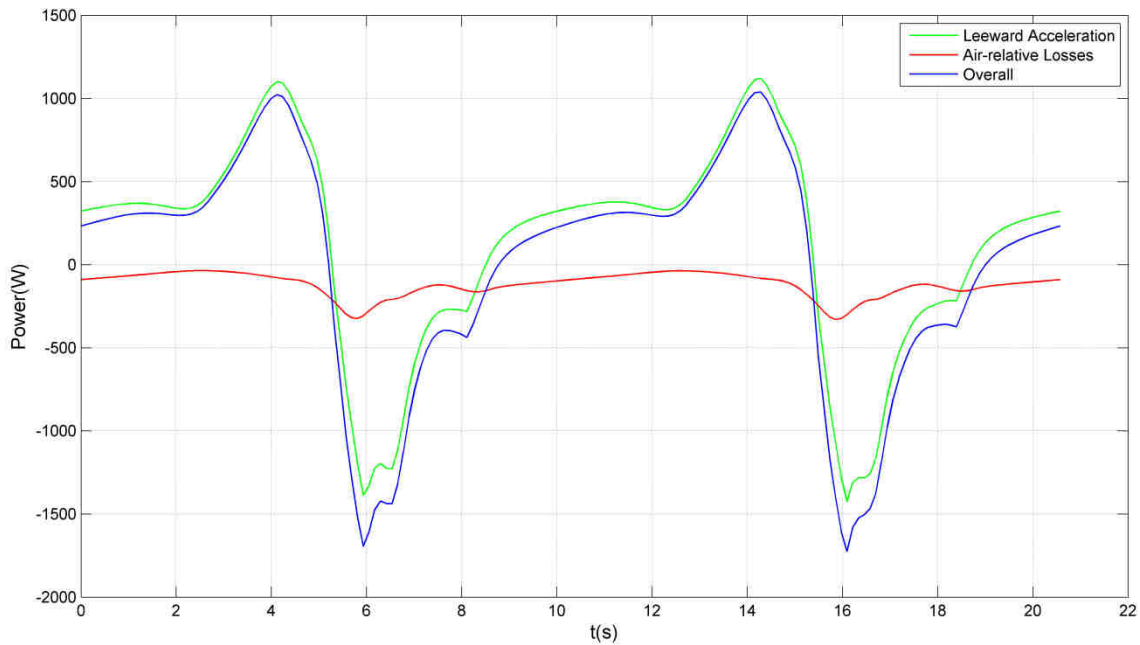


Figure V.8: Variation of power input contributions, with respect to time.

Figure V.8 globally shows the same evolution as Fig. V.6, with minor disparities, which tend to show that the positive contribution from the drag is somehow negligible. It confirms that the strongest contribution from acceleration terms comes during the lower turn, when the vehicle deflects its path towards the wind.

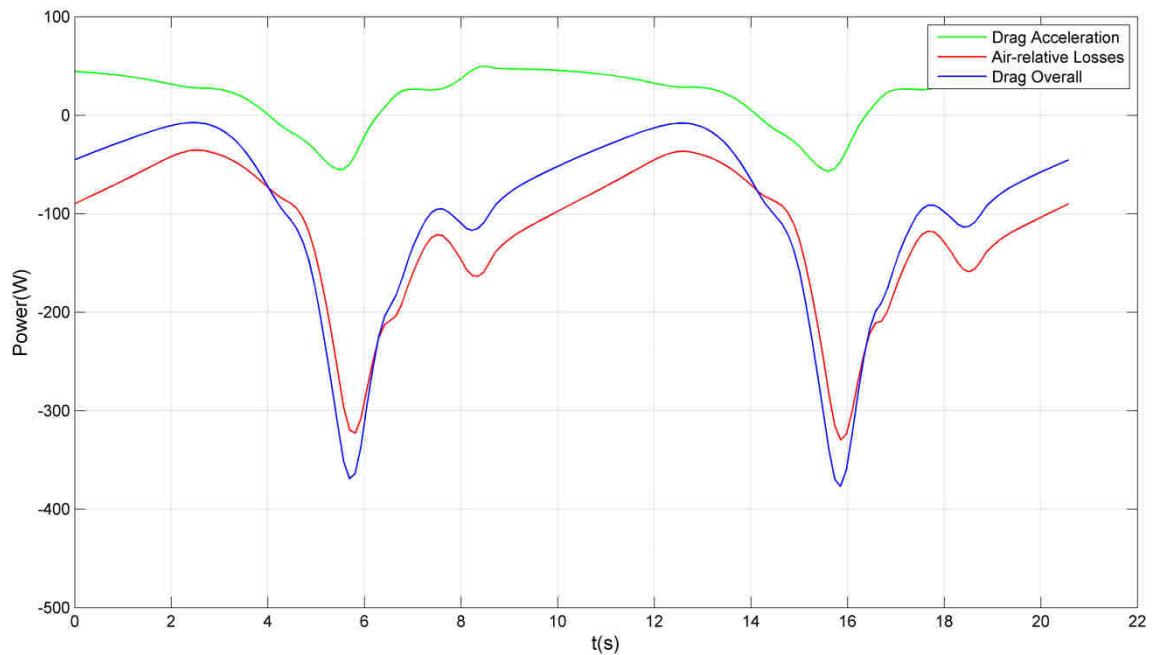


Figure V.9: Variation in power input contributions from the drag, with respect to time.

Figure V.9 details contributions from power which are broke down into two parts. The first, in green is the contribution of the drag to the acceleration in the direction of the wind. The second, in red, is the parasitic and unavoidable loss due to the air relative motion of the vehicle. Even though, in the present case, the overall contribution from the drag is always negative, it can be seen that, for most of the trajectory, the drag contributes to the acceleration in the direction of the wind. In theory, nothing hamper the overall drag to be positive, even though it requires the wind speed to be higher than the airspeed. It can occur if the vehicle is flying backwards, kept aloft by a strong headwind.

V.2.4 Exploiting Wind Power within the Wind Gradient

As it was underlined above, the main energy input comes from the upper part of the curve, while the biggest losses occur in the lower part of it. It may seem ironical, as DS is sometimes referred to as *gradient soaring* that energy is actually gained where the gradient is the lowest and lost where the gradient is the strongest, which is particularly emphasized by Fig. V.10. Once again, the energy is gained out of the wind underlying power and the gradient helps to combine gains with limited losses in order to achieve a neutral energy performance.

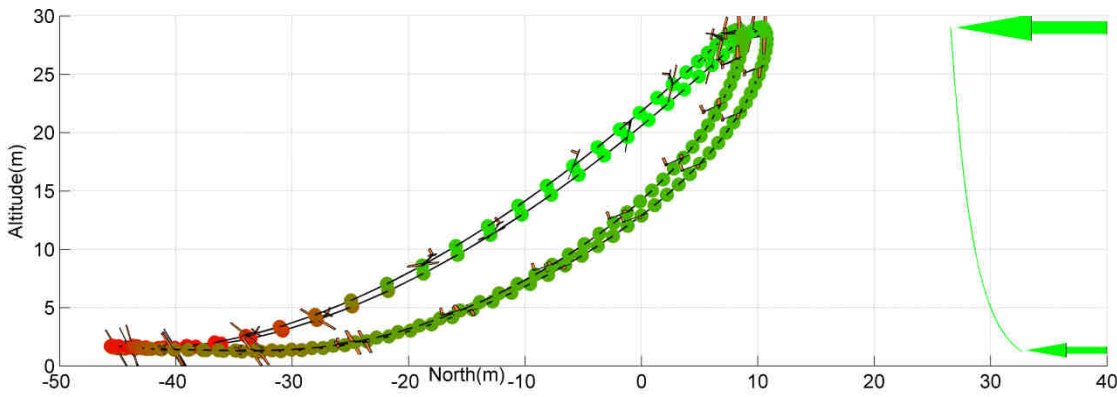


Figure V.10: 2-D side view of the closed trajectory. The length scale is identical between the two axes and the wind speed scale is adapted for good visualisation. The colour scale is identical to Fig. V.7.

The section view offered by Fig. V.10 displays the asymmetry that was mentioned for the two loops of the closed trajectory. Moreover, it appears that during the upwind climb, the inertial flight path angle increase progressively to reach values around 60° during the higher turn, which is achieved in a strong inclined plane. Inversely, the lower turn is carried out in an almost horizontal plane, as close as possible to the surface.

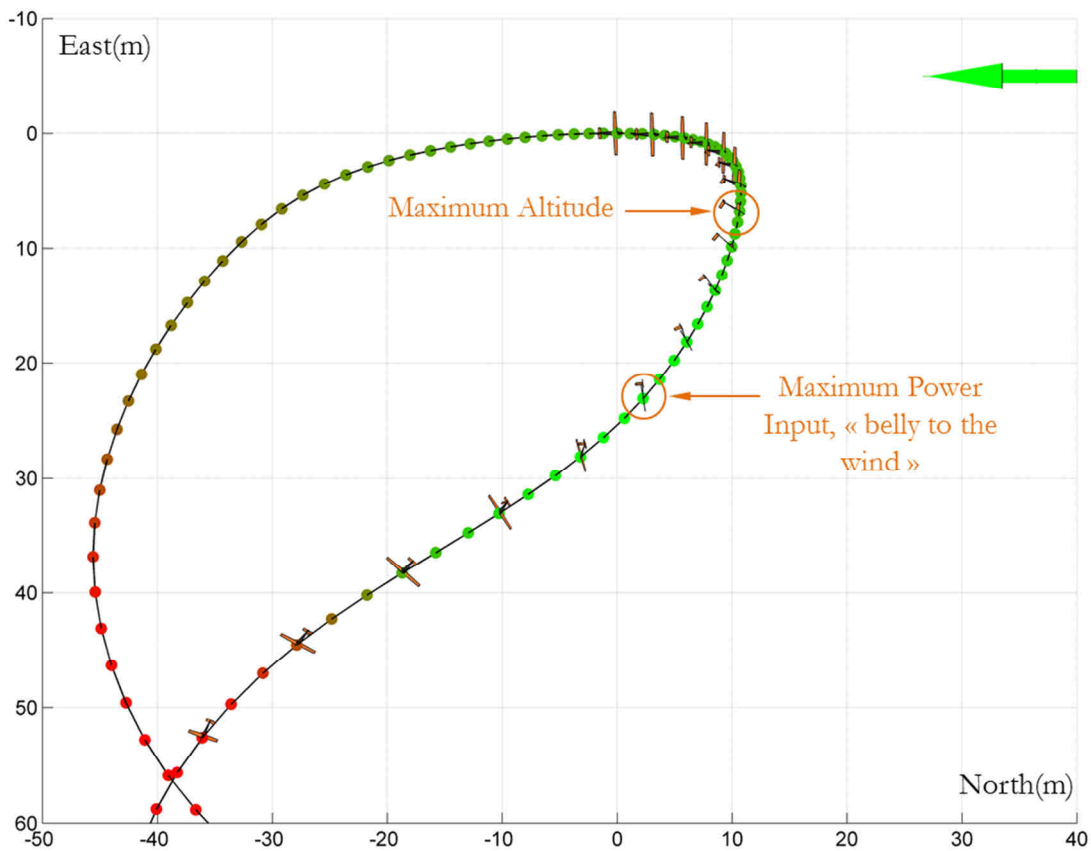


Figure V.11: Top view of one of the two loops, with remarkable points encircled.

The main interest of Fig. V.11 is to underline that the maximum power input does not occur at the highest point of the trajectory. Although the highest altitude provides the highest wind strength, the vehicle extracts energy at a higher rate moments later, when it carries on the turn to orientate the lift in the direction of the wind. This latter configuration, dubbed “belly to the wind” and detailed earlier, corresponds to the vehicle flying with its longitudinal axis perpendicular to the wind ($\psi_a = 90^\circ$), which is visible in Fig. V.11, and banked to the maximum in the direction of the wind. The acceleration in the direction of the wind is then at its maximum. A more precise evolution of the variable at stake is displayed in Fig. V.12. The reason this configuration is not achieved at the highest point of the path is due to the periodicity constraint of the closed trajectory, which imposes that the vehicle recovers the ground it loses in the direction of the wind during the energy-extraction. Hence, the highest altitude is reached at the northbound extreme of the path.

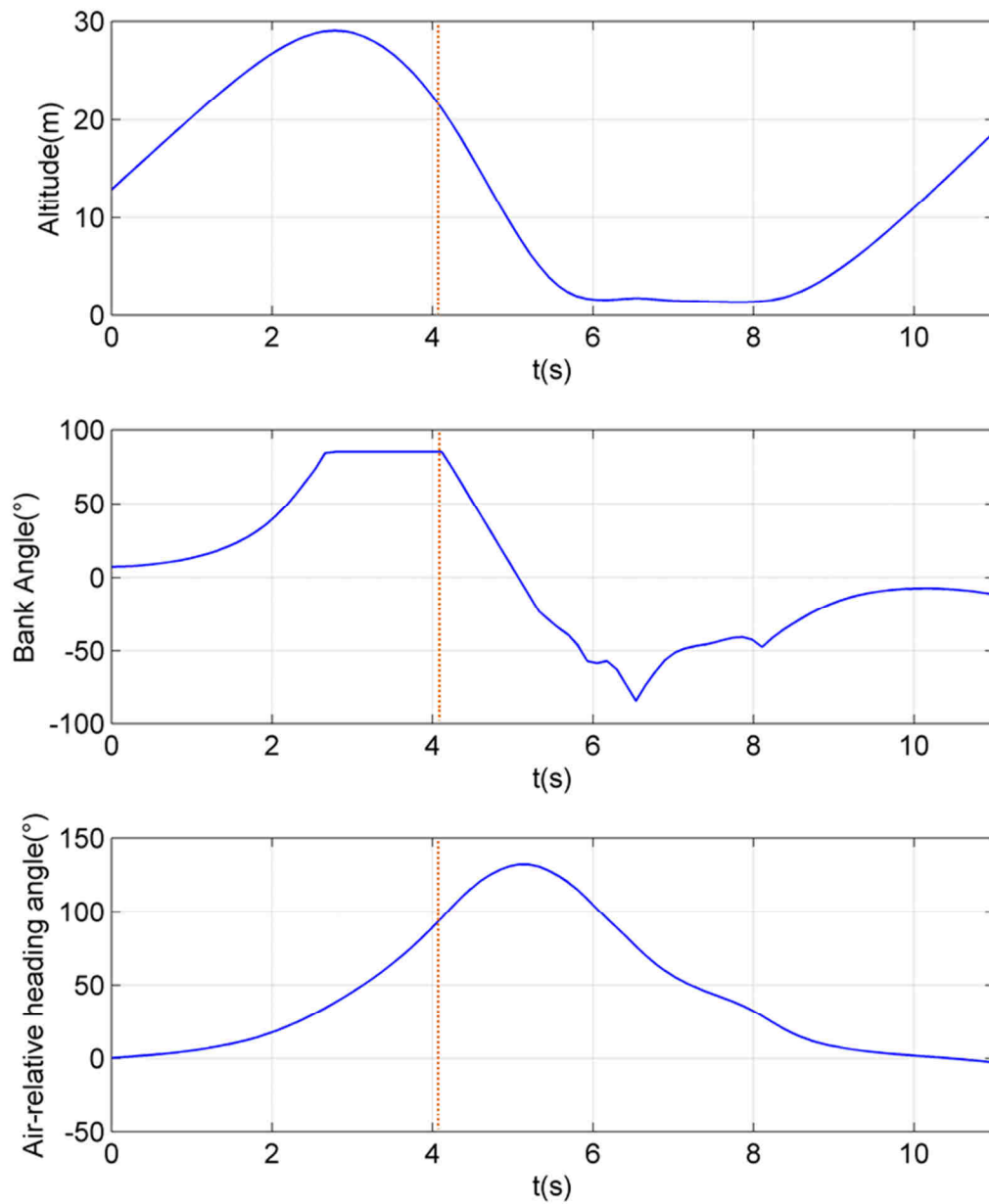


Figure V.12: Evolution of $-z$, ϕ and ψ_{air} during the first half of the cycle plotted in Fig. V.1. The moment of maximum power input is highlighted in dashed orange lines.

V.3 Opening the Loop

In the case of the open loop, two constraints are relaxed, that is the east and north position. Other than those, the problem and its parameters remain the same as before. Because the optimization problem is less constrained, it enables the vehicle to explore a wider space of solutions and potentially to reach a refined objective function.

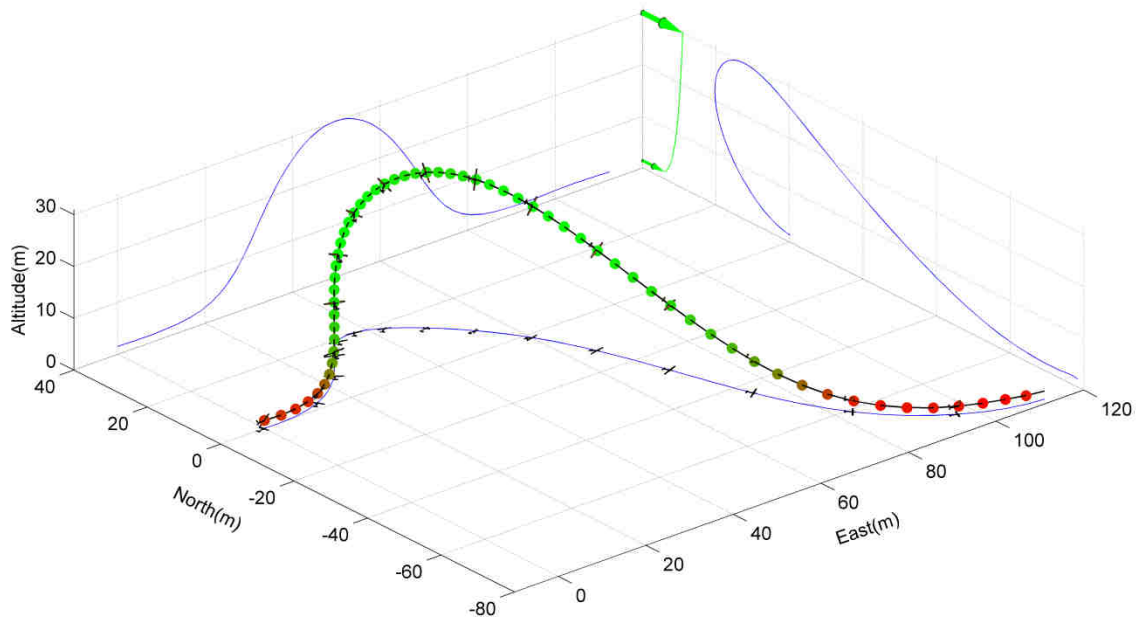


Figure V.13: Energy-neutral optimized open loop obtained for a 6.6 kg *Mariner*. The wind friction velocity obtained is 64.5 cm.s^{-1} , which corresponds to wind strength of 9.14 m.s^{-1} at a height of 10 metres. The cycle takes 9.25 seconds. The wind profile and direction is represented by the green arrow. The path is coloured following a red to green scale as a function of the local power input. Total energy is extracted at green-coloured positions and is lost at red-coloured positions. The scale of the vehicle is augmented by a factor 1.5 for better visibility.

The minimum wind friction velocity required to perform DS flight along an open path is 64.5 cm.s^{-1} . It corresponds to approximately a 20 % reduction compared to the open loop. The corresponding wind strength at 10 metres is 9.14 m.s^{-1} . The vehicle manages to find a solution that requires significantly lower wind strength than for the closed loop. Yet, the performance is accomplished at the cost of a displacement penalty in the direction of the wind. Over one cycle, pictured in Fig. V.13, the vehicle is pulled by 78.5 metres in the direction of the wind.

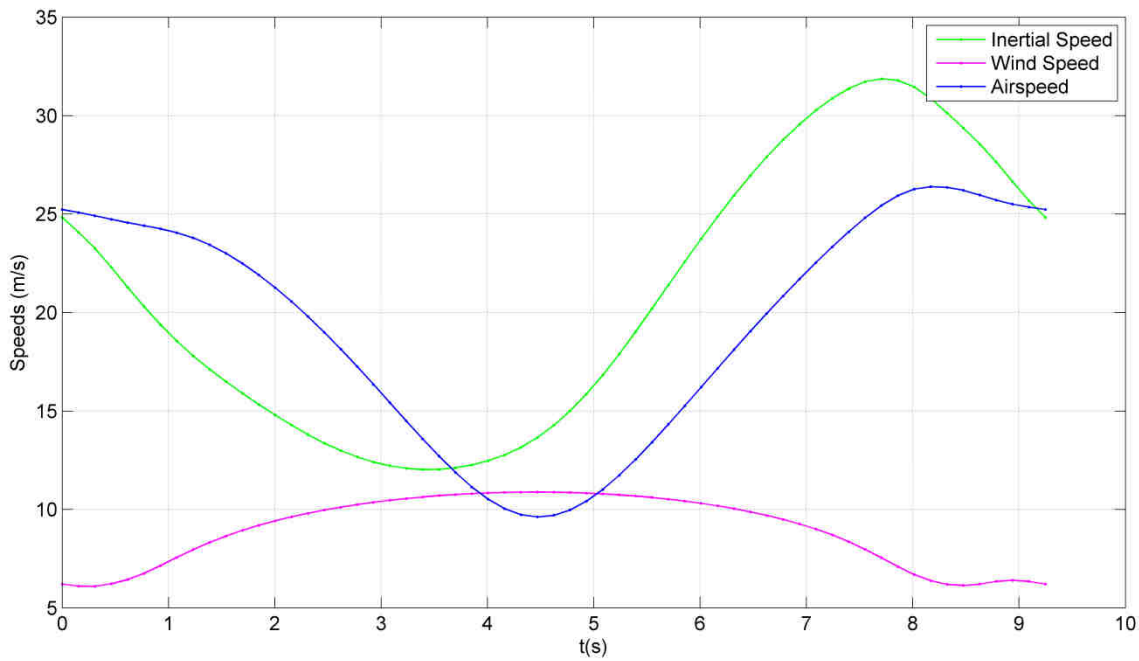


Figure V.14: Evolution of the inertial speed, the wind speed and the airspeed with time.

Compared to the closed loop, the amplitude of the inertial speed is shallower, while the airspeed gets to lower values. The net travelling speed is 14.82 m/s , which would theoretically enable the vehicle to cover 427 kilometres within 8 hours.

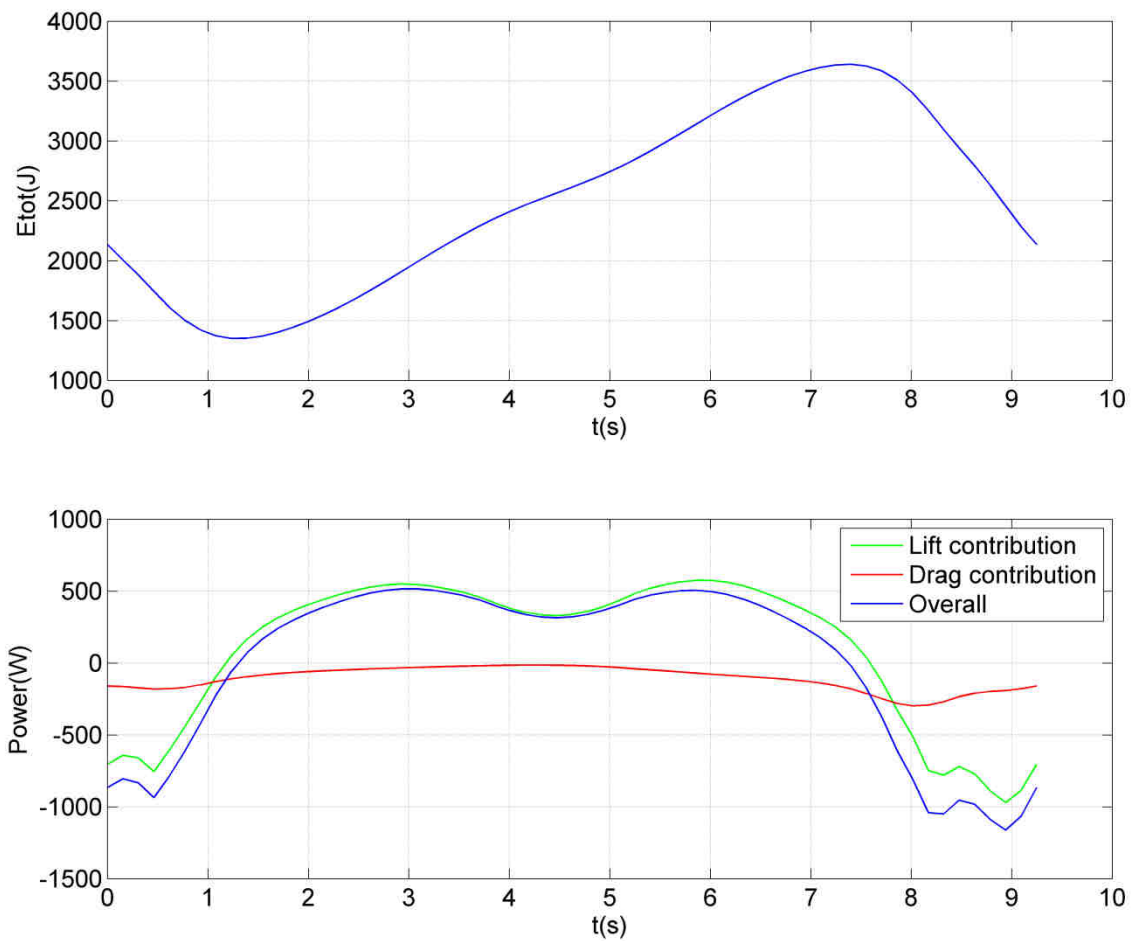


Figure V.15: Variation in total energy along the path, with the associated evolution of power contributions over time.

Although the energy-harvesting mechanisms as well as their combination along the path are very much identical to the closed-loop case, the overall power input shows a local minimum around 4.5 seconds into the cycle. It corresponds to the point of highest altitude and can be linked to the minimum in airspeed reached at the same instant, see Fig. V.14. Indeed, the aerodynamic forces, which govern the energy-extraction are limited in intensity at that point of the path. The effect is more pronounced than for the closed-loop case because the vehicle starts the higher turn well before it reaches its highest altitude, see Fig. V.16, such that the energy-extraction is already significant before that point.

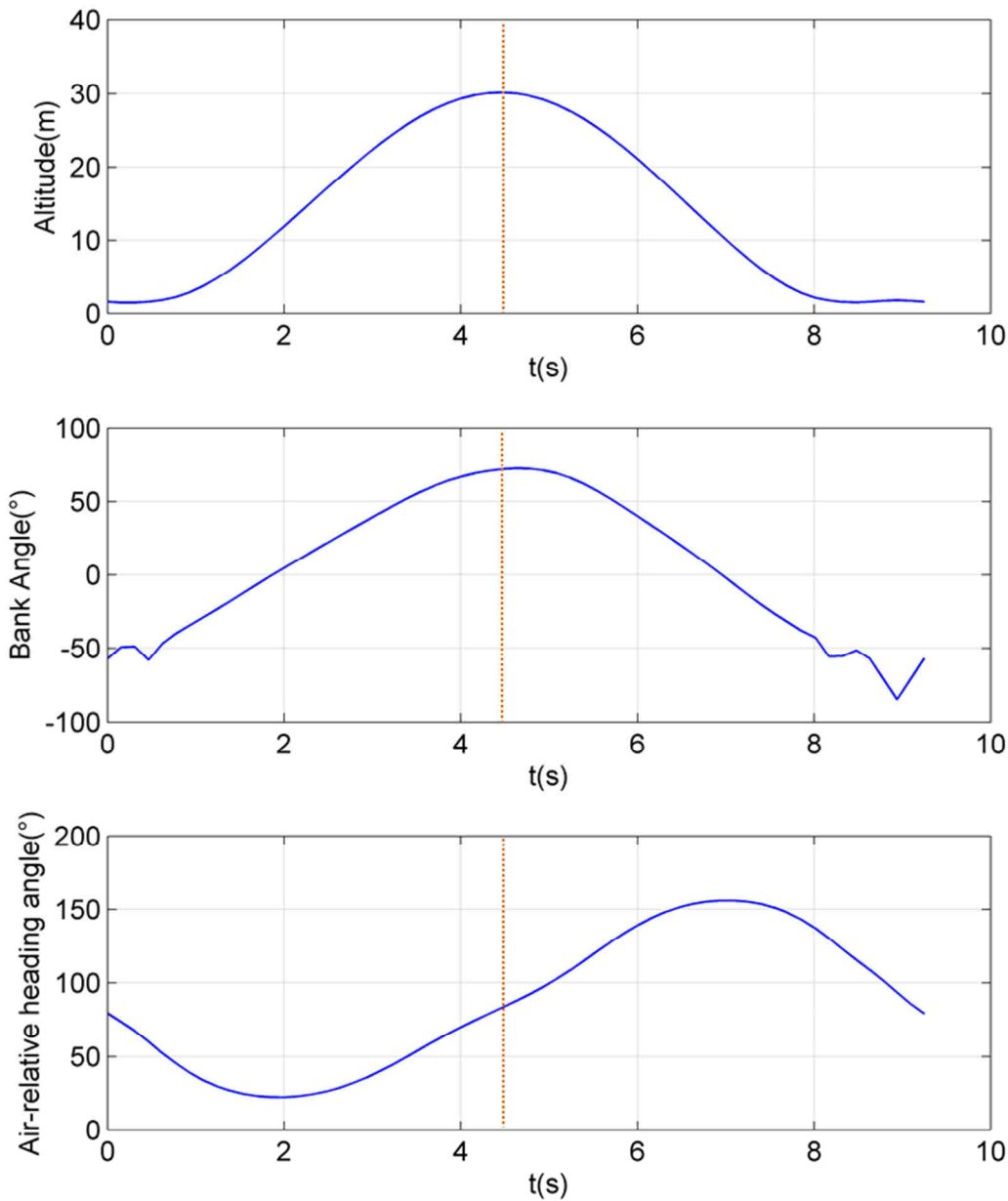


Figure V.16: Evolution of $-z$, ϕ and ψ_{air} during the cycle plotted in Fig. V.13. The point of maximum altitude is highlighted in dashed orange lines.

Contrary to the closed loop, the configuration “belly to the wind” occurs, more or less, at the point of maximum altitude. At 4.47 seconds into the cycle, the altitude reaches 30.13 metres, the bank angle hits 72° to the left (for a maximum of 72.5°) and the air relative heading is 83.3° , the wind coming almost perpendicularly to the right hand side of the vehicle. This analysis is of particular interest as it makes the higher turn very much similar, from the point of view of aerodynamic variables, to a simple turn within an inclined plane, in still air. This may prove a useful piece of information for the sake of DS control.

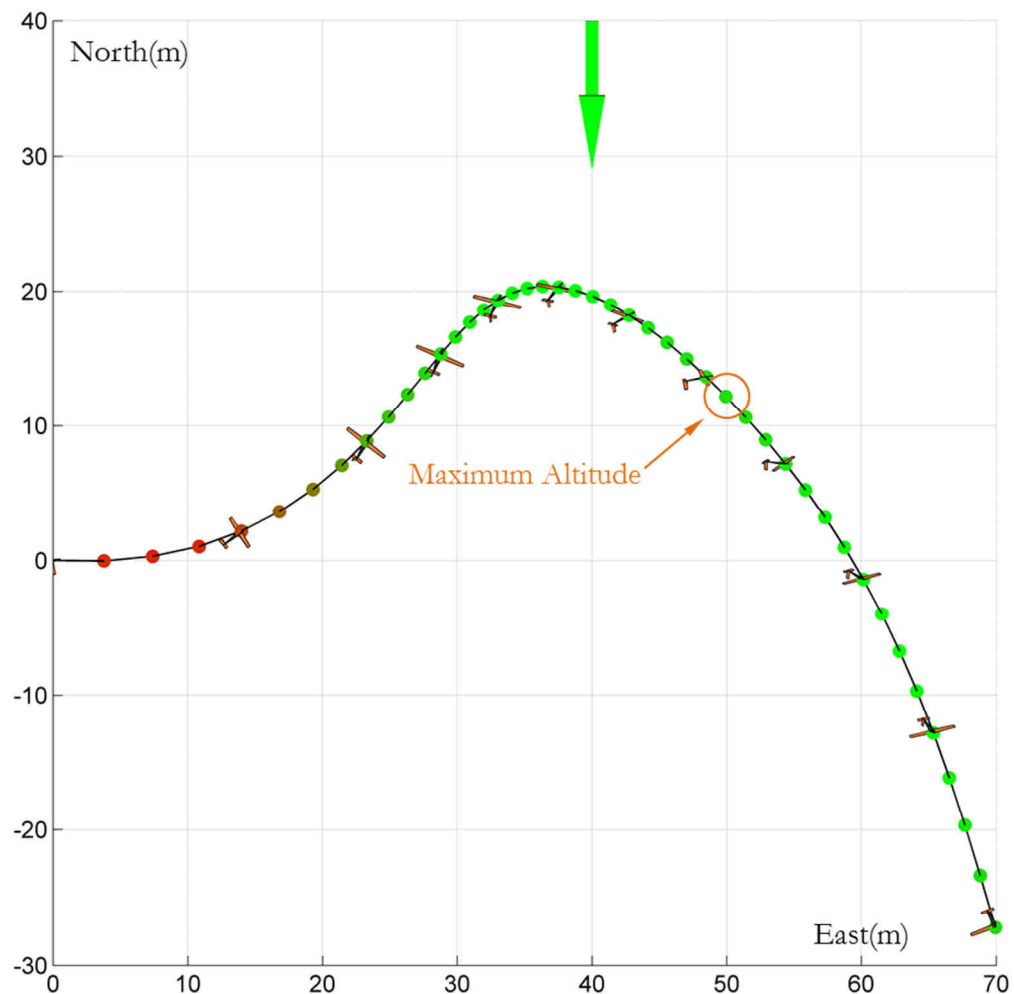


Figure V.17: Top and zoomed-in view of the open loop displayed in Fig. V.13, where the specific point of maximum altitude is encircled in orange.

The point of maximum altitude is not anymore at the northern extreme, but further down along the path, as displayed by Fig. V.17. It illustrates that, for the open loop, the higher turn is anticipated significantly before the vehicle reaches its maximum height.

V.4 Albatross Flight in the Ocean Boundary Layer

First simulations have established that the classical theory of DS could be applied for albatrosses (see Validation Case). Yet, it has been underlined that further refinements from the wind model could be rather significant as for their impact on DS flight simulation. Besides, several sources report the use of waves by albatrosses [41, 42] out of observation or conceptualization of albatross flight. This part aims at assessing the way a refined wind model impact DS trajectories, as well as providing a step forward in albatross flight simulation.

All along this part, the vehicle model is that of the *Wandering Albatross* (see Vehicle Model) and the wind model refers to terms explained earlier (see Wind Model).

V.4.1 Realistic Roughness

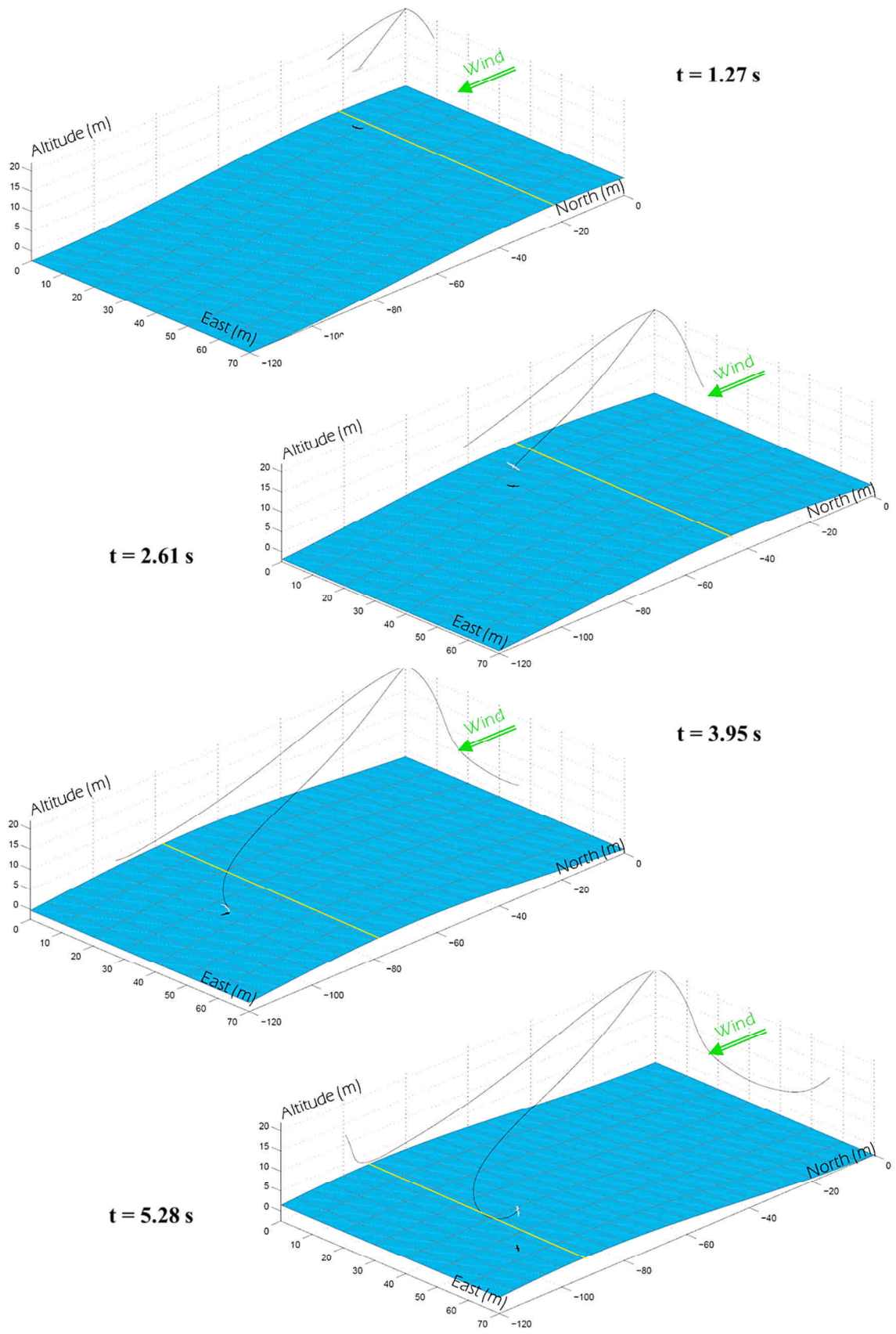
A first case was run without wave, but with a surface roughness length correlated to wind conditions through Charnock's model. Other than that, the optimization problem is almost identical to that of the validation case, the exception being about the ground clearance constraint, which is evaluated at the wing tip and limited to 5 cm . The solution gives a wind friction velocity 0.65 m/s , with a corresponding roughness length z_0 of 0.48 mm . The associated reference wind speed, at 10 metres is 15.8 m/s . Those values strongly differ from the validation case, mainly because the roughness length is calculated using Charnock's model and not fixed at 3 cm anymore. It can be argued that the roughness length could be higher than 0.48 mm , as a rather flat surface of a non-developed sea under recent winds has a higher roughness than old waves.

The wind strength required to maintain the *Wandering Albatross* in flight is quite higher when a supposedly realistic roughness length is taken into account. The literature mentions minimum wind speeds around $7\text{-}9\text{ m/s}$ rather than 15.8 m/s . This confirms the need for further improvements in the simulation in order to fully model, if necessary, the flight of albatrosses.

V.4.2 Influence of Waves

In order to take waves and the induced wind field into account, the amplitude a of waves was increased manually and given as an input fixed-parameter to the solver. It then worked towards minimizing u_* , within an environment with travelling waves of amplitude a and angular frequency $\omega_p(u_*)$, and surface roughness length $z_0(u_*)$. The amplitude a was then compared with the theoretical amplitude of the peak wave, see Eq. III.29, and adjusted by small increases. The process was eventually repeated until the two amplitudes were identical, hence simulating fully-developed waves under winds blowing at u_* .

The methodology converged to obtain the trajectory displayed in Fig. V.18. It is to be mentioned that a further periodicity standard was introduced with respect to the wave motion, with same aim to get a cycle identically repeatable. For the case displayed in Fig. V.18, the vehicle arbitrarily starts ($t=0\text{ s}$) and stops ($t=6.70\text{ s}$) above the crest of the wave, which is materialized by the yellow line.



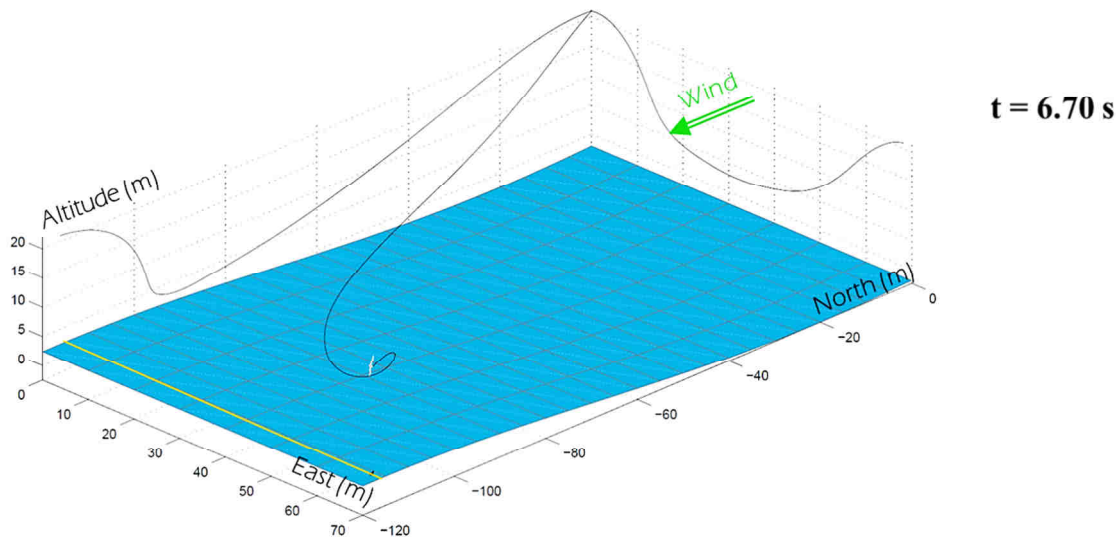


Figure V.18: Evolution of the vehicle above a wave. $u_* = 0.57$ m/s; $a = 2.47$ m; $\lambda = 193$ m; $c = 17.5$ m/s.

It can be observed that the vehicle gains ground towards the wave during the downwind dive ($t=2.61$ s). Hence it begins the lower turn close to the surface ($t=3.95$ s) ahead of the crest, on the forward face of the moving wave, which is the leeward side from a wind point of view. Then, the same type of upwind climb as for the open loop is achieved.

Although the net speed in the y -direction is imposed to be the same as the wave celerity c , the vehicle is “free” to manoeuvre between initial and final positions above the crest. Besides, it is observed during the convergence iteration process, when the amplitude is slightly increased step by step, that those changes are affecting both the trajectory and the minimal friction velocity required. The friction velocity varies from 65 cm/s without waves to 57 cm/s with waves. The vehicle is therefore getting benefits from the presence of the wave, by flying on the forward side which sees a local wind updraft, see Fig. III.15, during the lower turn close to the surface. Although this contribution is not sufficient to balance drag losses and therefore to gain energy, it can be compared as a superposition of wind-gradient soaring with slope soaring, where the slope would be a travelling wave. This result is in accordance with observations of birds exploiting waves by flying on the rising side or face [94], and avoiding the back side. Cases are even reported of birds exploiting a swell wave, without the presence of wind, the uplift from the wave being sufficient to propel the bird. If a higher ratio a/λ is met, that would increase the latter effect, by providing a stronger slope on the wave side.

Results from Fig. V.19 are obtained by displacing the initial/final position of the vehicle forward, relative to the wave, rather than at the crest. It allows the vehicle to spend a greater fraction of the trajectory in the location of local wind updraft. It shows that both the

required wind strength and the wind-related amplitude are lowered. Besides, as losses during the lower turn are decreased, the vehicle does not need to climb as much as before, and the maximal height reduces from 20 metres down to 15 metres and lower, in better accordance with on-the-field observations of albatrosses [41].

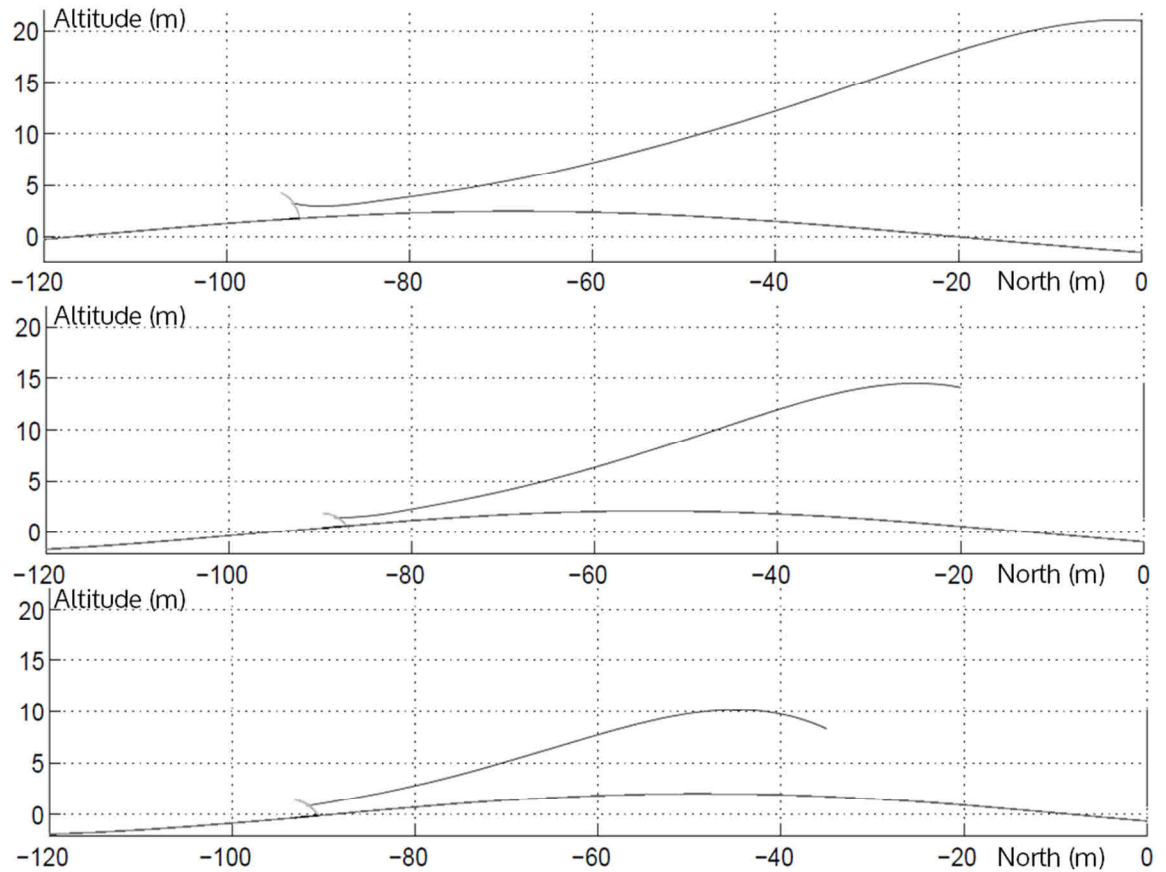


Figure V.19: From top to bottom, change in periodicity with respect to the wave.

$$\{a \text{ (m)}; u_s \text{ (m/s)}\} = \{2.46; 0.57\}; \{2.25; 0.53\}; \{2.05; 0.51\}$$

Even though the required wind strength is lowered to about 12.8 m/s for the bottom case of Fig. V.19, this is still rather high compared to what can be expected, such that those albatross flight simulations still lack realism somehow. A combination of rougher wave surface and deeper waves is probably the link to that ideal. In particular, waves of smaller scale, but of slope stronger than the swell wave taken into account in the framework of this study, could be significant for albatross flight. Further aerodynamic effects, like flow separation on the leeward side of the wave, have been suggested to be exploited by albatrosses [41]. Such induced energy-harvesting strategies are quite far down the path of UAV capabilities and have not been considered in the framework of this thesis. Besides, ground effect could also have a beneficial

influence energy-wise, since it would improve the gliding performance of the vehicle when it is close to the surface.

To sum-up, environment model refinements were integrated into the DS simulation model and their influence has been analysed. Although the presence of wave was investigated for the sake of general understanding, exploiting those is beyond the current capabilities of UAVs. However, it is useful to have a model of the ocean roughness length at disposal and quite fundamental to keep in mind that sea-surface roughness lengths are well below the centimetre, which may hamper the feasibility to exploit DS over oceans.

V.5 Summary of Chapter V

The basic characteristics of DS flight are explicated by using a specific closed-trajectory as a support. It is laid out that every trajectory can be decomposed into four phases, although their amplitudes may vary, depending on the periodicity constraints that apply to the trajectory. From an earth point of view, energy is gained by the vehicle in all phases of flight, but the lower turn into the wind, close to the surface.

The way energy transfers occur is detailed and the prevailing role of the lift is explained graphically and analysed analytically. It is responsible for the biggest increase in energy during the higher turn but is also accountable for the significant loss during the lower turn. By working on the expression of the power from aerodynamic forces, it is laid out that the drag can have a component that provides positive work, which is part of a wider resultant force oriented in the wind direction.

Although the overall pattern varies with the trajectory, depending on periodicity constraints, it appears that the vehicle attitude towards the air remains roughly unchanged, in particular the attitude “belly to the wind” at the top of the curve, which has been described in the flight of albatrosses.

Finally, the simulation of DS is enriched by a refined roughness length model and then by the presence of waves, where the wave amplitude is increased step by step until it corresponds to the prediction of the model. A particularity concerns periodicity constraints, which are established with respect to the wave and not to earth anymore. The roughness length predicted by the model considered is significantly lower than what is used in the DS literature. The required wind strength obtained for the *Wandering Albatross* is rather high compared to values that could be expected from biology input, even though the constraint of ground clearance is set to the minimum. The wave allows for DS flight at lower winds, since the vehicle takes advantage of the updraft created on the forward moving face, during its lower turn at the vicinity of the rising wave surface. By displacing the initial position of the vehicle, relative to the wave, from the crest to further down the wave slope, the vehicle benefits from a higher updraft and this lowers again the wind strength required. Yet, the wind strength obtained is still rather above values measured on the field, which suggests that albatrosses exploit mechanisms that are not represented by the current model.

CHAPTER VI

NON-DIMENSIONALIZATION OF DS FLIGHT

The chapter aims at presenting a different approach to gain understanding about DS principles, which is more mathematical and equation-focused. The understanding about DS laid out so far is based on simulations where the analysis of results is rather distant from that of EoM. This can be explained by the fact that multiple solutions exist and that therefore EoM are not sufficient to define the problem and its solution. Yet, the analysis of equations could permit to disclose some remarkable properties about DS. Besides, simulations obtained so far are dependent on the metric used for each variable, such that it is difficult to link ties between one simulation and another. There is hence an interest in considering equations and analysing simulations through a new system of dimensionless variables. Air relative equations are more adequate for this approach as the airspeed is directly a state variable. The associate set of EoM is dimensionless using specific reference variables. Simulations are then run, by using the unchanged methodology described earlier to support the theoretical analysis of a dimensionless set of different equations. Results validate both the non-dimensionalization and the simulation methodology, if necessary, as well as highlight interesting features about DS.

VI.1 Linear Wind Profile

VI.1.1 Theory

A first objective is to find an adequate non-dimensionalization of EoM so as to highlight some dimensionless coefficients formed from environment and vehicle parameters. Eventually, such coefficients would govern dimensionless solutions of EoM as well as DS performance, hence shedding a new light on the understanding of DS.

EoM are dimensionless by introducing some reference parameters, which could very well be arbitrary chosen, but would rather be selected such that equations can be simplified by gathering parameters into dimensionless coefficients. For the sake of simplicity, a linear wind gradient profile will be selected first, where β represents the wind gradient (s^{-1}), as introduced

in Eq. VI.1. It is to be reminded that in the present case, the wind is coming from x , β is positive and z is oriented downwards.

$$W_x = \beta z \quad (\text{VI.1})$$

In the particular case of a linear wind profile, both the local mean wind speed and the local wind gradient are determined by β . From the set of air relative EoM, given in Eqs. IV.35 to IV.40, the following non-dimensionalization can be defined [49].

$$\bar{V}_a = \frac{\beta}{g} V_a \quad (\text{VI.2})$$

$$(\bar{x}, \bar{y}, \bar{z}) = \frac{\beta^2}{g} (x, y, z) \quad (\text{VI.3})$$

$$\bar{t} = \beta t \quad (\text{VI.4})$$

$$\bar{F} = \frac{F}{mg} \quad (\text{VI.5})$$

For any given variable X , the accentuation \bar{X} refers to the associated dimensionless variable, while X_c refers to the associated reference value, such that:

$$\bar{X} = \frac{X}{X_c} \quad (\text{VI.6})$$

Besides, the notation X' refers to the dimensionless-time derivative of variable X .

$$X' = \frac{dX}{d\bar{t}} = t_c \frac{dX}{dt} \quad (\text{VI.7})$$

EoM are thus dimensionless as presented in Eq. VI.8.

$$\bar{V}_a' = -\bar{\rho} \bar{V}_a C_D(C_L) - \sin \gamma_a + \bar{V}_a \sin \gamma_a \cos \gamma_a \cos \psi_a \quad (\text{VI.8})$$

$$\psi_a' = \bar{\rho} \bar{V}_a C_L \frac{\sin \phi}{\cos \gamma_a} - \tan \gamma_a \sin \psi_a \quad (\text{VI.9})$$

$$\gamma_a' = \bar{\rho} \bar{V}_a C_L \cos \phi - \frac{\cos \gamma_a}{\bar{V}_a} - \cos \psi_a \sin^2 \psi_a \quad (\text{VI.10})$$

$$\bar{x}' = \bar{V}_a \cos \gamma_a \cos \psi_a + \bar{z} \quad (\text{VI.11})$$

$$\bar{y}' = \bar{V}_a \cos \gamma_a \sin \psi_a \quad (\text{VI.12})$$

$$\bar{z}' = -\bar{V}_a \sin \gamma_a \quad (\text{VI.13})$$

The dimensionless parameter $\bar{\rho}$ is defined in Eq. VI. 14

$$\bar{\rho} = \frac{\rho g^2}{2 (mg/S) \beta^2} \quad (\text{VI.14})$$

It is to be mentioned that before the non-dimensionalization, control variables are already represented by dimensionless values, which are the lift coefficient C_L and the bank angle ϕ .

Air relative standard EoM and reduced Eqs. VI.8 to VI.13 represent the same physics, but observed with different norms and therefore using differently weighted variables. It is to be noted that those equations are not specific to DS flight, but simply describe any in-flight evolution of a vehicle, within a linear wind profile. In Eqs. VI.8 to VI.13, the dimensionless parameter $\bar{\rho}$ is amongst the only parameters, together with $C_{D0}, C_{D1}, C_{D2}, C_{D3}, C_{D4}$ to influence equations.

From Eqs. VI.8 to VI.13, it can be learnt that if two vehicles are in similar state in terms of dimensionless variables, at a given instant, if the $\bar{\rho}$ parameter is identical between the two systems and if control variables follow the same evolution over dimensionless time, then the two system would evolve from that instant with the same dimensionless states.

Two sets of equations would be called equivalent if they can be dimensionless into the same form. Comparisons between coefficients, from the dimensionless equations, then serve as a standard to assert if the sets are equivalent or not. In the above case, two sets of air

relative EoM would be equivalent if, and only if, the two respective $\bar{\rho}$ parameters in Eqs. VI.8 to VI.13 are equals (assuming $C_{D0}, C_{D1}, C_{D2}, C_{D3}, C_{D4}$ are identical). In this regard, if m, ρ, S and β vary such that $\bar{\rho}$ is constant, then equations would be equivalent.

Besides, two solutions would be called equivalent if the respective dimensionless state variables follow identical sequences over dimensionless time. In the scope of the present work, solutions are not entirely determined by EoM, but also show a dependency on control variables. Consequently, two equivalent sets of EoM don't necessarily lead to two equivalent solutions since the evolution of control variables could differ between the two. Further conditions are required in order to yield equivalent solutions.

VI.1.2 Dimensionless Optimization Problem

Essentially, a non-dimensionalization process focuses on rewriting equations in order to highlight similarities between solutions without solving equations. Because in the present case solutions are not entirely determined by equations, broader aspects of the problem must be considered as part of the non-dimensionalization.

Solutions consist in sets of control variables and correlated state variables. Those are determined by solving an optimization problem, which is formed by an objective function and a set of constraints, including EoM, dimensionless or not. State variables are correlated to control variables through EoM, control variables are piloted in order to satisfy best the objective function and both state and control variables abide by further constraints.

In order to draw similarities between solutions, the focus should not be only on invariances among dimensionless coefficients of dimensionless EoM, but also within constraints and objective, as seen by dimensionless variables. For instance, the ground clearance is simplified to a minimum altitude, through the constraint expressed in Eq. VI.15.

$$z \leq z_{max} \quad (\text{VI.15})$$

By introducing the reference length z_c , the constraint is tweaked to Eq. VI.16.

$$\bar{z} \leq \frac{z_{max}}{z_c} \quad (\text{VI.16})$$

If the minimum altitude $-z_{max}$ is kept constant, the above constraint on the dimensionless height \bar{z} is different with every varying reference length z_c , leading to a different optimization problem and therefore to different solutions. Hence, for dimensionless solutions to be identical, the minimal altitude must be adapted such that it remains the same proportion of the reference length.

If two optimization problems show identical dimensionless constraints, including EoM, and objective, then they will trivially lead to equivalent solutions. In the scope of the present part, the equations that are passed to the solver are earth-relative EoM, described in Eqs. IV.23 to IV.28. Even though this set of equations is practically used to yield solutions, its parameters and constraints would be carefully adjusted so that the underlying optimization problem would be equivalent as if it was expressed through Eqs. VI.8 to VI.13.

VI.1.3 Simulation with Identical Wing Loading

The non-dimensionalization introduced above is tested using a linear wind profile [49], for different objective functions. The vehicle chosen for this part is *Mariner*, described in Table III-1, but different values of mass and wing area are applied. The aspect ratio is left unchanged and it is assumed, for the sake of this study, that aerodynamic coefficients $C_{D0}, C_{D1}, C_{D2}, C_{D3}, C_{D4}$ are unaltered by changes in mass and wing area. Besides, none of the associated rate constraints is applied in the following simulations, in order not to burden the optimization problem with varying dimensionless constraints.

First, the objective is to minimize the wind gradient β , which in this case is equivalent to minimizing the wind strength at a given height. The vehicle mass and wing area were varied by keeping an arbitrary constant wing loading of 141.6 N/m^2 , corresponding to a mass of 7 kg for *Mariner*.

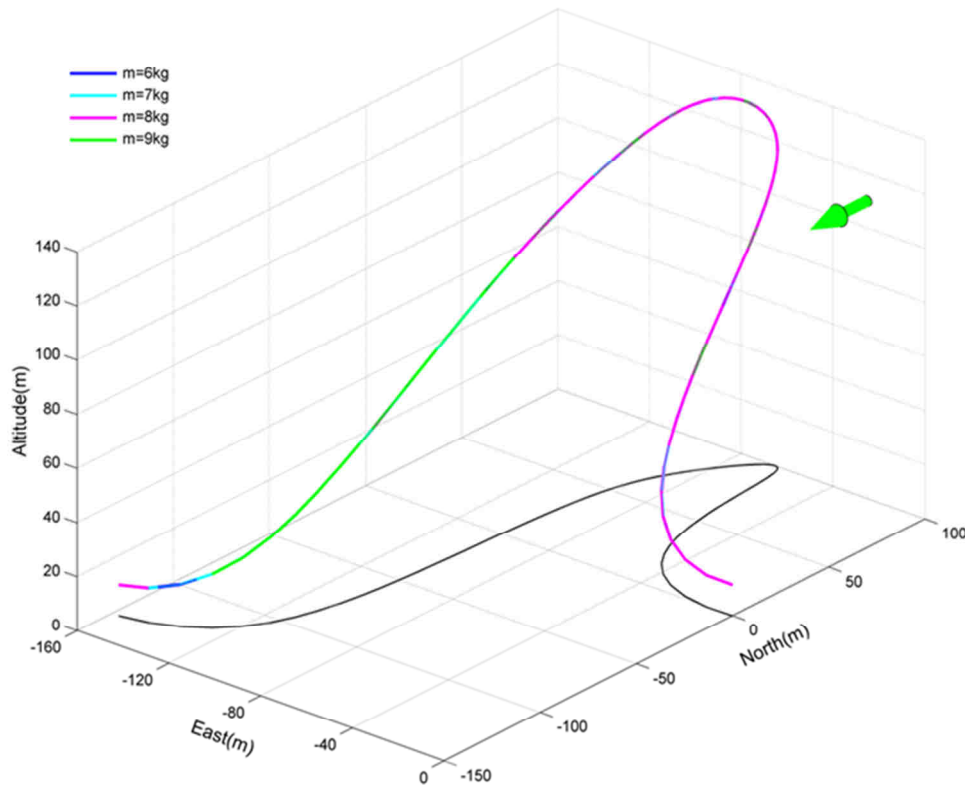


Figure VI.1: Optimal open-loop trajectories, minimizing the required wind gradient β , obtained for four vehicle mass, at the same wing loading. For all cases, the wing loading is 141.6 N/m^2 , the wind gradient is $\beta = 0.1076 \text{ s}^{-1}$ and $\bar{\rho} = 35.93$.

Identical wind gradient β of 0.1076 s^{-1} as well as identical solutions are obtained and it can be seen from Fig. VI.1 that all curves are superimposed. A remarkable result is that the corresponding wind strength at 10 metres, or more generally the required variation in horizontal wind strength over 10 metres height, is only 1.08 m.s^{-1} . Such conditions of wind shear do not seem very demanding and may widen the scope of potential DS application.

In the present case, β was set free for the solver to run on it which is tantamount to letting the solver choose $\bar{\rho}$ and alter the set of EoM it will also derive solutions from. Unsurprisingly, in accordance with what could be expected out of dimensionless Eqs. VI.8 to VI.13, the solver came out with the same value of $\bar{\rho}$, and therefore in wind gradient β , since all wing loadings are equivalent. What can be concluded out of this first simulation is that, in the case of a linear wind profile, the wing loading is a parameter of equivalence, which means that if two vehicles, with the same aerodynamic polar, have identical wing loadings, then they would perform identically by DS. Equations and simulations predict this result in accordance.

VI.1.4 Simulation with Various Wing Loadings

Different wing loadings are subsequently tested with the same objective function as before, which is to minimize the wind strength required to fly by DS. In results to follow, the vehicle has a fixed wing area S of 0.485 m^2 and the vehicle mass is changed, hence corresponding to a realistic operational case where the same vehicle platform is used to carry different loads. Solutions are expected to be different this time.

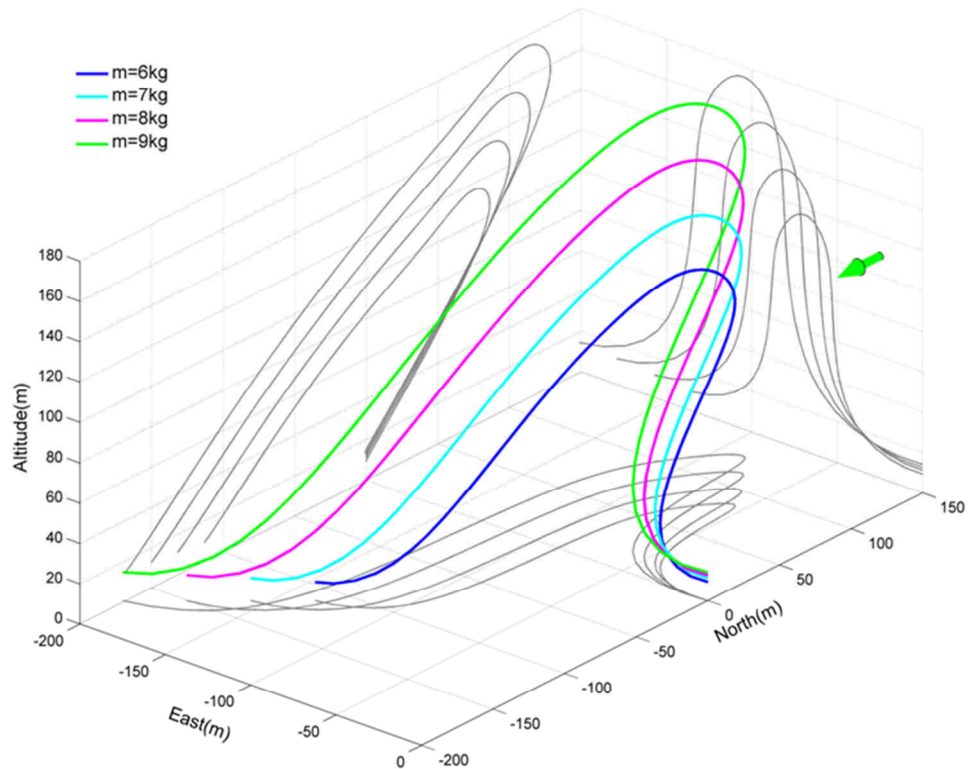


Figure VI.2: Optimal open-loop trajectories, minimizing the required wind gradient β , obtained for four vehicle mass, at the same wing area. For all cases, $\bar{\rho} = 35.93 \pm 0.02$.

It appears from Fig. VI.2 that flight paths are regularly spaced such that they seem to be results of a proportional transformation. The light blue curve corresponds to trajectories obtained before with constant wing loading, presented in Fig. VI.1. The higher mass goes with a bigger amplitude of flight. Further data are summed up in Table VI-1.

Table VI-1: Parameters about solutions displayed in Fig. VI.2.

Mass	$\frac{mg}{S}$ (N/m^2)	β (s^{-1})	$\bar{\rho}$	$-z_{max}$ (m)	$-\overline{z_{max}}$	t_f (s)
6 kg	121.36	0.1163	35.903	9.521	0.0131	14.55
7 kg	141.59	0.1076	35.929	11.384	0.0134	15.69
8 kg	161.81	0.1007	35.938	12.843	0.0133	16.77
9 kg	182.04	0.0949	35.945	14.265	0.0129	17.79

As expected, the wind gradient β was different for each wing loading and is actually getting higher for low wing loadings. Hence, for the same vehicle planform, although the energy required to maintain a heavier load in the air is higher by definition, the wind strength required to fly it by DS is actually lower. This should not conceal that the heavier vehicle still climbs higher to benefit from stronger winds. High wing loadings therefore enable the vehicle to take advantage of less favourable wind conditions.

Another important consideration is that the solver comes up with values of β between the different cases, which entail identical values for $\bar{\rho}$. The maximum relative disparity for $\bar{\rho}$ is of the order of 0.1 %. Small variations like this can be explained by the use of a constant number of time discretization nodes $N_t = 71$, while the total time of cycle is increasing from 14.55 seconds to 17.79 seconds, hence inducing varying time step length and different integration error.

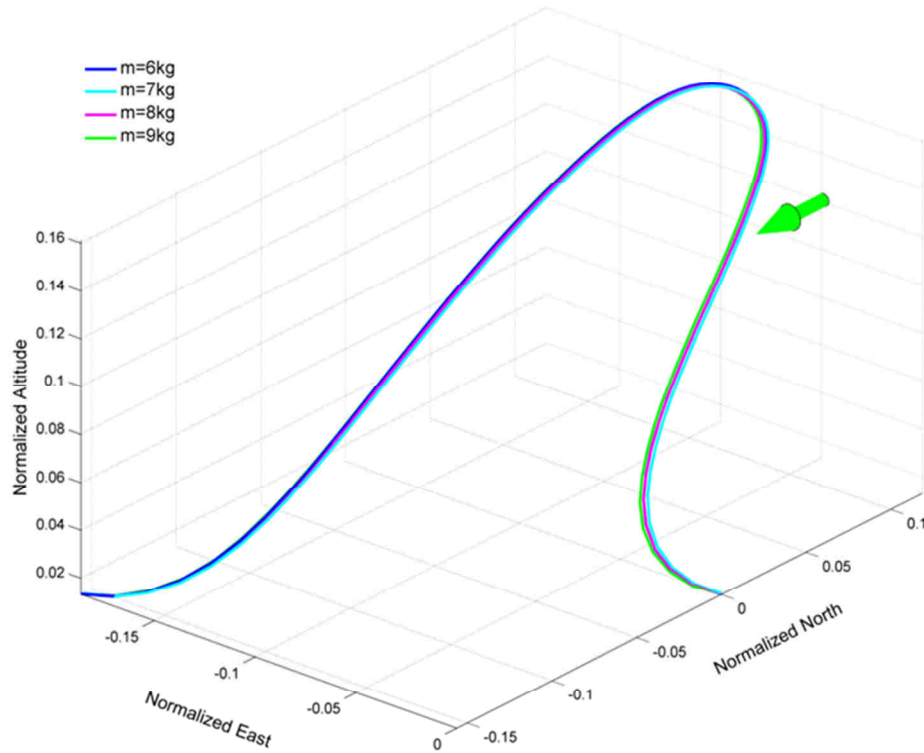


Figure VI.3: Three dimensional curves, plotted in dimensionless coordinates, obtained by minimizing the required wind gradient β , for four vehicle mass, at the same wing area. For all cases, $\bar{\rho} = 35.93 \pm 0.02$

Consequently, for a given vehicle with varying wing loading, the optimization selects β such that it sets equivalent dimensionless EoM for the vehicle. Indeed, Eqs. VI.8 to VI.13 are identical between cases run here, leading to similar dimensionless solutions, as plotted in Fig. VI.3. The overall parameter which is ultimately modified by the solver within that process is $\bar{\rho}$, whom we know from the non-dimensionalization analysis that it is the only parameter that defines dimensionless EoM. In this regard, $\bar{\rho}$ can be considered as a benchmark of DS performance. The value of $\bar{\rho}$ obtained actually represents the maximal value that allows the vehicle to fly effortlessly by taking advantage of the wind. For lower values of $\bar{\rho}$, conditions are more favourable and allow extra energy-harvesting. For higher values of $\bar{\rho}$, conditions become adverse and some extra energy is required from the vehicle to complete the cycle. The critical value of this parameter is actually a function of the only other varying parameters of dimensionless EoM, which are the drag coefficients $C_{D0}, C_{D1}, C_{D2}, C_{D3}, C_{D4}$ that defines the aerodynamic polar. A higher value of $\bar{\rho}$ would be obtained with a vehicle that drags less over the range of C_L travelled along the path, hence allowing DS flight in more adverse conditions.

It can be seen from Figs. VI.3 and VI.4, that the dimensionless variables match in such a way that the three dimensional curve of dimensionless coordinates are well superimposed. The order of magnitude of the maximum relative disparity is below 5 % and it can also be attributed to significant variations in time step length. It can be fairly concluded that solutions are all equivalent.

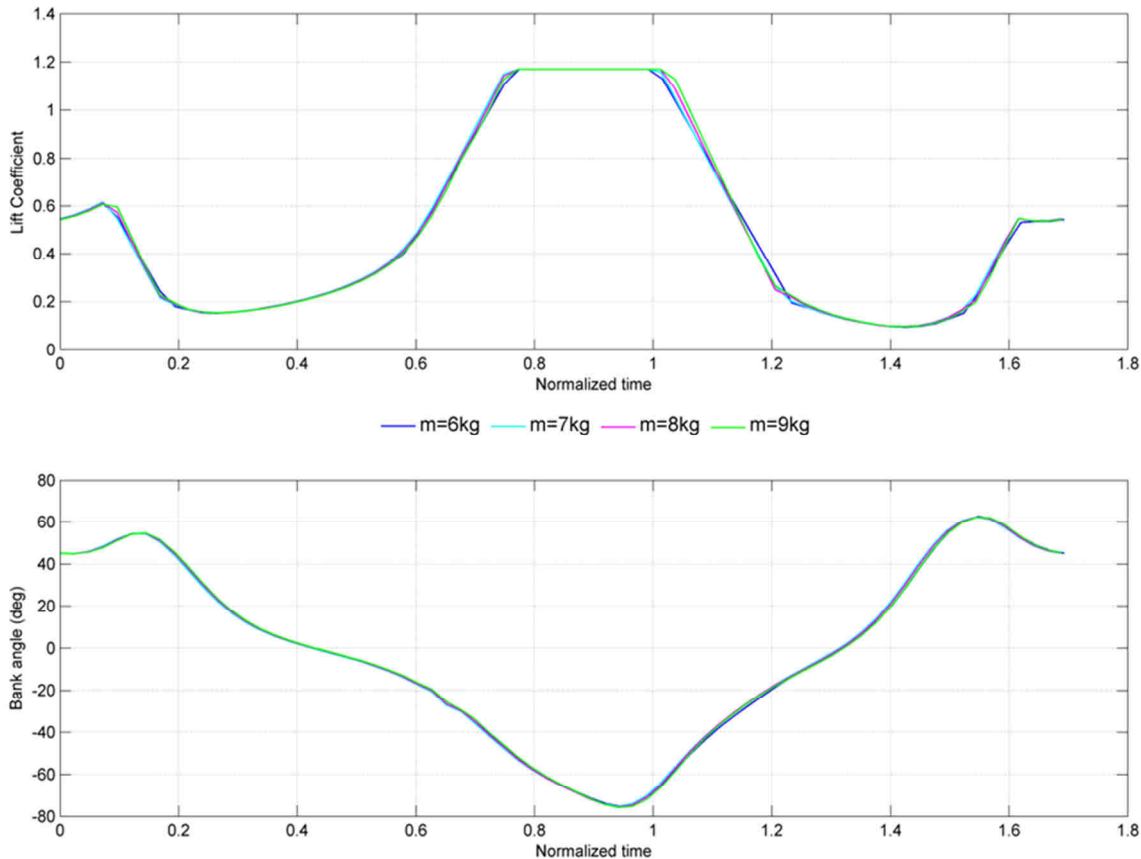


Figure VI.4: Evolution of control variables over dimensionless time, obtained by minimizing the required wind gradient β , for four vehicle mass, at the same wing area. For all cases, $\bar{\rho} = 35.93 \pm 0.02$.

One can observe from Table VI-1 that even though the lowest curve is reached by the lower wing loading case, its minimum altitude is still 9.5 metres above ground, while the ground clearance was much less restrictive and constrained in this case to a fixed minimum altitude of 1.7 metres, for all cases. Consequently, even though the optimization problem includes non-equivalent constraints as seen from dimensionless variables, variables do not reach the limit value and solutions are still equivalent to each other. It shows that non-equivalent constraints do not matter on the equivalence of solutions if those are not reached during the optimization.

Figure VI.4 shows a good match between control variables. The flattened part of the C_L curve corresponds to the lift coefficient reaching the maximum as stated in the “no stall” constraint. This constraint is equivalent to every dimensionless optimization problem since the coefficient of lift is dimensionless.

Consequently, it can first be learnt that, in the case of a linear wind profile, increasing the wing loading reduces the required wind gradient β . Besides, the evolution of β with the wing loading is such that the dimensionless parameter $\bar{\rho}$ remains the same. It can be interpreted as a benchmark of DS performance, depending only on the aerodynamic performances of the vehicle. Higher values of $\bar{\rho}$ can be associated with adverse conditions, more challenging for a vehicle to exploit. Therefore, refined aerodynamics for the vehicle would entail a higher value of $\bar{\rho}$ found by the solver for the problem of minimizing the wind gradient required. Besides, despite variations in β , the equivalence between dimensionless sets of EoM, representative of the different wing loading cases, provides equivalent sets of dimensionless solutions. It shows that, in the case of a linear wind profile, variations in the wind gradient required to sustain different wind loadings can be predicted by the theory. Furthermore, the non-dimensionalization approach is successful in the way that it highlights a dimensionless parameter which characterizes the equivalence between DS cases.

VI.2 Logarithmic Wind Profile

VI.2.1 Non-dimensionalization of EoM

The EoM governing the vehicle evolution within a logarithmic wind profile depart from the linear wind profile as the local wind gradient becomes a function of altitude and the local wind strength a function of roughness length. For a logarithmic profile, the local increase in horizontal wind with altitude, or local wind gradient is expressed is reminded in Eq. VI.17.

$$\frac{\partial W_x}{\partial z} = \frac{u_*}{\chi} \frac{1}{z} \quad (\text{VI.17})$$

As it was underlined in Chapter III, an important remark is that the local wind gradient is independent from the roughness length. Air relative EoM are developed in Eqs. VI.18 to VI.23.

$$m\dot{V}_a = -\frac{1}{2}\rho SC_D V_a^2 - mg \sin \gamma_a - m \frac{u_* V_a}{\chi z} \sin \gamma_a \cos \gamma_a \cos \psi_a \quad (\text{VI.18})$$

$$mV_a \cos \gamma_a \dot{\psi}_a = \frac{1}{2}\rho SC_L V_a^2 \sin \phi + m \frac{u_* V_a}{\chi z} \sin \gamma_a \sin \psi_a \quad (\text{VI.19})$$

$$-mV_a \dot{\gamma}_a = -\frac{1}{2}\rho SC_L V_a^2 \cos \phi + mg \cos \gamma_a - m \frac{u_* V_a}{\chi z} \cos \psi_a \sin^2 \gamma_a \quad (\text{VI.20})$$

$$\dot{x} = V_a \cos \gamma_a \cos \psi_a - \frac{u_*}{\chi} \log \left(\frac{-z}{z_0} \right) \quad (\text{VI.21})$$

$$\dot{y} = V_a \cos \gamma_a \sin \psi_a \quad (\text{VI.22})$$

$$\dot{z} = -V_a \sin \gamma_a \quad (\text{VI.23})$$

A significant departure from the linear wind profile equations is that the airspeed evolution becomes sensible to the altitude, as seen in Eq.VI.18. It can be physically linked to the consideration that the airspeed increase due to the wind gradient is not uniform anymore, but depends indeed on the altitude. Besides, the altitude also alters to ability of the vehicle to deviate both its air relative flight path and heading. An important note is that none of the air relative variable is directly affected by the surface roughness length, such that the air relative kinematics is therefore unrelated to the surface state. Only the absolute horizontal earth coordinate directed along the wind direction sees a dependence on the roughness length, in Eq. VI.21, since the vehicle is carried along the wind direction at a speed that depends on surface interactions.

The principle of establishing the non-dimensionalization based on the wind gradient proved successful for the linear wind profile. Therefore, a characteristic wind gradient of the wind profile would be sought to serve as an equivalent reference for the non-dimensionalization. As the local wind gradient depends on altitude, any given characteristic gradient could be associated with a local wind gradient at a certain height. The characteristic gradient β_c is defined to be the local gradient at an altitude corresponding to the reference height z_c , as in Eq. VI.24.

$$\beta_c = \frac{u_*}{\chi} \frac{1}{z_c} \quad (\text{VI.24})$$

Further properties about reference parameters are the same as the linear wind profile non-dimensionalization. Those are summed up in Eqs. VI.25 to VI.27.

$$t_c = \frac{1}{\beta_c} \quad (\text{VI.25})$$

$$V_c = \frac{g}{\beta_c} \quad (\text{VI.26})$$

$$z_c = V_c t_c \quad (\text{VI.27})$$

It gives the following values for reference parameters.

$$\beta_c = \frac{g \chi}{u_*} \quad (\text{VI.28})$$

$$t_c = \frac{u_*}{g \chi} \quad (\text{VI.29})$$

$$V_c = \frac{u_*}{\chi} \quad (\text{VI.30})$$

$$z_c = \frac{1}{g} \left(\frac{u_*}{\chi} \right)^2 \quad (\text{VI.31})$$

It entails the following non-dimensionalization of air relative EoM, described in Eqs. VI.32 to VI.37.

$$\bar{V}_a' = -\bar{\rho} \bar{V}_a C_D(C_L) - \sin \gamma_a - \frac{\bar{V}_a}{\bar{z}} \sin \gamma_a \cos \gamma_a \cos \psi_a \quad (\text{VI.32})$$

$$\psi_a' = \bar{\rho} \bar{V}_a C_L \frac{\sin \phi}{\cos \gamma_a} + \frac{1}{\bar{z}} \tan \gamma_a \sin \psi_a \quad (\text{VI.33})$$

$$\gamma_a' = \bar{\rho} \bar{V}_a C_L \cos \phi - \frac{\cos \gamma_a}{\bar{V}_a} + \frac{1}{\bar{z}} \cos \psi_a \sin^2 \psi_a \quad (\text{VI.34})$$

$$\bar{x}' = \bar{V}_a \cos \gamma_a \cos \psi_a - \log \left(\frac{-\bar{z} z_c}{z_0} \right) \quad (\text{VI.35})$$

$$\bar{y}' = \bar{V}_a \cos \gamma_a \sin \psi_a \quad (\text{VI.36})$$

$$\bar{z}' = -\bar{V}_a \sin \gamma_a \quad (\text{VI.37})$$

The expression of $\bar{\rho}$ includes the expression of the characteristic gradient.

$$\bar{\rho} = \frac{\rho g^2}{2 (mg/S) \beta_c^2} \quad (\text{VI.38})$$

Sets of Eqs. VI.32 to VI.34 would be equivalent if parameters $\bar{\rho}$ are equal. Sets of Eqs. VI.36 and VI.37 would be equivalent in any case. However, for two equations Eq. VI.35 to be equivalent to each other, it requires the condition expressed in Eq. VI.39 to be fulfilled.

$$\frac{z_0}{z_c} = \bar{z}_0 = \text{constant} \quad (\text{VI.39})$$

If the objective function of the optimization problem is to minimize the wind friction velocity u_* , whatever the net azimuth direction is, then the evolution of x does not come into play regarding any constraint nor the objective. The relation in Eq. VI.39 can therefore be ignored, the wind friction velocity obtained would be independent from the surface roughness length, albeit the local wind speed would depend on it. Consequently, all dimensionless variables but x would be comparable. Inversely, if the optimization problem refers to an objective or a constraint involving the variable x , then Eq. VI.35 influences the solution that the solver comes out with. Hence, Eq. VI.35 must be adapted, by validating the condition expressed in Eq. VI.39, such that the whole set of Eqs. VI.32 to VI.37 could lead to invariance in dimensionless solutions.

The same remark extends to the other constraints that would involve non dimensionless parameters, in particular the ground clearance constraint. Indeed, it has been observed that the vehicle tends to fly at the lowest possible altitude during the turn windward, in the case of logarithmic wind profiles. So on top of Eq. VI.39, another relation in Eq. VI.40 must be validated to ensure equivalent solutions.

$$\frac{z_{max}}{z_c} = \overline{z_{max}} = constant \quad (VI.40)$$

It is to be noted that Eq. VI.40 must be fulfilled in any case, while some optimization scenario can do without Eq. VI.39.

VI.2.2 Application with Identical Wing Loading

The sensitivity to mass is tested first, at a constant wing loading, for a problem which consists in minimizing the wind strength at a certain height, which is tantamount to minimizing the friction velocity. The vehicle mass and wing area were varied by keeping an arbitrary constant wing loading of 141.6 N/m^2 , corresponding to a mass of 7 kg for *Mariner*.

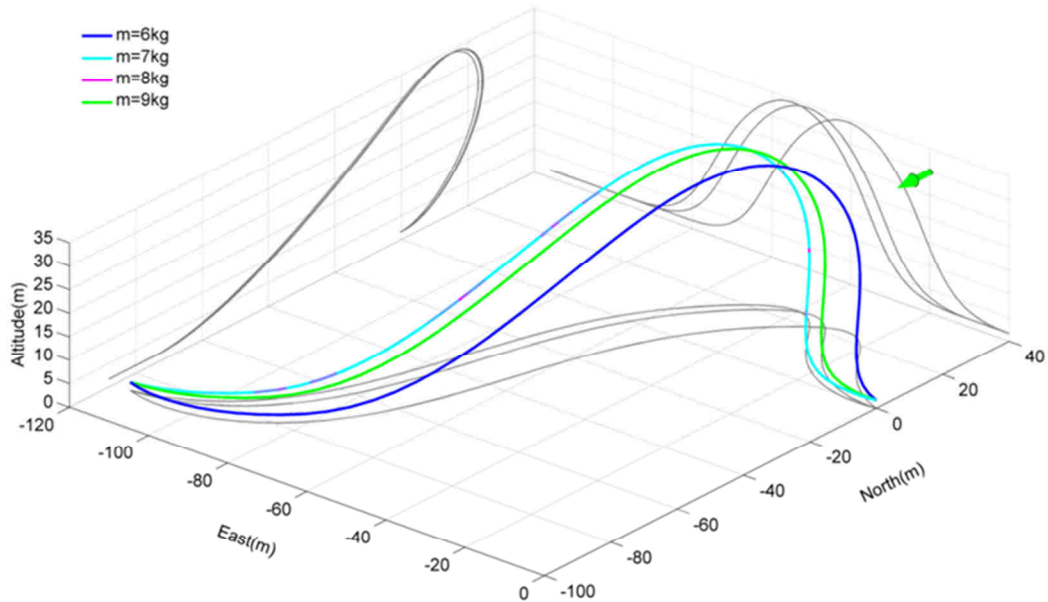


Figure VI.5: Optimal open-loop trajectories, minimizing the required friction velocity for various mass at a fixed wing loading of 141.6 N/m^2 . $\bar{\rho} = 0.0113$ for all cases, z_0 was unchanged at 3 cm .

A first remark is that the flight path obtained in Fig. VI.5 is fundamentally different to that corresponding to a linear profile, displayed in Fig. VI.1. Most significantly, the maximum altitude reached by the vehicle is about four times lower and the leeward turn is flattened at heights below 5 metres , while it never went under 10 metres in the case of a linear profile. It is to be mentioned that the wind strength at 10 metres height is 9.4 m.s^{-1} in the present case while it was only 1.08 m.s^{-1} in the case of linear wind profile. Those considerations confirm, if necessary, the predominant influence of the wind field on the overall DS trajectory and on the required wind strength.

Equations VI.32 to VI.37 suggests that trajectories should be invariant, since $\bar{\rho}$ would have the same value and this is verified with a constant value of 0.0113 for all cases, a characteristic wind gradient $\beta_C = 6.068 \text{ s}^{-1}$ and a reference length z_c of 0.2664 metres. The wind friction velocity obtained is 66.3 cm.s^{-1} and the roughness length was left untouched at 3 cm .

However, it can be observed that trajectories only match for 7 kg and 8 kg and that the other masses show significant altered trajectories. Those relative disparities would remain when comparing dimensionless coordinates, as the reference length is identical in the four cases. Those can be explained by the fact that state and control variables, which govern the evolution of the system over time, have sets that are equivalent to each other but with a time offset in some case. Indeed nothing constrains the solver to start from different parts of the cycle, as the overall solution is equivalent, with no influence on DS performances. The inner calculation process of optimization makes the solver choose a different starting point between cases. All variables, but horizontal coordinates, are governing the evolution of the system, as can be seen in Eqs. VI.32 to VI.37, and are therefore correlated by the same shift in time compared to another solution. Horizontal coordinates are set free to be piloted by equivalent sets of other variable, which leads to similar trajectories with a horizontal shift respectively to each other.

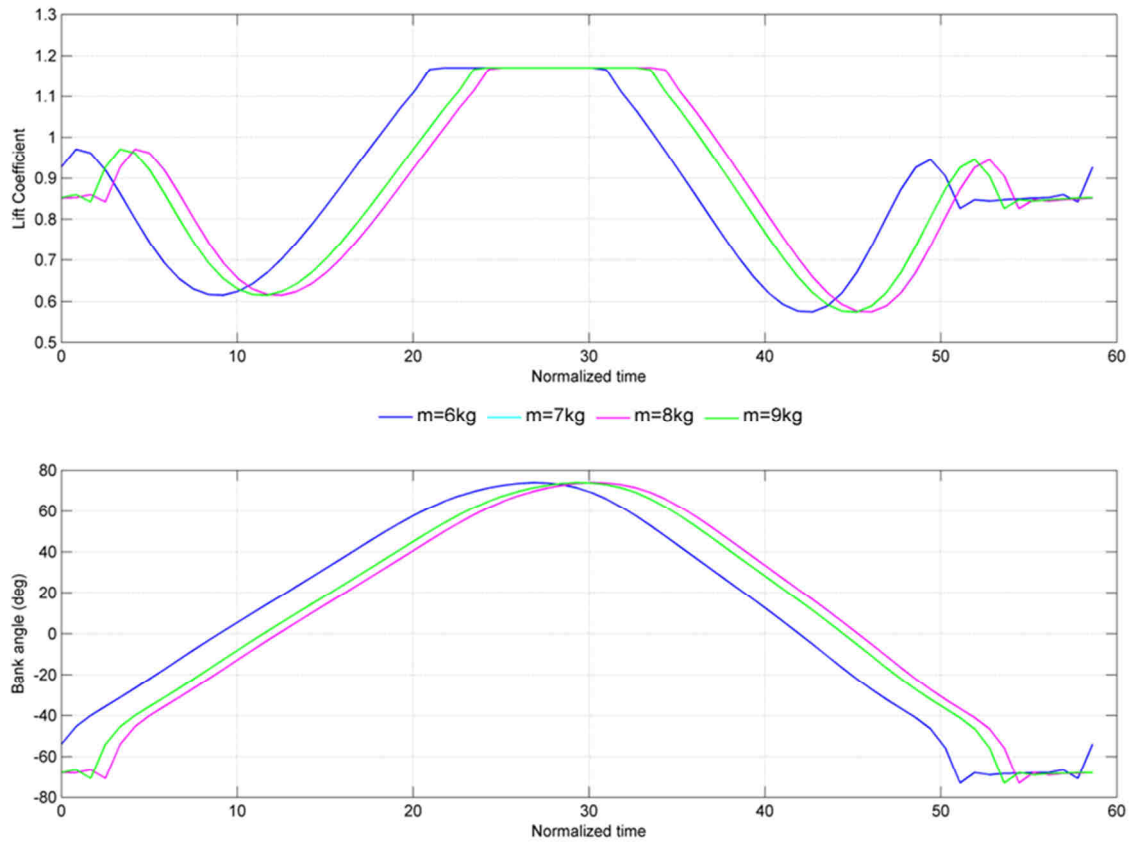


Figure VI.6: Evolution of control variables over dimensionless time, obtained by minimizing the required friction velocity, for various mass at a fixed wing loading of 141.6 N/m^2 . $\bar{\rho} = 0.0113$ for all cases.

Figure VI.6 shows the correlation between the evolution of the lift coefficient time and the evolution of the bank angle over time. The relative shift would be the same in time or in dimensionless time, given that the reference wind gradient is constant. Overall, DS within a logarithmic wind profile shows equivalent results for identical wing loadings.

VI.2.3 Application with Various Wing Loadings

For a fixed planform of *Mariner*, the mass is varied arbitrarily from 6 kg to 9 kg , which represents different wing loading cases. As it was underlined before, this indeed has an interest as it corresponds to an operational case of various loading for the same planform. Yet, this study is two-fold and also aims at highlighting a behaviour which could have been challenging to unlock without focusing on the non-dimensionalization of EoM. Thanks to this approach, the way the required wind strength relates to the wing loading can be anticipated theoretically, which it is being validated by means of simulations here. Besides, different wind strength are expected, leading to different dimensionless variables so the condition stipulated in Eq. VI.40 about adapting the minimum altitude comes into play. It means that in theory, simply changing

the wind strength is not sufficient to establish equivalent solutions for various wing loadings. None of the constraints expressed involve x , so there is in theory no need to adapt the roughness length as well, which was then unchanged at 3 cm . The methodology used here is to start with a baseline case and then adapt the minimum altitude imposed. Baseline conditions were a mass of 7 kg and a minimum altitude of 1.70 metres . No attention was paid to ground clearance conditions, meaning that the bank angle was not limited by wing tip clearance.

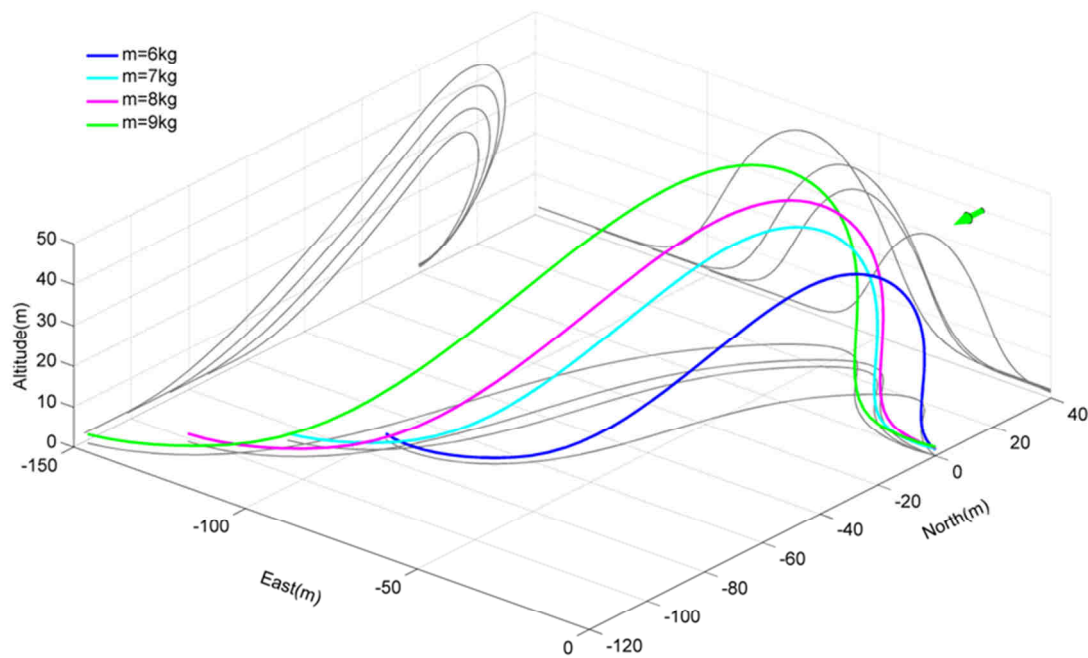


Figure VI.7: Three dimensional trajectories optimized to minimize the wind strength required, for different vehicle mass. $\bar{\rho} = 0.0113$ for all cases.

Some similarities can again be observed, in Fig. VI.7, between curves which seem to duplicate each other at a different scale. This is especially visible in the projected curves of trajectories in the *North-Altitude* plane. Just as in the case of a linear wind profile, the highest wing loadings correspond to greater amplitudes, reaching greater values in each coordinates. Table VI-2 gives some results about those solutions.

Table VI-2: Parameters about solutions displayed in Fig. VI.7.

Mass	$\frac{mg/S}{(N/m^2)}$	$\beta_c (s^{-1})$	$z_c (m)$	$V_c = \frac{u_*}{\chi}$ ($m.s^{-1}$)	$-z_{max} (m)$	$\bar{\rho}$
6 kg	121.36	6.5543	0.228	1.497	1.457	0.011306
7 kg	141.59	6.0681	0.266	1.617	1.700	0.011306
8 kg	161.81	5.6762	0.304	1.728	1.943	0.011306
9 kg	182.04	5.3516	0.343	1.833	2.186	0.011306

A first observation concerns the evolution of the required wind friction velocity with the wing loading. It is reminded that this evolution does not depend on the surface roughness length z_0 , which has however influences the wind speed required. When the wing loading increases, the required wind friction velocity increases with the square root of the wing loading (noted WL in the following expression), as detailed in the calculation detailed in Eq. VI.41.

$$\frac{[u_*]_{WL_2}}{[u_*]_{WL_1}} = \sqrt{WL_2/WL_1} \quad (VI.41)$$

This could be theoretically predicted by theory and can be verified from Table VI-2. In order to satisfy equivalence conditions, the minimum altitude is however raised when the mass increases such that the increase in wing loading alone cannot explain the increase in wind friction velocity. Identically to the case of a linear wind profile, the characteristic wind gradient β_c is adapted such that $\bar{\rho}$ gets a constant value which is necessary to get equivalent sets of EoM. Yet, in the case of the linear wind profile, the wind gradient was directly given by the physical model of the boundary layer that was taken into account. In the case of the log profile, it is a basically a parameter, directly function of u_* , which varies to ensure that sets of EoM are equivalent to each other. The fact that the characteristic gradient decreases when the wing loading increases, as it would in a linear wind profile case, teaches very few things about the physical properties of the boundary layer profile.

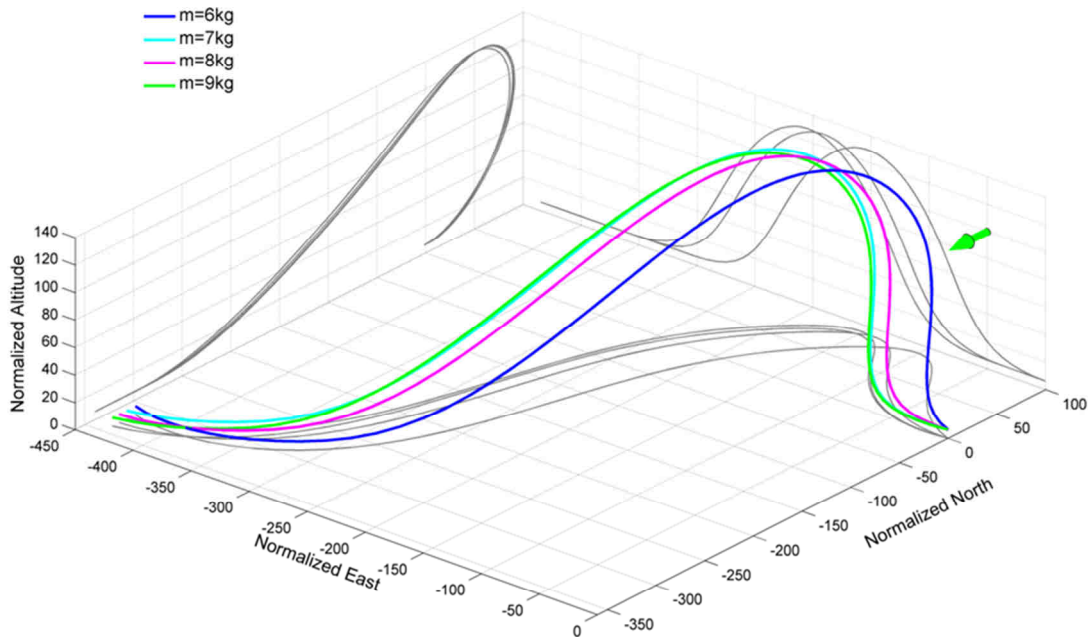


Figure VI.8: Three dimensional curves of dimensionless coordinates, representative of the evolution displayed in Fig. VI.7.

Figure VI.8 shows that despite the slight offset, curves in dimensionless coordinates match quite well. Along the \bar{x} coordinate (*Dimensionless North*), the offset that can be observed shows that the non-dimensionalization does not lead to an equivalent evolution. Indeed, the evolution of \bar{x} is a function of the roughness length, see Eq. VI.35, and the roughness length was not adapted for the dimensionless roughness length to be constant.

Control variables are all equivalent to evolutions displayed in Fig. VI.6. As a matter of fact, optimization problems were rendered equivalent, between cases, through the adjustment of constant $\bar{\rho}$ by the solver. Hence, sets of control variables were identical to the baseline case of $m=7\text{ kg}$, time shift aside. This result has a significant impact on the way DS trajectories could be piloted, since control variables could be identical for a wide range of cases corresponding to $\bar{\rho}$ constant.

VI.2.4 Non-dimensionalization of Thrust-Powered DS

The vehicle is able to propel itself via the thrust T , which adds to the control variables and modifies Eq. VI.32 in Eq. VI.42.

$$m\dot{V}_a = T - \frac{1}{2}\rho S C_D V_a^2 - mg \sin \gamma_a - m \frac{u_* V_a}{\chi z} \sin \gamma_a \cos \gamma_a \cos \psi_a \quad (\text{VI.42})$$

It can be dimensionless in the form specified by Eq. VI.43.

$$\bar{V}' = \bar{T} - \bar{\rho} \bar{V} C_D(C_L) - \sin \gamma_a + \frac{\bar{V}}{z} \sin \gamma_a \cos \gamma_a \cos \psi_a \quad (\text{VI.43})$$

The on board energetics is modelled through the battery state variable Bat , which varies due to the power expense from the propulsive system, which is governed by Eq. VI.44.

$$\dot{Bat} = -\frac{T V_a}{\eta_{prop}} \quad (\text{VI.44})$$

It can be reduced into the form expressed by Eq. VI.45, after the thrust is dimensionless by the weight mg .

$$\overline{Bat}' = -\frac{\bar{T} \bar{V}_a}{\eta_{prop}} \quad (\text{VI.45})$$

Another objective is tested for different wing loadings, but at constant $\bar{\rho}$, in order to find solutions that minimize the consumption per unit length travelled. In the case of DS flight, the length that is referred to is the horizontal net distance between the start and the end of the path. The consumption is expressed and dimensionless under $\overline{Co_s}$, in Eq. VI.46.

$$Co_s = -\frac{Bat_f}{\sqrt{x_f^2 + y_f^2}} = -mg \frac{\overline{Bat}_f}{\sqrt{\bar{x}_f^2 + \bar{y}_f^2}} = mg \overline{Co_s} \quad (\text{VI.46})$$

For a given mass, minimizing Co_s amounts to a minimum in dimensionless consumption $\overline{Co_s}$. The objective function is dependent on the final northbound position x_f which itself is a function of evolution of x . The surface roughness length must be adapted, in Eq. VI.39, so that the dimensionless roughness length is equivalent in each case.

In terms of methodology, the same baseline case is used, with a mass of 7 kg, a minimum altitude imposed at 1.70 metres and a surface roughness length of 3 cm. From results

obtained by minimizing the required friction velocity, u_* is then reduced. The lower wind strength requires some thrust from the vehicle to manage the full energy-neutral cycle, and the wind friction velocity is decreased step by step until $\overline{C_{O_s}}$ reaches an arbitrary value of 0.015 , without imposing any net heading. Then the same is applied for different masses, ranging from 6 kg to 9 kg . For each case, the minimum altitude and surface roughness length are adapted such that their respective dimensionless values are the same. Besides, u_* is manually adapted until $\overline{C_{O_s}}$ hits the 0.015 mark. The non-dimensionalization actually helps to predict what the friction velocity should be, by maintaining $\bar{\rho}$ the same, in order for optimization problems to be equivalent to each other.

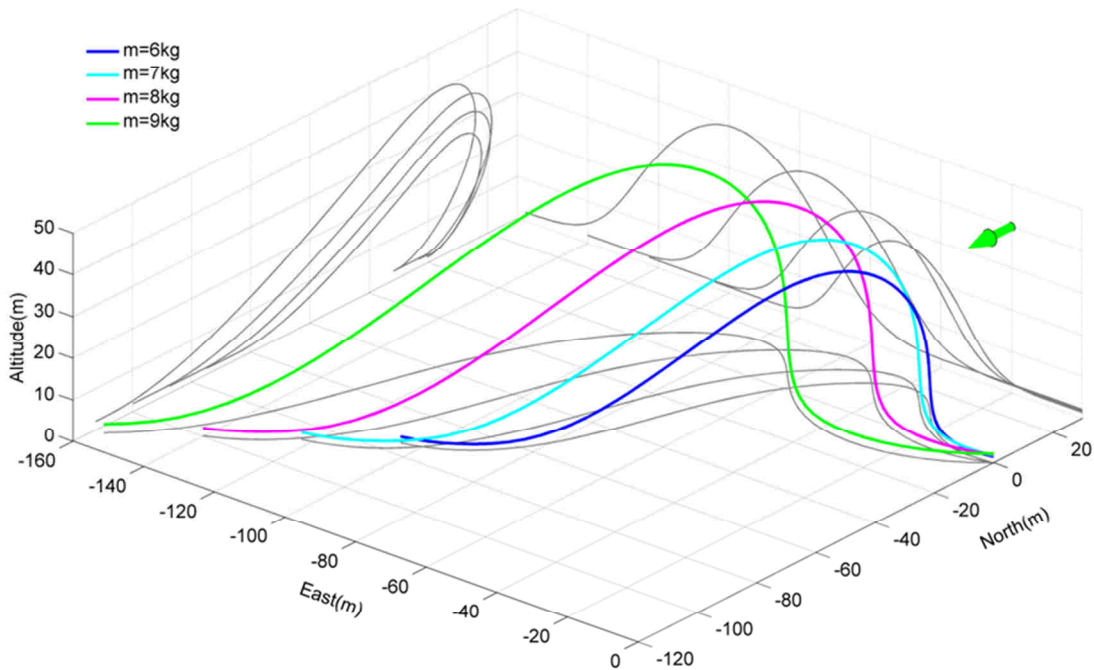
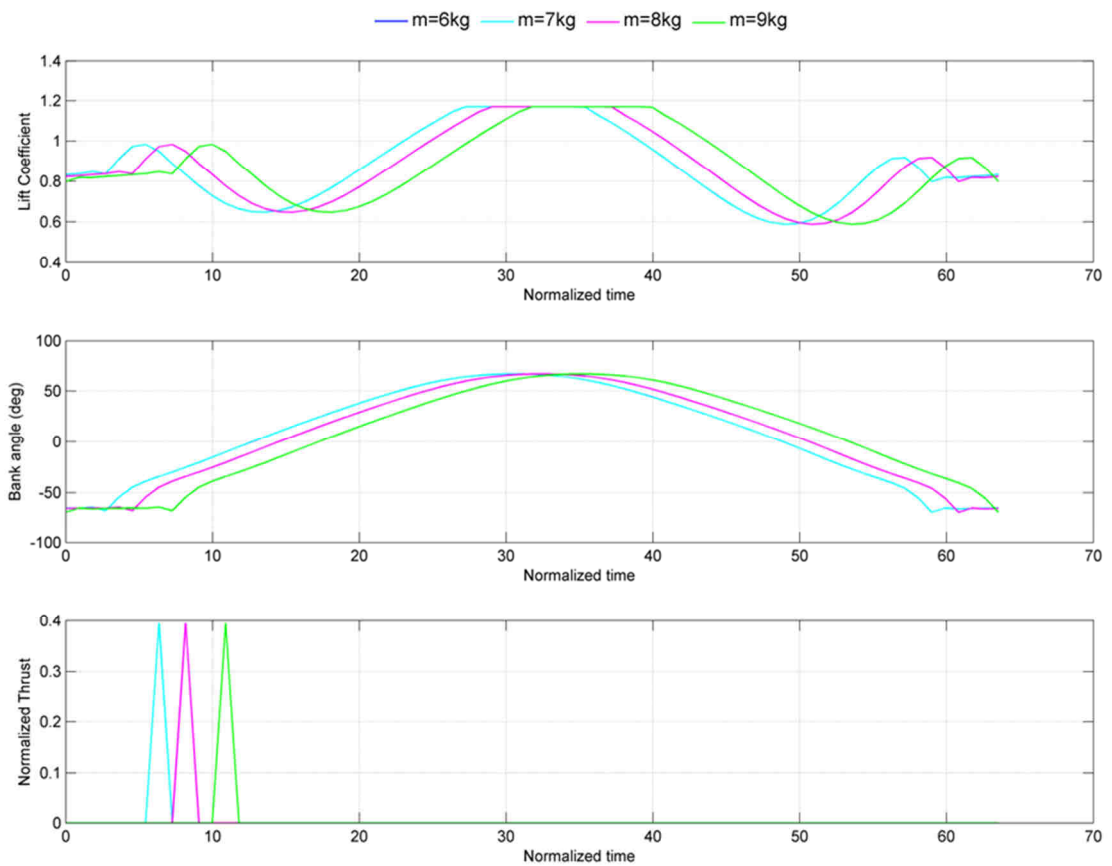


Figure VI.9: Three dimensional trajectories optimized to minimize $\overline{C_{O_s}}$, for different vehicle mass. $\overline{C_{O_s}} = 0.015$ and $\bar{\rho} = 0.00952$ for all cases.

Similarities between curves are of the same nature as observed before. Further results are summed up in Table VI-3.

Table VI-3: Parameters about solutions displayed in Fig. VI.9.

Mass	mg/S (N/m^2)	$\overline{C_{O_S}}$	$V_c = \frac{u_*}{\chi}$ ($m.s^{-1}$)	$-z_{max}$ (m)	z_0 (m)	$\bar{\rho}$
6 kg	121.36	0.015	1.373	1.457	0.0257	0.009518
7 kg	141.59	0.015	1.483	1.700	0.0300	0.009518
8 kg	161.81	0.015	1.586	1.943	0.0343	0.009518
9 kg	182.04	0.015	1.682	2.186	0.0386	0.009518

Figure VI.10: Evolution of dimensionless control variables over dimensionless time, for trajectories optimized to minimize $\overline{C_{O_S}}$ and for varying vehicle mass. $\overline{C_{O_S}} = 0.015$ and $\bar{\rho} = 0.00952$ for all cases.

The evolution of control variables is displayed in Fig. VI.10. The dimensionless thrust is pictured in order to highlight equivalences between solutions. For all cases, the contribution from the thrust is only an impulse, which is due to rate and double continuous constraints being ignored. Control variables are well correlated with a time shift between cases.

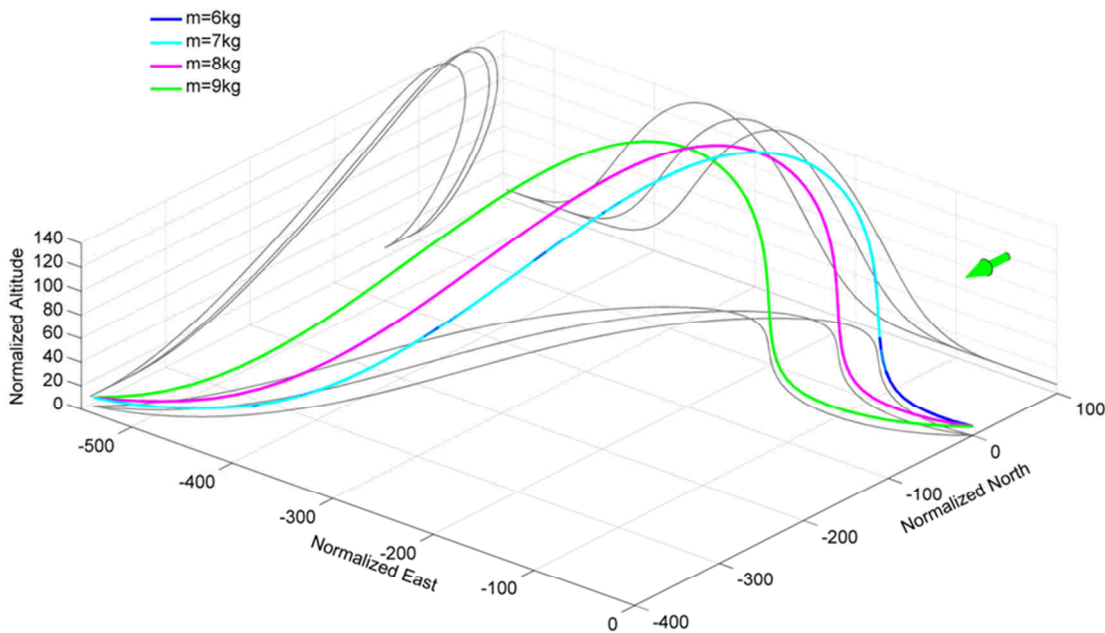


Figure VI.11: Three dimensional curves of dimensionless coordinates, corresponding to Fig. VI.9.

Higher wing loadings require a higher friction velocity in order to perform at a constant specific consumption, which is consistent with results obtained with a non-powered vehicle. Friction velocities obtained to get to the same $\overline{C_{O_s}}$ are also responsible for equal $\bar{\rho}$ between the four results, which validates the non-dimensionalization approach. In the present situation, the roughness length has also to be adapted in order to yield equivalent optimization problems. Simulation results highlight the equivalence predicted from the theory with great accuracy, as the four trajectories are all identical when seen from their dimensionless perspectives.

This final and refined comparison between simulations validates the approach undertaken to normalize the equations. Several test cases have been simulated, corresponding to different optimization problems. For each of those, simulations validated the similarities anticipated by theory, which is a strong assessment regarding the reliability of our methodology.

VI.2.5 Condition to equivalence

It is assumed that parameters such as the air density or the earth gravitational constant are not varying. Rather, following equations sum up the requirements on parameters for DS dimensionless solutions to be equivalent. Two separate cases are labelled “1” and “2” in the following equations.

Let's assume different wing loadings, whatever variations in mass and in area they could relate to.

$$\left(\frac{m}{S}\right)_1 \neq \left(\frac{m}{S}\right)_2 \quad (\text{VI.47})$$

The two cases would lead to equivalent dimensionless solutions only if the condition expressed in Eq. VI.48 is met.

$$\frac{(u_*)_2}{(u_*)_1} = \sqrt{\frac{(m/S)_2}{(m/S)_1}} \quad (\text{VI.48})$$

Besides, the minimum altitude must be adapted as detailed in Eq. VI.49.

$$\frac{(z_{min})_2}{(z_{min})_1} = \frac{(m/S)_2}{(m/S)_1} \quad (\text{VI.49})$$

And the same follows with the respective roughness lengths in Eq. VI.50.

$$\frac{(z_0)_2}{(z_0)_1} = \frac{(m/S)_2}{(m/S)_1} \quad (\text{VI.50})$$

If above conditions are met, then the induced wind strength W_N at any given height, between the two cases, would compare as described in Eq. VI.51.

$$(W_N)_2 = \sqrt{\frac{(m/S)_2}{(m/S)_1}} (W_N)_1 + \sqrt{\frac{(m/S)_2}{(m/S)_1}} \frac{(u_*)_1}{\chi} \log \frac{(m/S)_1}{(m/S)_2} \quad (\text{VI.51})$$

VI.3 Summary of Chapter VI

This chapter consists in looking at DS flight from a dimensionless point of view, in the aim of investigating remarkable properties. Reference values are introduced and related to each other to form dimensionless EoM. The approach should not only concern EoM, but the overall optimization problem in order to yield consistent solutions.

Non-dimensionalization is first considered in the case of a linear wind profile. Dimensionless EoM display a sensibility to a single parameter $\bar{\rho}$. It is verified that equivalent dimensionless solutions are obtained when the wind gradient β and the wing loading (WL) are adapted such that $\bar{\rho}$ is constant. In particular, the WL is shown to be a parameter of equivalence regarding the required β . Indeed, if two vehicles, with identical aerodynamic polars, have the same WL, they would behave identically as far as DS is concerned. It means that the required β is identical and that trajectories can be superimposed. Besides, $\bar{\rho}$ can be associated to a benchmark of DS performances. There is a maximal value of $\bar{\rho}$ which allows for gliding DS flight. For values above, the vehicle must provide some power, for values below, energy expenditure margins are allowed. An increase in WL leads to a lower required β , as can be anticipated by the theory. This result is independent from any aerodynamic consideration, but deduced out of dimensionless EoM. Heavier vehicles perform DS flight paths of larger amplitude, with higher altitudes to reach stronger winds. Finally, simulations show that the required wind shear for DS is rather weak, approximately 1 m.s^{-1} over a height of 10 metres.

Simulations within a logarithmic profile display flight paths that are much more flattened at lower altitudes and require a wind strength close to 10 m.s^{-1} at 10 metres height. An adequate non-dimensionalization is found and verified. Yet the adjustment of the minimal altitude and of z_0 is required to yield equivalent solutions. This has hence little practical use, since those parameters relate to operational and environment conditions. Besides, the interpretation of $\bar{\rho}$ as a benchmark of DS performance is no longer accurate as the characteristic wind gradient does not bear any particular physical meaning. Still, the correspondence between theory and simulations provides a valuable support for validation. Besides, it can be anticipated that z_0 only influences the required u_* if the variable x is involved in either the objective function or operational constraints. Hence, as far as air relative motion is concerned, z_0 does not come into play. Finally, an increase in WL requires a stronger u_* and therefore stronger winds, which again departs from the linear wind profile case.

CHAPTER VII

DS FLIGHT PERFORMANCES

In order to investigate the potential scope of DS flight for UAV-typed vehicles, the feasibility of DS flight and the related enhancements in performance should be assessed with respect to a vast range of variables. It has been established that, under certain conditions, it is possible to sustain gliding flight by extracting energy from the boundary layer. However, the range of mission scenario that offers this opportunity still has to be determined. The aim of this chapter is to investigate variations in DS performance with respect to parameters related to the vehicle, the flight path constraints and the environment. First, the study focuses on vehicles, with the three UAV designs compared in terms of minimum required wind strength. Because variations in mass were indirectly performed in the previous chapter, it is chosen to focus rather on the way the ground clearance G_{clear} and the surface roughness z_0 impact performances. It is to be noted that aerodynamic ground effects are not at stake here, since those are not taken into account. Then, new perspectives in DS flight are investigated by considering thrust-augmented trajectories.

VII.1 Comparisons between UAVs

Without getting into the detail of varying design variables, as those would alter the overall performances of each vehicle, it was rather chosen to apply the optimization methodology to each vehicle. Indeed, each vehicle embodies the feasible gliding performance at their scale. For this sake, similar conditions for all three cases were obviously adopted. It consists in a logarithmic boundary layer profile, with a surface roughness z_0 of 1 cm , and a ground clearance G_{clear} of 50 cm . Those values are chosen arbitrarily, but are estimated to be sound and conservative values that would be adequate to represent the evolution of a UAV over an open flat terrain, covered with low grass. The vehicle design variables, as well as operating constraints adopted, are those specified in Table III-1, masses are not increased from their baseline. Indeed, simulations show that an increase in wing loading, within the logarithmic boundary layer, entails a stronger required wind friction velocity, even without

equivalence considerations raised by chapter VI, where the minimum altitude is adapted. Results are presented first and then subsequently discussed.

VII.1.1 Delair-Tech DT-18

The first vehicle considered is the *DT-18*. It provides an interesting support for an insight into DS flight with rather small UAVs. The compromise between a reduced span at an expense of hampered gliding performances is of particular interest.

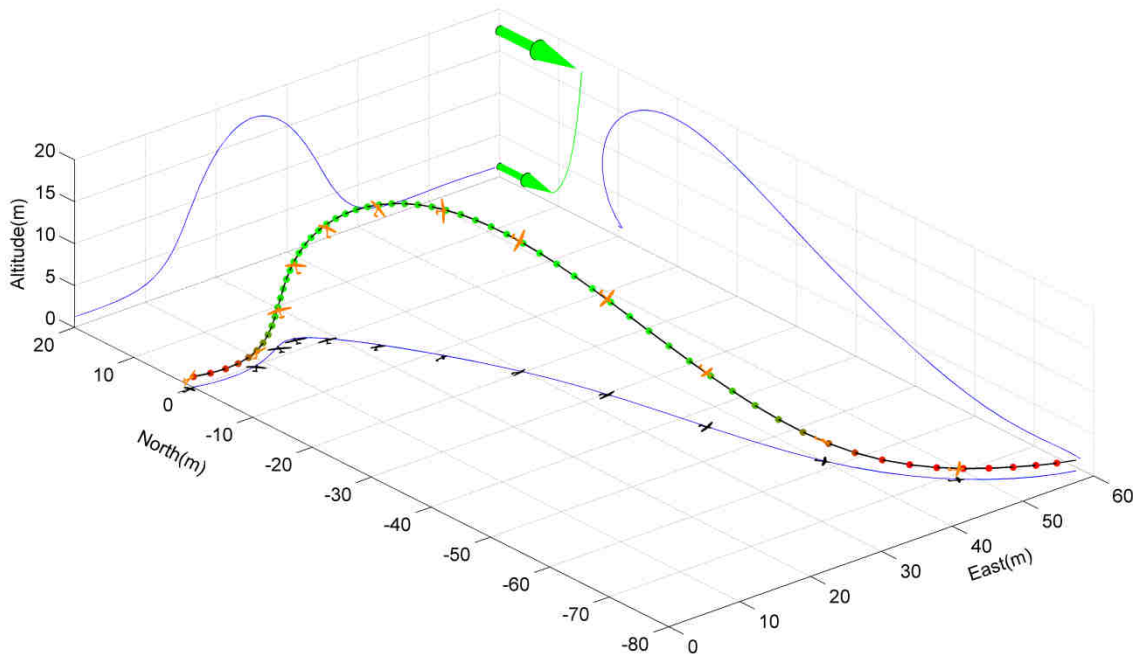


Figure VII.1: Energy-neutral open loop obtained for the *DT-18*. It takes 6.90 seconds to complete the cycle that is achieved for a minimum required friction velocity of 76 cm.s^{-1} , which corresponds to a wind strength of 12.80 m.s^{-1} at a height of 10 metres. The vehicle is pictured at a 1.5:1 scale.

The minimum wind friction velocity required for the *DT-18* is 76 cm.s^{-1} , which represents significant windy conditions, to the order of magnitude of 13 m.s^{-1} at 10 metres height. The lowest altitude (1.24 metres) is reached at the beginning of the trajectory, where the vehicle is banked at 55° to the left. The overall travelling directions corresponding to this trajectory is 142.6° .

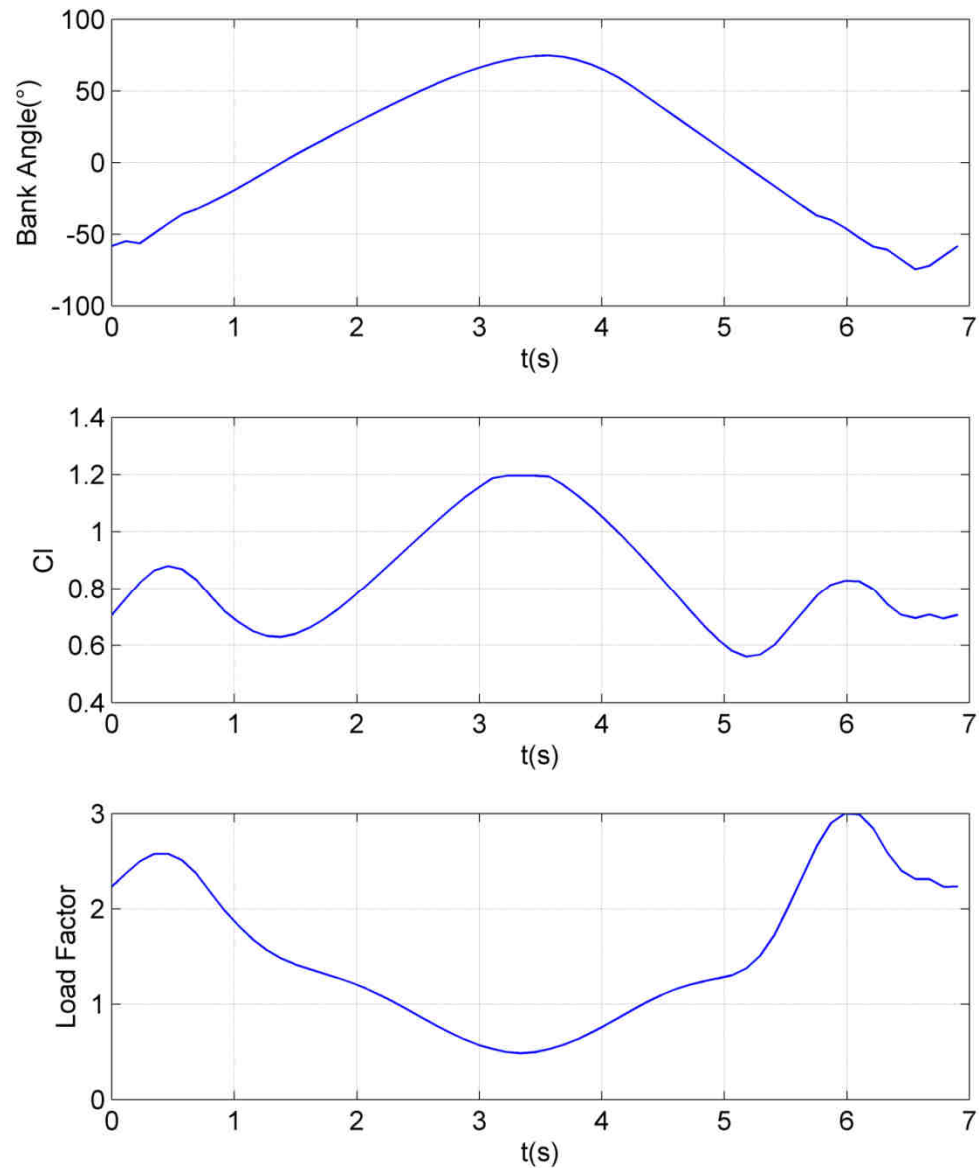


Figure VII.2: Evolution of the bank angle, the lift coefficient and the load factor with respect to time, for the *DT-18*, for the case pictured in Fig. VII.1.

The evolution of control variables along the path, together with the load factor, is presented in Fig. VII.2. It can be observed that apart from barely hitting the load factor limit of 3 and the limit of C_L around 1.2, the *DT-18* does not seem hampered in its evolution by any structural or control rate limits. To eliminate any doubt, the maximum rolling rate was augmented from $60^\circ/s$ to $90^\circ/s$, in order to assess the influence of this parameter on the minimum wind speed required. No significant improvement was observed.

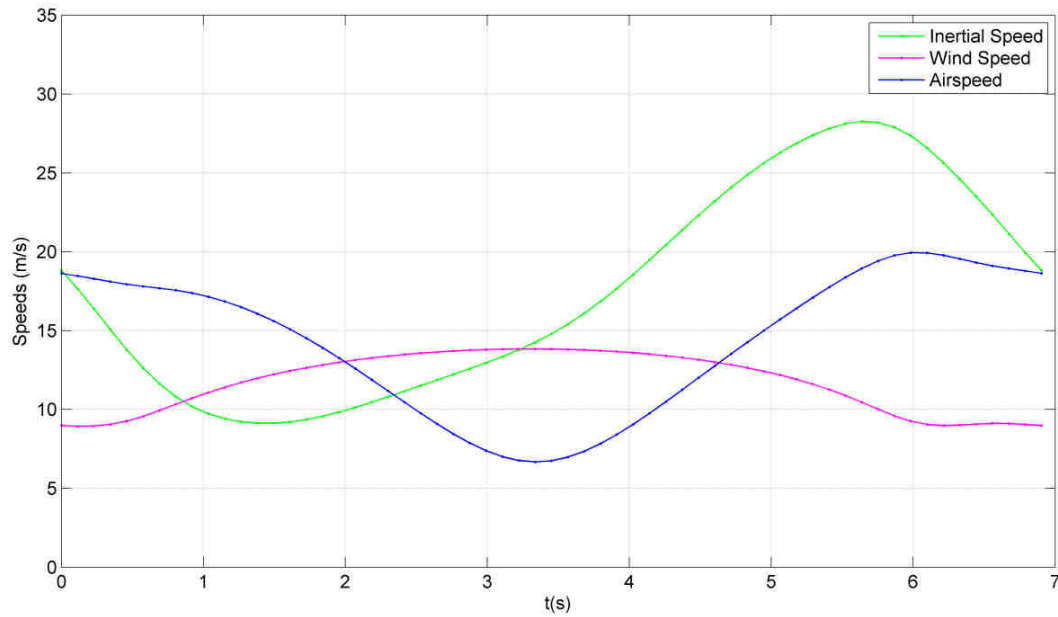


Figure VII.3: Evolution of the inertial speed, the airspeed and the local wind speed encountered by the *DT-18* along its optimized path, pictured in Fig. VII.1.

As displayed in Fig. VII.3, the airspeed along the path is less than 20 m/s , which should not pose any problem for the *DT-18*.

VII.1.2 Mariner

The second vehicle is *Mariner*, which was already used earlier. Still, it is used this time with its baseline mass of 2.0 kg and under the same operating constraints mentioned above.

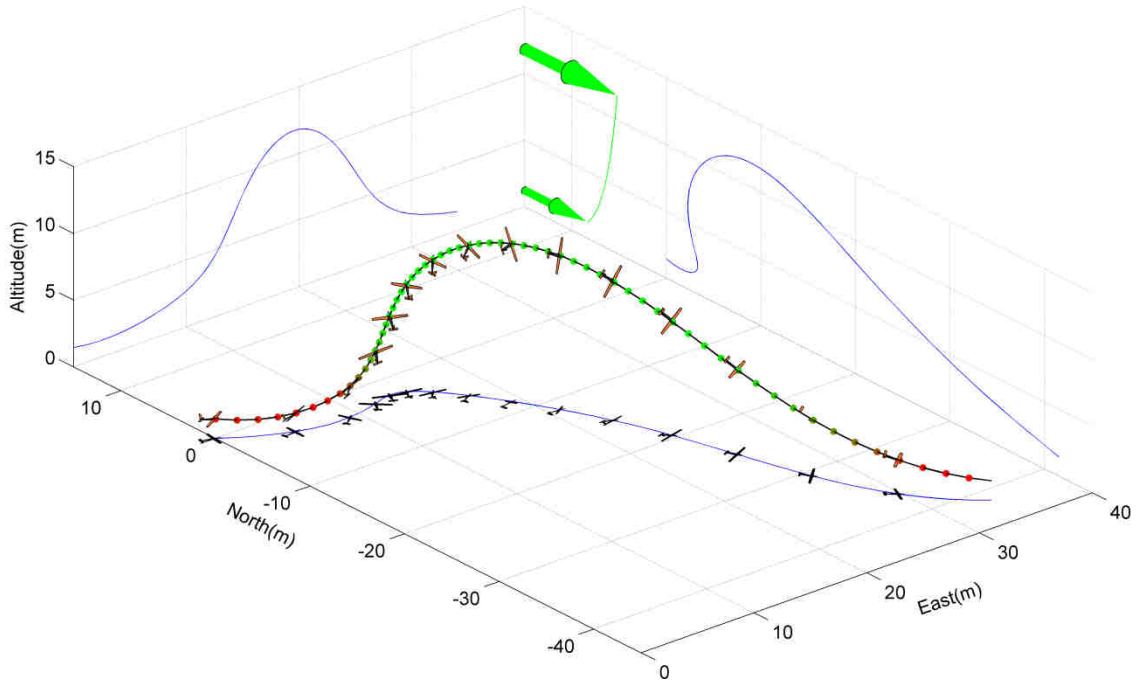


Figure VII.4: Energy-neutral open loop obtained for the *Mariner*. It takes 4.90 seconds to complete the cycle that is achieved for a minimum required friction velocity of 56.7 cm.s^{-1} , which corresponds to a wind strength of 9.55 m.s^{-1} at a height of 10 metres. The vehicle is pictured at a 1:1 scale.

The minimum wind friction velocity required for *Mariner* is 56.7 cm.s^{-1} , which represents a wind speed of 9.55 m.s^{-1} at 10 metres height. The lowest altitude (1.24 metres) is reached at the beginning of the trajectory, where the vehicle is banked at 36.4° against the wind. The overall net direction of travel is 140.6° .

Compared to the *DT-18*, *Mariner* offers a significant improvement in the objective function. Indeed, it requires lighter wind conditions for *Mariner* to be powered by DS than the *DT-18*. Overall, the basic cycle obtained with *Mariner* has much lower amplitude than that of the *DT-18*. Another interesting aspect concerns the minimum altitude reached by *Mariner* along the cycle. It is very much comparable to the *DT-18*, while the span of *Mariner* is around 40% larger, which indicates that *Mariner*, or the point mass that represents it, manages to get closer to the surface, relatively to its span.

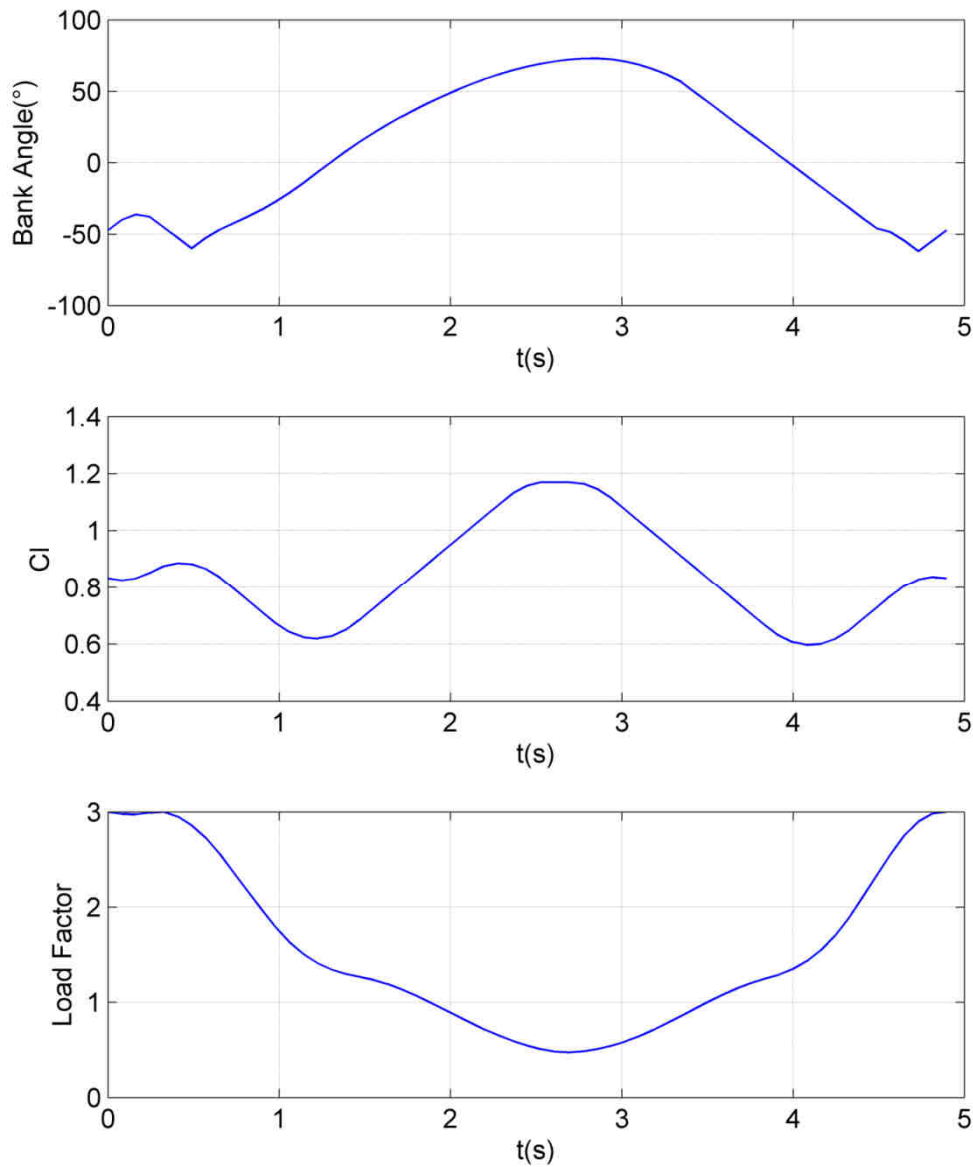


Figure VII.5: Evolution of the bank angle, the lift coefficient and the load factor with respect to time, for *Mariner*, for the case pictured in Fig. VII.4.

Mariner hits the maximum load factor of 3 during the lower turn. It can be deduced that a stronger airframe, which can allow for a higher load factor, has the potential to reduce further the minimum wind speed required. Besides, the limit in \dot{C}_L , of 0.5 s^{-1} is reached, which suggests that enlarging pitch control surfaces could also play a positive role. The rolling rate is already at its maximum for *Mariner* and no further computation is made.

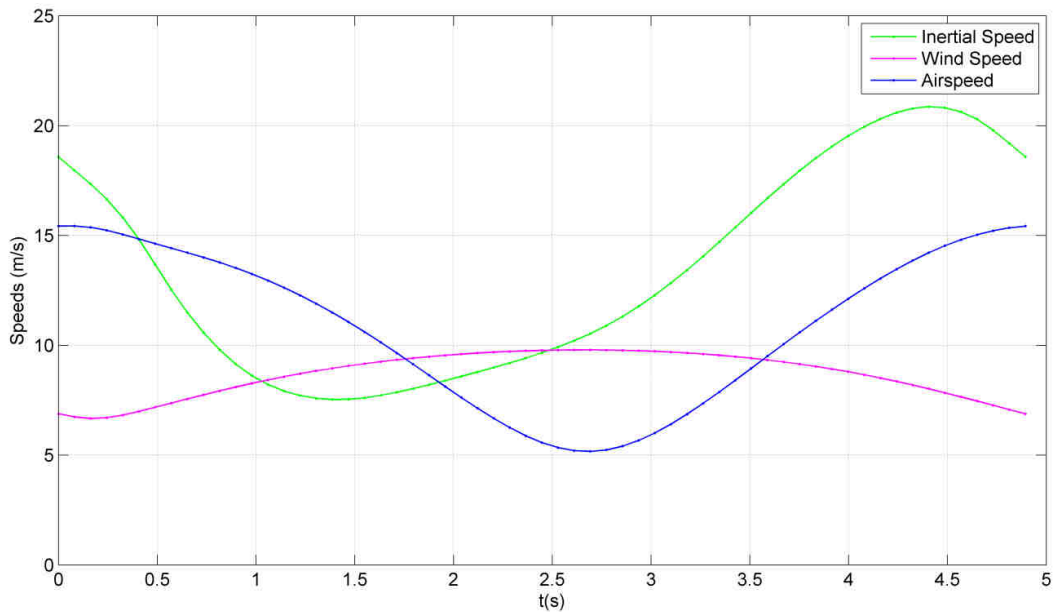


Figure VII.6: Evolution of the inertial speed, the airspeed and the local wind speed encountered by *Mariner* along its optimized path, pictured in Fig. VII.4.

Compared to the case computed earlier for *Mariner* and displayed in Fig. V.13, the vehicle has less inertia and therefore the evolution of the airspeed and the inertial speed are further out of phase. It is to be noticed that speeds, either air or inertial-based, are comparatively lower than that of the *DT-18*.

VII.1.3 Cloud Swift

The third vehicle considered is *Cloud Swift*, which is of significantly bigger scale compared to the two previous UAVs. Although the gliding performances of *Cloud Swift* stand out and would obviously play in its favour, it may be hampered precisely by its large span, during the lower turn. Beyond the comparison with the two other UAVs, simulations with *Cloud Swift* would provide an insight into DS for UAVs of the upper range. Indeed, at 4.32 metres of span, the analogy with the albatross may start to fade and it is of particular interest to assess whether or not DS can be scaled-up to bigger geometries.

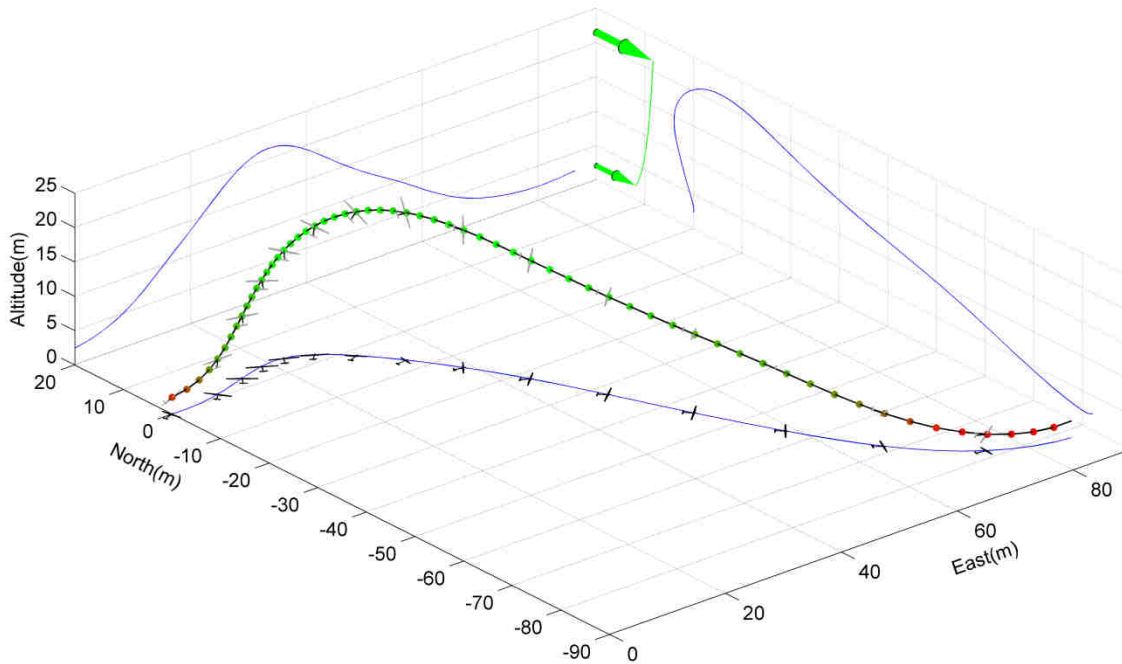


Figure VII.7: Energy-neutral open loop obtained for *Cloud Swift*. It takes 8.12 seconds to complete the cycle that is achieved for a minimum required friction velocity of 62.4 cm.s^{-1} , which corresponds to a wind strength of 10.52 m.s^{-1} at a height of 10 metres. The vehicle is pictured at a 1:1 scale.

The minimum wind friction velocity required for *Cloud Swift* is 62.4 cm.s^{-1} , which represents a wind speed of 10.52 m.s^{-1} at 10 metres height. The lowest altitude (2.06 metres) is reached at the end of the trajectory, where the vehicle is banked at 46.2° to the left. The overall net direction of travel is 133.6° . The flight path amplitude is the greatest so far, and so is the maximum altitude reached.

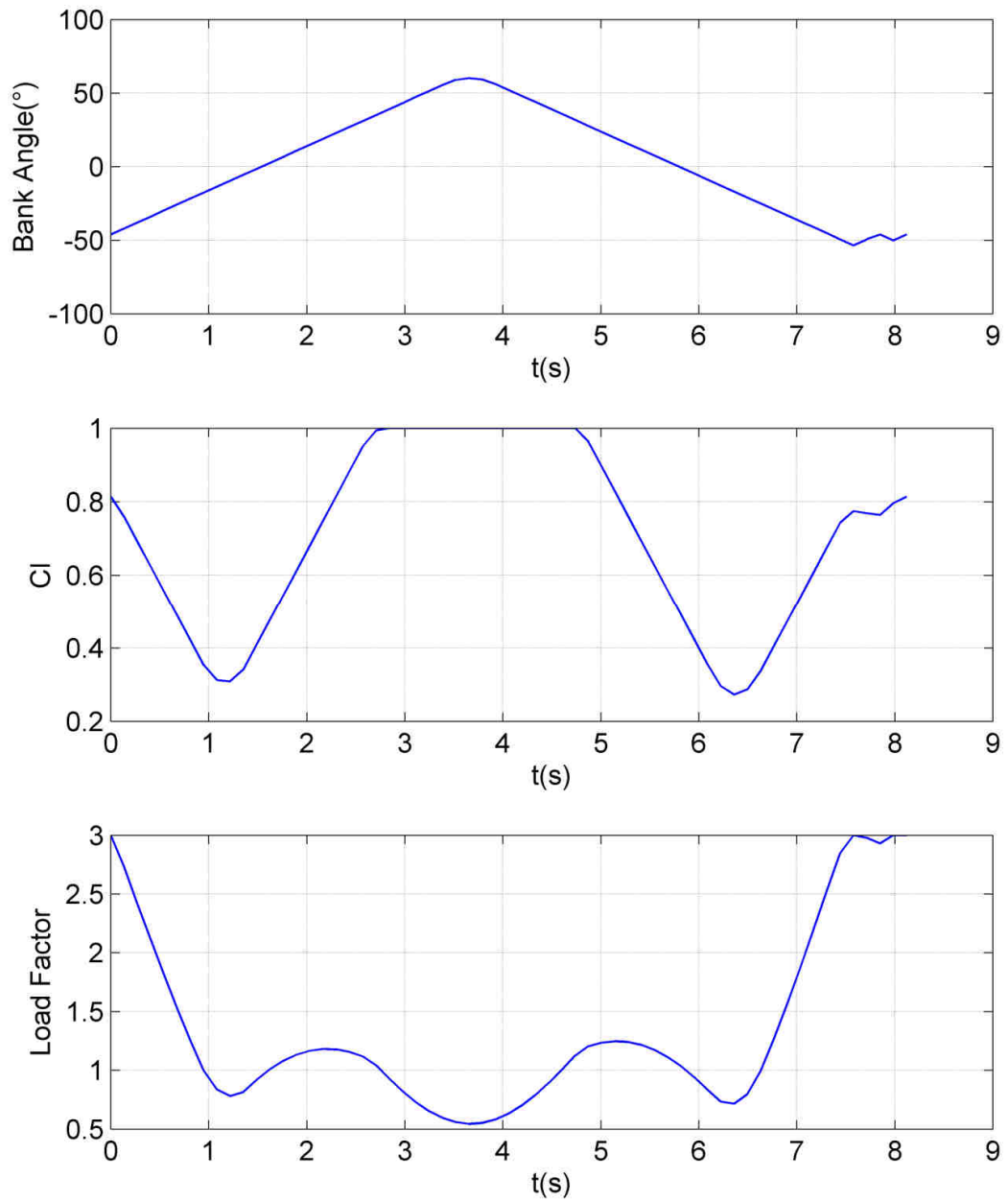


Figure VII.8: Evolution of the bank angle, the lift coefficient and the load factor with respect to time, for *Cloud Swift*, for the case pictured in Fig. VII.7.

Yet, it can be observed in Fig. VII.8 that both the evolution of the bank angle and of the coefficient of lift show piecewise linear patterns. The bank angle hits the maximum rolling rate limit, which is quite low at $30^\circ/s$ for *Cloud Swift*. Hence, the wind strength required for *Cloud Swift* could be lowered if the maximum rolling rate was increased, all the more as the vehicle is hampered by the constraint during most of the cycle. Besides, the coefficient of lift also reaches its maximum rate limit.

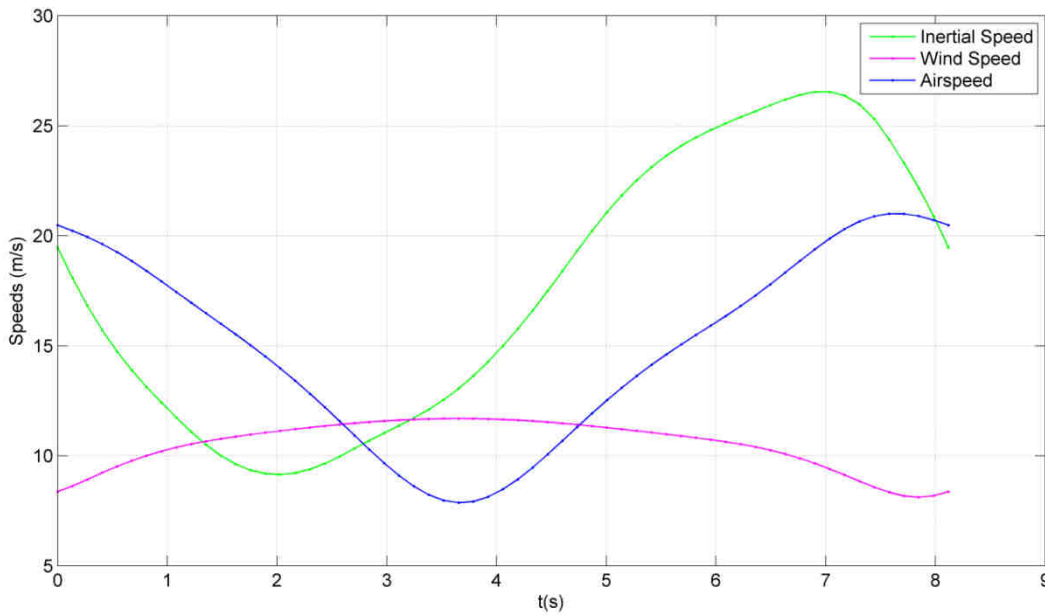


Figure VII.9: Evolution of the inertial speed, the airspeed and the local wind speed encountered by *Cloud Swift* along its optimized path, for the case pictured in Fig. VII.7.

Since *Cloud Swift* appears to be rather restricted in its DS evolution, another run was performed by increasing the limit maximum rolling rate, first to $60^\circ/s$ and then to $90^\circ/s$. The vehicle can reasonably achieve a higher rate of roll, by enlarging aileron surfaces, without sacrificing aerodynamic performances or adding too much weight. Besides, the $30^\circ/s$ limit is somehow a conservative value, obtained from the literature [70]. Therefore, the limit in rate of roll is increased without modifying any other parameter, in order to unlock the real DS potential of *Cloud Swift*.

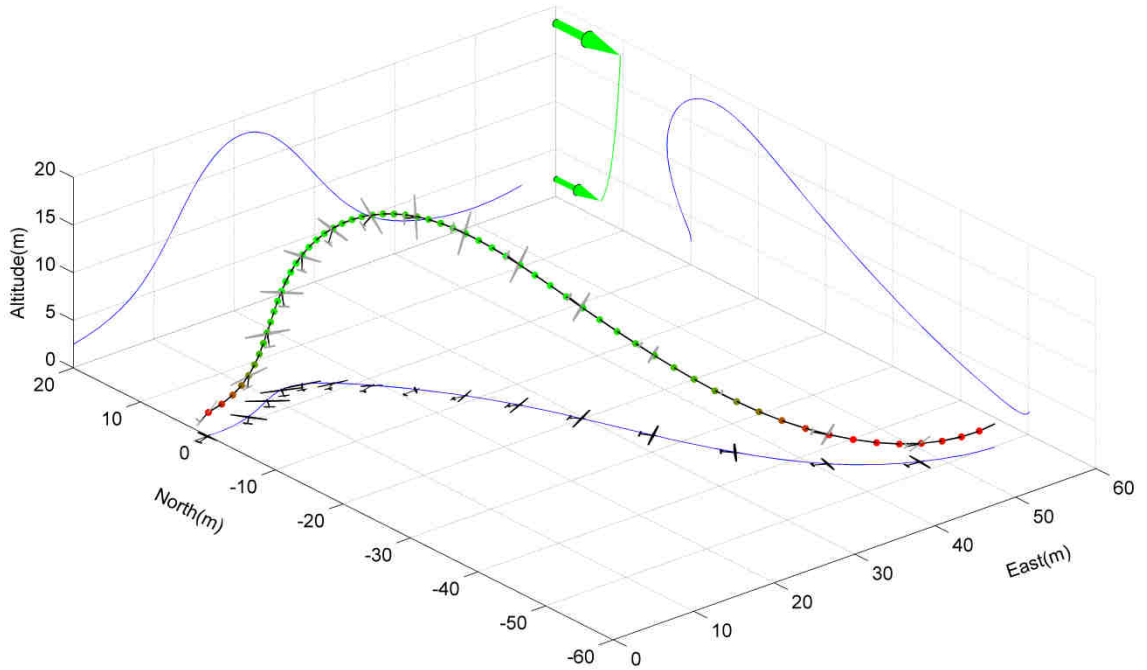


Figure VII.10: Energy-neutral open loop obtained for *Cloud Swift* for $|\dot{\phi}| \leq 60^\circ/s$. It takes 6.01 seconds to complete the cycle that is achieved for a minimum required friction velocity of 52.2 cm.s^{-1} , which corresponds to a wind strength of 8.80 m.s^{-1} at a height of 10 metres. The vehicle is pictured at a 1:1 scale.

The resulting trajectory is much closer, in its overall aspect, to that obtained for *Mariner* than before. The minimum wind friction velocity is quite lowered at 52.2 cm.s^{-1} , which represents a 16.35 % improvement from the previous case. The subsequent wind speed at 10 metres height is 8.80 m.s^{-1} . The minimum altitude is also lowered to 1.86 metres, down from 2.06 metres. It is reached at the end of the trajectory, where the vehicle is banked at 39.2° to the left. Hence, relaxing the constraint on the rate of roll has enabled *Cloud Swift* to turn at a lower altitude, reached for a reduced bank angle. The overall net direction of travel is 132° . The overall flight path amplitude is lowered compared to the previous run and so is the time of flight, down to 6.01 seconds from 8.12 seconds. More aggressive banking capabilities translate into a narrower evolution.

A further improvement can be achieved by increasing the maximum rolling rate to $90^\circ/s$. Yet, it is quite marginal as the corresponding wind friction velocity is then 51.1 cm.s^{-1} , only 2 % better than the $60^\circ/s$ case. All variables were quite similar in their evolutions and it was chosen to only display results relative to the $60^\circ/s$ case.

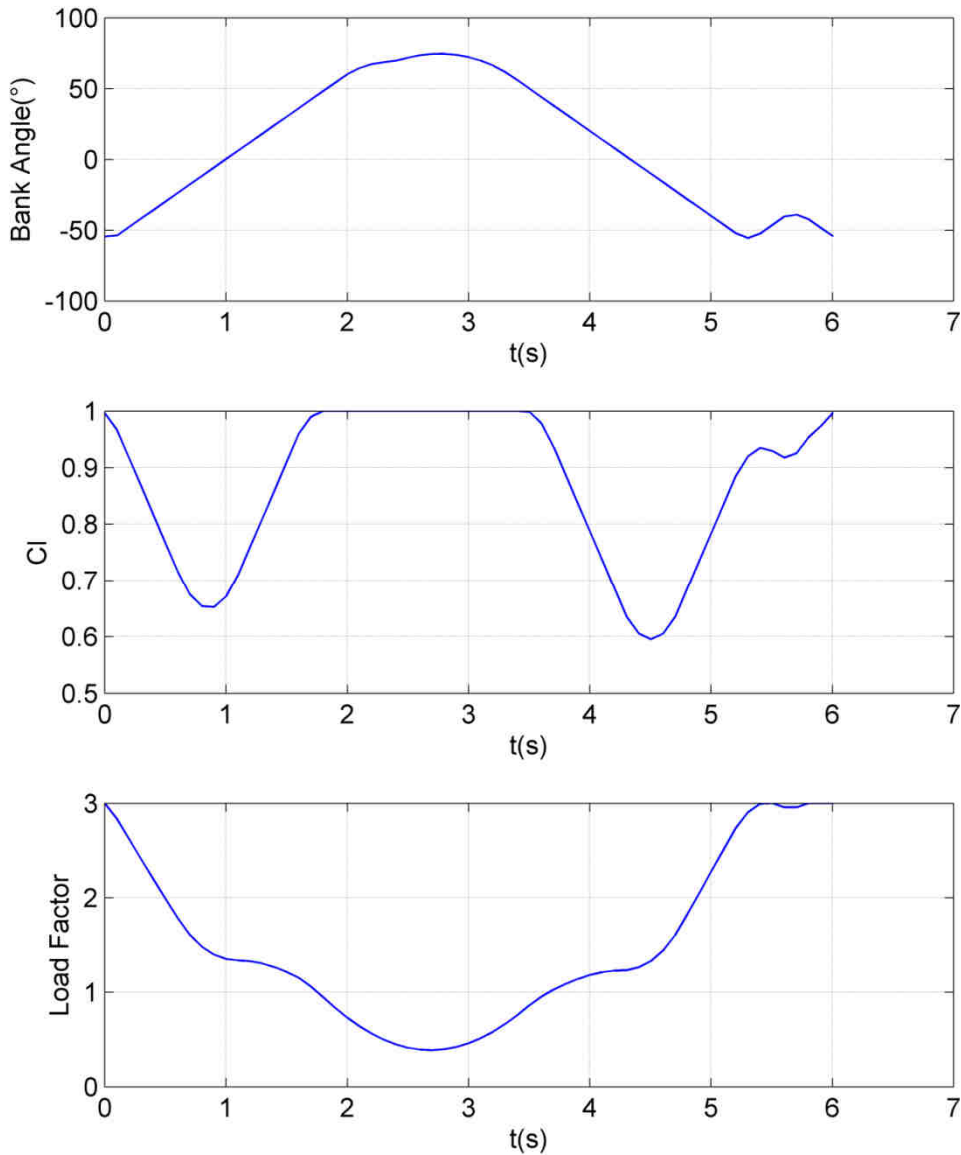


Figure VII.11: Evolution of the bank angle, the lift coefficient and the load factor with respect to time, for *Cloud Swift*, with a maximum rolling rate of $60^\circ/s$, corresponding to the flight path pictured in Fig. VII.10.

Another limitation arises, as can be observed from the evolution of variables, plotted in Fig. VII.11. Indeed, the maximum rate in coefficient of lift is reached again and C_L also hits the maximum value of 1 for a significant fraction of time, during most of the higher part of the curve. This suggests another way of improvement from the baseline design of *Cloud Swift*, which would focus on increasing the maximum C_L . Yet, a redesign of the wing section may hamper the best lift to drag ratio, such that a first approach could consist in controlling flaps deployment, when a high C_L is required. This usually occurs at low airspeeds, such that gains from the higher C_L should easily overcome the penalty induced by the increased drag. This

would add a single control variable and would allow to play with different aerodynamic polar while keeping a conventional design. It would constitute a promising study case which would approach the concept of dynamic flaps deployment.

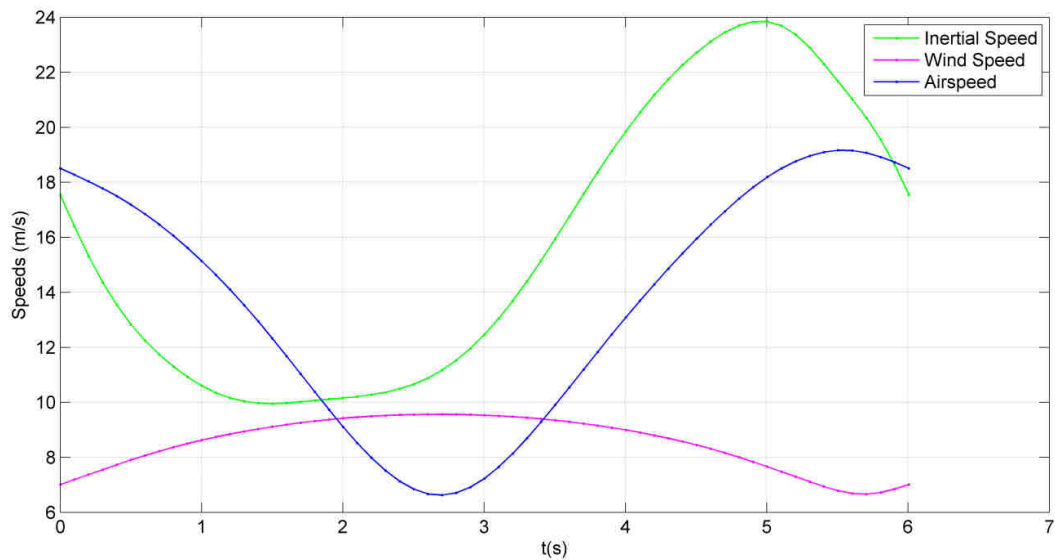


Figure VII.12: Evolution of the inertial speed, the airspeed and the local wind speed encountered by *Cloud Swift* along its optimized path, for a maximum rolling rate of $60^\circ/s$, corresponding to Fig. VII.10.

Compared to the case of restricted roll rate, the new trajectory is flown at a lower average airspeed. Compared to other vehicles, *Cloud Swift* achieves its energy neutral trajectory for less favourable wind conditions, which is a significant result that is discussed below.

VII.1.4 Discussion on Vehicle Performances

Different results regarding the energy-neutral open loops obtained for the three vehicles are summed up in Table VII-1.

Since *Mariner* was designed in order to minimize the wind strength required [67], it can serve as a baseline case for comparison. A first observation is that the *DT-18* is not especially suited for DS flight. Indeed, the wind strength required is significantly higher than all other cases and variables weren't observed to be limited by any specific rate constraint.

The maximum altitude reached by *Mariner* is significantly lower than that of the *DT-18*, 11.8 metres against 17.5 metres. Because of the lower wind strength and the lower altitude, *Mariner* therefore manages an energy-neutral trajectory which requires a lower wind power density than the *DT-18*. It may be correlated to the fact that *Mariner* needs a lower minimal power to be maintained aloft, see Table III-1.

Table VII-1: Summary of results regarding the DS trajectory obtained for minimum required wind friction velocity.

Variable	<i>DT-18</i>	<i>Mariner</i>	<i>Cloud Swift</i> (30°/s)	<i>Cloud Swift</i> (60°/s)
u_* (cm/s)	76.0	56.7	62.4	52.2
$ W_x _{max}$ (m/s)	13.8	9.8	11.7	9.6
t_f (s)	6.90	4.90	8.12	6.01
z_{min} (m)	1.24	1.24	2.06	1.86
z_{min}/b	70 %	50 %	48 %	43 %
n_{max}	3	3	3	3
ϕ_{max} (°)	74.8	72.9	60.0	74.4
ψ_{net} (°)	142.6	140.6	133.6	132.0

The lowest altitude reached by the *DT-18* accounts for 70 % of the span, while *Mariner* manages to reach the same lowest altitude which is only 50 % of its span. The *DT-18* is banked at a higher angle (55°) at its lowest altitude. It may be interpreted as a way to reduce the radius and the amplitude of the lower turn and therefore to limit the parasitic drag losses that occur at high airspeed. Our interpretation is that, in the framework of DS, the *DT-18* sacrifices too much gliding performances for the sake of a reduced size. It has to fly at a rather high airspeed in order to be able to reach favourable wind strength at high heights and hence has to bank aggressively during the lower turn to avoid losing momentum. This manoeuvre induces some performance penalty, due to the windward acceleration during the lower turn, on top of the parasitic drag.

Although different designs could be investigated for small fixed-wing UAVs, the deterioration of aerodynamic performances does not shed a promising light on the exploitation of DS on rather flat surfaces by very small UAVs. Yet, other environments, where the wind shear is restricted to limited areas, such as the leeward side of buildings could inversely favour small designs.

However, at the other extremity of the range, results are rather promising. Once the flight path limitations due to rolling rate constraints are fixed, *Cloud Swift* can actually exploit DS for a wind friction velocity 13 % lower than *Mariner*. It must be nuanced by the fact that *Cloud Swift* reaches a maximum altitude of around 18 metres, while *Mariner* does not exceed 12

metres. Hence, the maximum wind strength encountered is not that different, but still at the advantage of *Cloud Swift*, which encounters a maximum wind speed $|W_x|_{max}$ of ~ 9.6 m/s at the top of the path, while *Mariner* sees winds of ~ 9.8 m/s. The wind power density required by *Cloud Swift* is hence lower.

It does not put the design of *Mariner* into question as the authors voluntarily limited its span to 2.5 metres and imposed that the vehicle could be hand-launched [67]. Still, the interpretation of the comparison with *Cloud Swift* is not especially intuitive since the tentative explanation of the lower in-flight required power is not verified in this case. Quite the contrary actually, since *Cloud Swift* requires, for static flight, a minimum power that is more than three times that of *Mariner*, see Table III-1. Therefore, *Cloud Swift* exploits lighter winds even though it requires more power to balance drag losses. So the minimum required power isn't the driving parameter regarding the feasibility to exploit DS. Yet, the right consideration may have to be with minimum sink rate, as it is for thermal soaring or slope soaring [95], rather than minimum required power. Even though the two quantities are trivially related, the feasibility to exploit a thermal is theoretically assessed by comparing the vertical thermal velocity to the minimum sink rate of the vehicle. In this respect, *Cloud Swift* still has an edge over *Mariner*, with a minimum sink rate of 0.39 m.s⁻¹ (see Table III-1), against 0.42 m.s⁻¹ for *Mariner*.

On the lower part of the flight path, the minimum altitude reached by *Cloud Swift* is higher than for *Mariner*, and accounts for 43 % of its span, compared to 50 % for *Mariner*. This proportion is to be put on the fact that the minimum altitude is the sum of the wing tip clearance, imposed at 50 cm, and of the vertical projection of the span. Therefore, an increase in span can lead to a decrease in height-to-span ratio, even though the vehicle is banked at a higher angle. It happens in the present case, with *Cloud Swift* banked at 39.2° at its lowest point, compared to 36.4° for *Mariner*. It would be interesting, in further studies, to assess the influence of the wing tip clearance on the DS operating advantage of *Cloud Swift*. Anyway, the absolute height, encountered by *Cloud Swift* during the lower turn, is higher than for *Mariner*. In itself, it represents adverse conditions to DS flight, even though the increased span contributes to increase the lift-to-drag ratio.

To sum up, compared to *Mariner*, *Cloud Swift* exploits more adverse conditions (*ie* lower wind friction velocity) along a path that sees lower wind strength at the top of the curve. Hence, the increased mass, due to the bigger scale, as well as the minimum height penalty, induced by the higher span, can be overcome by refined aerodynamics (higher $(L/D)_{max}$, lower V_{zmin}), which enables *Cloud Swift* to maximize the energy extraction at minor parasitic expense.

Our results suggest that the DS scope could be enlarged by using UAVs of larger size with improved aerodynamic performances. The upper edge of that trend will be reached when the aerodynamic benefits of increasing the span are cancelled by the minimum height penalty. Besides, since the version of *Cloud Swift* used is not especially lightly built, using large lightweight planforms of the size of *Cloud Swift* could enable to lift higher payloads by DS.

VII.2 Variation in DS performance

VII.2.1 Sensitivity to Surface Roughness Length

The way the surface roughness length z_0 influences the required wind strength is of particular interest as z_0 is representative of irregularities of the surface and therefore of the type of terrain where the vehicle could possibly exploit DS. Besides, the relationship between the net travel heading ψ_{net} , with respect to the wind, and the wind strength required is also of particular interest.

Therefore, from the baseline case study of *Mariner*, presented in VII.1, the roughness length is altered from its value of 1 cm . A 0.4 mm value is chosen to approximately represents the roughness length of the open sea, while 25 cm is representative of high crops. Besides, the net travelling direction ψ_{net} is not set free anymore, but imposed through an added constraint. The ground clearance was fixed at 50 cm regardless of the chosen roughness length. Figure VII.13 displays results under the form of a polar plot. The radius is representative of u_* , while the angle is given by ψ_{net} .

Some discontinuities can be observed on the polar plot, especially marked on the red curve. Those happen because the optimization methodology, from one calculation point to the following one, identifies a better family of solutions and suddenly changes many of its variables. Such a discontinuity in the objective function, u_* in the present case, occurs due to the local nature of optimums yielded by the solver. If only global optimums were found, the transition between two calculation points could still lead to differences in nature between flight paths, but the objective function should be continuous as long as an optimum exists. In the current case, variables of the next calculation step are initiated by using results of the previous one and then passed to the solver with a 0.5° variation in the constrained ψ_{net} . This methodology entails solutions that therefore depend on the set of initiated variables, due to the local nature of the optimum point, and that hence have the potential to be improved. This happens suddenly for a given ψ_{net} , when the solver switches from one family of solution to

another. The fundamental difference between trajectories of different families is illustrated in Fig. VII.14, where three types of flight path are displayed, each being optimal for a certain range of ψ_{net} .

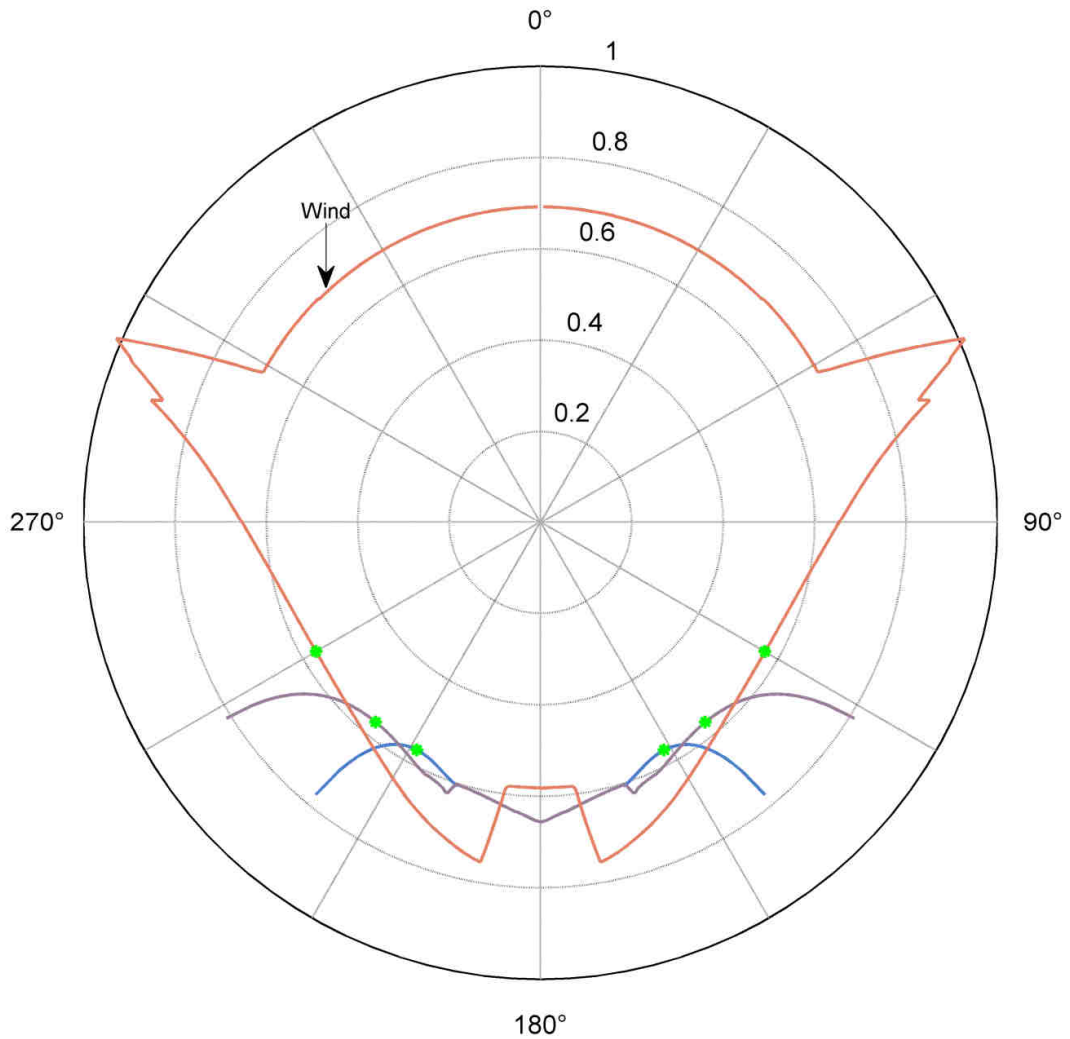


Figure VII.13: Evolution of the required friction velocity u_* (radius in m/s), with the net travelling direction ψ_{net} , for different surface roughness z_0 . In blue, $z_0=0.4\text{ mm}$, in purple $z_0=1\text{ cm}$ (baseline case) and in red, $z_0=25\text{ cm}$. Green dots correspond to simulation cases of unconstrained in ψ_{net} , which yield, for each value of z_0 , the lowest u_* .

All three curves of Fig. VII.13 are obtained by starting the iteration in ψ_{net} from respective simulation cases of unconstrained ψ_{net} , marked by green dots. Solutions are then obtained by either increasing or decreasing ψ_{net} , through the additional constraint. It can be observed that all discontinuities correspond to a sudden improvement of the objective function in the direction of the iteration in ψ_{net} . Going through ψ_{net} calculations an opposite way

would therefore yield different curves at the neighbourhood of the observed discontinuities, due to the same effect.

To sum up on the matter of discontinuities in the objective function, each calculation point corresponds to a consistent trajectory that represents a local solution. In the worst case, a better optimum than the one actually found is available. Before those discontinuities, relative to the iteration direction, the true optimum could belong to the family of curves corresponding to the other side of the discontinuity. Each discontinuity can therefore be interpreted as a region of uncertainty regarding the true optimum.

As it was determined by the non-dimensionalization study in Chapter VI, the minimum required friction velocity does not vary with z_0 . It indeed remains at 56.7 cm.s^{-1} , regardless of the roughness length, because air relative kinematics remains the same when only the roughness length is varied. Yet, in the earth-relative point of view, those trajectories translate differently. It can be seen for instance, that the net heading angle which corresponds to the minimum wind friction velocity, is shifted leeward when the roughness length decreases. Besides, it is all the more difficult for the vehicle to progress against the wind when z_0 decreases, meaning that the range of feasible ψ_{net} shrinks leeward when z_0 decreases. In Fig. VII.13, for a roughness length of 25 cm , *Mariner* can fly in any heading. The required wind friction velocity is then minimal for ψ_{net} around 120° and shows a maximum around 23° . Then, a new family of optimal trajectories is found and the vehicle manages to progress against the wind, for a friction velocity that remains around 69 cm.s^{-1} , regardless of ψ_{net} . It should be mentioned that if the required net heading is around 23° , the destination can still be reached by combining cycles of higher and lower net heading angles that requires lower wind strength.

As it was mentioned above, the following Fig. VII.14 illustrates the three families of optimal trajectories found by the solver. They each correspond to the three continuous regions $u_* = f(\psi_{net})$ seen on Fig. VII.13, for $z_0 = 25 \text{ cm}$. The significant disparities in shape between the three trajectories explain the discontinuities that can be observed in Fig. VII.13. When the vehicle is imposed to travel directly headwind, the trajectory obtained resembles that of the closed loop presented in Chapter V, except that there is a small distance gained against the wind. It is then feasible to progress directly against the wind, cycle after cycle, at the price of a rather small net speed of 0.4 m/s .

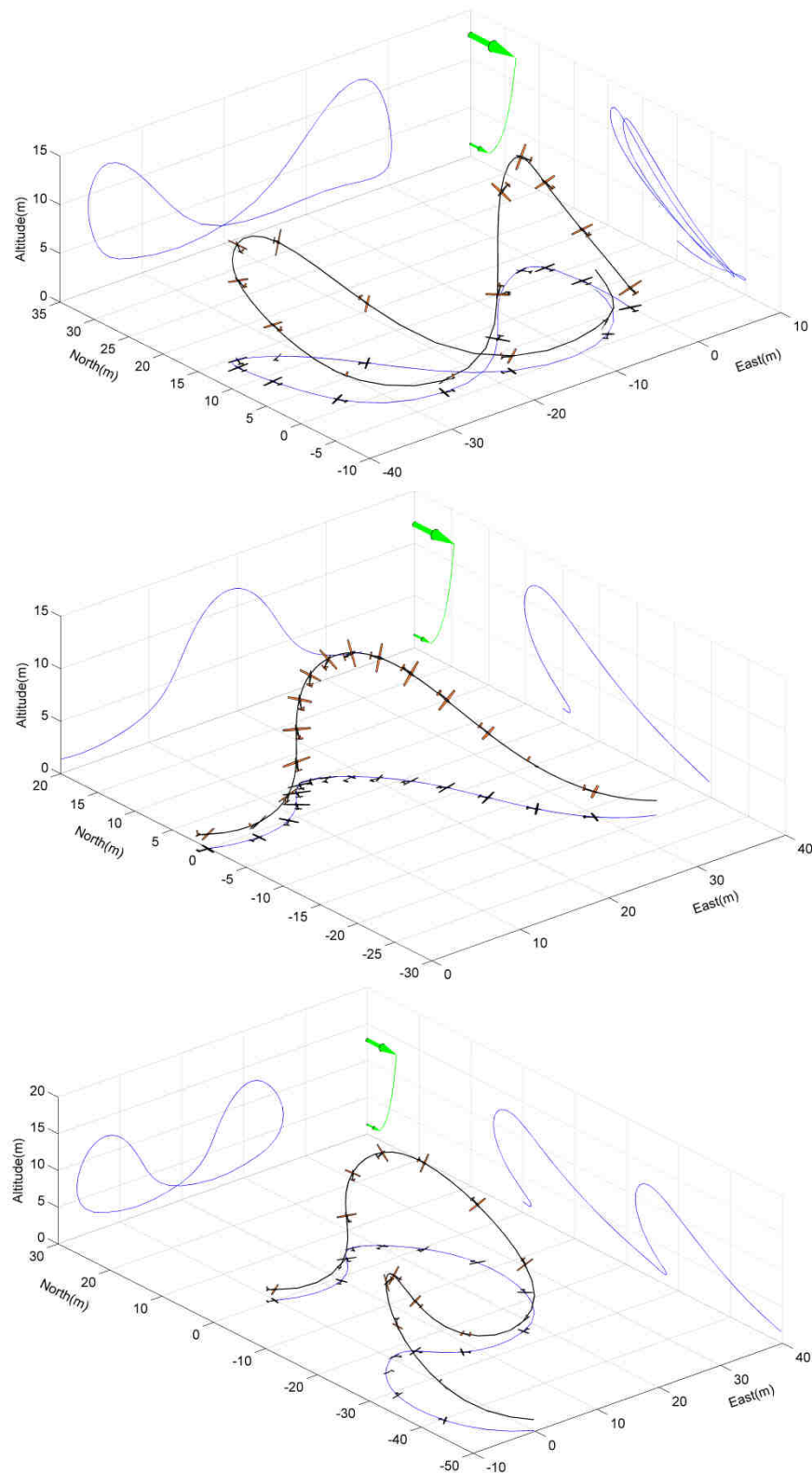


Figure VII.14: Solution cases corresponding to Fig. VII.13, for $z_0=25$ cm. Top: net flight path heading 0° , directed windward, $u_*=69.2$ cm/s, $V_{net}=0.4$ m/s. Middle: net flight path heading 120° , minimal $u_*=56.7$ cm/s, $V_{net}=8.0$ m/s. Bottom: net flight path heading 180° , directed leeward, $u_*=58.2$ cm/s, $V_{net}=4.8$ m/s.

The main result is to highlight that there exists a roughness length which permits the vehicle to progress against the wind. Inversely, the vehicle ability to progress against the wind, and therefore to fly in any heading on the long term, is highly dependent on the surface roughness length. This ability is hampered when the terrain has a lower roughness length.

VII.2.2 Sensitivity to Wing Tip Clearance

The issue of minimum ground clearance is of particular importance because it calls attention to the antinomic tendency between safe operations and favourable DS conditions. Therefore, investigating the influence of the ground constraint on DS performances may help to determine a compromise. The same methodology as before is adopted so that from the baseline case study of *Mariner*, presented in VII.1, the ground clearance is altered from its value of *50 cm*. The roughness length was fixed at *1 cm*, regardless of the chosen ground clearance.

Results are presented in Fig. VII.15. Each of the three curves shows, at their extremum, an asymptotic behaviour around certain values of ψ_{net} , where the required u_* sharply increases to suggest a diverging behaviour. Those values of ψ_{net} correspond to the extremum in feasible ψ_{net} that *Mariner* can exploit by DS, respectively to each ground clearance imposed. The vehicle cannot orientate its net heading further windward of those values. It can be observed that the vehicle covers a wider ψ_{net} range when the ground clearance is lower. Besides, for each available ψ_{net} , the required friction velocity is reduced when the ground clearance is lower. Furthermore, the net travelling angle that sees the minimum required u_* , marked by green dots on Fig. VII.15, moves windward when the ground clearance reduces.

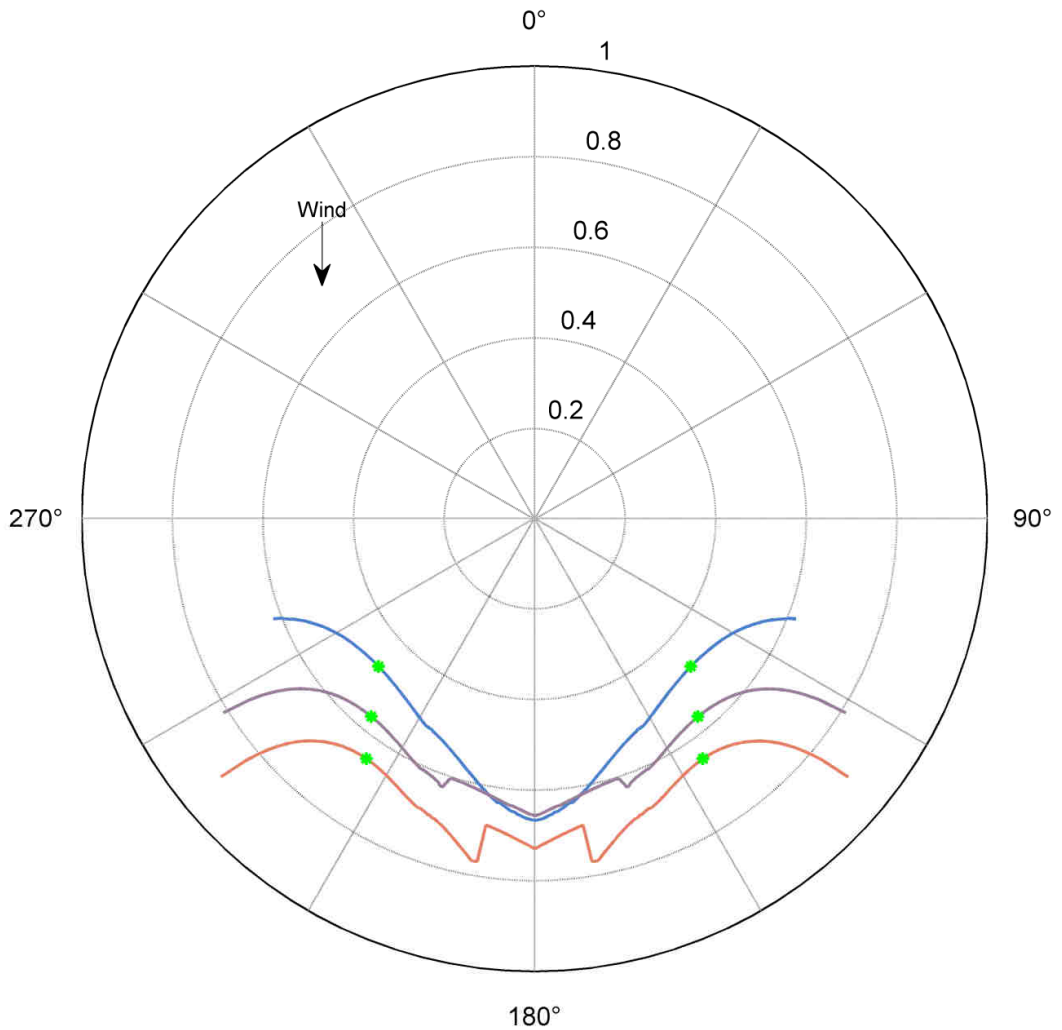


Figure VII.15: Evolution of the required friction velocity u_* with the net travelling direction ψ_{net} , for different ground clearance G_{clear} . In blue, $G_{clear}=0$ cm, in purple $G_{clear}=50$ cm (baseline case) and in red, $G_{clear}=1$ m. Green dots corresponds to the simulation case unconstrained in ψ_{net} , which yield, for each value of G_{clear} , the lowest u_* .

This indicates overall that when the vehicle is allowed to fly closer to the surface, it can exploit DS at lower wind strength and for a wider range of net travelling angles. Still, even when the ground clearance is set to zero, virtually allowing wingtips to touch the surface, *Mariner* is not able to make any headway against the wind. Indeed, the net travelling angle does not go below 111° .

VII.3 Thrust-Augmented Dynamic Soaring

The study case approached by varying the surface roughness and the ground clearance underlines that flying against the wind by pure DS flight requires a combination of high surface

roughness and low ground clearance. On top of that, requirements in terms of wind strength are sometimes demanding and the likelihood to meet favourable conditions can be assumed to be rather low. Rather than expecting a complete provision of the vehicle energy needs by the wind; those could be only partially covered by DS flight, while the vehicle would provide the rest on its own power. Such a configuration would widen the scope of DS application, by lowering requirements related to environmental conditions, while still benefiting from the same energy-harvesting principles. A thrust-augmented DS study case is presented before exposing some range-improvement charts.

VII.3.1 Basic features

The principle of adding thrust (T) as a third control variable is introduced in Chapter VI. In the following study, inspired by the baseline case obtained in VII.1 for *Mariner* in pure gliding flight, u_* is arbitrarily decreased from the minimum required, 56.7 cm.s^{-1} , down to 47.5 cm.s^{-1} , so the wind strength is 8.00 m.s^{-1} at 10 metres height. The wind friction velocity is not the objective function anymore and is determined as an input to the optimization problem.

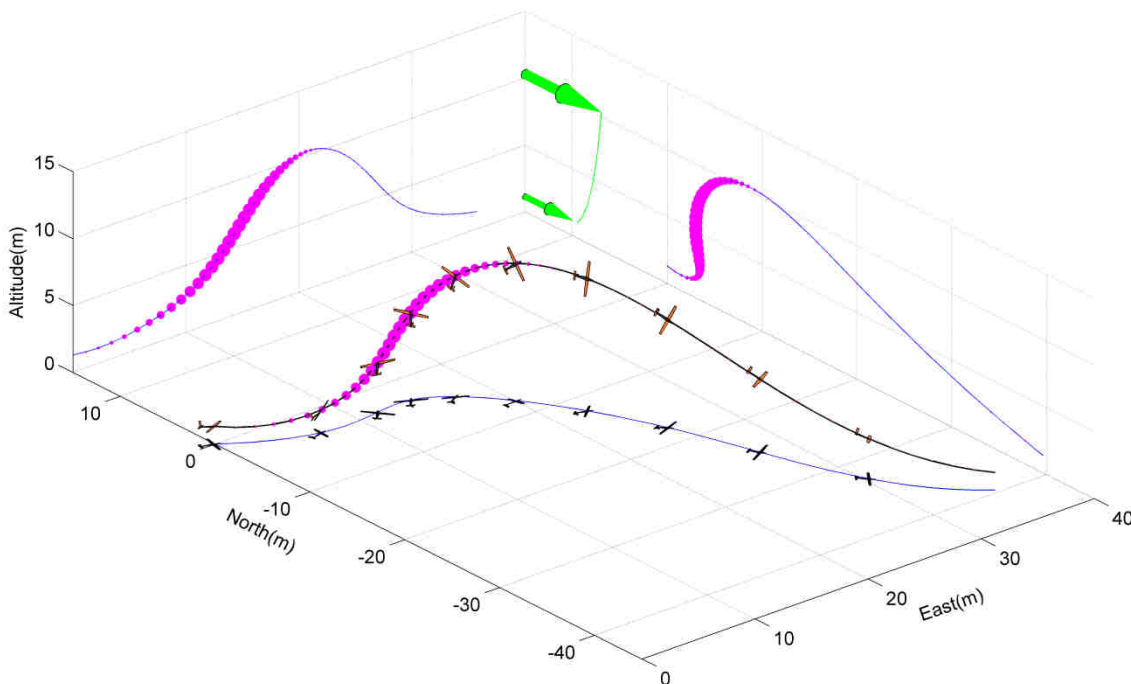


Figure VII.16: Thrust-augmented-energy-neutral open loop obtained for *Mariner*, achieved within 4.86 seconds, for $u_* = 47.5 \text{ cm.s}^{-1}$. The pink-coloured dots are proportional, in size, to the intensity of the thrust provided by the vehicle. The vehicle is pictured at a 1:1 scale.

The objective function is to minimize the energy consumption per unit distance travelled (Co_s), that is defined in Eq.VI.46. The corresponding trajectory is shown in Fig. VII.16,

with the variation of the thrust also pictured along the path. The flight path of minimal Co_s is performed with thrust applied during the climb, with a peak reached at the steepest climb slope. The maximal thrust intensity accounts to just under 5 % of the weight. The Co_s obtained represents only 45 % of $Conso_{min}$, suggesting that, under flight conditions specified by Fig. VII.16, the range could be more than doubled.

Subsequent variables, relative to Fig. VII.16, are plotted in Figs. VII.17 and VII.18. It shows the evolution of the thrust with respect to time and relative to other control and state variables. It can be observed that the peak in thrust occurs when wings are close to level, in the steepest part of the climb.

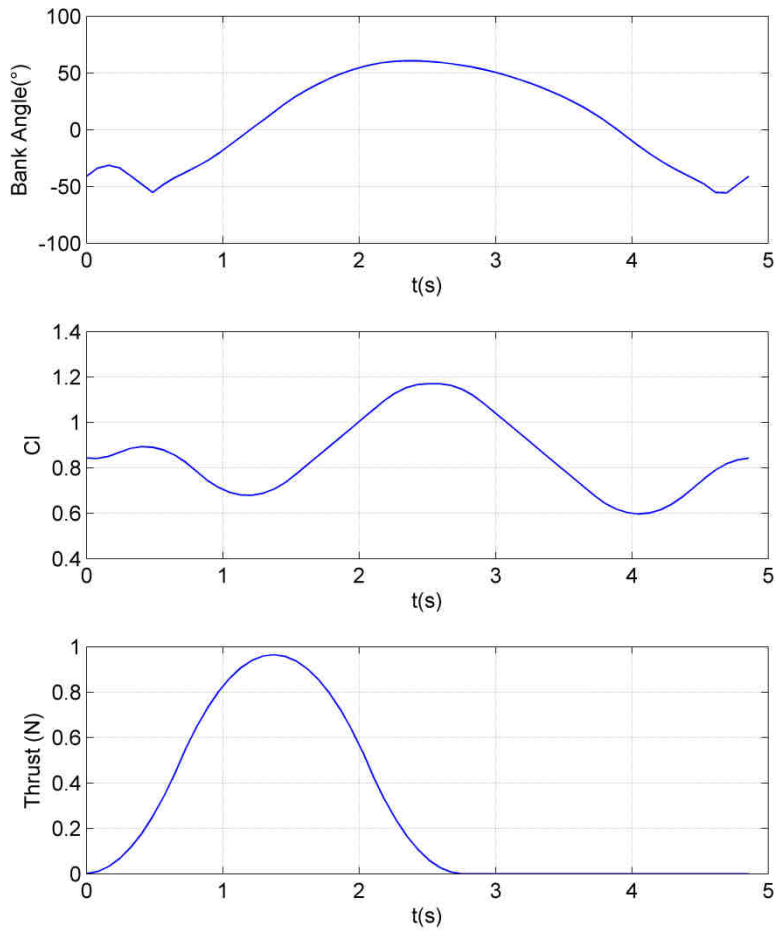


Figure VII.17: Evolution of ϕ , C_L and T with time, for *Mariner*, along the flight path that minimizes C_{O_S} .

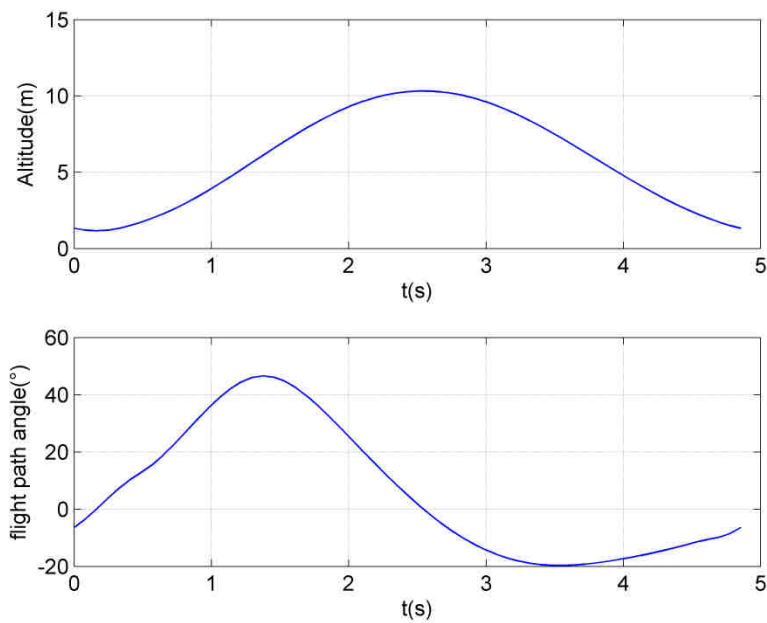


Figure VII.18: Evolution of the altitude and γ_i with time, for *Mariner*, along the flight path that minimizes C_{O_S} .

VII.3.2 Range Sensitivity to the Wind

Since DS flight is investigated as a way to enhance the vehicle range and endurance through the exploitation of wind, it is necessary to compare DS simulations with appropriate baseline cases. The approach undertaken in this part is to compare DS-induced performances with the nominal range of the vehicle in the presence of wind. Basic nominal performances calculations are introduced in Eq. III.4 and Eq. III.8 for the endurance and the range respectively. However, those are valid in still air and one may wonder how those vary with wind. Besides, as DS flight requires the presence of wind anyway, it is only consistent to compare DS-induced performances with wind-altered performances, before concluding on the eventual advantages of DS flight. The vehicle considered here is *Mariner*.

It has been presented earlier that endurance is directly related to the minimum sink rate of the vehicle. That latter parameter will not be influenced by the presence of horizontal wind, which basically means that the baseline maximum endurance of a vehicle would remain identical regardless of the presence of horizontal wind. However, the vehicle will be carried away by the wind during its flight. So if the endurance performance is required in association with the coverage of a specific area on the ground, the conclusion that the endurance does not depend on the wind strength is not so obvious. Still, let's try to address this question without calculations, but by conceptualizing a vehicle gliding in the wind. The endurance of the vehicle won't be affected if the vehicle manages to sustain its minimal sink rate. This functioning point is associated, among other parameters, to a specific airspeed, which would be called the airspeed of minimum sink rate. As long as the wind strength encountered is lower than the airspeed of minimum sink rate, the vehicle can make headway against the wind while maximizing its endurance. Hence, a closed trajectory, with respect to earth, can be flown without sacrificing the endurance. The extreme case of this later consideration happens if the wind speed is equal to the airspeed of minimum sink rate. In that case, the vehicle can face the wind, being motionless with respect to earth. It can be seen from Fig. III.9 that, in any case, the speed of minimum sink rate is just above 8 m.s^{-1} for *Mariner*, which gives an order of magnitude of the maximal wind strength the vehicle can handle without compromising on endurance. It can then be concluded that, unless specific cases, the endurance does not depend on the wind strength.

The case of the range is different. It refers indeed to a distance, while the vehicle flies with respect to the surrounding mass of air. The following lines detail a methodology that provides the functioning point of maximal range, for a vehicle in static flight within a windy

environment. A top view of that configuration case is provided by Fig. VII.19, the vehicle is flying in a straight line.

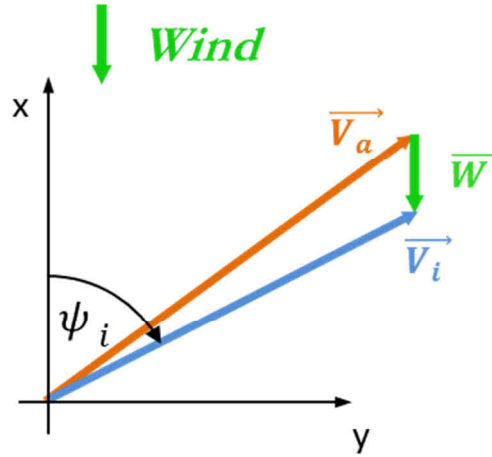


Figure VII.19: Top schematic view of the triangle of speed, between inertial speed, wind speed and airspeed, for a given inertial speed heading and a given wind speed.

The ratio between the distance flown, relative to earth, and the theoretical loss of height in gliding flight is expressed in Eq. VII.1.

$$\frac{Dist}{h} = \frac{\sqrt{V_{ix}^2 + V_{iy}^2}}{V_{iz}} \quad (VII.1)$$

The vectorial relation between speeds is reminded in Eq. VII.2.

$$\vec{V}_i = \vec{V}_a + \vec{W} \quad (VII.2)$$

It breaks down into three scalar equalities, detailed in Eq. VII.3.

$$\begin{cases} V_{ix} = V_{ax} - W_N \\ V_{iy} = V_{ay} \\ V_{iz} = V_{az} \end{cases} \quad (VII.3)$$

By combining Eq. VII.1 and Eq. VII.3, the ratio between the distance flown and the corresponding loss of height is expressed in Eq. VII.4.

$$\frac{Dist}{h} = \frac{\sqrt{V_{ax}^2 + V_{ay}^2 + W_N^2 - 2V_{ax}W_N}}{V_{az}} = \sqrt{\frac{V_{ax}^2 + V_{ay}^2}{V_{az}^2} + \frac{W_N^2}{V_{az}^2} - \frac{2V_{ax}W_N}{V_{az}^2}} \quad (VII.4)$$

Besides, the equilibrium state is translated into Eq. VII.5, regarding forces involved.

$$\begin{aligned} \frac{1}{2}\rho \cdot S \cdot C_L \cdot V_a^2 &= mg \cos \gamma_a \\ \frac{1}{2}\rho \cdot S \cdot C_D \cdot V_a^2 &= -mg \sin \gamma_a \end{aligned} \quad (VII.5)$$

Hence the lift to drag ratio is expressed in Eq. VII.6.

$$\frac{C_L}{C_D} = -\frac{1}{\tan \gamma_a} \quad (VII.6)$$

The airspeed components relate, by definition, as detailed in Eq. VII.7.

$$\begin{aligned} V_{az} &= -V_a \sin \gamma_a \\ \sqrt{V_{ax}^2 + V_{ay}^2} &= V_a \cos \gamma_a \end{aligned} \quad (VII.7)$$

By combining Eq. VII.6 and Eq. VII.7, it directly leads to Eq. VII.8.

$$\frac{C_L}{C_D} = \frac{\sqrt{V_{ax}^2 + V_{ay}^2}}{V_{az}} \quad (VII.8)$$

Hence, by replacing Eq. VII.8 into Eq. VII.4, the ratio between distance flown and loss of height is expressed in Eq. VII.9.

$$\frac{Dist}{h} = \sqrt{\left[\frac{C_L}{C_D}\right]^2 + \frac{W_N^2}{V_{az}^2} - \frac{2V_{ax}W_N}{V_{az}^2}} \quad (VII.9)$$

Equation VII.9 underlines that, with the presence of wind, the ratio between distance travelled and height lost is no longer equal to the lift to drag ratio. Rather, it involves, among

others, the wind speed. Yet, the ratio detailed in Eq. VII.9 is directly related to the in-flight energy-expenditure, as it is reminded in Eq. VII.10.

$$E_{expenditure} = mg * h = mg * \frac{h}{Dist} * Dist \quad (\text{VII.10})$$

The Eq. VII.11 is therefore obtained, specifying the minimum energy consumption per unit length travelled, which guarantees the maximal range.

$$Conso_{min} = \frac{mg}{(Dist/h)_{max}} \quad (\text{VII.11})$$

By replacing Eq. VII.9 in Eq. VII.11, the minimum consumption writes down as in Eq. VII.12.

$$Conso_{min} = \frac{mg}{\left[\sqrt{\left[\frac{C_L}{C_D} \right]^2 + \frac{W_N^2}{V_{az}^2} - \frac{2V_{ax}W_N}{V_{az}^2}} \right]_{max}} \quad (\text{VII.12})$$

In order to maximize the range in the presence of wind, the vehicle must not fly at the maximum lift to drag ratio anymore, but rather maximize the expression into brackets detailed in Eq. VII.12. Note that if the wind W_N is zero, Eq. VII.12 does well merge into Eq. III.7. The result highlighted by Eq. VII.12 is well known by glider pilots, which must adapt their airspeed to the wind intensity in order to optimize their range. This also applies when the motion of air is vertical, when meeting updrafts or downdrafts, albeit speed components obviously right down differently. An application is given by Chakrabarty *et al.* [96], which focuses on exploiting an a-priori map of vertical components of the air using heuristic search. Adapting the airspeed to in-flight conditions is part of the problem. In the present case, conditions in terms of flight path heading and wind speed are known, the objective consists in maximizing the range and is formalized in the Eq. VII.13.

$$Maximize \left(\left[\frac{C_L}{C_D} \right]^2 + \frac{W_N^2}{V_{az}^2} - \frac{2V_{ax}W_N}{V_{az}^2} \right) \quad (\text{VII.13})$$

It is a relatively straightforward optimization problem, as the airspeed is the only variable at stake. A simple methodology to find the extremum is derived in the following lines. First, an expression for the x -component V_{ax} of the airspeed is sought.

By definition, components of the horizontal inertial speed relate to the inertial flight heading angle as given in Eq. VII.14.

$$\tan \psi_i = \frac{V_{iy}}{V_{ix}} \quad (\text{VII.14})$$

Equation VII.15 is obtained by substituting Eq. VII.3 into Eq. VII.14.

$$\tan \psi_i = \frac{V_{ay}}{V_{ax} - W_N} \quad (\text{VII.15})$$

Equation VII.16 is given by definition.

$$V_{ax}^2 + V_{ay}^2 = (V_a \cos \gamma_a)^2 \quad (\text{VII.16})$$

Equation VII.15 and Equation VII.16 form a system with two unknowns, V_{ax} and V_{ay} , summed up in Eq. VII.17.

$$\begin{cases} (V_{ax} - W_N) \tan \psi_i = V_{ay} \\ V_{ax}^2 + V_{ay}^2 = (V_a \cos \gamma_a)^2 \end{cases} \quad (\text{VII.17})$$

The x -component of the airspeed can be found by solving the quadratic Eq. VII.18, obtained from Eq. VII.17.

$$V_{ax}^2(1 + \tan^2 \psi_i) - V_{ax} 2 W_N \tan^2 \psi_i + [W_N^2 \tan^2 \psi_i - (V_a \cos \gamma_a)^2] = 0 \quad (\text{VII.18})$$

Finally, the process to maximize the expression stated in Eq. VII.13 is to iterate through discrete values of the airspeed V_a . Steps are enumerated as follow. First, for a given value of the airspeed V_a , the corresponding aerodynamic coefficients at equilibrium are trivially computed through Eq. VII.19.

$$\begin{cases} C_D = C_{D0} + C_{D1}C_L + C_{D2}C_L^2 + C_{D3}C_L^3 + C_{D4}C_L^4 \\ \sqrt{C_L^2 + C_D^2} = \frac{mg}{1/2 \rho \cdot S \cdot V_a^2} \end{cases} \quad (\text{VII.19})$$

Then, the corresponding air relative glide angle is computed out of the aerodynamic coefficients C_D and C_L , as follow in Eq. VII.20.

$$\gamma_a = -atan \frac{C_D}{C_L} \quad (\text{VII.20})$$

So it directly gives Eq. VII.21, providing the air relative sink rate.

$$V_{az} = V_a \sin \gamma_a \quad (\text{VII.21})$$

The final step is to find V_{ax} by solving Eq. VII.18. Therefore, by knowing V_{ax} and V_{az} , the expression defined in Eq. VII.13 can be estimated. And so on so forth for various iterations on the input value of the airspeed V_a , until a maximum is reached.

Therefore, for any given travel heading ψ_i with respect to the wind direction, and for any given wind strength W_N , the airspeed corresponding to the minimal consumption per unit length travelled can be found. And so is the related consumption.

This methodology is applied, for *Mariner*, in a specific case, in order to illustrate the influence of W_N and ψ_i on the achievable range in straight flight. Since the vehicle's range depends on the capacity of its battery, which is undetermined, the ratio between the range with wind and the nominal range enables to draw performance comparisons. It can be expressed in Eq. VII. 22.

$$\text{Range Ratio} = \frac{\text{Range with Wind}}{\text{Nominal range}} = \frac{\left[\sqrt{\left[\frac{C_L}{C_D} \right]^2 + \frac{W_N^2}{V_{az}^2} - \frac{2V_{ax}W_N}{V_{az}^2}} \right]_{max}}{(L/D)_{max}} \quad (\text{VII.22})$$

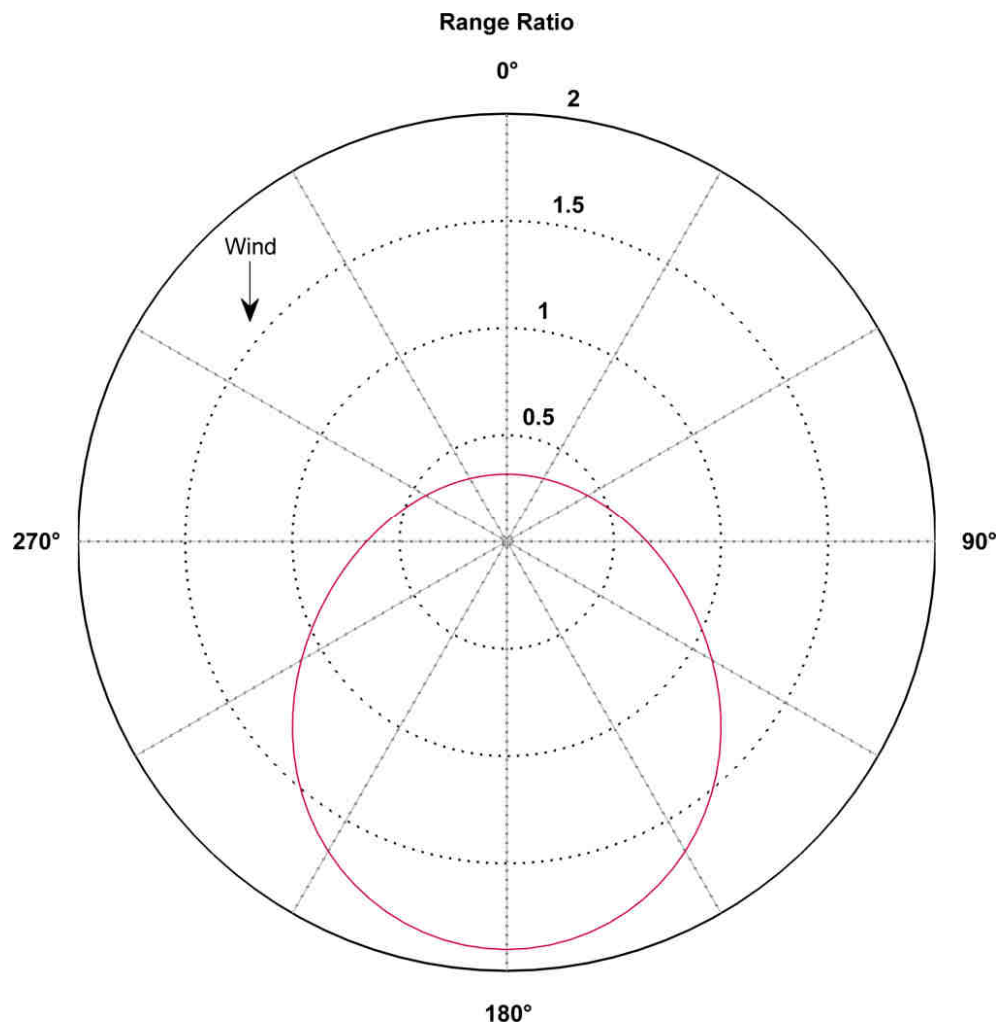


Figure VII.20: Evolution of the range ratio versus the flight heading, for a given wind. Chart obtained for *Mariner*, flying in straight line, under a wind strength of 8 m.s^{-1} .

The influence of the wind on the achievable range is clearly depicted on Fig. VII.20. It displays that if *Mariner* flies straight into 8 m.s^{-1} -strong headwind, its maximum range would be reduced by more than half compared to its nominal range without wind. On the opposite, if *Mariner* flies completely leeward, its range can almost be doubled. The overall “egg-shaped” pattern obtained is not a circle, as it would be if the vehicle was flying at a constant airspeed in all directions. An interesting aspect of the alteration of range performance can be observed. It concerns the case where the vehicle needs to follow a heading on the ground which is oriented crosswind, in this case, $\psi_i = 90^\circ$ (or 270°). It can be observed that the associated range is significantly reduced, by more than 25% compared to the nominal case. The proper explanation is that the vehicle is actually facing the wind to some extent in order to maintain an inertial crosswind heading. The airspeed has a component against the direction of the wind, which comes at a direct range penalty. A true air relative crosswind flight happens when the airspeed

is orthogonal to the wind. In this latter case, the range along the direction orthogonal to the wind is unaffected, but the vehicle is also carried away by the wind in the process, which means that the overall range is augmented. It happens, in Fig. VII.20, for $\psi_i=132^\circ$ (or 228°), where it can be observed that the crosswind component of the range ratio is equal to 1. Stated otherwise, it is the only inertial heading that gives the maximum range in the crosswind direction.

Now that the methodology to find the maximum range of a vehicle in straight static flight, under windy conditions, is laid down, it can be applied for the sake of comparison with DS-enabled range.

VII.3.3 Range enhancement by DS

For this last study case, the range in straight line is compared to the range obtained by DS, for various heading angles and for several wind speeds. The objective function is still to minimize Co_s . However, operational parameters were chosen carefully to match potential realistic operational conditions. Indeed, the aim is to get to a consistent quantification of the improvement DS could provide to the long range flight of a UAV.

The vehicle is *Mariner*, with a virtual payload of 2 kg, such that the overall mass is 4 kg. The surface roughness length $z_0=2\text{ cm}$ is chosen in order to match that of an open terrain, covered with low grass [76]. The altitude is limited directly through a minimal altitude constraint at the centre of gravity, as it is assumed it corresponds to a more realistic operational case than monitoring the wing tip clearance. A conservative value of 2 metres was chosen, such that even banked to the maximum, *Mariner* would clear the ground, at its wing tips, by a margin of at least 75 cm. Besides, since DS results would be compared to a straight line case, it is also necessary to limit the maximal altitude, otherwise the vehicle could opt for unlimited heights to seek for stronger winds and the problem would be unconstrained. We decided that 1000 metres was a fair order of magnitude, for both the upper validity bound of our log-wind profile model and the operational altitude of a small UAV. Other than that, all other parameters were kept identical.

The metric plotted consists in the range ratio, defined in Eq. VII.22. Straight line results are obtained by applying the methodology applied developed in VII.3.2, with a further degree of freedom since the altitude can vary between 2 and 1000 metres. A simple comparison loop is used to determine the altitude which optimizes the straight-line range. As for DS results, the net heading angle ψ_{net} is incremented step by step by intervals of 0.2° . Variables of the next

calculation point are initiated by using results from the previous calculation point, leading to potential discontinuities, in the objective function, related the local nature of the optimum found, as discussed earlier.

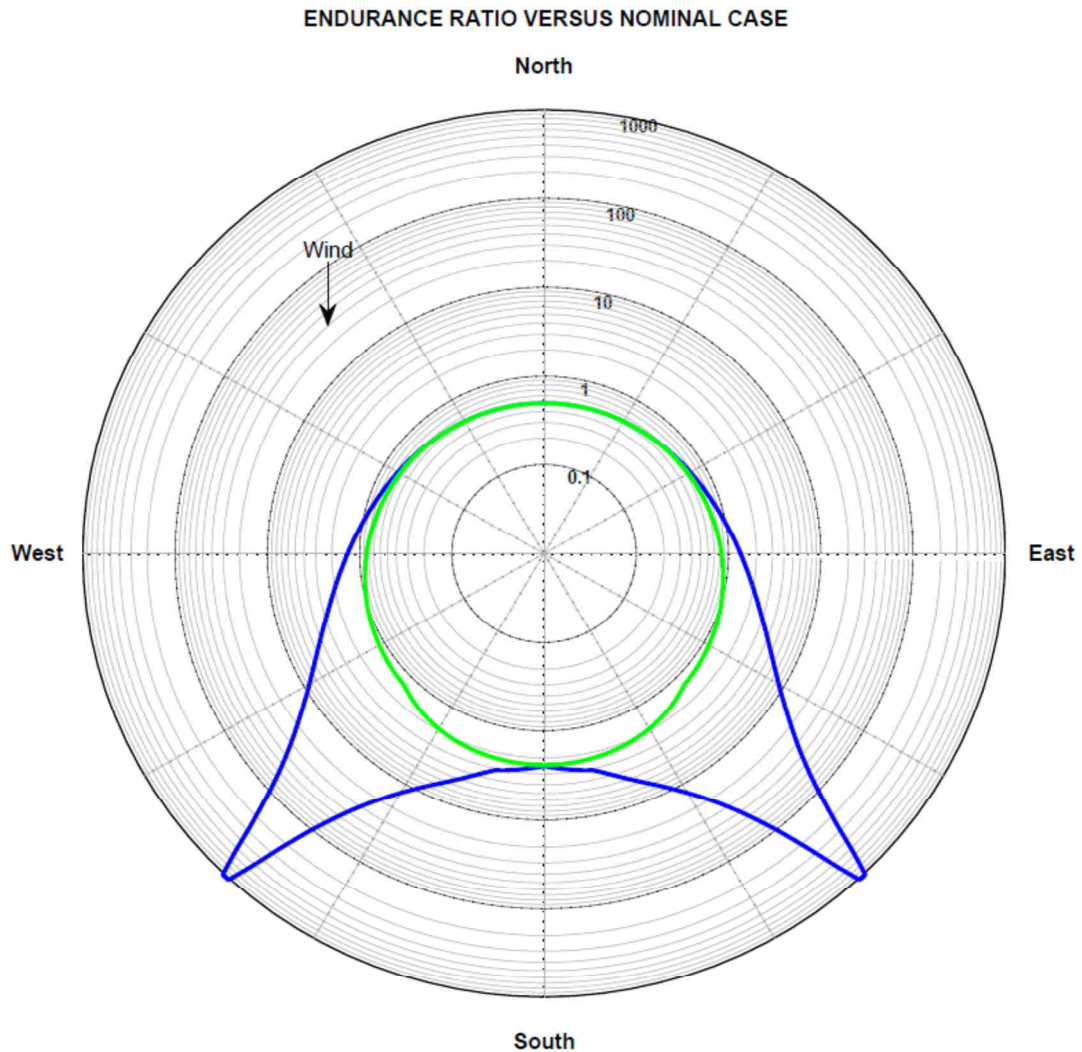


Figure VII.21: Variation of the range ratio with respect to the net heading angle, compared to the straight line case, for $u_* = 66 \text{ cm/s}$, which corresponds to a wind strength of 10 m/s at an height of 10 metres . In green, results from straight line, in blue, results from DS.

A first simulation is run for a wind friction velocity just below the minimum wind strength required for DS gliding flight. To begin with, the straight line case, seen in Fig. VII.21, displays the leeward shift that was described earlier. Yet, a variation in curvature can be noticed for $\psi_{net} \sim \pm 135^\circ$. It corresponds to the net heading angle at which the vehicle swap from a straight line at the lowest altitude to a straight line at the highest altitude. On the windward part of the curve, the vehicle flies as close as possible to the surface to get the lowest headwind as possible. On the contrary, on the leeward side, the vehicle takes advantage of the

strongest possible tailwind to increase its range. Regarding DS results, the range shows a significant maximum for ψ_{net} around 135° , which corresponds to values of the heading angle that were minimizing the required wind strength. It hence reinforces the assertion that DS flight largely favours flight headings in this area. Besides, it is also the zone that was identified by biologists as the predominant travel heading of albatrosses under strong wind conditions [29]. At the maximum, the range provided by DS is more than a *1000* times the straight line range. It almost diverges because the wind strength is close to that which allows virtually perpetual flight. An important aspect is that for windward flight headings, the DS curve merges with the straight line curve, suggesting that when heading $\pm 45^\circ$ into the wind, the best option is to fly straight, at the minimum altitude. DS proves more efficient than the straight line for some flight paths that have a windward facing component. This underlines that DS can be beneficial, even in some cases when the flight path has a windward component. The advantage of using DS versus straight line in those configurations is not to be underestimated by the log-scale applied, as the range offered by DS can be up to *30 %* higher. For leeward flight headings, even though the vehicle flies at the maximum altitude in straight line, the DS flight provides a significant range advantage all the way until $\psi_{net} = \pm 180^\circ$, where the two curves join.

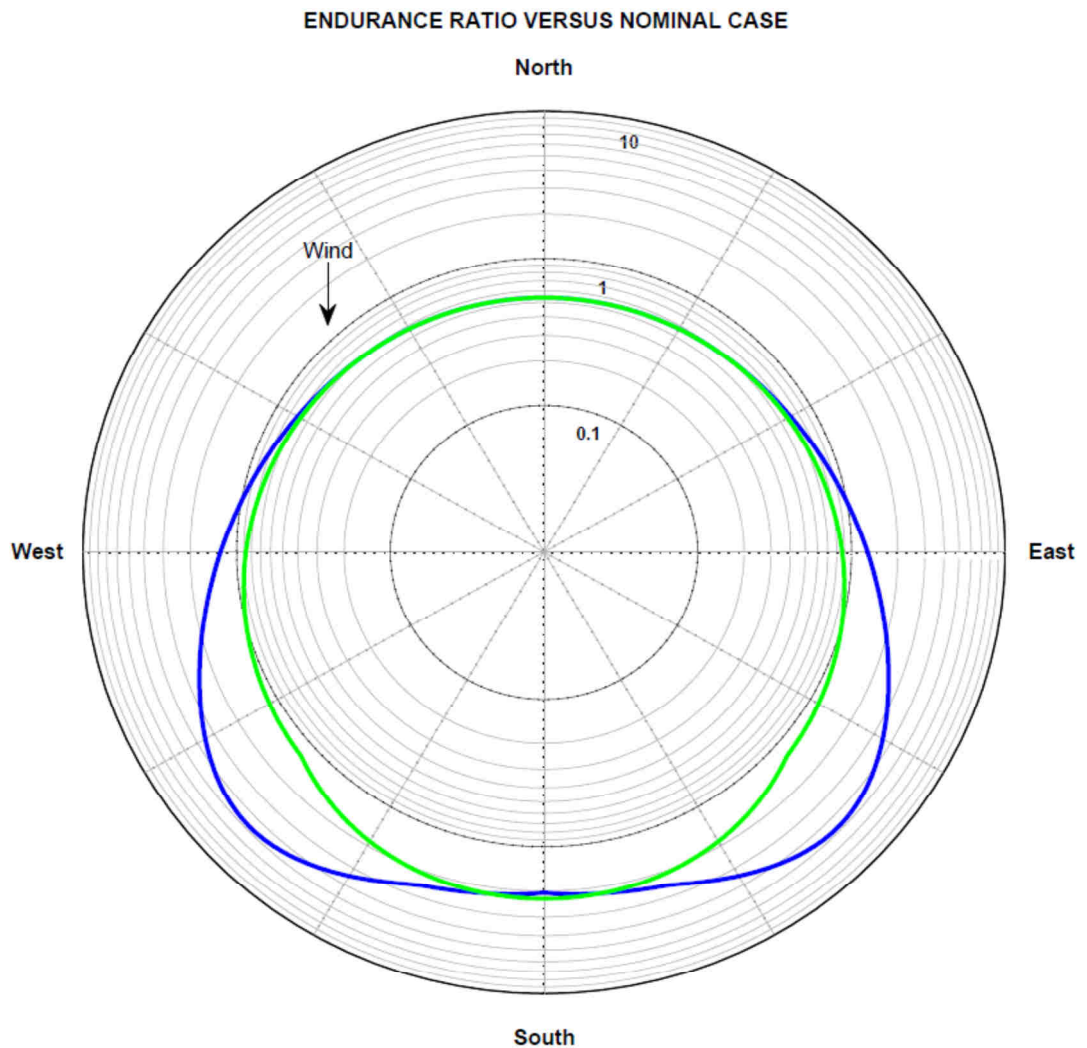


Figure VII.22: Variation of the range ratio with respect to the net heading angle, compared to the straight line case, for $u_* = 59.4 \text{ cm/s}$, which corresponds to a wind strength of 9 m/s at an height of 10 metres . In green, results from straight line, in blue, results from DS.

When the wind strength decreases to 9 m/s at 10 metres , as displayed in Fig. VII.22, the maximum of the DS range shrinks to only 5 times the nominal zero wind range, which is also almost 5 times the straight line range. All other aspects of the curves mentioned earlier are repeated here, to the exception of flight paths directly down wind, where the DS range is lower than the straight line range. This illustrates very well the fact that the optimum found by the optimization routine can be local and can therefore be outperformed by a trajectory which is also a solution of the optimization problem. Even though DS trajectories merge into a straight line, when the flight path orientates windward, it does not happen identically leeward.

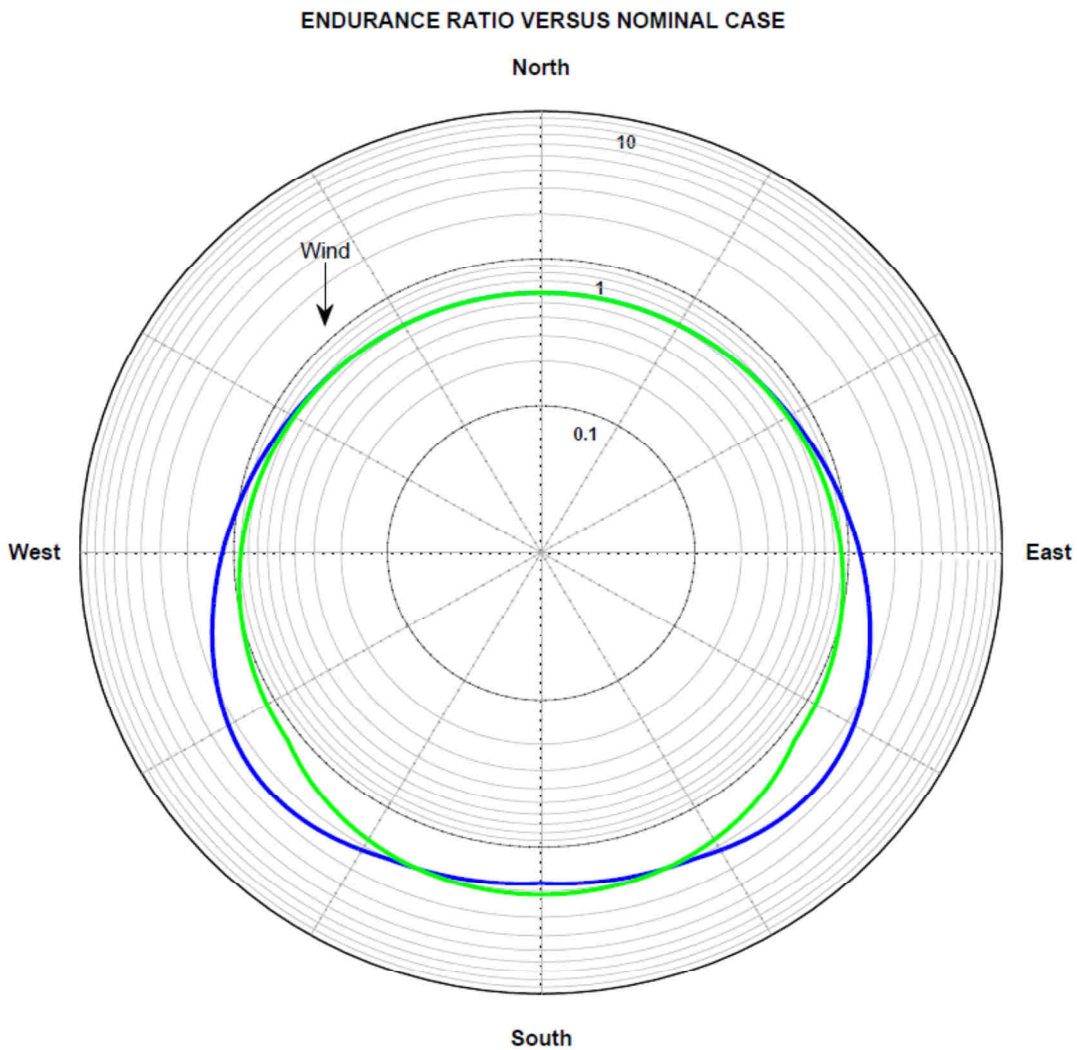


Figure VII.23: Variation of the range ratio with respect to the net heading angle, compared to the straight line case, for $u_* = 54.7 \text{ cm/s}$, which corresponds to a wind strength of 8 m/s at an height of 10 metres . In green, results from straight line, in blue, results from DS.

For a wind strength of 8 m/s at 10 metres , as presented in Fig. VII.23, the maximum in DS range shrinks to around 2 times the range of the straight line and the heading angle of that maximum is shifted windward. Overall, DS becomes advantageous over the straight line for only $\sim 50 \%$ of the flight headings. Besides, the gap, leeward, between straight line and DS, increases.

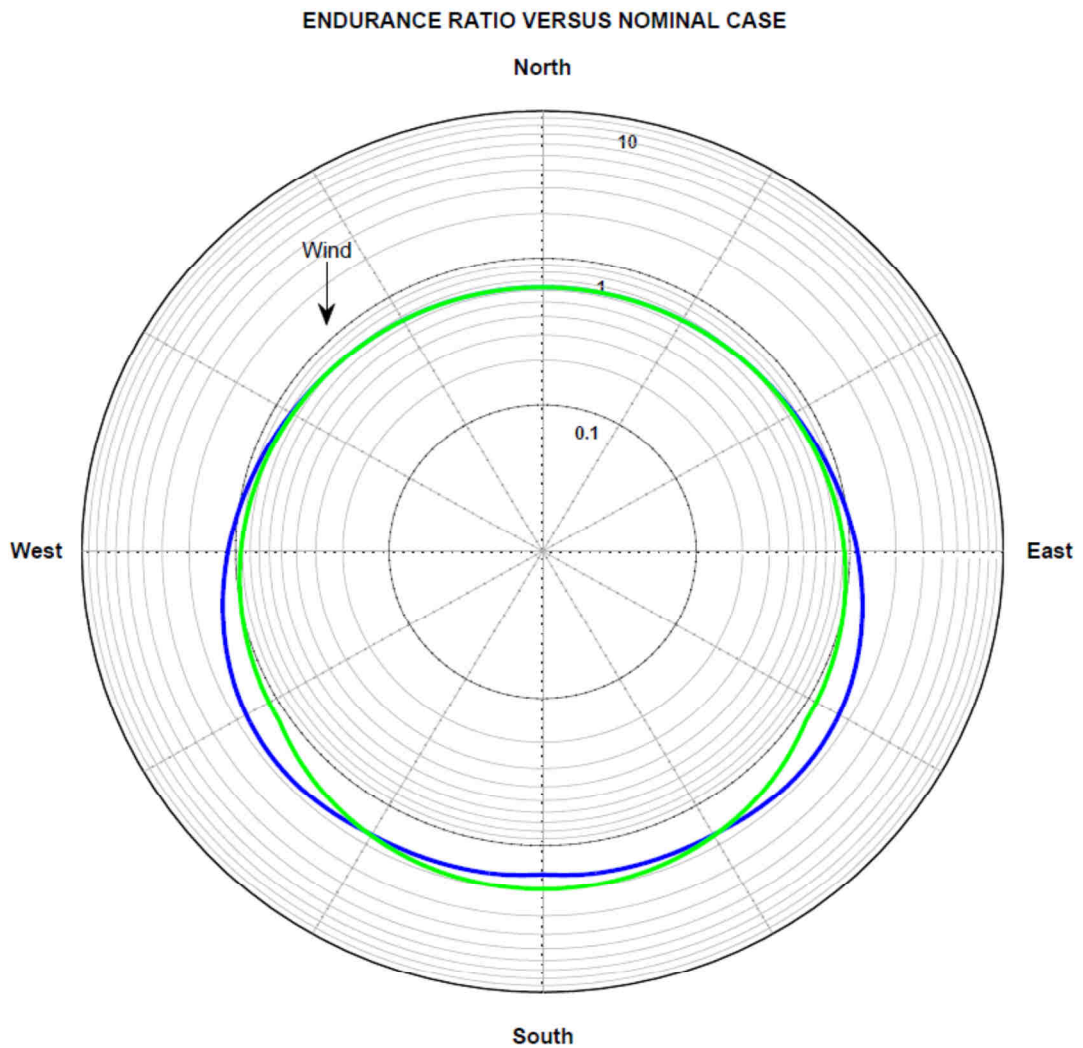


Figure VII.24: Variation of the range ratio with respect to the net heading angle, compared to the straight line case, for $u_* = 47.9 \text{ cm/s}$, which corresponds to a wind strength of 7 m/s at an height of 10 metres . In green, results from straight line, in blue, results from DS.

For a wind strength of 7 m/s at 10 metres , as displayed in Fig. VII.24, the improvements in range do not seem high enough, on most of the compass rose, to justify the complexity of DS flight. To the exception of flight path near $\psi_{net} = \pm 120^\circ$, where DS trajectories still manage around 50% better range compared to straight line.

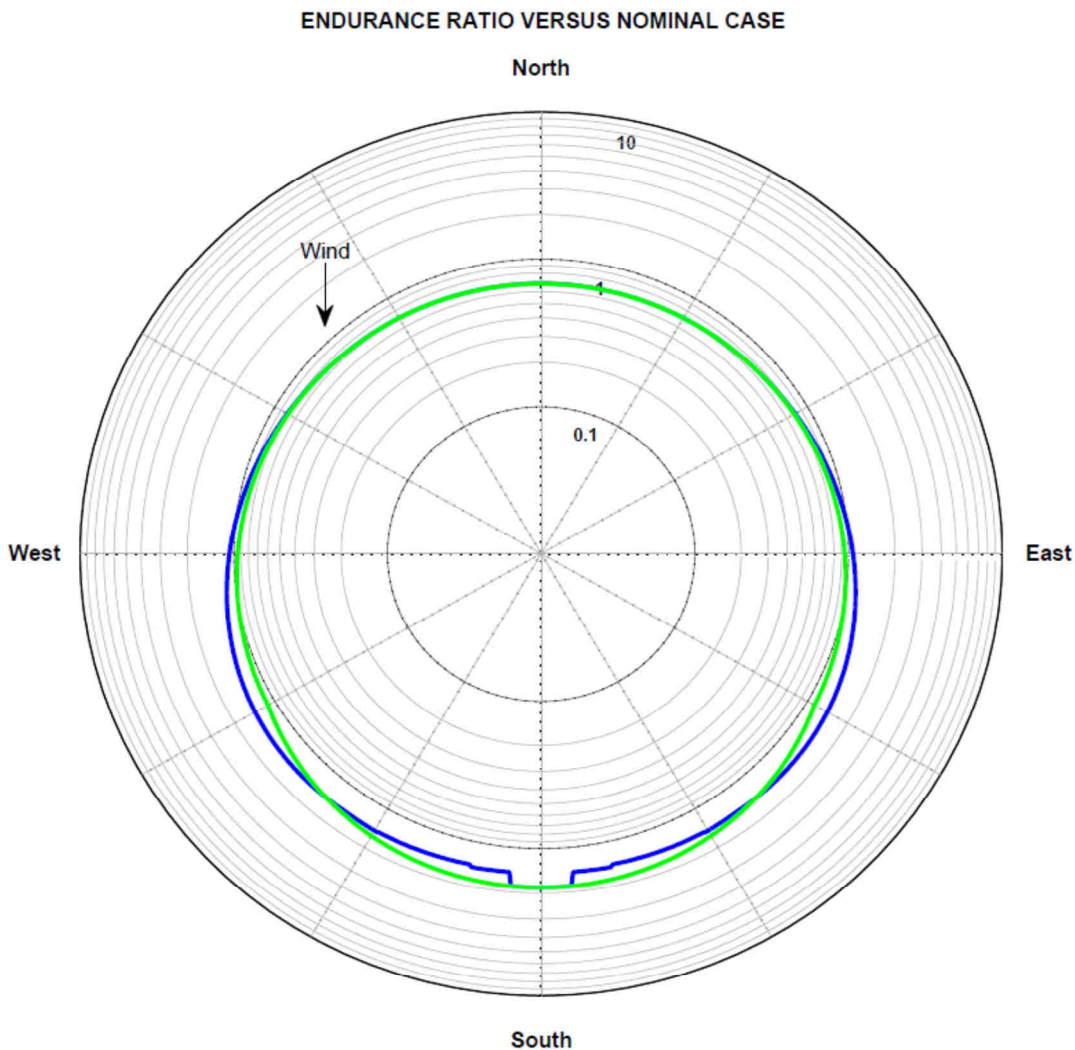


Figure VII.25: Variation of the range ratio with respect to the net heading angle, compared to the straight line case, for $u_* = 41.06 \text{ cm/s}$, which corresponds to a wind strength of 6 m/s at an height of 10 metres . In green, results from straight line, in blue, results from DS.

For wind strength of 6 m/s at 10 metres , as seen in Fig. VII.25, the difference in range between straight line and DS is marginal and do not justify the use of DS on any heading of the compass rose. An interesting aspect at leeward headings is that the DS curve finally merges with the straight line curve. The DS optimization process indeed yields a straight line at the maximum altitude for those headings. The subsequent discontinuity in the DS range curve confirms the local nature of the optimum before it merges with the straight line curve.

VII.4 Summary on DS Performances

It is first demonstrated that DS is potentially feasible for a wide array of vehicle size, with yet significant disparities in required wind strength. It is established that larger vehicles could benefit from less favourable conditions. Even though no specific driving aerodynamic parameter is outlined, aerodynamic refinements of larger vehicle enable to overbalance their induced mass and wingspan penalties. Ideally, lightweight architectures of small wing span, low sink rate and high lift to drag ratio would favour DS flight. Practically, some of those properties are antinomic and the compromise appears to favour larger vehicles. This result is somehow encouraging from an application's perspective, yet there must be an upper scale to that trend and limitations of the point mass model certainly arise when the scale of the wingspan becomes comparable to that of the wind gradient.

As for variations in DS performance, a specific focus is given to two governing variables: the ground clearance and the surface roughness length z_0 . The ground clearance directly affects the required wind strength and the array of feasible net travelling angle ψ_{net} towards the wind. A reduced ground clearance lowers the required u_* and widens the range of feasible ψ_{net} . Yet, for $z_0=1\text{ cm}$ and zero tip clearance, flight headings are still limited such that making headway against the wind is not possible. As for z_0 , in confirmation with the theory from Chapter VI, it does not affect the minimum required u_* . Yet it changes the earth-relative motion of the vehicle: a rougher surface enables to exploit DS for lower wind speeds and for a wider scope of ψ_{net} , eventually leading to DS opportunities all around the compass rose. Therefore, DS performances are intrinsically linked to surface characteristics and sea-surface conditions are challenging to exploit.

In order to widen the range of favourable DS conditions, thrust was added as an extra control variable. The wind hence only contributes to a fraction of the vehicle's energy needs. When thrust is applied during the upwind climb, the vehicle can take the most out of its propelling work by reaching stronger winds. The advantage of DS flight is assessed by comparing DS-enabled-range and straight-line-range. Significant improvements can be achieved by DS, even when the wind is 30 % lighter than previously required, but there are significant variations with ψ_{net} . Range enhancements are possible even when heading against the wind, but when u_* decreases, the advantage of DS reduces and becomes limited to values of ψ_{net} where DS is most efficient, around 135° , in accordance with albatross observations

CONCLUSION

The present work has focused on providing an in-depth analysis of DS flight, by detailing the methodology, the understanding and the performances associated with DS simulations. It completes past studies on DS by investigating further many multidisciplinary aspects associated with the topic and by its intention to give shape to a consistent and extensive overview of DS challenges.

Summary of findings

An extensive review of the engineering inputs from albatross biology studies is undertaken in the first Chapter. Although many publications on DS mention some aspects related to the albatross flight, this part aims at gathering in a single document all the pieces of information that can raise interest and guidance out of the observation of albatrosses. Then this literature review is extended to publications in the domain of in-flight energy extraction.

A methodology is set up in order to adequately model the flying system and its environment. In particular, the choice of a point mass model for the vehicle is explained and is quantified for one of the three geometries chosen, through a wind tunnel testing campaign. Besides, a methodology to relate wind and ocean surface state is extensively detailed, which constitutes a first step towards conciliating wave soaring with dynamic soaring. The main contribution from this part is to underline that realistic ocean surface roughness lengths are an order of magnitude lower than what has been considered in DS literature so far. Only shallow wave trains are considered, representative of a well-developed swell and the hypothesis behind the model are developed.

Equations of motion are derived by beginning to underline the significance of the point of view considered. Both earth-relative and air relative systems of EoM are derived before selecting inertial equations for the remaining of the methodology. An optimization problem is set up, laid out in its structure before a particular focus is given to numerical integration techniques required to convert the underlying problem. Collocation methods are presented step by step, by highlighting the underlying mathematical hypothesis. The induced parameter optimization problem is detailed and numerical values for operational constraints are given for each vehicle. The solving methodology and the associated tools are presented with a brief

description of their mathematical background. The problematic of variable initiation and of local optimizer is introduced, to be reminded for results obtained. Eventually, a trajectory of similar conditions as in the literature is run before validating the methodology thanks to the analogy obtained.

A specific closed-trajectory is produced to highlight the loitering potential of DS flight, as well as to serve as a support for developing an understanding of energy-harvesting mechanisms. Local power input expressions are established for various contributions and explained in their variations, before integrating those along the whole flight path into evolution in total energy. A particular focus is given to wind energy exchange within the boundary layer. Periodicity constraints are partly relaxed to get to an open loop which combines the same phases of flight as the closed loop. Then a specific study case that optimizes DS within the wavy ocean boundary layer model is established. It shows that the methodology of DS flight simulation can be applied to a three dimensional moving wind field to produce trajectories that associates classical DS with a kind of slope soaring on the forward moving face of wave. The positive contribution from the wave updraft is detailed and changes in wave phase periodicity are performed.

Fundamentals of DS flight are then approached by non-dimensionalization of the air relative EoM. First with a linear wind profile, as inspired from the literature, then by achieving for the first time a non-dimensionalization with a logarithmic wind profile. Several objective functions are tested and a thrust-augmented case is introduced. Conditions to equivalences in dimensionless solutions are given. On top of providing a strong support for validating the simulation methodology, the approach permits to highlight certain remarkable behaviour about DS, such as the sensitivity to wing loading and the invariance of the minimum required wind friction velocity with the roughness length.

Then, the focus was given to flight performances by DS. The three different vehicle architectures are tested under identical operational constraints, before concluding that the planform of the biggest scale is the most promising for maximizing the likelihood of DS flight. Then, the influence of the net heading angle, the ground clearance and the surface roughness length was established for DS gliding flight. It leads to the conclusion that favourable conditions for DS flight over a wide range of heading angles are difficult to meet. Hence an alternative is presented by assisting thrust-powered flight with DS. The evolution of that third control variable is detailed before DS range charts are produced and compared against the case of straight line case.

With the benefit of hindsight, this project managed to outline a methodology that successfully simulates DS flight. It shows to be rather robust and can accommodate varying constraints and objectives. One of the strongest assumptions is the choice of a point mass model, which imposes that the operational constraints linked with the vehicle dynamics are artificially imposed rather than modelled. Besides, this model reaches its limit when the length scale of the wind gradient gets similar to that of the vehicle. This may happen especially during the low turn, when the vehicle is banked at low altitude within the zone of strong shear. Furthermore, the initiation of variables, before passing the problem to the solver, is also critical and may lead to different solutions. It requires a careful approach and eventually a guess of what the solution may look like.

Then, mechanisms of energy-harvesting are properly understood and thoroughly detailed. The work of aerodynamic forces is the main parameter at stake and the DS flight path is a cycle that orientates those forces successively such that gains overbalance losses. The upper turn is the main contributor to the energy gain, through the attitude belly-to-the-wind-attitude that sees a strong acceleration of the vehicle in the direction of the wind. The lower turn is all the more critical as it concentrates the biggest losses. As such, the minimum altitude allowed is a key parameter since it directly impacts the wind strength opposed to the vehicle. The wind gradient does not alter the local work of aerodynamic forces but plays a role when the vehicle kinematics is integrated over the whole flight path, as it introduces disparities in wind strength between the top and the bottom of the trajectory.

Finally, variations in DS performances were quantified against variations in vehicle design, ground clearance and surface roughness length, before drawing DS-induced range performance charts. A first conclusion is that practical flight applications are favourable for a lightweight planform of bigger scale than the albatross, with refined gliding performances. A second result is that unless very rough terrain is met, with close ground clearance margins, the scope of DS is limited to certain flight headings with respect to the wind. Hence, one approach to cope with such limitations is to introduce thrust-augmented DS, where the vehicle provides only a fraction of the energy it requires to stay aloft. Results show that the range can be improved for a wide range of flight path headings, for winds that are lighter than those required for pure gliding DS flight.

Perspectives

Given that even thrust-augmented DS requires rather demanding windy conditions in order to stand out performance-wise, the challenge of future DS research is to find solutions that lower the required wind strength and hence widen the scope of exploitable environment conditions. As such, several direction of research can be followed.

- Investigate the vehicle planform optimized for lowering the required wind strength to exploit DS, without a-priori limitations regarding the vehicle design, in order to yield the absolute lowest wind strength exploitable, given state of the art designs. Orientate the design towards a planform of bigger scale than the albatross.
- Integrate further refined control behaviours, by investigating the potential advantage of active flap deflection. Since the vehicle is defined by an aerodynamic polar, morphing the polar along the flight path has obvious promising prospective, and a simple and known way to do so is to introduce flap deflection. Besides, ground effect would also influence the aerodynamic polar at low altitudes and it would be interesting to weigh the influence it has on DS trajectories by implementing a simple model of ground effect. Also, the theme of regenerative soaring can be approached by first investigating the influence of a thrust which can be negative, in order to model in-flight energy recuperation.
- In the case of DS within a turbulent boundary layer, develop an objective function which integrates DS inputs of various frequencies due to different wind contributions. Hence, augment classical DS within the mean wind profile of the boundary layer with gust soaring contributions that benefit from the stochastic turbulent behaviour of the boundary layer. It would be essential to model the influence of a local span-wise variation in wind strength on the flight dynamics and energetics and hence move to a six-degree-of freedom-model to fully investigate its influence.

- Approach DS within various wind shear regions to benefit from stronger wind gradients or from a linear spatial variation. As for the first case, DS on the leeward side of a hill, or a building, may benefit from a stronger wind shear, without the inconvenience of very close ground proximity. As for the second case, it is shown in Chapter VI that a linear wind profile could be exploited for much lower wind speeds. An environment where this happens and is rather predictable is the so-called jet stream.

Another area requires further research in order to conclude on the feasibility to perform DS for a UAV. The demonstration would be indeed completed when a proper vehicle manages to autonomously exploit DS trajectories and when the subsequent energy-harvesting mechanisms are measured and validated. To that extent, several directions of research can be outlined.

- Propose a flight control strategy that uses only limited a-priori knowledge of the wind field, together with in-flight wind measurements and ground proximity sensors in order to autonomously pilot DS trajectories.
- Apply the state of the art DS methodology within a stochastic turbulent boundary layer to assess the influence of gusts on the flight path for unchanged flight controls and quantify the influence on the energy-harvesting. Conclude on the feasibility to apply the current DS strategy to the real-world.
- Finally, set-up an experiment using a well-quantified platform over an open field covered with regular low grass, such as an airfield. The vehicle has to be equipped with the appropriate airspeed and GPS sensors to be able to reconstruct the local wind speed. The experiment can be guided by a human-pilot at first, that approximately reproduce DS flight path, and then the guidance should be left to an auto-pilot in order to validate the flight path strategy. A robust design should be chosen, as the close ground proximity would likely induce accidental collisions until the ground clearance constraint is well integrated into the flight path management.

References

- [1] “Nature's Lessons”, *Flight international*, pp. 22-28, August 2010.
- [2] “SmartBird,” FESTO, 2011. [Online]. Available:
http://www.festo.com/cms/en_corp/11369.htm.
- [3] “Nano Hummingbird”, AeroVironment, 2011. [Online]. Available:
<http://www.avinc.com/nano>.
- [4] “robot-dragonfly”, Techjet, 2012. [Online]. Available: <http://techject.com/robot-dragonfly/>.
- [5] “X-47B UCAS”, Northrop Grumman, 2013. [Online]. Available:
<http://www.northropgrumman.com/Capabilities/X47BUCAS/Pages/default.aspx>.
- [6] “Giant Solar-Powered UAVs Are Atmospheric Satellites”, *IEEE Spectrum*, August 2013. [Online]. Available: <http://spectrum.ieee.org/automaton/robotics/aerial-robots/giant-solar-powered-uavs-are-atmospheric-satellites>.
- [7] “Swiss pilots attempt first around-the-world solar flight”, *The Guardian*, 9 March 2015. [Online]. Available: <http://www.theguardian.com/environment/2015/mar/08/swiss-pilots-attempt-worlds-first-around-world-solar-flight>.
- [8] US Department of Defense, “Unmanned Aircraft Systems Road Map 2005-2030”, July 2005, p.51.

- [9] K. E. Swider-Lyons, J. A. MacKrell and J. A. Rodgers, "Hydrogen Fuel Cell Propulsion for Long Endurance Small UAVs", in *AIAA Centennial of Naval Aviation Forum "100 Years of Achievement and Progress"*, AIAA 2011-6975, Virginia Beach, VA, 21-22 September 2011,.
- [10] K. Swider-Lyons, R. Stroman, J. Rodgers, D. Edwards and J. Mackrell, "Liquid Hydrogen Fuel System for Small Unmanned Air Vehicles", in *51st AIAA Aerospace Sciences Meeting including the New Horizons Forum and Aerospace Exposition*, AIAA 2013-467, Grapevine, Texas, 2013.
- [11] "Liquid hydrogen extends fuel cell-powered UAV to 48h aloft", Flight International, June 2013. [Online]. Available: <http://www.flightglobal.com/news/articles/liquid-hydrogen-extends-fuel-cell-powered-uav-to-48h-386686/>.
- [12] "UAV flies on laser light", IEEE Spectrum, 2012. [Online]. Available: <http://spectrum.ieee.org/tech-talk/aerospace/military/uav-flies-on-laser-light>.
- [13] LaserMotive LLC, "Laser Power for UAVs", *LaserMotive White Paper*, 2010.
- [14] RAND Project Air Force, "Feasibility of Laser Power Transmission to a High Altitude UAV", 2011.
- [15] Robert J. Boucher; Astro Flight Inc, "History of Solar Flight", in *AIAA/SAE/ASME 20th Joint Propulsion Conference*, AIAA 1984-1429, Cincinnati, Ohio, June 11-13, 1984.
- [16] "Introducing Solara the atmospheric satellite", IEEE Spectrum, December 2013. [Online]. Available: <http://spectrum.ieee.org/aerospace/aviation/introducing-solara-the-atmospheric-satellite>.
- [17] "FAI Record ID #16052", Federation Aeronautique Internationale , 2012. [Online]. Available: <http://www.fai.org/fai-record-file/?recordId=16052>.

- [18] AeroVironment, "AeroVironment Solar-Powered Puma AE UAV Achieves Continuous Flight for More than Nine Hours", 12 August 2013. [Online]. Available: www.avinc.com/resources/presse_release/aerovironment-solar-powered-puma-ae-small-unmanned-aircraft-achieves-contin.
- [19] M. J. Allen, "Guidance and Control of an Autonomous Soaring UAV", *NASA Dryden Flight Research Center*, 2007.
- [20] C. J. Pennycuick, "Soaring Behaviour and Performances of Some East African Birds, Observed from a Motor Glider", *IBIS* 114, pp. 178-218, 1972.
- [21] N. R. J. Lawrance and S. Sukkarieh, "Path Planning for Autonomous Soaring Flight in Dynamic Wind Fields", in *IEEE International Conference on Robotics and Auto*, Shanghai, China, 2011.
- [22] G. Wood, *The Guinness Book of Animals Facts and Feats*, Sterling Pub Co Inc, 1983.
- [23] C. J. Pennycuick, "The flight of petrels and albatrosses (Procellariiformes), observed in South Georgia and its vicinity", *Phil. Trans. R. Soc. Lond.*, vol. B. 300, pp. 75-106, 1982.
- [24] S. A. Shaffer, H. Weimerskirch and D. P. Costa, "Functional significance of sexual dimorphism in Wandering Albatrosses, *Diomedea Exulans*", *Functional Ecology*, no. 15, pp. 203-210, 2001.
- [25] C. J. Pennycuick, *Modelling the Flying Bird*, Academic Press, 2008.
- [26] C. J. Pennycuick, "Gliding flight of the white-backed vulture *Gyps Africanus*", *J. Exp. Biol.*, no. 55, pp. 13-38, 1971.

- [27] L. Rayleigh, "The Soaring of Birds", *Nature*, vol. 27, no. 701, pp. 534-535, April 1883.
- [28] L. B. Spear and D. G. Ainley, "Flight speed of seabirds in relation to wind speed and direction", *Ibis*, no. 139, pp. 234-251, 1997.
- [29] T. Alerstam, G. A. Gudmunsson and B. Larsson, "Flight Tracks and Speeds of Antarctic Seabirds: Radar and Optical Measurements", *Philosophical Transactions: Biological Sciences*, vol. 340, no. 1291, pp. 55-67, 1993.
- [30] P. Jouventin and H. Weimerskirch, "Satellite tracking of Wandering albatrosses", *Nature*, no. 343, pp. 746-748, 1990.
- [31] P. A. Prince, A. G. Wood, T. Barton and J. P. Croxall, "Satellite tracking of wandering albatrosses (*Diomedea exulans*) in the South Atlantic", *Antarctic Science*, vol. 4, no. 1, pp. 31-36, 1992.
- [32] H. Weimerskirch, M. Salamolard, F. Sarrazin and P. Jouventin, "Foraging Strategies of Wandering Albatrosses through the Breeding Season: A Study Using Satellite Telemetry", *The Auk*, vol. 110, no. 2, pp. 325-342, April 1993.
- [33] H. Weimerskirch, F. Bonadonna, F. Bailleul, G. Mabile, G. Dell'Omo and H.-P. Lipp, "GPS Tracking of Foraging Albatross", *Science*, vol. 295, p. 1259, 2002.
- [34] J. P. Croxall, J. R. D. Silk, R. A. Phillips, V. Afanasyev and D. R. Briggs, "Global Circumnavigations: Tracking Year-Round Ranges of Nonbreeding Albatrosses", *Science*, vol. 307, pp. 249-250, January 2005.
- [35] H. Weimerskirch, T. Guionnet, J. Martin, S. A. Shaffer and D. P. Costa, "Fast and Fuel Efficient? Optimal use of wind by flying albatrosses", *Proc. R. Soc. Lond.*, no. 267, pp. 1869-1874, 2000.

- [36] Birdlife International, "Tracking Ocean Wanderers", Birdlife International, Cambridge, UK, 2004.
- [37] NASA, "Surface meteorology and solar energy: Methodology", 2004.
- [38] H. Weimerskirch and al., "Changes in Wind Pattern Alter Albatross Distribution and Life-History Traits", *Science*, no. 335, pp. 211-214, 2012.
- [39] R. M. Suryan, D. J. Anderson and S. A. Shaffer, "Wind, Waves, and Wing Loading : Morphological Specialization May Limit Range Expansion of Endangered Albatrosses", *Plosone*, vol. 3, no. 12, pp. 1-8, December 2008.
- [40] A. Lippisch, "Effect of Aerodynamic Design on Glider Performance", *Luftfahrtforschung*, vol. 11, no. 5, 1934.
- [41] C. Pennycuik, "Gust soaring as the basis for the flight of petrels and albatrosses (Procellariiformes)", *Avian Science*, vol. 2, no. 1, 2002.
- [42] P. L. Richardson, "How do albatrosses fly around the world without flapping their wing?", *Progress in Oceanography*, vol. 88, pp. 46-58, 2011.
- [43] G. Sachs, J. Traugott and F. Holzapfel, "Progress against the Wind with Dynamic Soaring- Results from In-Flight Measurements of Albatrosses -", in *AIAA Guidance, Navigation, and control Conference, AIAA 2011-6225*, Portland, Oregon, 2011.
- [44] G. Sachs, J. Traugott, A. P. Nesterova and F. Bonadonna, "Experimental verification of dynamic soaring in albatrosses", *The Journal of Experimental Biology*, no. 216, pp. 4222-4232, 2013.

- [45] P. Idراع, “Etude expérimentale et analytique du vol sans battements des oiseaux voiliers des mers australes, de l’Albatross en particulier”, *La Technique Aéronautique*, no. 16, pp. 9-22, 1925.
- [46] C. J. Wood, “The flight of albatrosses (a computer simulation)”, *Ibis*, no. 115, pp. 244-256, 1973.
- [47] G. Sachs, “Minimum shear wind strength required for dynamic soaring of albatrosses”, *Ibis*, vol. 147, pp. 1-10, 2005.
- [48] Y. J. Zhao, “Optimal patterns of glider dynamic soaring”, *Optim. Control Appl. Meth.*, no. 25, pp. 67-89, 2004.
- [49] Y. J. Zhao and Y. C. Qi, “Minimal fuel powered dynamic soaring of unmanned aerial vehicle utilizing wind gradients”, *Optim. Control Appl. Meth.*, no. 25, pp. 211-233, 2004.
- [50] M. Deittert, A. Richards and C. A. Toomer, “Engineless Unmanned Aerial Vehicle Propulsion by Dynamic Soaring”, *Journal of Guidance, Control and Dynamics*, vol. 35, no. 5, September-October 2009.
- [51] P. Lissaman, “Wind Energy Extraction by Birds and Flight Vehicles”, in *43rd AIAA Aerospace Sciences Meeting and Exhibit, AIAA 2005-241*, Reno, Nevada, 2005.
- [52] N. R. J. Lawrance and S. Sukkarieh, “A guidance and control strategy for dynamic soaring with a gliding UAV”, in *IEEE International Conference on Robotics and Automation*, Kobe, Japan, 2009.
- [53] P. P. Sukumar and M. S. Selig, “Dynamic Soaring of Sailplanes over Open Fields”, *Journal of Aircraft*, vol. 50, no. 5, pp. 1420-1430, 2013.

- [54] N. Akhtar, J. F. Whidborne and A. K. Cooke, "Wind Shear Energy Extraction using Dynamic Soaring Techniques", in *47th AIAA Aerospace Sciences Meeting Including The New Horizons Forum and Aerospace Exposition, AIAA 2009-734*, Orlando, Florida, 2009.
- [55] R. Barate, S. Doncieux and J.-A. Meyer, "Design of a bio-inspired controller for dynamic soaring in a simulated UAV", *Bioinspir. Biomim.*, vol. 1, pp. 76-88, 2006.
- [56] X.-Z. Gao, Z.-X. Hou, Z. Guo, R.-F. Fan and X.-Q. Chen, "Analysis and Design of Guidance-Strategy for Dynamic Soaring UAVs", *Control Engineering Practice*, 2013.
- [57] J. L. Grenestedt and J. R. Spletzer, "Towards Perpetual Flight of a Gliding Unmanned Aerial Vehicle in the Jet Stream", in *IEEE Int. Conf. on Decision and Control (CDC)*, Atlanta, USA, December 2010.
- [58] J. Grenestedt and J. Spletzer, "Optimal Energy Extraction During Dynamic Jet Stream Soaring", in *AIAA Guidance, Navigation and Control Conference, AIAA 2010-8036*, Toronto, Canada, 2010.
- [59] J. Grenestedt, C. Montella and J. Spletzer, "Dynamic Soaring in Hurricanes", in *International Conference on Unmanned Aircraft Systems*, Philadelphia, PA, June 2012.
- [60] P. Richardson, "High speed Dynamic Soaring", *RC Soaring Digest*, vol. 29, no. 4, pp. 36-49, 2012
- [61] P. Richardson, "High-Speed Robotic Albatross: Unmanned Aerial Vehicle powered by dynamic soaring", *RC Soaring Digest*, vol. 29, no. 6, pp. 4-18, 2012.
- [62] C. K. Patel, H.-T. Lee and I. M. Kroo, "Extracting Energy from Atmospheric Turbulence", *Technical Soaring*, vol. 33, no. 4, pp. 100-108, 2009.

- [63] P. Lissaman and C. K. Patel, "Neutral Energy Cycles for a Vehicle in Sinusoidal and Turbulent Vertical Gusts", in *45th AIAA Aerospace Sciences Meeting and Exhibit, AIAA 2007-863*, Reno, Nevada, 2007.
- [64] J. W. Langelaan, "Gust Energy Extraction for Mini and Micro Uninhabited Aerial Vehicles", *Journal of Guidance, Control, and Dynamics*, vol. 32, no. 2, pp. 464-473, 2009.
- [65] J. W. Langelaan, "Biologically Inspired Flight Techniques for Small and Micro Unmanned Aerial Vehicles", in *AIAA Guidance, Navigation and Control Conference and Exhibit, AIAA 2008-6511*, Honolulu, Hawaii, 2008.
- [66] J. W. Langelaan, N. Alley and J. Neidhoefer, "Wind Field Estimation for Small UAV", *Journal of Guidance, Control, and Dynamics*, vol. 34, no. 4, pp. 1016-1030, 2011.
- [67] G. C. Bower, "Boundary Layer Dynamic Soaring for Autonomous Aircraft: Design and Validation. Ph.D. Dissertation", Aeronautics and Astronautics Dept., Stanford, December 2011.
- [68] G. C. Bower, T. C. Flanzer and I. M. Kroo, "Conceptual Design of a Small UAV for Continuous Flight Over the Ocean", in *11th AIAA Aviation Technology, Integration, and Operations (ATIO) Conference, AIAA 2011-7072*, Virginia Beach, VA, 2011.
- [69] Delair-Tech, "DT-18", Delair-Tech, 2015. [Online]. Available: <http://www.delair-tech.com/wp-content/uploads/2015/02/DT18.pdf>.
- [70] N. R. Lawrance, "Autonomous Soaring Flight for Unmanned Aerial Vehicles, Ph.D. thesis", The University of Sydney, 2011.
- [71] A. Deperrois, "XFLR5", 2015. [Online]. Available: <http://www.xflr5.com/xflr5.htm>.

- [72] M. Drela and H. Youngren, “AVL”, 2015. [Online]. Available: <http://web.mit.edu/drela/Public/web/avl/>.
- [73] J. D. Anderson Jr., FUNDAMENTALS OF AERODYNAMICS, McGraw-Hill, 1984.
- [74] V. Allain, “DAEP-SOUFFLERIE S4, CATALOGUE DES MOYENS D’ESSAIS DE LA SOUFFLERIE S4”, ISAE, Toulouse, October 2011.
- [75] A. S. Monin and A. M. Yaglom, Statistical Fluid Mechanics, the MIT press, 5th printing 1987.
- [76] R. B. Stull, An Introduction to Boundary Layer Meteorology, Atmospheric Science Library, 1994.
- [77] C. W. Fairall, A. A. Grachev, A. J. Bedard and R. T. Nishiyama, “Wind, Wave, Stress, and Surface Roughness Relationships from Turbulence Measurements made on R/P FLIP in the SCOPE experiment”, A report for the DoD ASAP Program, April 1996.
- [78] M. A. Donelan, F. W. Dobson, S. D. Smith and R. J. Anderson, “On the Dependence of Sea Surface Roughness on Wave Development”, *J. Phys. Oceanogr.*, no. 23, p. 2143–2149, 1993.
- [79] D. J. Carter, “Prediction of Wave Height and Period for a Constant Wind Velocity using the JONSWAP Results”, *Ocean Engineering*, vol. 9, no. 1, pp. 17-33, 1982.
- [80] P. Sullivan, J. McWilliams and C.-H. Moeng, “Simulation of turbulent flow over idealized water waves”, *J. Fluid. Mech.*, vol. 404, pp. 47-85, 2000.

- [81] T. B. Benjamin, "Shearing flow over a wavy boundary", *J. Fluid. Mech.*, vol. 6, pp. 161-205, 1959.
- [82] D. G. Hull, "Conversion of Optimal Control Problem into Parameter Optimization Problems", *Journal of Guidance, Control and Dynamics*, vol. 20, no. 1, pp. 57-60, 1997.
- [83] A. L. Hermann and B. A. Conway, "Direct Optimization Using Collocation Based on High Order Gauss-Lobatto Quadrature Rules", *Journal of Guidance, Control and Dynamics*, vol. 19, no. 3, pp. 592-599, 1996.
- [84] C. R. Hargraves and S. W. Paris, "Direct Trajectory Optimization using Nonlinear Programming and Collocation", *Journal of Guidance, Control, and Dynamics*, vol. 10, no. 4, pp. 338-342, 1987.
- [85] J. Nocedal and S. J. Wright, *Numerical Optimization*, Springer, 2006.
- [86] P. Venkataraman, *Applied Optimization with MATLAB Programming*, Wiley, April 2009.
- [87] "NEOS server", Wisconsin Institute for Discovery, 2014. [Online]. Available: www.neos-server.org/neos/.
- [88] J. Czyzyk, M. P. Mesnier and J. Moré, "The NEOS server", *IEEE Journal on Computational Science and Engineering*, vol. 5, no. 3, pp. 68-75, 1998.
- [89] E. Dolan, "The NEOS Server 4.0 Administrative Guide", Mathematics and Computer Science Division, Argonne National Laboratory, 2001.
- [90] W. Gropp and J. J. Moré, "Optimization Environments and the NEOS Server", *Approximation Theory and Optimization*, pp. 167-182, 1997.

- [91] P. E. Gill, W. Murray and M. A. Saunders, “An SQP Algorithm for Large-Scale Constrained Optimization”, *SIAM Review*, vol. 47, no. 1, pp. 99-131, March 2005.
- [92] R. Fourer, D. M. Gay and B. W. Kernighan, *AMPL: A Modeling Language for Mathematical Programming*, Second Edition, 2003.
- [93] D. M. Gay, “Automatic Differentiation of Nonlinear AMPL Models”, 1991.
- [94] L. Hargrave, “Sailing Birds are Dependent on Wave Power”, *Royal Society of New South Wales*, September 1899.
- [95] Z. Akos, M. Nagy, S. Leven and T. Vicsek, “Thermal soaring flight of birds and UAVs”, *Bioinspir. Biomim.*, vol. 5, no. 4, 2010.
- [96] A. Chakrabarty and J. W. Langelaan, “Flight Path Planning for UAV Atmospheric Energy Harvesting Using Heuristic Search”, in *AIAA Guidance, Navigation and Control Conference*, AIAA 2010-8033, Toronto, Canada, 2010.

Appendix A

List of publications:

- V. Bonnin, E. Benard, C.A. Toomer, J.M. Moschetta, “Dynamic Soaring in the Ocean Boundary Layer”, *International Journal of Engineering Systems Modelling and Simulation*, Vol 8, 2016.
- V. Bonnin, C.A. Toomer, E. Benard, J.M. Moschetta, “Energy-Harvesting Mechanisms for UAV flight by Dynamic Soaring”, *International Journal of Micro Air Vehicles*, Vol 7, No 3, September 2015.